



A NOVEL METHOD FOR CHARACTERIZING THE IMPACT
RESPONSE OF FUNCTIONALLY GRADED PLATES

DISSERTATION

Reid A. Larson, Captain, USAF

AFIT/DS/ENY/08-06

DEPARTMENT OF THE AIR FORCE
AIR UNIVERSITY

AIR FORCE INSTITUTE OF TECHNOLOGY

Wright-Patterson Air Force Base, Ohio

APPROVED FOR PUBLIC RELEASE; DISTRIBUTION UNLIMITED.

The views expressed in this thesis are those of the author and do not reflect the official policy or position of the United States Air Force, Department of Defense, or the United States Government.

AFIT/DS/ENY/08-06

A NOVEL METHOD FOR CHARACTERIZING THE IMPACT
RESPONSE OF FUNCTIONALLY GRADED PLATES

DISSERTATION

Presented to the Faculty
Graduate School of Engineering and Management
Air Force Institute of Technology
Air University
Air Education and Training Command
In Partial Fulfillment of the Requirements for the
Degree of Doctor of Philosophy

Reid A. Larson, B.S.M.E., M.S.M.E.
Captain, USAF

September 2008

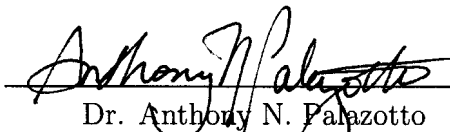
APPROVED FOR PUBLIC RELEASE; DISTRIBUTION UNLIMITED.

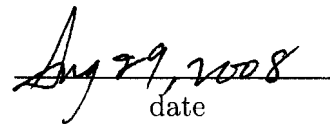
A NOVEL METHOD FOR CHARACTERIZING THE IMPACT
RESPONSE OF FUNCTIONALLY GRADED PLATES

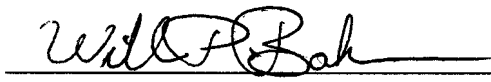
Reid A. Larson, B.S.M.E., M.S.M.E.

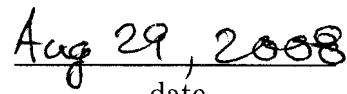
Captain, USAF

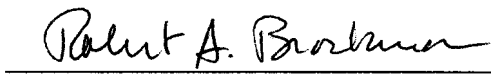
Approved:


Dr. Anthony N. Palazotto
Committee Chairman

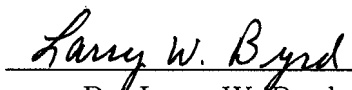

date

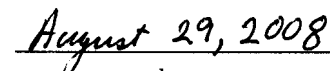

Dr. William P. Baker
Committee Member

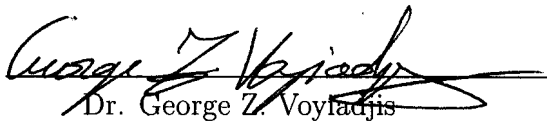

date

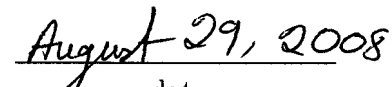

Dr. Robert A. Brockman
Committee Member


date



Dr. Larry W. Byrd
Committee Member

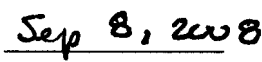

date


Dr. George Z. Voyiadjis
Committee Member


date

Accepted:


M. U. THOMAS
Dean, Graduate School of Engineering
and Management


date

Abstract

Functionally graded materials (FGMs) are advanced composites with mechanical properties that vary continuously through a given dimension. The properties are graded by combining two or more constituents and varying the volume fractions of the constituents to locally tailor the structure to suit specific applications. FGMs, especially metal-ceramic composites, have generated a great deal of interest in the aerospace community in recent years due to their potential flexibility for use in structural applications where extreme thermal and corrosion resistance are required. A proposed application for FGMs is the combination of exterior thermal protection with flight load-bearing structure into a single construction for space-access vehicles. A critical design requirement of any such material used as external thermal protection is the ability to withstand an impact from a foreign object in either the atmosphere or space without compromising the underlying structure. Modeling such impacts involves a deep understanding of the complex physics involved, especially the local and global dynamic response of the material and structure. Impact response and stress wave propagation in FGMs have been given almost no treatment in the current literature. Characterization of FGM impacts is therefore an area of rich research and great interest. This dissertation demonstrates a novel methodology for characterizing the impact response of FGM plates. Since this work is an early study in the response of FGMs subject to impact, the problem was simplified to studying the impact response of metal-ceramic FGM plates subject to a low-velocity, low- to medium-energy impact load in a room-temperature environment.

The methodology involved in characterizing the impact response of FGM plates consists of the following steps: (1) obtain experimental strain histories from FGM plate specimens subject to impact loading, (2) construct a finite element model of the FGM impact experiment given available material properties and material models

for the constituents and constituent mixtures, (3) utilize an analytical parameter estimation sequence to determine the local material properties of an anisotropic, non-homogeneous mixture by minimizing the error between the finite element models and experiments, and (4) study the physics of the impact experiments through the optimized finite element model and extend the findings to other applications of the FGM system studied.

The novel method to characterize the impact response of FGM plates was demonstrated in the following manner. First, a set of monolithic and functionally graded titanium-titanium boride metal-ceramic plate specimens was obtained for impact experiments. A gravity-driven impact test apparatus was used to deliver concentrated impact loads of various energies and velocities to the center of each plate specimen. The specimens were placed in a fixture that configured the plates very closely to a simply-supported circular plate. Strain histories were collected during the experiments to gain insight into the behavior of the plates under impact loading. A sophisticated finite element model of the experiment was developed capable of incorporating various material models to study the impact experiments. Once the finite element model was validated based on correlation with the results from the impact tests, a novel parameter estimation sequence was used to refine the estimates for local material properties in the metal-ceramic FGMs. The parameter estimation sequence resulted in a finite element model that more closely reflected the impact experiments and determined local properties consistent with published values for the FGM system. The refined finite element model was then used to carefully study the impact tests more closely where valuable conclusions with respect to the physics and behavior of FGM plates under impact were drawn. The method detailed in this work provides key contributions to the knowledge and understanding of functionally graded composites subject to impact loading from which future research efforts can build on.

Acknowledgements

I would first like to acknowledge the support and guidance of my academic and research advisor, Dr. Anthony Palazotto. I am very much indebted to him for the countless hours he dedicated to helping me attain my degree. He is indeed a great mentor and friend. I would additionally like to thank each member of my research committee for volunteering to support and guide me through this difficult endeavor: Dr. William Baker, AFIT/ENC; Dr. Robert Brockman, University of Dayton; Dr. Larry Byrd, AFRL/RBSM; and Dr. George Voyiadjis, Louisiana State University. I am deeply indebted to each of these men for their advice, guidance, and encouragement.

This research project was sponsored and funded through a number of organizations. First, the primary sponsor of this work was the Air Force Research Laboratory's Air Vehicles Directorate Structural Science Center (AFRL/RBS) located at Wright-Patterson AFB, OH. The Dayton Area Graduate Studies Institute (DAGSI) initially awarded Dr. Palazotto and I the AFRL/DAGSI Ohio Student-Faculty Research Fellowship for the 2006-2008 academic years. Next, the Air Force Research Laboratory's Munitions Directorate (AFRL/MNAC) at Eglin AFB, FL, had taken interest in our efforts to characterize functionally graded materials and funded portions of this work.

I would like to acknowledge the following individuals who directly contributed to this research in various capacities: Dr. Ravinder Chona, Dr. Andrew Sparks, Mr. Brian Smyers, Mr. Richard Wiggins, & Mr. Brett Hauber (AFRL/RBS); Capt Hugh E. Gardenier, Mr. Dan Ryan, & Mr. Jay Anderson (AFIT); Mr. Kevin Poormon (Univ. of Dayton Research Institute); Cadet Rachael DeRoche (Pennsylvania State University); Cadet Joseph Sabat (Air Force Academy); Dr. Glaucio Paulino (Univ. of Illinois, Urbana-Champaign); and Dr. George Bibel (Univ. of North Dakota).

I would also like to thank my wife for her patience and encouragement during the last several years. My wife patiently and lovingly watched her husband working countless nights and weekends during this pursuit. I am also thankful to my children

for patiently enduring while I completed my college degrees. Lastly, I would thank all my friends and family members for their support and encouragement over the last several years.

Most importantly, I am very humbled and thankful to my Lord for granting to me the honor of pursuing and achieving my doctorate degree.

“The Lord has done great things for us; we are glad!”—Psalm 126:3

“With men these things are impossible; with God all things are possible.”—Mark 10:27

Reid A. Larson

Table of Contents

	Page
Abstract	iv
Acknowledgements	vi
List of Figures	xii
List of Tables	xxiii
List of Symbols	xxvii
List of Abbreviations	xxxii
 I. Introduction	 1
II. Literature Review of FGM Studies	9
2.1 Residual Stress Studies	9
2.2 Thermoelastic Static Analyses	13
2.3 Thermomechanical Buckling Studies	16
2.4 Vibration Analyses of FGMs	19
2.5 Stress Wave and Impact Analyses	22
2.6 Concluding Remarks	25
III. Material Models and Relevant Plate Theory	26
3.1 Material Models	26
3.1.1 Classical Rule-of-Mixtures	26
3.1.2 Modified Rule-of-Mixtures	29
3.1.3 Self-Consistent Estimates	30
3.1.4 Mori-Tanaka Estimates	32
3.1.5 Other Models	34
3.2 Relevant Plate Theory	35
3.2.1 Rectangular Flat Plates	35
3.2.2 Circular Plates Subject to Axisymmetric Bending	47
3.3 Closing	52
IV. Titanium-Titanium Boride FGM System	53
4.1 Manufacturing Titanium-Titanium Boride FGMs	54
4.2 Titanium, Titanium Boride Constituents	54
4.2.1 Titanium	55
4.2.2 Titanium Boride	58

	Page
4.3 Ti-TiB MMC and FGM Specimens	61
4.4 Closing	68
V. FGM Plate Impact Experiments	70
5.1 Plate Impact Experiments and Set-Up	71
5.1.1 Test Hardware	71
5.1.2 Instrumentation	84
5.1.3 Strain History Measurement	93
5.2 Plate Impact Test Results	94
5.2.1 Pre-Test Inspection of the Ti-TiB Plates	94
5.2.2 Dynatup Plate Impacts	101
5.2.3 Post-Test Inspection of Plate Specimens	112
5.3 Closing Remarks	113
VI. Finite Element Modeling of Plate Impact Experiments	116
6.1 Finite Element Model Development	116
6.1.1 Plate Fixture Finite Element Model	116
6.1.2 Tup and Load Cell Finite Element Model	122
6.1.3 FGM Plate Specimen Models	124
6.1.4 FEM Loads and Constraints	131
6.2 Validation of Finite Element Model	137
6.2.1 Solution of the FEM	137
6.2.2 Strain Distribution Under Strain Gages	140
6.2.3 FEM vs. Experiment—Maximum Strains	142
6.2.4 FEM vs. Experiment—Strain Histories	147
6.3 Closing Remarks	159
VII. Analytical Treatment of the FGM Plate Impacts	160
7.1 Dynamic Considerations From Impact Loading	160
7.2 Analytical Model for Estimating Plate Impact Response	165
7.2.1 Formulation	166
7.2.2 Clamped Boundary Condition	172
7.2.3 Simply-Supported Boundary Condition	175
7.3 Validation of Analytical Model	177
7.4 Closing	183

	Page
VIII. Estimation of Ti-TiB Material Parameters	184
8.1 Problem Formulation & Overview	185
8.2 Estimating Transverse Deflection from the Two-Phase FEM	189
8.3 Solution to the Minimization Problem	200
8.3.1 General Constrained Minimization Problem	201
8.3.2 FGM Plate Parameter Estimation Problem	205
8.3.3 Numerical Solution	207
8.4 Implementation	211
8.5 Results	212
8.6 Closing	221
IX. Study of the Impact Response of the FGM Plates	223
9.1 Tup and Plate Interaction	223
9.2 Loading and Unloading of the FGM Plates	226
9.3 Stresses in the FGM Plates	233
9.4 Effects of Non-Central Impact Load	250
9.5 Closing Remarks	252
X. Conclusions	254
10.1 Summary of Research Conducted	255
10.2 Key Contributions	258
10.3 General Discussion	259
Appendix A. Strain Gage Instrumentation	263
A.1 Strain Gages	263
A.2 Signal Conditioner	264
A.3 Data Acquisition Unit	271
Appendix B. Plate Experiments Raw Data	274
B.1 Plate #1: Monolithic 100% Ti-0% TiB Specimen	276
B.2 Plate #2: Monolithic 100% Ti-0% TiB Specimen	278
B.3 Plate #3: Monolithic 85% Ti-15% TiB Specimen	280
B.4 Plate #4: Monolithic 85% Ti-15% TiB Specimen	282
B.5 Plate #5: Monolithic 15% Ti-85% TiB Specimen	284
B.6 Plate #6: Monolithic 15% Ti-85% TiB Specimen	286
B.7 Plate #7: Seven Layer Ti-TiB FGM Specimen	288
B.8 Plate #8: Seven Layer Ti-TiB FGM Specimen	290
B.9 Plate #9: Seven Layer Ti-TiB FGM Specimen	292
B.10 Plate #10: Seven Layer Ti-TiB FGM Specimen	294

	Page
Appendix C. Overview of Relevant Finite Element Theory	296
C.1 Explicit Integration Solution Scheme	296
C.2 Deformation, Strain, and Stress Definitions	300
C.2.1 Deformation	300
C.2.2 Strain and Strain Rate	303
C.2.3 Stress	305
C.3 Governing Equations	307
C.4 Solid Continuum Finite Elements	310
C.4.1 Isoparametric Element Formulation	311
C.4.2 Constitutive Relation	312
C.4.3 Quadrature	314
C.5 Contact Algorithm	316
Bibliography	323
Vita	333

List of Figures

Figure		Page
1.1.	Power-law distribution of ceramic in terms of volume fraction for a metal-ceramic FGM plate graded through the thickness given various n exponents.	3
1.2.	Cross-section of FGM plate with power-law ceramic volume fraction distribution; $n = 2.0$. Dark regions are ceramic rich, light regions metal-rich [32].	3
3.1.	Illustration of modified rule-of-mixtures approach for obtaining stress-strain constitutive data for two-phase mixtures. A metal-ceramic combination is shown here, with constituent 1 being ceramic and constituent 2 being a ductile metal. [122], [134]. . .	31
3.2.	Visual comparison of displacement fields of (a) classical plate theory & (b) first-order shear deformation theory (adapted from [100]).	38
3.3.	Coordinate notation for through-thickness layup of composite plate.	46
4.1.	Microscopic view of Ti-TiB FGM [26]. TiB rich areas are near the top surface; Ti rich areas are near the bottom surface. . .	55
4.2.	Hexagonal close-packed crystal structure of titanium at room-temperature. The dimensions of the crystal shown are $a = 295$ picometers and $c = 468$ picometers (1 picometer = 1×10^{-12} meters) [40].	56
4.3.	Trigonal prism building block for the orthorhombic crystal structure of TiB [109].	60
4.4.	Illustration of layers in FGM plate specimens.	62
4.5.	Scanning electron microscope image of 100% Ti (courtesy of Mr. Brett Hauber, AFRL).	63
4.6.	Scanning electron microscope image of 85% Ti, 15% TiB mixture (courtesy of Mr. Brett Hauber, AFRL).	63
4.7.	Scanning electron microscope image of 70% Ti, 30% TiB mixture (courtesy of Mr. Brett Hauber, AFRL).	64

Figure		Page
4.8.	Scanning electron microscope image of 55% Ti, 45% TiB mixture (courtesy of Mr. Brett Hauber, AFRL).	64
4.9.	Scanning electron microscope image of 40% Ti, 60% TiB mixture (courtesy of Mr. Brett Hauber, AFRL).	65
4.10.	Scanning electron microscope image of 25% Ti, 75% TiB mixture (courtesy of Mr. Brett Hauber, AFRL).	65
4.11.	Scanning electron microscope image of 15% Ti, 85% TiB mixture (courtesy of Mr. Brett Hauber, AFRL).	66
5.1.	Dynatup apparatus used for low- to medium-energy impact testing.	73
5.2.	Schematic showing the major components of the Dynatup apparatus.	74
5.3.	Dynatup apparatus with plate fixture installed.	75
5.4.	Assembled and exploded view of the plate specimen fixture used in the Dynatup apparatus.	76
5.5.	Bottom plate in the Dynatup plate specimen fixture assembly. The plate was machined from 304 stainless steel plate stock 1.27-cm thick. All dimensions are in <i>cm</i> unless otherwise specified.	79
5.6.	Spacer plate in the Dynatup plate specimen fixture assembly. The plate was machined from 304 stainless steel plate stock 1.27-cm thick. All dimensions are in <i>cm</i> unless otherwise specified.	80
5.7.	Top plate in the Dynatup plate specimen fixture assembly. The plate was machined from 304 stainless steel plate stock 1.27-cm thick. All dimensions are in <i>cm</i> unless otherwise specified.	81
5.8.	Plate fixture with FGM specimen plate installed in Dynatup.	82
5.9.	Illustration of layers in FGM plate specimens.	84
5.10.	Plate specimen. Titanium, Ti-TiB monolithic, and Ti-TiB FGM specimens were machined using this specification. Placement of strain gages also shown. All dimensions are in <i>cm</i> unless otherwise specified.	85
5.11.	FGM plate specimen with strain gages installed.	86

Figure		Page
5.12.	Vishay 125AC series strain gage used in impact tests for collecting strain histories [127].	88
5.13.	Illustration of strain gage configuration with separate bonded terminal for attachment of the wire leads to signal conditioner and two single-stranded jumper wires from the terminal soldered to the strain gages [130].	89
5.14.	Schematic showing the sytem components for collecting strain histories from Dynatup impact events.	95
5.15.	Through-transmission immersed ultrasonic C-scans of Ti-TiB monolithic and functionally graded plate specimens prior to impact testing. The color contours represent the percentage of the peak signal from the piezoelectric emitter (51 dB at 2.25 MHz frequency) detected by the piezoelectric receiver underneath the specimen according to the scale shown.	99
5.16.	Illustration of areas requiring data processing from raw strain history.	104
5.17.	Strain histories for strain gages 1-3, 100% Ti monolithic plate, plate test no. 1.	107
5.18.	Strain histories for strain gages 1-3, 100% Ti monolithic plate, plate test no. 2.	107
5.19.	Strain histories for strain gages 1-3, 85% Ti–15% TiB monolithic plate, plate test no. 3.	108
5.20.	Strain histories for strain gages 1-3, 85% Ti–15% TiB monolithic plate, plate test no. 4.	108
5.21.	Strain histories for strain gages 1-3, Ti-TiB FGM plate, plate test no. 7.	109
5.22.	Strain histories for strain gages 1-3, Ti-TiB FGM plate, plate test no. 8.	109
5.23.	Strain histories for strain gages 1-3, Ti-TiB FGM plate, plate test no. 9.	110
5.24.	Strain histories for strain gages 1-3, Ti-TiB FGM plate, plate test no. 10.	110

Figure		Page
5.25.	Apparent flexure of plate during impact events in Dynatup tests.	112
5.26.	Through-transmission immersed ultrasonic C-scans of Ti-TiB monolithic and functionally graded plate specimens after impact testing. The color contours represent the percentage of the peak signal from the piezoelectric emitter (51 dB at 2.25 MHz frequency) detected by the piezoelectric receiver underneath the specimen according to the scale shown. Note that three specimens failed the initial impact tests.	114
6.1.	Finite element mesh and model for the plate impact experiments.	117
6.2.	Eight-noded linear brick element as used in the finite element model.	118
6.3.	Plate specimen fixture; bottom plate component finite element mesh.	119
6.4.	Plate specimen fixture; spacer plate component finite element mesh.	119
6.5.	Plate specimen fixture; top plate component finite element mesh.	120
6.6.	Simplified finite element models for the eight plate fastener screws (left) and four Dynatup attachment screws (right).	122
6.7.	Simplified finite element model of mass, load cell, and tup in Dynatup apparatus.	123
6.8.	Comparison of actual seven-layer Ti-TiB FGM (left) and FEM representations: homogenized-layers model (middle) and two-phase model (right). In the FEM representations, Ti-rich areas are white and TiB-rich areas are black.	125
6.9.	Comparison of homogenized-layers and two-phase plate specimen FEMs; see also Figure 6.8.	127
6.10.	Reference planes used in FEM constraints.	132
6.11.	Illustration of selected contact areas between the plate fixture, specimen plates, and fastener screws.	135
6.12.	Bottom view of experiment FEM showing nodal locations corresponding to nominal location of strain gages 1-3; also node at center of plate on bottom surface of specimen.	139

Figure		Page
6.13.	Strain gage used in impact tests for collecting strain histories [127], shown with the approximate location of the corresponding 12 nodes as arranged in the FEM analyses.	141
6.14.	Strain variation that occurs along strain gage axes, for (a) two-phase model, (b) homogenized-layers model (Mori-Tanaka needles) in Dynatup test 8 at instant of maximum plate deflection.	141
6.15.	Test 8 FEM strain histories across strain gage 1; twelve in all, one plot for each node (Mori-Tanaka Needles FEM model) as shown in Figures 6.12 and 6.13. The histories of higher strain magnitude are closer to the center of the plate.	142
6.16.	Test 1 (monolithic) experimental strain histories & FEM comparison using two-phase plate model: a) strain gage 2, b) strain gage 3.	149
6.17.	Test 2 (monolithic) experimental strain histories & FEM comparison using two-phase plate models: a) strain gage 2, b) strain gage 3.	149
6.18.	Test 3 (monolithic) experimental strain histories & FEM comparison using two-phase and Mori-Tanaka Needles plate models: a) strain gage 2, b) strain gage 3.	150
6.19.	Test 4 (monolithic) experimental strain histories & FEM comparison using two-phase and Mori-Tanaka Needles plate models: a) strain gage 2, b) strain gage 3.	150
6.20.	Test 7 (FGM) experimental strain histories & FEM comparison using two-phase and Mori-Tanaka Needles plate models: a) strain gage 2, b) strain gage 3.	151
6.21.	Test 8 (FGM) experimental strain histories & FEM comparison using two-phase and Mori-Tanaka Needles plate models: a) strain gage 2, b) strain gage 3.	151
6.22.	Test 9 (FGM) experimental strain histories & FEM comparison using two-phase and Mori-Tanaka Needles plate models: a) strain gage 2, b) strain gage 3.	152

Figure		Page
6.23.	Test 10 (FGM) experimental strain histories & FEM comparison using two-phase and Mori-Tanaka Needles plate models: a) strain gage 2, b) strain gage 3.	152
6.24.	Test 9 (FGM) finite element strain histories using the Mori-Tanaka Needles plate model at the locations of: a) strain gage 2, b) strain gage 3. The histories are plotted for coefficients of sliding friction ranging from 0.00-1.00.	157
7.1.	Specimen plate with gages, with key reference positions annotated.	179
7.2.	Transverse displacement of the plate in test 1 at maximum center displacement given the FEM and analytical predictions with clamped BC.	181
7.3.	Transverse displacement of the plate in test 1 at maximum center displacement given the FEM and analytical predictions with simply-supported BC.	181
7.4.	Radial strain distributions on the bottom surface of the plate (experiment, FEM, and analytical) in test 1 at maximum center displacement with clamped BC.	182
7.5.	Radial strain distributions on the bottom surface of the plate (experiment, FEM, and analytical) in test 1 at maximum center displacement with simply-supported BC.	182
8.1.	Test 7 experimental strain histories & FEM comparison using optimized Mori-Tanaka Needles plate models: a) strain gage 2, b) strain gage 3.	219
8.2.	Test 8 experimental strain histories & FEM comparison using optimized Mori-Tanaka Needles plate models: a) strain gage 2, b) strain gage 3.	219
8.3.	Test 9 experimental strain histories & FEM comparison using optimized Mori-Tanaka Needles plate models: a) strain gage 2, b) strain gage 3.	220
8.4.	Test 10 experimental strain histories & FEM comparison using optimized Mori-Tanaka Needles plate models: a) strain gage 2, b) strain gage 3.	220

Figure		Page
9.1.	Transverse (a) displacement and (b) velocity profiles for the node at the tip of the tup (in contact with the plate) and the node on the bottom surface of the FGM plate at the center for the optimized FEM of test 9.	226
9.2.	Four stages of the tup-plate interaction. Coordinate systems for positive deflections (u), velocities(v), and accelerations (a) are shown.	227
9.3.	A straight line was fit to the data in the loading and unloading portions of the strain history curves to determine the strain rates in each respective part of the curve. Shown are the data from FGM plate test 9, strain gage 2: (a) experimental and (b) optimized FEM with homogenized-layers MT-N model.	228
9.4.	Top view of homogenized-layers FGM plate (plate impact test 9) subject to stresses at six snapshots in time. Contours of von Mises stress, in Pascals, are plotted.	236
9.5.	Top view with section cut through middle of homogenized-layers FGM plate (plate impact test 9) subject to stresses at four snapshots in time. Contours of von Mises stress, in Pascals, are plotted.	237
9.6.	Top view with 45° section cut through middle of homogenized-layers FGM plate (plate impact test 9) subject to stresses at four snapshots in time. Contours of von Mises stress, in Pascals, are plotted.	238
9.7.	Top view of two-phase FGM plate (plate impact test 9) subject to stresses at six snapshots in time. Contours of von Mises stress, in Pascals, are plotted.	239
9.8.	Top view with section cut through middle of two-phase FGM plate (plate impact test 9) subject to stresses at four snapshots in time. Contours of von Mises stress, in Pascals, are plotted.	240
9.9.	Top view with 45° section cut through middle of two-phase FGM plate (plate impact test 9) subject to stresses at four snapshots in time. Contours of von Mises stress, in Pascals, are plotted.	241

Figure		Page
9.10.	Top view of homogenized-layers 85% Ti-15% TiB monolithic (comparable to plate impact test 9) subject to stresses at six snapshots in time. Contours of von Mises stress, in Pascals, are plotted.	242
9.11.	Top view with section cut through middle of homogenized-layers 85% Ti-15% TiB monolithic (comparable to plate impact test 9) subject to stresses at four snapshots in time. Contours of von Mises stress, in Pascals, are plotted.	243
9.12.	Top view with 45° section cut through middle of homogenized-layers 85% Ti-15% TiB monolithic (comparable to plate impact test 9) subject to stresses at four snapshots in time. Contours of von Mises stress, in Pascals, are plotted.	244
9.13.	Top view with section cut through middle of homogenized-layers 85% Ti-15% TiB monolithic, homogenized-layers Ti-TiB FGM, and two-phase Ti-TiB FGM (comparable to plate impact test 9) subject to transverse shear stresses at snapshot of maximum deflection. Section cut taken 1.0 cm from the center plane of plate. Contours of transverse shear stress on plane in section cut, in Pascals, are plotted.	247
9.14.	Transverse shear distribution through thickness of the 85% Ti-15% TiB monolithic homogenized-layers plate (MT-Needles material model) at three snapshots in time under conditions of impact test 9. Distribution is taken from 15 nodes through thickness of the plate at center of cross-section in Figure 9.13.	248
9.15.	Transverse shear distribution through thickness of the FGM homogenized layers plate (MT-Needles material model) at three snapshots in time under conditions of impact test 9. Distribution is taken from 15 nodes through thickness of the plate at center of cross-section in Figure 9.13.	248
9.16.	Transverse shear distribution through thickness of the FGM two-phase plate at three snapshots in time under conditions of impact test 9. Distribution is taken from 15 nodes through thickness of the plate at center of cross-section in Figure 9.13.	249

Figure		Page
9.17.	Specimen plate with gages and reference positions annotated. Impact sites 1 & 2 are 0.898 cm from center.	251
9.18.	Test 9 strain histories & FEM comparisons with off-centered tup impact sites per Figure 9.17 using the Mori-Tanaka Needles model: a) strain gage 2, b) strain gage 3.	251
A.1.	Vishay 125AC series strain gage used in impact tests for collecting strain histories [127].	264
A.2.	Typical Wheatstone bridge circuit [13].	266
A.3.	Typical operational amplifier [13].	268
A.4.	Typical DC differential amplifier [13].	268
A.5.	Typical Wheatstone bridge circuit with a shunt resistance for calibration purposes [13].	270
B.1.	Specimen plate with locations of strain gages for reference; see Figure 5.10 and 5.11. The fourth gage shown was not used. . .	274
B.2.	Raw data strain history for specimen plate #1, 100% Ti - 0% TiB monolithic, strain gage 1.	276
B.3.	Raw data strain history for specimen plate #1, 100% Ti - 0% TiB monolithic, strain gage 2.	277
B.4.	Raw data strain history for specimen plate #1, 100% Ti - 0% TiB monolithic, strain gage 3.	277
B.5.	Raw data strain history for specimen plate #2, 100% Ti - 0% TiB monolithic, strain gage 1.	278
B.6.	Raw data strain history for specimen plate #2, 100% Ti - 0% TiB monolithic, strain gage 2.	279
B.7.	Raw data strain history for specimen plate #2, 100% Ti - 0% TiB monolithic, strain gage 3.	279
B.8.	Raw data strain history for specimen plate #3, 85% Ti - 15% TiB monolithic, strain gage 1.	280
B.9.	Raw data strain history for specimen plate #3, 85% Ti - 15% TiB monolithic, strain gage 2.	281

Figure		Page
B.10.	Raw data strain history for specimen plate #3, 85% Ti - 15% TiB monolithic, strain gage 3.	281
B.11.	Raw data strain history for specimen plate #4, 85% Ti - 15% TiB monolithic, strain gage 1.	282
B.12.	Raw data strain history for specimen plate #4, 85% Ti - 15% TiB monolithic, strain gage 2.	283
B.13.	Raw data strain history for specimen plate #4, 85% Ti - 15% TiB monolithic, strain gage 3.	283
B.14.	Raw data strain history for specimen plate #5, 15% Ti - 85% TiB monolithic, strain gage 1.	284
B.15.	Raw data strain history for specimen plate #5, 15% Ti - 85% TiB monolithic, strain gage 2.	285
B.16.	Raw data strain history for specimen plate #5, 15% Ti - 85% TiB monolithic, strain gage 3.	285
B.17.	Raw data strain history for specimen plate #6, 15% Ti - 85% TiB monolithic, strain gage 1.	286
B.18.	Raw data strain history for specimen plate #6, 15% Ti - 85% TiB monolithic, strain gage 2.	287
B.19.	Raw data strain history for specimen plate #6, 15% Ti - 85% TiB monolithic, strain gage 3.	287
B.20.	Raw data strain history for specimen plate #7, seven-layer Ti-TiB FGM, strain gage 1.	288
B.21.	Raw data strain history for specimen plate #7, seven-layer Ti-TiB FGM, strain gage 2.	289
B.22.	Raw data strain history for specimen plate #7, seven-layer Ti-TiB FGM, strain gage 3.	289
B.23.	Raw data strain history for specimen plate #8, seven-layer Ti-TiB FGM, strain gage 1.	290
B.24.	Raw data strain history for specimen plate #8, seven-layer Ti-TiB FGM, strain gage 2.	291
B.25.	Raw data strain history for specimen plate #8, seven-layer Ti-TiB FGM, strain gage 3.	291

Figure		Page
B.26.	Raw data strain history for specimen plate #9, seven-layer Ti-TiB FGM, strain gage 1.	292
B.27.	Raw data strain history for specimen plate #9, seven-layer Ti-TiB FGM, strain gage 2.	293
B.28.	Raw data strain history for specimen plate #9, seven-layer Ti-TiB FGM, strain gage 3.	293
B.29.	Raw data strain history for specimen plate #10, seven-layer Ti-TiB FGM, strain gage 1.	294
B.30.	Raw data strain history for specimen plate #10, seven-layer Ti-TiB FGM, strain gage 2.	295
B.31.	Raw data strain history for specimen plate #10, seven-layer Ti-TiB FGM, strain gage 3.	295
C.1.	Displacement, stretch, and rotation of material vector $d\mathbf{X}$ to new position $d\mathbf{x}$ [76].	302
C.2.	Relative velocity $d\mathbf{v}$ of particle Q at point q relative to the particle P at point p [76].	303
C.3.	Force vectors for stress definitions in the undeformed state (subscript 0) and the deformed state [76].	307
C.4.	Isoparametric hexahedral element geometry. The (g,h,r) coordinates of nodes 1-8 in the parent domain are $(-1,-1,-1)$, $(+1,-1,-1)$, $(+1,+1,-1)$, $(-1,+1,-1)$, $(-1,-1,+1)$, $(+1,-1,+1)$, $(+1,+1,+1)$, $(-1,+1,+1)$, respectively.	313
C.5.	Two bodies, Ω_A & Ω_B , in contact over surface Γ_C [14].	317

List of Tables

Table		Page
4.1.	Typical material property data for commercially pure titanium at room temperature [86], [4].	56
4.2.	Typical material property data for titanium boride at room temperature [4].	59
4.3.	Composition data for Ti-TiB monolithic composites manufactured by reaction sintering [109].	60
4.4.	BAE Systems Ti-TiB FGM through-the-thickness configuration of the plate specimens shown in Figure 4.4.	62
4.5.	Elastic property data for Ti-TiB volume ratios compared with predicted values from the classical rule-of-mixtures (ROM), self-consistent model (SC), and the Mori-Tanaka (MT) estimates assuming spherical (S) and needle (N) shaped TiB embedded in a titanium matrix. Data from [4] was used to calculate properties from the material models.	67
5.1.	BAE Systems Ti-TiB FGM through-the-thickness configuration of the plate specimens shown in Figure 5.9.	84
5.2.	Strain gage and signal conditioner specifications common to all plate impact experiments. These values are necessary in order to convert voltage readings in the oscilloscope from the gages to physical strain.	95
5.3.	Summary of plate impact tests using Dynatup apparatus. . . .	101
5.4.	Comparison of predicted and actual velocities and impact energies from Dynatup impact tests.	103
5.5.	Maximum strains and associated time occurrence of maximum strains from impact tests.	111
6.1.	Material properties for 304 stainless steel applied to fixture plates and all screws in the FEM [10], [86].	118
6.2.	Material properties for 4340 hardened alloy steel applied to tup section of tup finite element model [21], [10], [86].	124

Table		Page
6.3.	Material properties for the pseudo-material applied to the crosshead-mass section of tup finite element model.	124
6.4.	Summary of plate impact tests using the Dynatup apparatus.	144
6.5.	Maximum strain from experiments compared to upper and lower bound strains directly from strain gage area in FEM from two material models (two-phase and Mori-Tanaka-Needles); strain gage 1.	145
6.6.	Maximum strain from experiments compared to upper and lower bound strains directly from strain gage area in FEM from two material models (two-phase and Mori-Tanaka-Needles); strain gage 2.	145
6.7.	Maximum strain from experiments compared to upper and lower bound strains directly from strain gage area in FEM from two material models (two-phase and Mori-Tanaka-Needles); strain gage 3.	146
6.8.	Maximum strain comparison between experiment and FEM results, strain gage 1.	157
6.9.	Maximum strain comparison between experiment and FEM results, strain gage 2.	158
6.10.	Maximum strain comparison between experiment and FEM results, strain gage 3.	158
8.1.	Factors used in Box-Behnken designed experiment.	191
8.2.	Box-Behnken designed experiment for four factors (TiB material coefficients and tup velocity) with results from FEM (maximum transverse displacement at center of plate w_0^{FEM}) using coded and actual variables.	194
8.3.	Box-Behnken [22] designed experiment for four factors with effects and interactions in coded form. The \mathbf{X} 27 x 15 array is tabulated here for the <i>coded</i> variables.	196
8.4.	Box-Behnken designed experiment for four factors (TiB material coefficients and tup velocity) with results from FEM (maximum transverse displacement at center of plate w_0) in coded form. .	199

Table		Page
8.5.	Summary of FGM plate impact tests using Dynatup apparatus.	213
8.6.	Comparison of predicted coefficients for TiB material properties using the parameter estimation technique and four different material models. Initial estimates for the material parameters were $C_1 = 3.40$, $C_2 = 0.40$, and $C_3 = 1.00$	214
8.7.	Comparison of predicted coefficients for TiB material properties based on average from results shown in Table 8.6.	214
8.8.	Predicted maximum center displacement of plate at center of bottom surface using the predicted TiB coefficients in Table 8.6. All units in millimeters.	215
8.9.	Elastic property data from parameter estimation scheme for Ti-TiB volume ratios using the (averaged) predicted values from the four material models in the estimation sequence, compared to properties determined experimentally in the literature. . . .	216
8.10.	Predicted maximum force applied to the plate at instant of maximum center displacement using the predicted TiB coefficients in Table 8.6. All units are in kilonewtons.	217
8.11.	Maximum strains from the three strain gages for the tests, the Mori-Tanaka needles estimates (MT-N, reproduced from Chapter VI) and the Mori-Tanaka needles estimates using the parameter estimation scheme (MT-N/PE).	218
9.1.	Summary of loading strain rates from plate impact tests using Dynatup apparatus. Strain rate is in units of strain/sec = (mm/mm)/sec.	230
9.2.	Summary of loading strain rates from optimized finite element models with homogenized-layers and Mori-Tanaka-needles material model. Strain rate is in units of strain/sec = (mm/mm)/sec.	230
9.3.	Summary of unloading strain rates from plate impact tests using Dynatup apparatus. Strain rate is in units of strain/sec = (mm/mm)/sec.	231
9.4.	Summary of unloading strain rates from optimized finite element models with homogenized-layers and Mori-Tanaka-needles material model. Strain rate is in units of strain/sec = (mm/mm)/sec	231

Table		Page
C.1.	Sampling point locations and weight factors for Gauss quadrature over the interval $g = -1$ to $g = +1$ [31], [143].	315

List of Symbols

Symbol		Page
V^f	Volume Fraction	1
z	Plate Thickness Coordinate	1
h	Total Plate Thickness	1
n	Power-Law Exponent	1
\mathcal{P}	Arbitrary Material Property	26
E	Elastic Modulus	27
ν	Poisson's Ratio	27
ρ	Density	27
G	Shear Modulus	28
σ	Stress	29
ϵ	Strain	29
σ_y	Yield Stress	29
H	Uniaxial Plastic Modulus	30
K	Bulk Modulus	30
ϵ_{ii}	Normal Strains	37
γ_{ij}	Engineering Shear Strains	37
ϕ	Rotation of Transverse Normal	39
N	Extensional Force Resultants	42
M	Bending Moment Resultants	43
Q	Vertical Shear Force Resultants	43
K_s	Shear Correction Factor	43
$[A_{ij}]$	In-Plane Stiffness Matrix	44
$[B_{ij}]$	Bending-Extension Coupling Matrix	45
$[D_{ij}]$	Bending Stiffness Matrix	45
$[A_{mn}]$	Transverse Shear Stiffness Matrix	45

Symbol		Page
p	Transversely Distributed Load	46
D	Flexural Rigidity	46
σ_{ult}	Ultimate Stress or Strength	56
α	Coefficient of Thermal Expansion	56
K	Kelvin	57
R	Resistance	87
ΔR	Change in Resistance	87
L	Gage Length of Strain Gage	87
ΔL	Change in Gage Length of Strain Gage	87
m	Mass	101
v	Velocity	101
$W_{1 \rightarrow 2}$	External Work Between Two States	102
H	Height	102
g	Gravitational Constant	102
c	Dilatational Wave Speed	154
c_s	Distortional Wave Speed	154
[K]	Global Stiffness Matrix	163
[M]	Global Mass Matrix	163
ω	Modal Frequencies	163
$\{\bar{D}\}$	Mode Shape Displacements	163
r	Radial Cylindrical Coordinate	166
θ	Angular Cylindrical Coordinate	166
z	Transverse Cylindrical Coordinate	166
h	Thickness	166
ϕ	Rotation of Transverse Normal	166
Ω_i	Material Parameters Used to Link CPT & FST	169
\mathcal{M}^C	Moment Sum, CPT	170
w_0^F	Transverse Displacement, FST	171

Symbol		Page
w_0^C	Transverse Displacement for Isotropic Plate, CPT	171
P	Magnitude of Concentrated Load	173
\mathcal{P}_i	Material Property	185
C_i	Material Property Coefficient	185
w_0^{FST}	Transverse Displacement, Analytical FST Model	187
w_0^{FEM}	Transverse Displacement, Finite Element Model	187
v_{tup}	Tup Velocity	190
\hat{y}	Measured Dependent Variable	190
x_i	Coded Independent Variable	190
X	Coded Variables 2nd-Order Math Model	193
Y	Vector of Results of Box-Behnken Tests	195
b	Coefficients for 2nd-Order Math Model	195
f	Objective Function	201
x	Vector of Design Variables	201
h	Equality Constraint Equations	201
g	Inequality Constraint Equations	201
\mathcal{L}	Lagrange Function	201
λ	Lagrange Multiplier, Equality Constraints	201
μ	Lagrange Multiplier, Inequality Constraints	201
H	Hessian	202
C	Vector of Material Property Coefficients	205
Γ_k	Coefficient in Modified Newton's Method	209
I	Identity Matrix	209
τ	Numerical Incremental Step-Size	209
e_i	Unit Vector	209
σ_e	von Mises Stress	234
R	Resistance	264
ΔR	Change in Resistance	264

Symbol		Page
L	Gage Length of Strain Gage	264
ΔL	Change in Gage Length of Strain Gage	264
e_i	Input DC Voltage	265
e_o	Output DC Voltage	265
i	DC Current	265
G	Gain	267
ϵ_e	Equivalent Strain	272
e_{cal}	Calibration Voltage	272
ϵ_g	Strain in Strain Gage	272
\mathbf{u}	Displacement Vector	297
$\dot{\mathbf{u}}$	Velocity Vector	297
$\ddot{\mathbf{u}}$	Acceleration Vector	297
\mathbf{M}	Diagonal Mass Matrix	297
\mathbf{F}_{EXT}	Applied Load Vector	297
\mathbf{F}_{INT}	Internal Force Vector	297
\mathbf{X}	Lagrangian or Material Coordinate Vector	300
\mathbf{x}	Eulerian or Spatial Coordinate Vector	300
\mathbf{F}	Deformation Gradient	301
\mathbf{R}	Rigid Body Rotation Tensor	301
\mathbf{V}	Left Stretch Tensor	301
\mathbf{U}	Right Stretch Tensor	301
\mathbf{v}	Particle Velocity Vector	302
\mathbf{L}	Velocity Gradient	302
\mathbf{D}	Rate of Deformation Tensor	303
\mathbf{W}	Spin Tensor	303
\mathbf{E}^G	Green Strain Tensor	304
$\dot{\mathbf{E}}^G$	Green Strain Rate Tensor	304
\mathbf{E}	Eulerian Strain Tensor	304

Symbol		Page
$\dot{\mathbf{E}}$	Eulerian Strain Rate Tensor	304
$\Sigma^{\mathbf{II}}$	2nd Piola-Kirchhoff Stress Tensor	306
σ	Cauchy Stress Tensor	306
\dot{W}	Rate of Work, or Power	308
\mathcal{F}	Body Forces	308
Φ	Surface Traction	308
$[\mathbf{N}]$	Shape Functions	308
$[\mathbf{C}_{el}]$	Elastic Stiffness Matrix	314
W	Weight Factor in Quadrature	315
$\bar{\mathbf{e}}_{Ax}$	Tangent Unit Vector	318
$\bar{\mathbf{n}}_{\mathbf{A}}$	Vector Normal to Surface	318

List of Abbreviations

Abbreviation		Page
FGMs	Functionally Graded Materials	iv
FGM	Functionally Graded Material	1
TPS	Thermal Protection System	2
°C	Degrees Celsius	2
RLV	Reusable Launch Vehicle	2
cm	Centimeters	4
Al ₂ O ₃	Aluminum Oxide	10
Ni	Nickel	10
mm	Millimeter	11
MPa	Mega-Pascals	13
μ -sec	Microseconds	24
CPT	Classic Plate Theory	36
FST	First-Order Shear Deformation Theory	39
Ti	Titanium	53
TiB	Titanium Boride	53
TiB ₂	Titanium Diboride	54
HCP	Hexagonal Close-Packed	55
α -Ti	α -Phase Titanium	55
BCC	Body-Centered Cubic	55
β -Ti	β -Phase Titanium	55
CP-Ti	Commercially Pure Titanium	55
ASTM	American Society for Testing and Materials	55
kg	Kilograms	56
m	Meters	56
GPa	Gigapascals	56

Abbreviation		Page
μm	Micrometers	56
MMCs	Metal-Matrix Composites	58
cm	Centimeters	62
SEM	Scanning Electron Microscope	62
AFRL	Air Force Research Laboratory	71
N-m	Newton-Meter	78
cm	Centimeters	84
GF	Gage Factor	87
NDE	Non-Destructive Evaluation	94
dB	Decibels	98
MHz	Megahertz	98
KE	Kinetic Energy	101
PE	Potential Energy	102
FEM	Finite Element Model	116
UNF	Unified Fine Thread Standard	120
UNC	Unified Coarse Thread Standard	121
FST	First-Order Shear Deformation Theory	166
BC	Boundary Condition	179
SSE	Sum of the Squared Errors	198
SST	Sum of the Squared Totals	198
K-T	Kuhn-Tucker	203
GF	Gage Factor	264
DC	Direct Current	265

A NOVEL METHOD FOR CHARACTERIZING THE IMPACT RESPONSE OF FUNCTIONALLY GRADED PLATES

I. Introduction

Functionally graded materials (FGMs) have generated a great deal of interest in recent years as advanced composites. FGMs are materials that have mechanical properties that vary continuously along a given dimension. In the case of functionally graded plates and shells, the property gradation occurs through the thickness. The property gradation is achieved by either chemically treating a single material to locally alter its properties or combining two or more separate materials with locally prescribed volume fractions. FGMs composed of two material constituents mixed together with locally prescribed volume fractions have been the focus of the majority of the literature concerning FGMs and will be the focus of the study here. The material distribution through a plate has been often conveniently described by adopting a power-law function to define the volume fraction V^f of the constituent 1 material at any given coordinate through the plate thickness [98]:

$$V_1^f(z) = \left(\frac{z}{h} + \frac{1}{2} \right)^n \quad (1.1)$$

V_1^f is the volume fraction of constituent 1, z is the depth coordinate measured from the plate's mid-surface, h is the overall plate thickness, and n is an arbitrary exponent value greater than or equal to zero. The volume fraction of constituent 2 material at any z coordinate is then given by the relation

$$V_2^f(z) = 1 - V_1^f(z) \quad (1.2)$$

Refer to Figures 1.1 and 1.2. The distribution of constituents for a metal-ceramic FGM are shown, where constituent 1 is ceramic and constituent 2 is a metal. Figure 1.1

shows plots of the local volume fraction of constituent 1 (ceramic) for various n values through the plate thickness, and Figure 1.2 shows an example of how the material distribution through the plate thickness might appear. Special FGM distributions using the power-law relation include (1) $n = 0$, a plate fully composed of material 1, (2) $n = \infty$, a plate fully composed of material 2, and (3) $n = 1$, a linear gradation of constituent 1 to constituent 2. The power-law distribution of constituents is merely an example of a formula that might be used to describe the gradation through a plate or shell's thickness. The exponent n in this case controls the shape of the transition from constituent 2 on the bottom surface to constituent 1 on the top surface. Virtually any mathematical function could be devised to serve the same purpose as the power-law function here. The FGM can be customized to an application by specifying the form of the gradation to fit the design requirements.

A very attractive feature of functionally graded materials is that they can be locally tailored to suit specific applications. For instance, a metal-ceramic FGM could potentially provide corrosion resistance and thermal protection on one surface while simultaneously providing resistance to mechanical loads through the remaining structure. The fusion of thermal resistance and mechanical load-bearing structure into a single construction has obvious potential for weight savings on an air or space vehicle. This is precisely why FGMs have been proposed for use in thermal protection systems. Thermal protection systems (TPS) are an integral part of any space-access vehicle due to the extreme temperatures that can be experienced during flight, especially in a planetary atmosphere when traveling at high speeds. The Space Shuttle Orbiters, for example, are subject to temperatures as high as 1500 °C at the nose during re-entry while the temperature of the internal structure must be maintained at 177 °C or less [33]. Reusable launch vehicles (RLVs) generally refer to the class of developmental platforms designed to operate at hypervelocity speeds in the upper atmosphere. The TPS for RLVs are being designed to handle flight temperatures on the order of 1500 °C and yet only requiring minimum refurbishment to send the vehicle back to flight in a manner of days [20]. The recent successful test of the X-43A hypersonic research

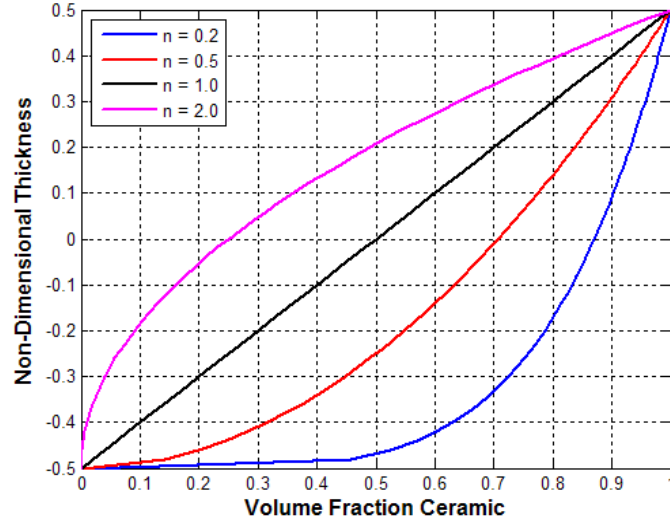


Figure 1.1: Power-law distribution of ceramic in terms of volume fraction for a metal-ceramic FGM plate graded through the thickness given various n exponents.

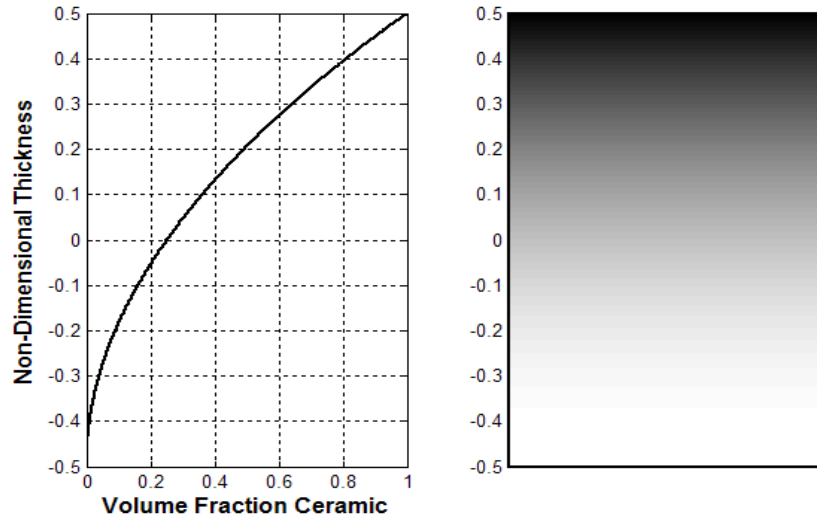


Figure 1.2: Cross-section of FGM plate with power-law ceramic volume fraction distribution; $n = 2.0$. Dark regions are ceramic rich, light regions metal-rich [32].

vehicle at Mach 7 in March 2004 provided thermal flight data at various locations near the vehicle's TPS. At this speed, temperatures at the nose of the X-43A reached as high as 871 °C [6].

The properties in an FGM plate or shell change through the thickness, and thus FGMs can potentially provide designers with tailored material response and exceptional performance in thermal environments. As an example, the TPS on the space shuttle consists of ceramic tiles bonded to the vehicles superstructure. These tiles are prone to cracking and debonding at the superstructure/tile interface due to abrupt transition between thermal expansion coefficients. Essentially, the ceramic tile expands a different amount than the substructure it is protecting during thermal loading. The difference in expansion causes stress concentrations at the interface of the tile and superstructure which can result in cracking or debonding. Such defects in the thermal protection system can lead to catastrophic failure during flight. The gradual change in material properties with an FGM alleviates this problem by mitigating the local stress concentrations from abrupt transitions in material properties [32].

Thermal protection on most vehicles are designed simply to resist the thermal environment and are not generally assumed to carry any significant mechanical loads over the flight envelope. The TPS system can, however, constitute the single point of failure of an entire structure. No better example of this can be illustrated than that of the Columbia Space Shuttle disaster (STS-107) that occurred February 1, 2003. The catastrophic loss of the entire shuttle was the result of a flat piece of insulating foam (roughly 61 cm x 38 cm) that separated from the left bipod ramp of the external fuel tank during launch and struck the left wing's leading edge thermal protection at a relative speed of approximately 240 meters per second [1]. The thermal protection was compromised, and the underlying structure failed during the extreme temperatures upon re-entry in the atmosphere. Impact damage to the shuttle TPS has occurred on every flight, and approximately 2-3% of all the high-temperature reinforced carbon-carbon TPS tiles must be replaced after each flight with the remaining tiles inspected and repaired as required. The impact damage comes from sources such

as insulation fragments, ice-frost particles during launch, debris at the landing site, and micrometeoroids and debris found in the upper atmosphere and space [33].

There is undoubtedly a great need for development of durable TPS that not only can withstand extreme thermal environments, but also one that requires little maintenance. The conventional approach to this problem has generally been to coat a structural member with refractory or adhesively bond thermal-resistant composites (i.e., tiles) to its exterior. Under harsh environments, the thermal barrier and/or adhesive may degrade over time which can pose considerable danger to the underlying structure. Further, most TPS materials are notoriously brittle and not resilient to any magnitude of dynamic loading. This fact has led to the prototypical development of metallic TPS as a potential replacement for space-access vehicles (see [20], [35]). An ideal TPS would not only protect internal structures from thermal effects but also support mechanical flight loads and still be robust to external damage and impacts.

A functionally graded material system must demonstrate its potential to resist impact damage before it can seriously be considered as a replacement to a current thermal protection system. Nearly all the research to date in the area of FGMs has been limited to analytical predictions and computer simulations of the static and vibration response of the composites under thermal and mechanical loading. Almost no studies of any kind have been undertaken related to impulsive or impact loading of FGM structures. Further, almost no experimental data is available related to FGMs of any kind. Given these two major holes in the available body of work related to FGMs, it is extremely difficult to make any reasonable assumptions of how a graded composite might perform in an aerospace application.

The FGM impact problem is, in general, highly complex and nonlinear in nature. For instance, the application involves detailed analysis in the areas of:

- **Wave Propagation.** The impact will dynamically load the structure and send a stress wave of significant amplitude through the structure. If the amplitude of the stress wave is sufficiently high, a plastic or shock wave could potentially

propagate through the medium inducing permanent deformation or failure. The material gradation in the plate structure further complicates the problem with respect to the constant reflection, refraction, and transmission effects at the numerous material and geometric boundaries.

- **Displacement Nonlinearity.** The target FGM plates are assumed to be thick and shear-deformable. The large strains that develop during a high-energy impact and the gradation of properties through the plate thickness require that nonlinear displacement theory be developed to describe the response of the structure. Further, if the impact pressures are sufficiently high, the FGM may exhibit fluid-like behavior local to the contact point.
- **Material Nonlinearity.** A suitable ceramic and metal FGM combination for a TPS very likely would exhibit plastic behavior as the plate loading induces local stresses beyond the functionally graded material's yield point. The amount of plastic deformation may indeed be a function of the thermal gradient and the strain rate imposed by the impact event.
- **Heat Transfer.** The extreme temperatures from the space and atmospheric environments will undoubtedly subject the FGM plates to thermal gradients that could alter local properties and generate residual stresses that change the response from that of a similar plate without surroundings of elevated temperature.
- **Contact & Pressure Distribution.** A projectile in contact with a structure during impact generates a time-dependent pressure distribution that must be defined. At high velocities, the form of the distribution may change if the geometries of the target and impactor are sufficiently transformed due to large deformations between the objects.
- **Damage Evolution & Failure.** Manufacturing processes that produce functionally graded materials are sufficiently harsh on its constituents that micro-defects (i.e., voids and micro-cracks) in the FGM must be assumed. Loading of

the structure lends itself to damage propagation over time. Damage in the material must be accounted for to obtain an accurate model for failure prediction.

This research work represents a first-of-its-kind study to characterize the impact response of FGM plates. Addressing all of the aspects of the FGM impact problem discussed above would involve a great deal of study that is beyond the scope of this work. The problem has therefore been simplified here by eliminating the thermal environment and limiting the severity of impact loads to the low- and medium-energy regimes.

*The **overall goal** of this study is to provide a unique method by which the impact response of functionally graded plates can be determined for low-velocity, low- to medium-energy impact events. Additionally, adequate material models for the anisotropic, non-homogeneous FGM must be determined to properly study the physics of the local and global response of the structure subject to an impulsive load of large magnitude. The **objectives** of this research, to meet these overall goals, are to:*

1. Design and conduct impact experiments on metal-ceramic FGM plates to record strain histories at various locations on the plate over the duration of the impact event (Chapter V).
2. Construct a finite element simulation of the impact experiment that is sufficiently sophisticated to capture the dynamic effects of an impact load that is at the same time easily replicated by scientists and engineers in practice (Chapter VI).
3. Correlate the results from the experiments and finite element models to available analytical theory while drawing conclusions regarding the validity of analytical techniques commonly used in the literature (Chapters VII and VIII).
4. Refine the FGM material models using a parameter estimation sequence to more effectively and accurately simulate the FGM plate impact experiments (Chapter VIII).

5. Provide analysis of the impact response of the FGM plates and make recommendations for engineers and scientists to improve performance and suitability for applications where resistance of impact loads are required (Chapter IX).

*Each of these **objectives** was met in this research work and each represents a significant contribution to the emerging field of functionally graded composites. This report documents each of these contributions in detail.*

This dissertation is organized as follows. Chapter II provides a comprehensive literature review of the current state of the art in the field of thermoelastic analysis of functionally graded materials. Chapter III outlines relevant theory associated with homogeneous and composite plates directly applicable to this research. Chapter IV presents details pertinent to the titanium-titanium boride metal-ceramic FGM system chosen specifically for this study. *These first three chapters summarize the background information necessary to the understanding and discussion presented in the remaining Chapters V-IX where the majority of the research and contributions are detailed.* Chapter V describes the design of the FGM plate impact experiments and presents the results of the plate impact experiments. Chapter VI describes the finite element model constructed to simulate the FGM plate impact experiments and details comparisons between the simulations and the strain histories collected from the impact experiments in order to validate the models. An analytical treatment of the FGM plate impacts is explored in Chapter VII and validated through experimental results and finite element simulations. This analytical treatment is a key component of a parameter estimation sequence that refines the local FGM material models by minimizing the error between the finite element models of the FGM plate impacts and the predicted response of the plates using analytical theory and the experimental results, described in Chapter VIII. Chapter IX describes some of the interesting physics associated with the impact events that can be further studied as a result of the method described to characterize the impact response of FGM plates. Finally, Chapter X lists important conclusions and recommendations for scientists and engineers studying the FGM plate impact problem in the future.

II. Literature Review of FGM Studies

The goal of this chapter is to *present a comprehensive literature review detailing the state of the art in functionally graded plate and shell research*. The body of work in FGMs has grown extensively in the last 20 years, and it is prudent to reduce the review to a manageable level by focusing on the FGM plate and shell problem. This chapter will demonstrate that there is a definite need for more extensive research into the FGM plate impact problem, and few have studied this application to date. Further, while FGMs have been studied extensively in the last two decades, almost no experimental data has been accumulated to substantiate many of the claims made by scientists and engineers working directly in the field. *The method for characterizing the impact response of FGM plates in this dissertation is thus a significant contribution to the field that has not been available to date.*

The literature review presented here is of interest to a wide variety of FGM applications, including thermal protection systems. Note, however, that not all of the literature discussed is directly relevant to the work presented in this dissertation. This literature review is intended to give the reader a feel for the variety of studies and applications intended for graded composites while highlighting that there are many areas of FGM plate and shell analysis that have not yet been explored. Suresh and Mortensen [122] published a very detailed literature review in functionally graded material technology in 1998, and Birman and Byrd [18] very recently documented an exhaustive literature review of developments in FGM research covering extensively the period (approximately) 1997-2007. This chapter will concentrate on those works published in the last decade. The topic areas include the following: (1) residual stress studies, (2) thermoelastic static analyses, (3) thermomechanical buckling, (4) FGM plate vibrations, and (5) stress wave and impact studies.

2.1 Residual Stress Studies

Residual stress studies related to FGM research are first discussed. These stresses can be associated with the various manufacturing techniques used to con-

struct the FGM structures or they can be the result of thermal loading and thermal cycling of the FGMs (such as in a thermal protection system). Residual stresses can occur when two materials with mismatching thermal expansion coefficients are bonded together in a two-phase composite. *Although residual stress effects are not being directly studied here, they will need to be considered before candidate FGMs can be fully integrated into thermal protection systems subject to high-temperature environments.* Significant residual stresses in an FGM structure can potentially decrease an FGM's ability to survive a subsequent impact load while in service on an aerospace platform.

An early finite element investigation into this FGM problem was conducted by Williamson, Drake, and Rabin [134], [38] in 1993. They considered aluminum oxide-nickel ($\text{Al}_2\text{O}_3\text{-Ni}$) functionally graded specimens in three configurations: (a) a disk, (b) a rod, and (c) a thin film with substrate. The goal of the work was to assess the effects of residual stress on FGMs when cooled. Sharp and gradual transitions between Al_2O_3 -rich and Ni-rich regions were considered with elastic-plastic constitutive models based on the modified rule-of-mixtures (explained in Chapter III). The authors additionally attempted to reduce the residual stress profiles in the FGM specimens by optimizing the graded region profiles. They concluded that reducing residual stresses in graded regions required optimized profiles and gradual transitions of material properties over thick regions.

Giannakopoulos et al. [46] examined the behavior of FGM beams and FGM plates under thermal cycling. The structural members were essentially three-layer composites similar to those presented by Williamson et al. The FGMs were constructed with $\text{Al}_2\text{O}_3\text{-Ni}$ constituents. The top layer of the beams and plates was constructed with nickel and the bottom layer was ceramic Al_2O_3 of equal thickness. A graded region of FGM, composed of a mixture of $\text{Al}_2\text{O}_3\text{-Ni}$, was sandwiched in between the ceramic and metal layers. The classic rule-of-mixtures (explained in Chapter III) was used to determine the Poisson's ratio and coefficient of thermal expansion in the graded layer. The modified rule-of-mixtures was used to estimate the flow stress and the plastic tangent modulus. Temperature cycles were imposed that

induced plastic deformation in the members. The investigators developed analytical equations to predict the stress distributions and onset of plasticity in the members as a function of height in the beam and depth in the plate. Finite element models were developed in ABAQUS to predict the accumulated plastic strain as thermal cycles progressed over time. The work presented a framework for analyzing problems of this nature. Finot et al. [41] continued this work by conducting experiments with actual FGM specimens. The specimens were plates 21 mm x 21 mm and 3.85 mm thick. The plates were constructed with a nickel layer 1.2 mm thick on the bottom, an FGM layer 2.2 mm thick with a linear gradation of volume fractions of Al_2O_3 -Ni generated in 13 discrete steps, and a top layer of Al_2O_3 0.45 mm thick. An individual FGM plate was placed on a heating table with no other constraints. The heating table applied various thermal cycles while curvature of the plate was measured. The curvatures were then related to numerical models predicting stress and curvature under the same conditions. The modified rule-of-mixtures was found to reasonably approximate the response demonstrated through the tests. This result is important in that it demonstrated the utility of the modified rule-of-mixtures as a viable material model in analysis.

In 1995, Ravichandran [96] investigated residual stresses in Al_2O_3 -Ni FGM systems that occur during high-temperature fabrication. The objective of this study was to determine the effects of the residual stresses and propose guidelines for optimum processing conditions. Elastic modulus and coefficient of thermal expansion were assumed to be temperature-dependent, although the residual stresses were found to not change appreciably from analyses conducted with temperature-independent properties. Net material properties in graded regions were determined based on functions of the volume fraction ratios of the constituents. These functions were specifically developed for this study and were not associated with some of the more common models used (discussed in the next chapter). The FGM structures consisted of plates of finite thickness and infinite span with FGM regions transitioning metal and ceramic layers on the top and bottom of the plates. Ceramic, metal, and FGM layers were allowed

to vary in thickness and the graded regions used a power-law distribution to define the volume fraction ratios of metal to ceramic. It was found that linear variation of metal-to-ceramic volume fraction ratio produced the lowest residual stresses. Further, if the FGM layer must be constructed in discrete rather than continuous steps, many discrete layers of constant volume fraction ratio are much more desirable than few layers with abrupt changes in volume fraction ratio.

Becker et al. [61] studied the FGM residual stress problem in a slightly different fashion. Here, equations were developed from classic thermo-elasticity where the displacement, stress, and strain fields induced to an FGM under loading were decomposed into two separate contributions to the overall solution. The first contribution to the fields was associated with the solution of a homogeneous medium with the same geometry, loads, and boundary conditions as the FGM. The second contribution to the fields was associated with the varying material properties as a function of position. The contribution from the locally varying material properties in the FGM was treated as a residual effect in a thermo-mechanical analysis that could be used to approximate the effects of various grading schemes with regard to constituents. The approximate method was compared to exact solutions and finite element solutions to assorted graded structural members under different boundary conditions. The approximate solution was found to provide a good qualitative (and occasionally quantitative) measure of FGM behavior under steady-state thermal loading conditions thereby reducing the need for expensive finite element analyses for some FGM configurations.

Hill and Lin [55] performed an experimental and numerical study of residual stresses in functionally graded titanium-titanium boride plate specimens manufactured by Cercom, Inc. (now BAE Systems-Advanced Ceramics). The plate specimens were 150 mm x 150 mm – 17 mm thick. The FGM consisted of seven homogeneous layers through the thickness transitioning commercially pure titanium to a mixture of 85% titanium boride and 15% titanium. Two beam samples were cut out of the parent plate near the center, 150 mm long x 17 mm high x 6.4 mm deep. Residual

stresses were experimentally determined by cutting slots at incremental depths into beams (these samples used the entire FGM thickness with all seven layers) at strategic locations and measuring the relaxation in the beams using strain gages. In this fashion, a strain profile can be obtained as successive cuts are made and the stress distribution is obtained through a superposition method (this technique is named the crack-compliance method, attributed to Prime [95]). The average peak residual stress was found to be 40 MPa, which the authors claimed is 11% of the tensile strength of commercially pure titanium (4.4% of the maximum flexural strength of monolithic titanium boride). A separate study was discussed in the paper where critical fracture loads could be reduced by as much as 34% as found in experiments with the same FGM system given the residual stresses reported here.

2.2 Thermoelastic Static Analyses

Here, a review of the current state of the art in analytical thermoelastic static relationships of FGM plates and shells is presented. A desirable feature of FGMs is integration of thermal protection (ceramic) and mechanical load-bearing structure (metal) into a single construction. A candidate FGM system for a given application must demonstrate its ability to withstand simultaneous thermal and mechanical loading. *The FGMs studied in this work were subjected to room-temperature environments to simplify the scope of the project, however, a candidate FGM for use in TPS applications must be studied with thermal effects in mind.* The reason for this is that inherent material properties and structural member geometry can change with changing temperatures. Material and configurational changes can affect an FGM's ability to withstand impact loads from foreign objects. Further, the quasi-static response of any structural member under load on an aerospace platform must be considered before the dynamic effects of flight loading are addressed.

Praveen and Reddy [94] presented one of the earliest and most widely used developments of thermoelastic behavior of functionally graded rectangular plates that included nonlinear effects. Praveen and Reddy essentially adapted the plate theory

from laminated composites and adapted the material stiffness parameters (i.e., the $[A_{ij}]$, $[B_{ij}]$, $[D_{ij}]$ matrices and other material parameters) from summations over discrete layers to integrals of the continuous function defining the material variation through the plate and shell thicknesses. A more thorough explanation of this and other similar work will be presented in Chapter III.

Praveen and Reddy's formulation for rectangular functionally graded plates was extended to an axisymmetric formulation for first-order shear deformable FGM circular and annular plates in bending by Reddy et al [103]. Solutions for the deflection, force resultants, and moment resultants were given in terms of the corresponding quantities of isotropic plates based on classical Kirchhoff plate theory. The solutions to these problems are then available provided the Kirchhoff solutions to the same problems for isotropic, homogeneous plates are available. *The theory from this work will play a very important role in the analytical treatment of the FGM plate impact problem and will be rigorously discussed in Chapter VII.* The theory originally formulated by Praveen and Reddy was further extended by Reddy [98] to more general relations for functionally graded plates allowing third-order shear-deformable plates to be considered. Reddy also derived the finite element models consistent with the third-order shear deformable plate theory and additionally incorporated thermal and nonlinear effects. Woo and Meguid [136] in 2001 published an early formulation of large deformation of thin functionally graded plates and shallow shells under combined mechanical and thermal loading using classical nonlinear plate theory. A further advance in FGM plate analysis was provided by Reddy and Cheng [101] where a three-dimensional solution technique accounted for boundary and edge effects and made use of an asymptotic method to transition to the exact solution from available plate theory near the interior regions of the plate structure (see also [116], [117]).

Vel and Batra [126] studied small elastic deformations in thick, simply supported functionally graded plates. Displacement and temperature fields were generated by imposing thermal and mechanical loads to the top and bottom surfaces of the plate either individually or simultaneously. Three-dimensional displacement and temper-

ature fields were assumed to have the form of a power-series solution that solve the constitutive equations for a linear isotropic thermoelastic material and satisfy the boundary conditions. The key assumption was that a plate graded through the thickness had smoothly varying material properties (no discrete jumps) and infinitesimally small adjoining layers were homogeneous, isotropic, and perfectly bonded together. The power series solutions to the FGM problem were then compared to solutions generated by classical plate theory as well as first-order and third-order shear-deformable plate theories. In general, the power series exact solutions matched previous results only qualitatively. Three material models were considered, namely the Mori-Tanaka estimates, the self-consistent model, and a combination of the two (these material models are discussed in detail in Chapter III).

Theoretical equations were developed by Shao [111] for a piping and pressure vessel application using FGM hollow cylinders graded through the pipe thickness direction. Shao simplified the analysis to an axisymmetric, two-dimensional model where stresses could be resolved for general pressure and thermal load distributions on the exterior and interior surfaces. The pressure and thermal load distributions depended only on the axial coordinate of the cylinder. The hollow cylinders studied were of finite length and supported at the ends. In 2006, Shao and Wang [112] continued this work to a more general theory applying to FGM cylindrical panels of finite length under general loading conditions. Three-dimensional solutions were assumed so that thin or thick panels could be accommodated. The response of an FGM cylindrical shell subject to a thermal shock load was subsequently studied using a finite element formulation by Bahtui and Eslami [11].

Hsieh and Lee [57] recently developed FGM plate theory for an unusual application. Here, the two investigators studied classic nonlinear von Kármán plate theory applied to elliptical FGM plates. The plates were rigidly fixed around a boundary that was allowed to be slightly disturbed (i.e., not perfectly elliptical in shape). A perturbation technique was used to solve the governing equations for displacements, although only approximate solutions were presented. The theory was tested given a

measured plate center deflection. The complete displacement field was obtained from the presented solutions, and the stress resultants throughout the plate were then available.

Pai and Palazotto [87] in 2007 introduced a sublamination theory for analyzing the response of functionally graded plates. Essentially the through-the-thickness gradation was divided into individual sub-layers to increase the degrees-of-freedom through the thickness and improve the numerical accuracy in predicting the three-dimensional stress state in the plate. The sublamination theory is extremely flexible in that it can be formulated to satisfy assumptions of either classical plate theory or more complicated higher-order shear deformable plate theories. Further, the governing equations for a plate composed of several sublaminates converges to the usual governing equations in plate theories when the number of sublamine layers equals one. The theory was shown to match the exact solutions of plates extremely well to include the prediction of mode shapes.

Abrate [5] recently demonstrated that functionally graded plates actually behave more like homogeneous plates than originally thought. The usual method for determining the in-plane stiffness, bending-extension coupling, and bending stiffness matrices ($[A]$, $[B]$, $[D]$, respectively) is to use the mid-surface of a composite plate as the reference surface. Abrate shows that if the reference surface is chosen judiciously such that the bending-extension coupling disappears, the in-plane and bending stiffness matrices derived from the new reference surface are the only material parameters required to solve the governing equations for plate deflections and vibrations. This new approach was shown to dramatically simplify the analyses while simultaneously matching identically the results published by other investigators for FGM plates assuming both classical plate theory and higher-order shear deformable plate theories.

2.3 Thermomechanical Buckling Studies

Buckling of FGM plates and shells is an important topic that is being studied by some researchers. Many FGM plates and shells are graded in a fashion such that

the material composition is non-symmetric about the mid-plane of the plate or shell. FGMs of this type will undergo changes in curvature as mechanical and thermal loads are applied due to bending-extension coupling effects. Accounting for this fact is critical in a buckling analysis, as buckling loads may be much lower in magnitude than those of the same structural member composed of a homogeneous or symmetric material composition. FGM plate buckling becomes very important when considering FGMs for use in thermal protection systems, and a plate or shell structure that has buckled may be less resilient to an impact event.

One of the first studies into the FGM buckling problem was performed by Shen [117] in 2002. Shen was concerned with post-buckling analyses of axially loaded FGM cylindrical panels that additionally contended with thermal environments. The panels were graded through the thickness and a classical rule-of-mixtures approach was used to model temperature-dependent material properties. Shen used a higher-order shear deformation shell theory to describe the governing equations under thermo-mechanical loading. A perturbation technique (similar to one used by the same author to model the bending response of FGM plates [116]) was used to not only construct the asymptotic relations between the boundary layer and the regular solution, but another perturbation relation was applied to simultaneously account for any geometric imperfections in the cylindrical panels. Shen verifies his developed equations by comparison to published results for isotropic cylindrical panels, and then provides buckling data for various FGM systems, although there is no available test or simulation data to compare results to.

The FGM buckling problem has been extensively studied by Javaheri, Eslami, and Samsam Shariat ([59], [58], [60], [115], [113], [114]). In 2002, Javaheri and Eslami [59] developed closed-form solutions to the thermal buckling problem with rectangular FGM plates graded through-the-thickness using a power-law distribution of metal and ceramic constituents. Classical plate theory formed the basis for their solutions. The critical buckling loads were characterized by changes in temperature from the ceramic-rich surface to the metal-rich surface under various temperature

profiles (linear and nonlinear) across the thickness of the plate. Their results reduced well to previous solutions to the same problem for homogeneous plates. Two important observations from their work regarding an alumina-aluminum FGM system were that (1) critical buckling temperature change is predicted to be lower for FGMs than for homogeneous plates and (2) increasing the power-law exponent n in equation (1.1) reduces the critical temperature difference before buckling occurs. The same analysis was extended to higher-order, shear deformable plate theory by the same authors [60]. Similar observations were recorded considering the higher-order theory, and it was also found that the higher-order theory underestimated critical buckling temperature difference predicted by classical plate theory. Buckling due to mechanical in-plane loads applied to FGM rectangular plates was first studied by Javaheri and Eslami [58] and later by the the same authors with Samsam Shariat [115] considering rectangular FGM plates with small imperfections in shape. Imperfections here were defined to be small deviations of the mid-plane from a perfectly flat surface, later idealized to follow a sinusoidal relation with an amplitude parameter to characterize the net imperfection. Comparing the results of the studies, based on classical plate theory, the authors found that increasing magnitude of small imperfections in the plate actually increase the critical buckling load over a perfect plate and increasing power-law exponent n decreases the critical buckling loads. Samsam Shariat and Eslami [113] used the same ideas to study thermal buckling of imperfect FGM plates, concluding again that imperfect FGM plates have higher critical temperature differences than those of perfect FGM plates. Finally, Samsam Shariat and Eslami again collaborated to develop equations to predict the combined critical mechanical and thermal loads necessary to induce buckling for thick rectangular plates, here applying higher-order shear deformable plate theory [114].

Na and Kim [83] studied the FGM plate buckling under combined thermal and mechanical loads by using the finite element method. They developed an 18-node solid element that includes the grading function as part of the element's formulation. The theory is very generalized such that almost any continuous grading function can

be used to describe the material mixtures and an assumed-strain mixed formulation is used to construct the global stiffness matrix and global nodal load vector. Their finite element model was compared to results from previous investigators for both isotropic and FGM plates, and the authors present suggestions for design to prevent buckling in application.

Yang et al. [137] presented another post-buckling analysis where imperfection sensitivity of higher-order shear deformable FGM plates was considered. Mechanical loading in the form of uniform edge compression and thermal loading in the form of a uniform temperature change were applied to the FGM plate. Various gradations, boundary conditions, and plate configurations were studied parametrically with local and global imperfections applied to the plate. An important observation in the article was that post-buckling strength was not significantly affected by global imperfections to the plate, but local imperfections in close proximity to the center of the plate could significantly reduce the post-buckling strength.

2.4 Vibration Analyses of FGMs

The three previous sections summarized some of the recent ground-breaking works in static analyses of FGM plates and shells. This section and the following will present an outline of the body of literature available on FGM plate dynamics; specifically, vibration and modal analysis of FGM plate structures (this section) and impact and wave analysis (next section).

One of the first studies in FGM plate and shell vibration analysis was presented by Loy et al. [74] in 1999. In this paper, a specific application of simply-supported FGM cylindrical shells was addressed. Cylindrical FGM shells are of interest particularly in pressure vessel and piping technologies. The authors assumed a power-law variation in volume fraction of constituents from the inner to the outer shell surface and the material properties varied through the shell thickness according to the classical rule-of-mixtures with handbook material properties for the individual constituents. Once the constitutive relations were formulated, the authors employed the Rayleigh-

Ritz method to solve for the natural frequencies of the shell structure. The authors compared results for various volume fraction distributions of a metal-ceramic FGM system and found that natural frequencies for an FGM shell lie between the natural frequencies calculated for a purely metal or purely ceramic shell. A qualitative study was also performed when the geometry of the shell was allowed to vary. Pradhan et al. [92] in 2000 extended this same work and studied the vibration characteristics of FGM cylindrical shells under all possible combinations of clamped, free, and simply-supported boundary conditions. The authors compared results for various volume fraction distributions of a metal-ceramic FGM system and found that natural frequencies for an FGM shell lie between the natural frequencies calculated for a purely metal or purely ceramic shell, precisely the same conclusion as the previous study. Reddy and Cheng [102] in 2002 extended the FGM shell frequency analysis further by considering a simply-supported shallow spherical shell of polygonal planform resting on an elastic foundation.

The dynamic response of initially stressed rectangular FGM plates was studied by Yang and Shen [138] in 2001. A rectangular plate, graded through the thickness with a power-law distribution and material properties governed by the classical rule-of-mixtures, was assumed to be clamped on all sides or clamped on two sides and simply-supported on two sides. The plate was allowed to rest on an elastic foundation and be subjected to initial in-plane uniaxial or biaxial stresses, although both or neither of these features need be included. The plate was subjected to a pulse load that was either constant, linear, sinusoidal, or exponential with respect to time over a rectangular patch of the plate surface and was removed abruptly at a given time in order that the plate entered free vibration. Classic plate theory was used to model the dynamic and transient responses of FGM plates under these conditions. The results, as expected, were found to vary greatly depending on the power-law exponent n , plate aspect ratio, foundation stiffness, shape and duration of pulse load, and initial stress magnitude. The authors continued this work by extending their analyses to thick, shear-deformable FGM plates in thermal environments in a paper published

in 2002 [139]. Yang and Shen developed a very general plate theory (minus the case of an elastic foundation) where the response of the plate could be semi-analytically determined under general load and boundary conditions, including the case of an initially stressed plate.

Another engineering problem associated with FGM plates and shells pertains to buckling caused by dynamic loading. An early study into this problem was undertaken by Ng et al. [85] in 2001. Their work focused on dynamic stability of FGM cylindrical shells simply-supported at the ends under periodic axial loads. The applied axial load was decomposed into a static contribution and dynamic contribution, either or both of which could be included in analysis without loss of generality. The equations of motion for the FGM cylindrical shell were presented and solutions for the displacements under static and dynamic conditions were generated as were the conditions for the onset of buckling. Regions of shell instability were determined based on shell configuration and load parameters. The main conclusion of this work is that tailoring the FGM material distribution is the best way to improve the dynamic stability of the cylindrical shells. Another study of dynamic buckling of FGM shells was performed by Sofiyev [120]. Sofiyev's work was rooted in solving for stability of truncated conical FGM shells subject to a uniform external pressure load. The pressure magnitude applied to the truncated cone was a power-function of time. Sofiyev used analytical theory to predict the critical external pressure impulse and application time that induces buckling on such a structure. The same conclusion that the distribution of material properties can significantly alter the stability of the FGM shell was found in Sofiyev's study. A recent study of particular interest was conducted by Sundararajan et al. [121] in 2006 where dynamic buckling of FGM spherical caps was investigated. The von Kármán large deformation theory was employed in the constitutive equations and the FGM caps were clamped or simply-supported with an external uniform pressure pulse applied over a prescribed duration. The authors conclude again here that material distribution can affect critical buckling loads, but shell geometry, boundary conditions, and pulse duration also significantly affect the

onset of buckling and must be considered. Prakash and Ganapathi [93] in 2006 also performed a study of FGM shear-deformable circular plates under a temperature distribution where both structural stability and modal frequencies were simultaneously considered using a customized finite element.

2.5 Stress Wave and Impact Analyses

Here, recent work published to study impact response and stress wave propagation in functionally graded plate and shell structures will be reviewed. Many of the concepts in wave motion and structural vibrations are the same (except in applications with very high pressures, large displacements, and failure), but a few notes regarding the response of structures subject to impact loading are in order. Impact problems where the impact velocity is relatively low (for instance, 10 meters per second or less) can typically be studied using quasi-static or vibration theory. In higher velocity impact events, the structural loading typically occurs over a very short period of time, usually on the order of microseconds (1.0×10^{-6} seconds). In these problems, the initial disturbance in the structure due to the impulsive load is traced locally. The magnitude of the disturbance is of the most interest for two reasons: (1) an impulsive load spans a large part of the frequency spectrum and thus modal excitation occurs over a large number of structural modes and (2) the length and scope of the structure's primary response will occur locally and much more quickly than the period of the first natural frequency of the structure. In structural vibrations, usually the global movement of the structure is of greater interest since the loading occurs over sufficiently long periods of time that the response of the global structure dominates the response history. Applications where an impact load was applied to an FGM structure (regardless of velocity) or a general wave analysis was performed will be considered in this section in the context of the points made in this paragraph. (See [48], [50], [142], [39] for explanations on these points.)

A purely analytical study of the low-velocity, elastic impact of hollow FGM cylinders was performed by Gong et al. in 1999 [49]. The cylinders were assumed suf-

ficiently thick to apply third-order shear deformable theory to the governing equations of motion. Fourier series solutions were assumed to solve the equations of motion, and an impulsive load was applied to the cylindrical shell based on the mass and velocity of the striker. Four FGM configurations were considered consisting of stainless steel and silicon nitride. The cylinders were divided into single and two-layer models, where each layer was graded according to a power-law distribution. The cylinders all had the same length, thickness, and diameters. The dynamic hoop strains were determined at select locations in the cylinders. The cylinder configuration found to have the best impact resistance (determined by the lowest magnitudes of hoop stress and strain transients and a minimal transverse shear stress profile) was a two-layer FGM with the shell having stainless steel surfaces on the inner and outer diameters and transitions to a silicon nitride-rich surface midway through the shell thickness. Heat transfer and thermal stress analyses were not included in the study.

An analytical method for tracing one-dimensional stress waves in FGMs was proposed by Bruck [23] in 2000. The contribution of this paper is very important in that it is an early analysis of transmission and reflection as a wave propagates through a graded medium. The medium considered was a cylinder composed of three sections: (1) a sufficiently long section of a single homogeneous material; (2) a region that is functionally graded either discretely or continuously; and (3) a sufficiently long section of a second homogeneous material. The homogeneous base materials are assumed to have different material properties and the graded region transitions from one base material to the next following a function similar to a power-law relation defining the volume fraction of one base material to the other (see equation (1.1)). Bruck used these assumptions to derive formulas to trace the stress history in the cylinder given an incident wave traveling through section (1) that constantly transmits and reflects as it moves through the graded region. The magnitude of the reflected stress waves at a point over time was shown to be a function involving a summation of individual reflected waves in each graded layer for a discretely graded FGM and integration of a continuous function (relating transmission and reflection of waves through the

region) for a continuously graded FGM. Note that stress wave propagation analysis in plates or other multi-dimensional structures must consider transmission, reflection, and refraction effects in multiple dimensions.

Li et al. [73] studied impact of thick circular FGM plates under impulsive loading. A circular plate 200 mm in diameter and 24.5 mm thick was composed of an aluminum matrix with ceramic reinforcement particulate inclusions. The plate was fixed along the outer perimeter of the plate, but the authors note that the boundary effects are not important because the time scales studied are small compared to the time for the stress waves to reach the boundaries. The circular plate was subjected to a 3.0 GPa pressure load, such as might occur from a high-energy impact, that ramped from zero to 3.0 GPa over 0.1 microseconds (μ -sec), remained constant at 3.0 GPa for another 2.90 μ -sec, then ramped down from 3.0 GPa to zero over an additional 0.1 μ -sec. Several discrete-layer grading configurations were studied in an axisymmetric model using the commercial finite element analysis code ABAQUS. The elastic properties of the FGM were determined using the Hashin-Shtrikman formulation [53] and the Li-Ramesh Constitutive Model [71], [72] (a specific strain-rate sensitive constitutive model for metal-matrix composites developed by the authors) was used to determine the plastic behavior of the FGMs based on local reinforcement volume fraction ratio and applied strain-rate. The authors studied the effects of axial stress distribution, plastic strain distribution, and energy dissipation. Based on their analysis, the authors made a few important conclusions: (1) the grading configuration and layer thicknesses can be designed to control location and timing of spall failure; (2) grading configuration and layer thicknesses can be designed to control location, timing, and size of the overall plastic zone in the material; (3) the evolution of dissipated energy is directly related to the gradation of material properties.

Banks-Sills et al. [12] looked at the dynamic response of a simulated strip of FGM infinitely long and graded through the height under plane strain conditions. The FGM was a metal-ceramic combination modeled by determining material properties using three microstructure models: (1) non-random two-phase model with metal

and ceramic cells; (2) homogeneous discrete layers; and (3) continuously changing microstructure. A time-dependent compressive pressure load was applied to the top of the FGM through a special functional relation such that the rise time characteristics of the pressure load could be manipulated. The pressure load applied varied between an abrupt step input to a very slowly applied load near quasi-static conditions. A specialized finite element code was used to measure the von Mises effective stress under the different load conditions. For gradual load application, the FGM slowly reached a final deformation. For abrupt pressure applications, the FGM exhibited wave characteristics where the FGM stresses oscillated in a periodic fashion (no damping, elastic deformations only). All three microstructure models generated similar results, although the authors preferred the layered and continuous models for use in practice.

2.6 Concluding Remarks

This chapter highlighted the most pertinent literature available to research engineers studying FGM plate and shell structures. The topic areas included the following: (1) residual stress studies, (2) thermoelastic static analyses, (3) thermomechanical buckling, (4) FGM plate vibrations, and (5) FGM stress wave and impact studies. Having reviewed a large segment of the FGM research available, it is apparent that nearly all the research conducted has been purely analytical or in computer simulation. *Almost no experimental work has been conducted with FGMs to reinforce the claims made by these and other investigators.* Therefore, any successful experiments with accompanying data represent an important contribution to the field of study in FGMs. Further, impact studies with FGMs have not been vigorously undertaken to this point. *This dissertation therefore represents an important first step in developing this rich area of research, and the following chapters will describe in greater detail a method for characterizing the impact response of FGM plates.*

III. Material Models and Relevant Plate Theory

The goal of this chapter is to *present a review of specific theory directly relevant to understanding the FGM plate impact problem studied specifically in this dissertation*. The first part of the chapter presents material models that are commonly applied to metal-ceramic functionally graded materials; specifically, the classic rule-of-mixtures, the modified rule-of-mixtures, the self-consistent model, and the Mori-Tanaka estimates. The second part of this chapter presents select portions of classic and shear-deformable plate theory that are basic to this research, including a more specific case of circular plates under axisymmetric loading. A key assumption behind the use of these material models and the plate theory presented is that the behavior of the FGMs is linear-elastic. It will be shown in later chapters that FGM specimens used in the impact experiments designed for this work behaved nearly linear-elastic to failure. *The theory in this chapter will be referred to frequently throughout the remainder of this dissertation, especially in the discussions of the FGM plate impact experiments and their associated computational and analytical models.*

3.1 Material Models

In this section, an overview of commonly used material models in FGM research is presented. *These material models are important in the sense that most attempt to describe the constitutive relationship with a closed-form analytical formula based on the volume fraction ratio of constituents.* The most commonly used material models for FGM studies are the classical and modified rules-of-mixtures, the self-consistent model, and the Mori-Tanaka estimates; all are presented here in detail. A few other more mathematically complex material models are briefly listed for reference purposes.

3.1.1 Classical Rule-of-Mixtures. The classical rule-of-mixtures attempts to directly relate the net material properties of multi-phase materials to the ratio of volume fractions of the constituents. If \mathcal{P} is an arbitrary property of a two-phase

mixture and \mathcal{P}_1 and \mathcal{P}_2 are arbitrary properties of the two phases, then the relation

$$\mathcal{P} = V_1^f \mathcal{P}_1 + V_2^f \mathcal{P}_2 \quad (3.1)$$

is assumed to describe the local properties of the FGM under the classical rule-of-mixtures. In an FGM plate, the volume fractions of the two phases change as position changes through the thickness. Therefore, a more appropriate version of (3.1) can be written as

$$\mathcal{P}(z) = V_1^f(z) \mathcal{P}_1 + V_2^f(z) \mathcal{P}_2 \quad (3.2)$$

Equation (3.1) is based on the Voigt model for determining longitudinal stiffnesses if both FGM phases are in a state of *equal strain* [122], [34]. The assumption that the two phases in the FGM are in a state of equal strain can be thought of as analagous to (two) springs acting in parallel to resist a longitudinal force. A force extends or compresses two springs in parallel an equal distance (i.e., equal strain) and the springs exert forces based on their appropriate spring constants (i.e., elastic moduli adjusted by volume fractions). For this reason, the Voigt model is often referred to as a “parallel” model in composite theory. The rule-of-mixtures is frequently applied to determining longitudinal properties in fibrous-woven composites and was originally developed for determining a net elastic modulus for a two-phase mixture, although it is also frequently applied to determine other properties such as Poisson’s ratio and density. In terms of typical elastic properties, (3.2) takes the following forms:

$$E(z) = V_1^f(z) E_1 + V_2^f(z) E_2 \quad (3.3)$$

$$\nu(z) = V_1^f(z) \nu_1 + V_2^f(z) \nu_2 \quad (3.4)$$

$$\rho(z) = V_1^f(z) \rho_1 + V_2^f(z) \rho_2 \quad (3.5)$$

E is the elastic modulus, ν is the Poisson’s ratio, and ρ is the material density of the individual phases.

Occasionally properties in the transverse direction are associated with the Reuss model [122], [34] where

$$\mathcal{P} = \left(\frac{V_1^f}{\mathcal{P}_1} + \frac{V_2^f}{\mathcal{P}_2} \right)^{-1} \quad (3.6)$$

If a local property is required of a continuous FGM, then

$$\mathcal{P}(z) = \left(\frac{V_1^f(z)}{\mathcal{P}_1} + \frac{V_2^f(z)}{\mathcal{P}_2} \right)^{-1} \quad (3.7)$$

also applies. The Reuss model assumes that the phases in the composite are under a state of *equal stress* and is typically applied to the elastic modulus, shear modulus, and Poisson's ratio. The assumption that the two phases in the FGM are in a state of equal stress can be thought of as analagous to (two) springs acting in series to resist a longitudinal force. A force extends or compresses two springs in series with a force applied over more or less an equal area (i.e., equal stress) and the springs exert forces based on their appropriate spring constants. The springs are compressed or extended by different lengths, as determined by their spring constants (i.e., elastic moduli adjusted by volume fractions). For this reason, the Reuss model is often referred to as a “series” model in composite theory. In terms of elastic modulus, shear modulus, and Poisson's ratio, (3.7) takes the following forms:

$$E(z) = \left(\frac{V_1^f(z)}{E_1} + \frac{V_2^f(z)}{E_2} \right)^{-1} \quad (3.8)$$

$$G(z) = \left(\frac{V_1^f(z)}{G_1} + \frac{V_2^f(z)}{G_2} \right)^{-1} \quad (3.9)$$

$$\nu(z) = \left(\frac{V_1^f(z)}{\nu_1} + \frac{V_2^f(z)}{\nu_2} \right)^{-1} \quad (3.10)$$

G is the shear modulus of the material. Often the actual value of the composite properties can be found to be bounded between equations (3.1) and (3.6), yet both

estimates are crude and limited in application [34]. Nevertheless, both the Voigt and Reuss models allow for very simple estimation of elastic properties.

3.1.2 Modified Rule-of-Mixtures. A modification to the classical rule-of-mixtures was originally proposed by Tamura et al. [123] for a two-phase mixture where one phase (subscript 1) was purely elastic and a second phase (subscript 2) exhibits plasticity. This modification was shown to match relatively well with experimental data [42]. The theory is explained briefly here. It is first assumed that at an infinitesimal local z -coordinate in the plate thickness the FGM behaves isotropically. If such is the case, the uniaxial stress σ and strain ϵ are related to the average strains in the individual constituent phases by

$$\begin{aligned}\sigma &= V_1^f \sigma_1 + V_2^f \sigma_2 \\ \epsilon &= V_1^f \epsilon_1 + V_2^f \epsilon_2\end{aligned}\tag{3.11}$$

The ratio of stress to strain transfer between the phases can be defined by the parameter

$$q = \frac{\sigma_1 - \sigma_2}{\epsilon_1 - \epsilon_2}\tag{3.12}$$

which is bounded by $0 < q < \infty$. When $q = 0$, the constituents are under a state of equal stress (i.e., parallel Voigt model); when $q = \infty$, the constituents are under a state of equal strain (i.e., series Reuss model). The elastic (or Young's) modulus of the mixture can be determined by combining equations (3.11) and (3.12) assuming uniaxial Hooke's law ($\sigma = E \epsilon$) applies:

$$E = \left\{ V_2^f \left(\frac{q + E_1}{q + E_2} \right) + V_1^f \right\}^{-1} \left\{ V_2^f E_2 \left(\frac{q + E_1}{q + E_2} \right) + V_1^f E_1 \right\}\tag{3.13}$$

The yield stress σ_y (that is, the stress above which yielding in the material occurs and permanent plastic deformation must be considered in the structure) in the FGM

mixture can be determined using the previous equations and Figure 3.1:

$$\sigma_y = \sigma_{y2} \left\{ V_2^f + \left(\frac{q + E_2}{q + E_1} \right) \frac{E_1}{E_2} V_1^f \right\} \quad (3.14)$$

σ_{y2} is the yield stress of constituent 2. The uniaxial plastic modulus H (that is, the modulus used to relate stress and strain above the yield stress) can also be evaluated to be

$$H = \left\{ V_2^f \left(\frac{q + E_1}{q + H_2} \right) + V_1^f \right\}^{-1} \left\{ V_2^f H_2 \left(\frac{q + E_1}{q + H_2} \right) + V_1^f E_1 \right\} \quad (3.15)$$

The modified rule-of-mixtures has been implemented for analysis of functionally graded materials (for early examples, see [134], [38], [46], and [41]; more recently refer to [28]). The modified rule-of-mixtures is not as convenient as the classical form, however, it is of great interest because it allows the design engineer to estimate the yield stress and plastic tangent modulus for a ductile-brittle combination of materials such as metal and ceramic. The key to using the equations is finding an appropriate value for q , which must be determined experimentally.

3.1.3 Self-Consistent Estimates. Hill [56] developed a self-consistent material model for two-phase composite materials. The model is general enough to be assumed applicable to FGMs. Hill showed that *if a series of randomly dispersed isotropic spheres served as inclusions in a homogeneous matrix and if the matrix-inclusion composite bulk material displayed statistical isotropy (that is, a significant percentage of the composite behaves isotropically and can be reasonably assumed to behave as such), then the net bulk modulus K and shear modulus G for the composite are given by the following relations:*

$$\frac{\delta}{K} = \frac{V_1^f}{K - K_2} + \frac{V_2^f}{K - K_1} \quad (3.16)$$

$$\frac{\eta}{G} = \frac{V_1^f}{G - G_2} + \frac{V_2^f}{G - G_1} \quad (3.17)$$

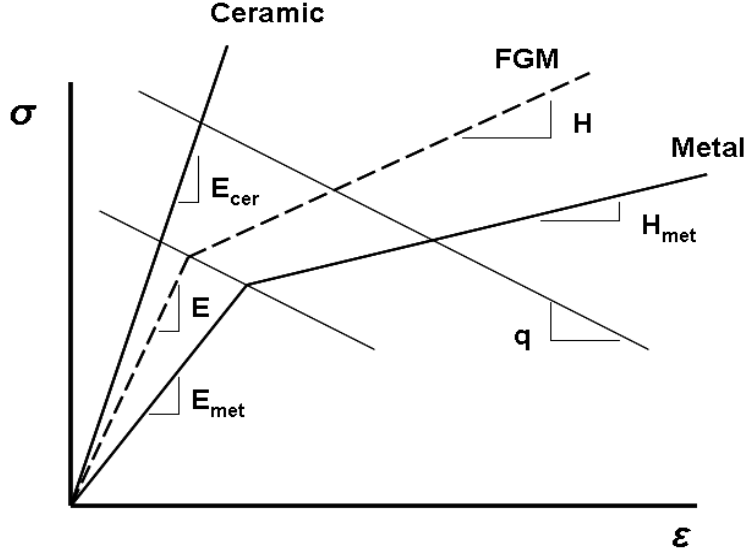


Figure 3.1: Illustration of modified rule-of-mixtures approach for obtaining stress-strain constitutive data for two-phase mixtures. A metal-ceramic combination is shown here, with constituent 1 being ceramic and constituent 2 being a ductile metal. [122], [134].

where $\delta = 3 - 5\eta = K/(K + 4G/3)$, and subscripts 1 and 2 refer to the individual phases, respectively. Equations (3.16) and (3.17) must be solved for K and G simultaneously. The bulk and shear moduli are related to the Young's modulus E and Poisson ratio ν by

$$K = \frac{E}{3(1 - 2\nu)} \quad (3.18)$$

$$G = \frac{E}{2(1 + \nu)} \quad (3.19)$$

Hill noted that equations (3.16) and (3.17) will always satisfy the Hashin-Shtrikman bounds [53] (presented here without derivation):

$$\begin{aligned} K_1^* &< K < K_2^* \\ G_1^* &< G < G_2^* \end{aligned} \quad (3.20)$$

where

$$K_1^* = K_1 + \frac{V_2^f}{\frac{1}{K_2 - K_1} + \frac{3V_1^f}{3K_1 + 4G_1}} \quad (3.21)$$

$$K_2^* = K_2 + \frac{V_1^f}{\frac{1}{K_1 - K_2} + \frac{3V_2^f}{3K_2 + 4G_2}} \quad (3.22)$$

$$G_1^* = G_1 + \frac{V_2^f}{\frac{1}{G_2 - G_1} + \frac{6(K_1 + 2G_1)V_1^f}{5G_1(3K_1 + 4G_1)}} \quad (3.23)$$

$$G_2^* = G_2 + \frac{V_1^f}{\frac{1}{G_1 - G_2} + \frac{6(K_2 + 2G_2)V_2^f}{5G_2(3K_2 + 4G_2)}} \quad (3.24)$$

for a two-phase material provided that $(K_1 - K_2)(G_1 - G_2) > 0$. Note that the Hashin-Shtrikman bounds in (3.20) were derived assuming that $K_2 > K_1$ and $G_2 > G_1$. If the opposite is true for both the bulk and shear moduli, the subscripts can be switched for all variables and the same expressions apply without loss of generality [56].

Examples of the self-consistent estimates for material properties can be found in [105], [106], and [126]. The self-consistent model provides relationships for two-phase composites that are perhaps more physically realistic than the rule-of-mixtures. The main disadvantages of the self-consistent model are that they only apply to elastic solids and a set of nonlinear implicit equations must be solved to obtain the elastic modulus and Poisson's ratio. Further, if the properties of the two constituent materials vary greatly, it can be difficult to find a solution to the implicit equations if good estimates of the net composite properties are not known *a priori*.

3.1.4 Mori-Tanaka Estimates. Mori and Tanaka [81] demonstrated that *in two-phase composites, i.e., a matrix with randomly distributed misfitting inclusions, the average internal stress in the matrix is uniform throughout the material and independent of the position of the domain where the average is obtained. They also showed that the actual stress in the matrix is the average stress in the composite plus a locally*

varying stress, the average of which is zero in the matrix phase. Benveniste [15] used their analysis as the basis for developing equations that can be used to determine bulk and shear moduli for the composite material as a whole:

$$\frac{K - K_1}{K_2 - K_1} = \frac{V_2^f C_1}{\left(1 - V_2^f\right) + V_2^f C_1} \quad (3.25)$$

$$\frac{G - G_1}{G_2 - G_1} = \frac{V_2^f C_2}{\left(1 - V_2^f\right) + V_2^f C_2} \quad (3.26)$$

C_1 and C_2 are constants, based on the geometry of the inclusions. Berryman [16], [17] provides a formulation for inclusions with spherical and ellipsoid geometries. General ellipsoids can be complicated, but spherical inclusions are special cases with simple formulas for C_1 and C_2 :

$$\begin{aligned} C_1 &= \frac{K_1 + (4/3)G_1}{K_2 + (4/3)G_1} \\ C_2 &= \frac{G_1 + f_1}{G_2 + f_1} \\ f_1 &= \frac{G_1 (9K_1 + 8G_1)}{6(K_1 + 2G_1)} \end{aligned} \quad (3.27)$$

Another special case of ellipsoid inclusions is that of needle-shaped inclusions; the constants C_1 and C_2 are given by:

$$\begin{aligned} C_1 &= \frac{K_1 + G_1 + (1/3)G_2}{K_2 + G_1 + (1/3)G_2} \\ C_2 &= \frac{1}{5} \left(\frac{4G_1}{G_1 + G_2} + 2 \frac{G_1 + f'_1}{G_2 + f'_1} + \frac{K_2 + (4/3)G_1}{K_2 + G_1 + (1/3)G_2} \right) \\ f'_1 &= \frac{G_1 (3K_1 + G_1)}{(3K_1 + 7G_1)} \end{aligned} \quad (3.28)$$

The mathematics behind these relations are very complicated and these material models are presented without derivation. Some practical examples of the use of the Mori-Tanaka estimates for material properties can be found in [105], [106], and [126]. The Mori-Tanaka estimates have a distinct advantage over the self-consistent models

in that material properties are obtained by solving explicit formulas for the bulk and shear moduli of the composite and obtaining the elastic modulus and Poisson's ratio from those results. The Mori-Tanaka estimates account for spherical or needle-shaped inclusions easily (important for the titanium-titanium boride FGM discussed in Chapter IV) where the self-consistent theory does not easily account for inclusions other than those of spherical geometry. Unfortunately, the Mori-Tanaka estimates are constrained to purely elastic analyses and are thus somewhat limited in application.

3.1.5 Other Models. The four material models discussed (rule-of-mixtures, modified rule-of-mixtures, self-consistent model, and Mori-Tanaka estimates) are not the only models available. In fact, there are many micromechanics-based models available. Luciano and Willis noted that the rule-of-mixtures, self-consistent method, Mori-Tanaka estimates, and others are typically only applicable in functionally graded materials where volume fractions of constituents are within certain bounds. Further, some of the assumptions concerning the load and material distributions may not be entirely accurate when applied to FGMs vs. typical laminated composites. Some researchers have attempted to combine two or more FGM functional models together for use in specified regions, although this is not desirable [75]. In 2004, these investigators derived a single mathematical operator that allows one to develop a thermoelastic constitutive relation regardless of the local load or material distribution. The operator is formulated to allow coupling of the load and property distributions given little or partial knowledge of the microstructure and displacement fields from a statistical basis. If complete knowledge of the material and displacement fields is available (e.g., through experimentation), an exact solution for the constitutive relation is available using the mathematical operator. In 2007, Yin et al. [140] published a micromechanics model that looks at representative volume elements on a scale small enough to address the FGM microstructure on the basis of a continuous matrix with spherical particulate inclusions randomly distributed based on the local volume fraction ratio. The model is very complicated yet was found to reflect experimental FGM data very

well. Their material model can account for regions in the FGM where matrix phase and inclusion phase materials are reversed, i.e., the matrix material becomes the inclusion material and the inclusion material becomes the matrix material. The model is thus applicable to the spectrum of volume fraction ratios, where models such as those presented previously may be valid only under certain volume fraction ratio bounds. While both models described here are more physically accurate than other models presented, the primary disadvantage in using them is they are very mathematically complex and are not easily implemented in design practice.

3.2 Relevant Plate Theory

This research is concerned with the impact response of functionally graded plates. A series of plate impact experiments were conducted with FGM specimens, and these experiments will be discussed at length in Chapter V. A key finding in the impact tests was that the FGM plate specimens used in the experiments behaved nearly linear-elastic to failure. Additionally, the impact velocity was relatively low and the plate loading occurred over a sufficiently long period of time that global deformations of the plate dominated the net impact response of the plate. Given these findings, discussed in the later chapters of this dissertation, the composite plate theory of this section will be limited to the realm of *linear-elastic, small-strain, global structural dynamics*. The localized wave solution to the impact problem will not be considered in this work. Concepts in rectangular plates will be presented first, followed by the same concepts applied to circular plates. The theory in this section will be referred to frequently throughout the remainder of this dissertation and will play an important role in the analytical treatment of the impact tests in Chapters VII-VIII.

3.2.1 Rectangular Flat Plates. The theory of thin plates and shells is well-developed, and the reader is referred to Timoshenko & Woinowsky-Krieger [124], Palazotto & Dennis [88], Ugural [125], Soedel [119], and Reddy [100] for complete

development of the theory from first principles. Only the equations and theory directly relevant to understanding this research will be included and these are summarized from the listed references as appropriate for brevity.

The assumptions that govern *classical plate theory* (CPT) of isotropic *thin* plates, attributed generally to Kirchhoff, are as follows:

1. The deflection of the mid-surface of the plate is small compared to its thickness.
2. The midplane of the plate remains unstrained subsequent to bending.
3. Plane sections initially normal to the mid-surface of the plate remain plane and normal to that surface after bending.
4. The stress normal to the midplane is small compared to the other stress components and can be neglected (except locally in the case of a highly concentrated load).

Consider an isotropic plate whose mid-surface occupies the xy plane at $z = 0$ in Cartesian coordinates with total thickness h (thickness extends from $z = -h/2$ to $z = +h/2$). In CPT, the displacement field of the plate is assumed to be

$$\begin{aligned} u(x, y, z, t) &= u_0(x, y, t) - z \frac{\partial w_0}{\partial x} \\ v(x, y, z, t) &= v_0(x, y, t) - z \frac{\partial w_0}{\partial y} \\ w(x, y, z, t) &= w_0(x, y, t) \end{aligned} \tag{3.29}$$

u , v , and w are the displacements in the x , y , z directions, respectively, and the subscript 0 denotes the displacement of the mid-surface. The displacement field of the plate is illustrated in Figure 3.2. In the absence of in-plane extensional loads, u_0 and v_0 are zero in these displacement equations (per assumption 2 of CPT). Now, the

strain-displacement relations from linear elasticity are:

$$\begin{aligned}
\epsilon_{xx} &= \frac{\partial u}{\partial x} & \gamma_{xy} &= \left(\frac{\partial u}{\partial y} + \frac{\partial v}{\partial x} \right) \\
\epsilon_{yy} &= \frac{\partial v}{\partial y} & \gamma_{xz} &= \left(\frac{\partial w}{\partial x} + \frac{\partial u}{\partial z} \right) \\
\epsilon_{zz} &= \frac{\partial w}{\partial z} & \gamma_{yz} &= \left(\frac{\partial w}{\partial y} + \frac{\partial v}{\partial z} \right)
\end{aligned} \tag{3.30}$$

ϵ_{ii} are the normal strains and γ_{ij} are the engineering shear strains. The normal strain ϵ_{zz} and the transverse shear strains γ_{xz} and γ_{yz} are required to be zero according to CPT assumptions 3 and 4. The form of the displacement field in (3.29) is to ensure that these strains are zero and satisfy assumptions 3 and 4. Instead of assuming the displacement field in (3.29), one can begin with the strain-displacement relations (3.30), set ϵ_{zz} , γ_{xz} , and γ_{yz} equal to zero, then integrate the three equations to obtain (3.29).

Applying the strain-displacement equations to the displacement field results in

$$\begin{aligned}
\epsilon_{xx} &= \frac{\partial u_0}{\partial x} - z \frac{\partial^2 w_0}{\partial x^2} & \gamma_{xy} &= \frac{\partial u_0}{\partial y} + \frac{\partial v_0}{\partial x} - 2z \frac{\partial^2 w_0}{\partial x \partial y} \\
\epsilon_{yy} &= \frac{\partial v_0}{\partial y} - z \frac{\partial^2 w_0}{\partial y^2} & \gamma_{xz} &= -\frac{\partial w_0}{\partial x} + \frac{\partial w_0}{\partial x} = 0 \\
\epsilon_{zz} &= 0 & \gamma_{yz} &= -\frac{\partial w_0}{\partial y} + \frac{\partial w_0}{\partial y} = 0
\end{aligned} \tag{3.31}$$

In the case of thick plates, assumption 3 (and assumption 4 in certain cases) no longer applies and the transverse strains are not necessarily zero. A modified theory, called shear-deformable plate theory, assumes the shape of the plane sections initially

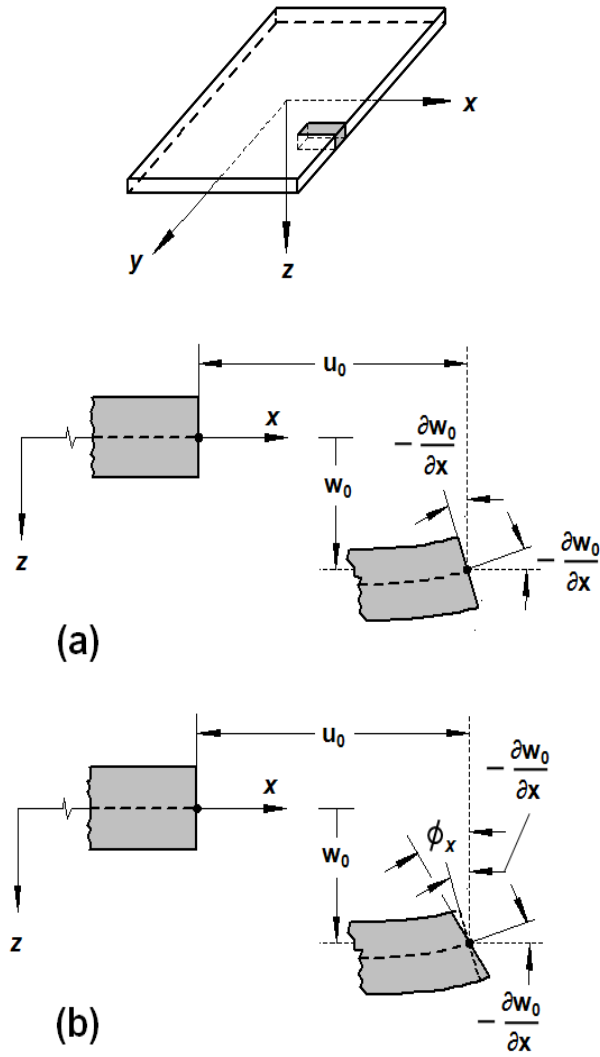


Figure 3.2: Visual comparison of displacement fields of (a) classical plate theory & (b) first-order shear deformation theory (adapted from [100]).

normal to the mid-surface after bending occurs. The first-order shear deformable plate theory (FST) developed primarily by Mindlin [80] and Reissner [104] relaxes assumption 3 of CPT by stating instead that plane sections initially normal to the mid-surface of the plate remain plane *but not necessarily normal* to that surface after bending. The displacement field for FST is

$$\begin{aligned} u(x, y, z, t) &= u_0(x, y, t) + z\phi_x(x, y, t) \\ v(x, y, z, t) &= v_0(x, y, t) + z\phi_y(x, y, t) \\ w(x, y, z, t) &= w_0(x, y, t) \end{aligned} \tag{3.32}$$

where ϕ denotes rotation of the transverse normal and ϕ_x and ϕ_y are rotations of the transverse normal about the y and x -axes, respectively. The displacement field of FST is illustrated in Figure 3.2 along with that associated to CPT. The normal strain ϵ_{zz} in FST is assumed to be zero by assumption 4 but the relaxation of assumption 3 implies that the transverse shear strains γ_{xz} and γ_{yz} are now non-zero. The form of the displacement field in (3.32) is to ensure that these conditions are satisfied. Instead of assuming the displacement field in (3.32), one can begin with the strain-displacement relations (3.30), set $\epsilon_{zz} = 0$, γ_{xz} & γ_{yz} equal to a function of in-plane coordinates (x, y) , then integrate the three equations to obtain (3.32). The quantities $z\phi_x$ and $z\phi_y$ have positive signs here to account for the fact that the shear strains are non-zero in FST. The negative sign in front of the quantities $z(\partial w_0/\partial x)$ and $z(\partial w_0/\partial y)$ in (3.29) is a consequence of the assumption that the shear strains are zero. The displacement field of FST in (3.32) can be applied to CPT noting that

$$\phi_x \rightarrow -\frac{\partial w_0}{\partial x} \quad , \quad \phi_y \rightarrow -\frac{\partial w_0}{\partial y}$$

applies as a plate becomes sufficiently thin to allow the assumptions of CPT for analysis purposes.

Returning to the strain-displacement relations of (3.30), the strains in FST now take the form:

$$\begin{aligned}
\epsilon_{xx} &= \frac{\partial u_0}{\partial x} + z \frac{\partial \phi_x}{\partial x} & \gamma_{xy} &= \frac{\partial u_0}{\partial y} + \frac{\partial v_0}{\partial x} + z \left(\frac{\partial \phi_x}{\partial y} + \frac{\partial \phi_y}{\partial x} \right) \\
\epsilon_{yy} &= \frac{\partial v_0}{\partial y} + z \frac{\partial \phi_y}{\partial y} & \gamma_{xz} &= \frac{\partial w_0}{\partial x} + \phi_x \\
\epsilon_{zz} &= 0 & \gamma_{yz} &= \frac{\partial w_0}{\partial y} + \phi_y
\end{aligned} \tag{3.33}$$

Comparing the relations (3.31) to (3.33), the obvious difference from CPT is that the transverse shear strains are now non-zero. In fact, since the transverse shear strains γ_{xz} and γ_{yz} are only functions of x and y in spatial coordinates, their values will be constant through the thickness of the plate at any local (x, y, z) coordinate. Given that this is the case, the transverse shear stresses will also be constant. In beam theory, a shear-deformable beam has a parabolic stress distribution. The transverse stress distribution through a shear-deformable plate is essentially the same. Thus, the FST for plates needs to be corrected to account for the discrepancy. The use of shear correction factors to accomplish this will be discussed later. Higher-order shear deformable theories have been developed to account for the parabolic distribution in stress [132], [100]. The displacement field used to describe the plate deformation is more complicated with higher-order theories yet is generally much more accurate for thick plates. First and higher-order shear deformable theories have been developed extensively by J. N. Reddy for many applications, including composite and functionally graded materials (see [103], [132], [98], [99], and [100]).

Another note regarding the strain relations in (3.31) and (3.33): the in-plane strains $(\epsilon_{xx}, \epsilon_{yy}, \gamma_{xy})$ have terms containing u_0 and v_0 . These terms relate the effects of the straining of the mid-surface of the plate to the overall in-plane strains. The remaining terms in these expressions for the in-plane strains are related to the bending

curvature of the plate. In a purely bending analysis, the mid-surface deflections u_0 and v_0 would be zero and thus only the terms related to the bending curvatures remain. It is therefore convenient to express the strains in (3.31) and (3.33) in the following manner:

$$\begin{aligned}
\begin{Bmatrix} \epsilon_{xx} \\ \epsilon_{yy} \\ \gamma_{xy} \\ \gamma_{xz} \\ \gamma_{yz} \end{Bmatrix} &= \begin{Bmatrix} \frac{\partial u_0}{\partial x} \\ \frac{\partial v_0}{\partial y} \\ \frac{\partial u_0}{\partial y} + \frac{\partial v_0}{\partial x} \\ \frac{\partial w_0}{\partial x} + \phi_x \\ \frac{\partial w_0}{\partial y} + \phi_y \end{Bmatrix} + z \begin{Bmatrix} \frac{\partial \phi_x}{\partial x} \\ \frac{\partial \phi_y}{\partial y} \\ \frac{\partial \phi_x}{\partial y} + \frac{\partial \phi_y}{\partial x} \\ 0 \\ 0 \end{Bmatrix} \\
&= \begin{Bmatrix} \epsilon_{xx}^0 \\ \epsilon_{yy}^0 \\ \gamma_{xy}^0 \\ \gamma_{xz} \\ \gamma_{yz} \end{Bmatrix} + z \begin{Bmatrix} \epsilon_{xx}^1 \\ \epsilon_{yy}^1 \\ \gamma_{xy}^1 \\ 0 \\ 0 \end{Bmatrix} \tag{3.34}
\end{aligned}$$

The superscripts 0 and 1 on the in-plane strain terms refer to the strain effects related to mid-surface extensions and bending curvatures, respectively. The transverse shear strains are generally treated separately and thus have no superscripts. Again, the relations in (3.34) apply to both CPT and FST noting that

$$\phi_x \rightarrow -\frac{\partial w_0}{\partial x} \quad , \quad \phi_y \rightarrow -\frac{\partial w_0}{\partial y}$$

as a plate becomes sufficiently thin to allow the assumptions of CPT for analysis purposes.

For a linear-elastic three-dimensional state of stress, the relationships between stress and strain for an isotropic material are given by the following relations:

$$\begin{aligned}
\epsilon_{xx} &= +\frac{1}{E} [\sigma_{xx} - \nu (\sigma_{yy} + \sigma_{zz})] & \gamma_{xy} &= \frac{\sigma_{xy}}{G} \\
\epsilon_{yy} &= +\frac{1}{E} [\sigma_{yy} - \nu (\sigma_{xx} + \sigma_{zz})] & \gamma_{xz} &= \frac{\sigma_{xz}}{G} \\
\epsilon_{zz} &= +\frac{1}{E} [\sigma_{zz} - \nu (\sigma_{xx} + \sigma_{yy})] & \gamma_{yz} &= \frac{\sigma_{yz}}{G}
\end{aligned} \tag{3.35}$$

Assumption 3 from CPT implies that σ_{zz} is zero. The stress-strain relations for an isotropic plate assuming CPT are then simplified to

$$\begin{aligned}
\sigma_{xx} &= \frac{E}{1 - \nu^2} (\epsilon_{xx} + \nu \epsilon_{yy}) \\
\sigma_{yy} &= \frac{E}{1 - \nu^2} (\epsilon_{yy} + \nu \epsilon_{xx}) \\
\sigma_{xy} &= G \gamma_{xy}
\end{aligned} \tag{3.36}$$

The stress-strain relations for an isotropic plate assuming FST are

$$\begin{aligned}
\sigma_{xx} &= \frac{E}{1 - \nu^2} (\epsilon_{xx} + \nu \epsilon_{yy}) \\
\sigma_{yy} &= \frac{E}{1 - \nu^2} (\epsilon_{yy} + \nu \epsilon_{xx}) \\
\sigma_{xy} &= G \gamma_{xy} \\
\sigma_{xz} &= G \gamma_{xz} \\
\sigma_{yz} &= G \gamma_{yz}
\end{aligned} \tag{3.37}$$

The stresses in the plates can be integrated over the thickness of the plate to produce resultants (per unit width) for in-plane extensional & shear forces (N), bending &

twisting moments (M), and vertical shear forces (Q) governed by

$$\begin{pmatrix} N_{xx} \\ N_{yy} \\ N_{xy} \end{pmatrix} = \int_{-h/2}^{h/2} \begin{pmatrix} \sigma_{xx} \\ \sigma_{yy} \\ \sigma_{xy} \end{pmatrix} dz \quad (3.38)$$

$$\begin{pmatrix} M_{xx} \\ M_{yy} \\ M_{xy} \end{pmatrix} = \int_{-h/2}^{h/2} \begin{pmatrix} \sigma_{xx} \\ \sigma_{yy} \\ \sigma_{xy} \end{pmatrix} z dz \quad (3.39)$$

$$\begin{pmatrix} Q_x \\ Q_y \end{pmatrix} = \int_{-h/2}^{h/2} \begin{pmatrix} \sigma_{xz} \\ \sigma_{yz} \end{pmatrix} dz \quad (3.40)$$

The integral equations (3.38)-(3.40) are applicable to both CPT and shear deformable plate theories. Note that in CPT, σ_{xz} and σ_{yz} are zero and thus it would seem intuitive that the vertical shear force resultants Q are also zero. This is not the case, in fact, expressions for the vertical shear resultants are obtained from the equations of equilibrium governing the plate behavior and cannot be neglected. In FST, a shear correction factor is applied to equation (3.40) to account for the discrepancy between the constant value of shear stress through the thickness in FST versus the actual parabolic distribution of stress through the thickness:

$$\begin{pmatrix} Q_x \\ Q_y \end{pmatrix} = K_s \int_{-h/2}^{h/2} \begin{pmatrix} \sigma_{xz} \\ \sigma_{yz} \end{pmatrix} dz \quad (3.41)$$

Where K_s is the shear correction factor taken generally to be 5/6.

Substituting (3.34) into the stress-strain relations (3.37) and taking the results and applying them to (3.38)-(3.40), one can write the result in the following form:

$$\begin{Bmatrix} N_{xx} \\ N_{yy} \\ N_{xy} \\ M_{xx} \\ M_{yy} \\ M_{xy} \end{Bmatrix} = \begin{bmatrix} A_{11} & A_{12} & A_{16} & B_{11} & B_{12} & B_{16} \\ A_{12} & A_{22} & A_{26} & B_{12} & B_{22} & B_{26} \\ A_{16} & A_{26} & A_{66} & B_{16} & B_{26} & B_{66} \\ B_{11} & B_{12} & B_{16} & D_{11} & D_{12} & D_{16} \\ B_{12} & B_{22} & B_{26} & D_{12} & D_{22} & D_{26} \\ B_{16} & B_{26} & B_{66} & D_{16} & D_{26} & D_{66} \end{bmatrix} \begin{Bmatrix} \epsilon_{xx}^0 \\ \epsilon_{yy}^0 \\ \gamma_{xy}^0 \\ \epsilon_{xx}^1 \\ \epsilon_{yy}^1 \\ \gamma_{xy}^1 \end{Bmatrix} \quad (3.42)$$

$$\begin{Bmatrix} Q_y \\ Q_x \end{Bmatrix} = \begin{bmatrix} A_{44} & A_{45} \\ A_{45} & A_{55} \end{bmatrix} \begin{Bmatrix} \epsilon_{yz} \\ \epsilon_{xz} \end{Bmatrix} \quad (3.43)$$

The strains through the plate thickness are continuous. The stresses will be continuous through the thickness for a plate with a single isotropic layer, but not necessarily so for a plate with multiple layers of varying composition. Such a plate is shown in Figure 3.3. In this case, the strains remain linear through the plate thickness but the stresses in each layer are determined by the material stiffnesses of each individual layer. For a plate composed of n discrete isotropic layers, the material constants in the 6 x 6 array in (3.42) and the material constants in the 2 x 2 array in (3.43) are given by:

$$A_{ij} = \sum_{k=1}^n (\bar{Q}_{ij})_k (z_k - z_{k-1}) = \sum_{k=1}^n (\bar{Q}_{ij})_k t_k \quad (3.44)$$

$$B_{ij} = \frac{1}{2} \sum_{k=1}^n (\bar{Q}_{ij})_k (z_k^2 - z_{k-1}^2) = \sum_{k=1}^n (\bar{Q}_{ij})_k t_k \bar{z}_k \quad (3.45)$$

$$D_{ij} = \frac{1}{3} \sum_{k=1}^n (\bar{Q}_{ij})_k (z_k^3 - z_{k-1}^3) = \sum_{k=1}^n (\bar{Q}_{ij})_k \left(t_k \bar{z}_k^2 + \frac{t_k^3}{12} \right) \quad (3.46)$$

$$A_{mn} = K_s \sum_{k=1}^n (\bar{Q}_{mn})_k (z_k - z_{k-1}) = K_s \sum_{k=1}^n (\bar{Q}_{mn})_k t_k \quad (3.47)$$

where t_k is the thickness of an individual layer k ; z_k and \bar{z}_k are illustrated in Figure 3.3 in the given coordinate system; $i, j = 1, 2, 6$; and $m, n = 4, 5$. The $[A_{ij}]$ matrix

is called the in-plane stiffness matrix; the $[B_{ij}]$ matrix is called the bending-extension coupling matrix; the $[D_{ij}]$ matrix is called the bending stiffness matrix; and the $[A_{mn}]$ matrix is called the transverse shear stiffness matrix and is not used with CPT. The stiffnesses \bar{Q}_{ij} and \bar{Q}_{mn} for an individual *isotropic layer* are given by:

$$\bar{Q}_{11} = \bar{Q}_{22} = \frac{E}{1 - \nu^2} \quad (3.48)$$

$$\bar{Q}_{12} = \nu \bar{Q}_{11} \quad (3.49)$$

$$\bar{Q}_{66} = \frac{E}{2(1 + \nu)} \quad (3.50)$$

$$\bar{Q}_{44} = \bar{Q}_{55} = \frac{E}{2(1 + \nu)} \quad (3.51)$$

$$\bar{Q}_{16} = \bar{Q}_{26} = \bar{Q}_{45} = 0 \quad (3.52)$$

E is the modulus of elasticity, ν is Poisson's ratio, and K_s is a shear correction factor. In the case of a functionally graded material with a *continuous* distribution of material through-the-thickness of the plate (i.e., E and ν are functions of the thickness coordinate z such that $E(z)$ and $\nu(z)$), the elements of the $[A_{ij}]$, $[B_{ij}]$, $[D_{ij}]$, and $[A_{mn}]$ matrices are determined by replacing the summations of equations (3.44)-(3.47) to an integral operation over the thickness h of the plate:

$$(A_{ij}, B_{ij}, D_{ij}) = \int_{-\frac{h}{2}}^{\frac{h}{2}} \bar{Q}_{ij} (1, z, z^2) dz \quad (3.53)$$

$$A_{mn} = K_s \int_{-\frac{h}{2}}^{\frac{h}{2}} \bar{Q}_{mn} dz \quad (3.54)$$

The last remaining item is to determine the displacement equations that fit into the framework of (3.29) and (3.32). Once the displacement equations for u_0 , v_0 , and w_0 are known, the stresses and strains in the plate can be determined. It happens that a plate subject to bending is of primary interest in this work, and thus u_0 and v_0 are set to zero. The equations of motion for a plate subject to *bending* are derived from an energy approach involving Hamilton's Principle with strain energy, kinetic energy, and work from external forces and applying the calculus of variations [100].

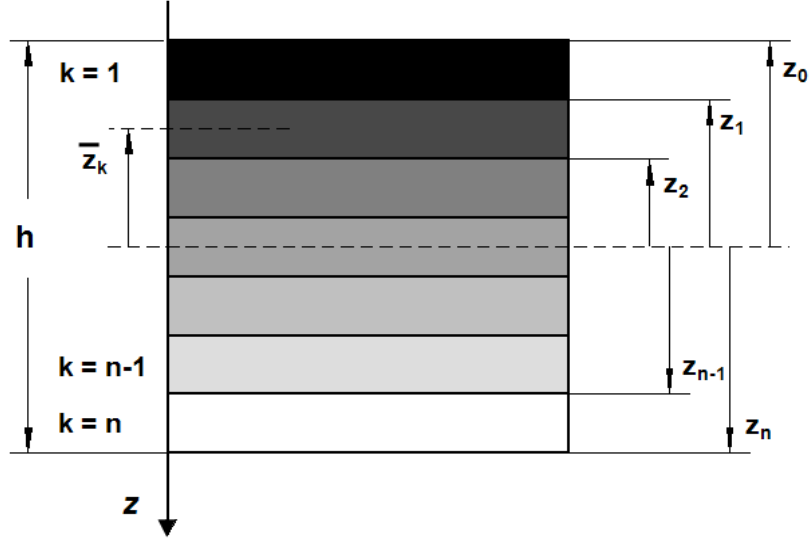


Figure 3.3: Coordinate notation for through-thickness layup of composite plate.

For a thin plate under the assumptions of CPT, the equation of motion is:

$$D \left(\frac{\partial^4 w}{\partial x^4} + 2 \frac{\partial^4 w}{\partial x^2 \partial y^2} + \frac{\partial^4 w}{\partial y^4} \right) + \rho h \frac{\partial^2 w}{\partial t^2} = p \quad (3.55)$$

$p = p(x, y, t)$ is a transversely distributed load that is a function of x , y , and t and D is the flexural rigidity of the plate given by

$$D = \frac{Eh^3}{12(1 - \nu^2)} \quad (3.56)$$

For static analyses, the derivative with respect to time in (3.55) disappears. The equations of motion for a plate under FST assumptions are more complicated since the effects of ϕ_x and ϕ_y rotations must be accounted for. For the case of bending only,

the three necessary equations of motion are (first developed by Mindlin [80]):

$$-K_s Gh \left(\frac{\partial^2 w}{\partial x^2} + \frac{\partial^2 w}{\partial y^2} + \frac{\partial \phi_x}{\partial x} + \frac{\partial \phi_y}{\partial y} \right) + \rho h \frac{\partial^2 w}{\partial t^2} = p \quad (3.57)$$

$$\begin{aligned} \frac{D}{2} \left[(1 - \nu) \left(\frac{\partial^2 \phi_x}{\partial x^2} + \frac{\partial^2 \phi_x}{\partial y^2} \right) + (1 + \nu) \frac{\partial}{\partial x} \left(\frac{\partial \phi_x}{\partial x} + \frac{\partial \phi_y}{\partial y} \right) \right] \\ - K_s Gh \left(\frac{\partial w}{\partial x} + \phi_x \right) - \frac{\rho h^3}{12} \frac{\partial^2 \phi_x}{\partial t^2} = 0 \end{aligned} \quad (3.58)$$

$$\begin{aligned} \frac{D}{2} \left[(1 - \nu) \left(\frac{\partial^2 \phi_y}{\partial x^2} + \frac{\partial^2 \phi_y}{\partial y^2} \right) + (1 + \nu) \frac{\partial}{\partial y} \left(\frac{\partial \phi_x}{\partial x} + \frac{\partial \phi_y}{\partial y} \right) \right] \\ - K_s Gh \left(\frac{\partial w}{\partial y} + \phi_y \right) - \frac{\rho h^3}{12} \frac{\partial^2 \phi_y}{\partial t^2} = 0 \end{aligned} \quad (3.59)$$

Equation (3.57) accounts for the transverse deflection and equations (3.58) and (3.59) account for the rotations owing to shear. Again, equations (3.57)-(3.59) simplify as a shear-deformable plate becomes sufficiently thin to allow the assumptions of CPT; that is:

$$\phi_x \rightarrow -\frac{\partial w_0}{\partial x} \quad , \quad \phi_y \rightarrow -\frac{\partial w_0}{\partial y}$$

The differential equations of motion governing CPT, (3.55), and FST, (3.57)-(3.59), can be solved once boundary conditions are applied. In the case of CPT, (3.55) is solved for w . In the case of FST, (3.57)-(3.59) are solved simultaneously for w , ϕ_x , and ϕ_y .

3.2.2 Circular Plates Subject to Axisymmetric Bending. The general elements of plate theory discussed in the previous section provide some insight into the behavior of plates given assumptions of classical plate theory and the first-order shear deformable plate theory. The plate impact experiments conducted for this research (presented in Chapter V) used functionally graded plates installed into a specially designed fixture with a circular opening. It will be shown in Chapter V that the plates in the fixture tended to behave very closely to a thick circular plate with a simply-supported boundary condition along the circumference of the circular open-

ing. Additionally, the plates were loaded with a central impact load normal to the ceramic-rich surface of the plate. The plate, under these loading conditions, tended to behave very nearly as a plate with a concentrated load at the center that follows the assumptions of axisymmetric bending. The theory behind the behavior of circular plates in axisymmetric bending is essentially the same as with rectangular plates, yet some important simplifications can be made that are very convenient for analysis purposes.

If a plate has a circular geometry with radius a , then it is advantageous to consider the plate in polar/cylindrical coordinates. The familiar relations between Cartesian and cylindrical coordinates (r, θ, z) , namely $x = r \cos \theta$, $y = r \sin \theta$, $z = z$, allow the CPT displacement field (3.29) to be rewritten as

$$\begin{aligned} u_r(r, \theta, z, t) &= u_0(r, \theta, t) - z \frac{dw_0}{dr} \\ u_\theta(r, \theta, z, t) &= v_0(r, \theta, t) - z \left(\frac{1}{r} \frac{dw_0}{d\theta} \right) \\ u_z(r, \theta, z, t) &= w_0(r, \theta, t) \end{aligned} \quad (3.60)$$

u again is the displacement along a given coordinate direction (subscripts r , θ , and z). The FST displacement field (3.32) is similarly rewritten

$$\begin{aligned} u_r(r, \theta, z, t) &= u_0(r, \theta, t) + z \phi_r(r, \theta, t) \\ u_\theta(r, \theta, z, t) &= v_0(r, \theta, t) + z \left(\frac{1}{r} \phi_\theta(r, \theta, t) \right) \\ u_z(r, \theta, z, t) &= w_0(r, \theta, t) \end{aligned} \quad (3.61)$$

Given axisymmetric loads only, the displacement field for CPT is more conveniently expressed

$$\begin{aligned} u_r(r, z, t) &= u_0(r, t) - z \frac{dw_0}{dr} \\ u_z(r, z, t) &= w_0(r, t) \end{aligned} \quad (3.62)$$

and in FST

$$\begin{aligned} u_r(r, z, t) &= u_0(r, t) + z\phi_r(r) \\ u_z(r, z, t) &= w_0(r, t) \end{aligned} \quad (3.63)$$

Note that the key assumption of a plate exhibiting axisymmetric behavior is that the displacements are independent of the angular coordinate θ and u_θ is zero. The strain-displacement in polar coordinates are [108]:

$$\begin{aligned} \epsilon_{rr} &= \frac{\partial u_r}{\partial r} \\ \epsilon_{\theta\theta} &= \frac{1}{r} \frac{\partial u_\theta}{\partial \theta} + \frac{u_r}{r} \\ \epsilon_{zz} &= \frac{\partial u_z}{\partial z} \\ \gamma_{r\theta} &= \frac{1}{r} \frac{\partial u_r}{\partial \theta} + \frac{\partial u_\theta}{\partial r} - \frac{u_\theta}{r} \\ \gamma_{\theta z} &= \frac{1}{r} \frac{\partial u_z}{\partial \theta} + \frac{\partial u_\theta}{\partial z} \\ \gamma_{rz} &= \frac{\partial u_r}{\partial z} + \frac{\partial u_z}{\partial r} \end{aligned} \quad (3.64)$$

Given axisymmetric assumptions these relations simplify dramatically. In CPT, the only nonzero strains are ϵ_{rr} and $\epsilon_{\theta\theta}$. In FST, ϵ_{rr} and $\epsilon_{\theta\theta}$ again are nonzero and ϵ_{rz} is the only nonzero shear strain. It is convenient to express the strains in the following manner:

$$\begin{aligned} \begin{Bmatrix} \epsilon_{rr} \\ \epsilon_{\theta\theta} \\ \gamma_{rz} \end{Bmatrix} &= \begin{Bmatrix} \frac{\partial u_0}{\partial r} \\ \frac{u_0}{r} \\ \frac{\partial w_0}{\partial r} + \phi_r \end{Bmatrix} + z \begin{Bmatrix} \frac{\partial \phi_r}{\partial r} \\ \frac{\phi_r}{r} \\ 0 \end{Bmatrix} \\ &= \begin{Bmatrix} \epsilon_{rr}^0 \\ \epsilon_{\theta\theta}^0 \\ \gamma_{rz}^0 \end{Bmatrix} + z \begin{Bmatrix} \epsilon_{rr}^1 \\ \epsilon_{\theta\theta}^1 \\ 0 \end{Bmatrix} \end{aligned} \quad (3.65)$$

The linear-elastic stress-strain relations in cylindrical coordinates are:

$$\begin{aligned}\sigma_{rr} &= \frac{E}{1-\nu^2} (\epsilon_{rr} + \nu\epsilon_{\theta\theta}) \\ \sigma_{\theta\theta} &= \frac{E}{1-\nu^2} (\epsilon_{\theta\theta} + \nu\epsilon_{rr})\end{aligned}\tag{3.66}$$

The stress-strain relations for an isotropic plate assuming FST are

$$\begin{aligned}\sigma_{rr} &= \frac{E}{1-\nu^2} (\epsilon_{rr} + \nu\epsilon_{\theta\theta}) \\ \sigma_{\theta\theta} &= \frac{E}{1-\nu^2} (\epsilon_{\theta\theta} + \nu\epsilon_{rr}) \\ \sigma_{rz} &= G \gamma_{rz}\end{aligned}\tag{3.67}$$

The force, moment, and shear resultants are determined by

$$\begin{Bmatrix} N_{rr} \\ N_{\theta\theta} \end{Bmatrix} = \int_{-h/2}^{h/2} \begin{Bmatrix} \sigma_{rr} \\ \sigma_{\theta\theta} \end{Bmatrix} dz\tag{3.68}$$

$$\begin{Bmatrix} M_{rr} \\ M_{\theta\theta} \end{Bmatrix} = \int_{-h/2}^{h/2} \begin{Bmatrix} \sigma_{rr} \\ \sigma_{\theta\theta} \end{Bmatrix} z dz\tag{3.69}$$

$$\begin{Bmatrix} Q_{rz} \end{Bmatrix} = \int_{-h/2}^{h/2} \begin{Bmatrix} \sigma_{rz} \end{Bmatrix} dz\tag{3.70}$$

Substituting (3.65) into the stress-strain relations (3.67) and taking the results and applying them to (3.68)-(3.70), one can write the result in the following form:

$$\begin{Bmatrix} N_{rr} \\ N_{\theta\theta} \\ M_{rr} \\ M_{\theta\theta} \end{Bmatrix} = \begin{bmatrix} A_{11} & A_{12} & B_{11} & B_{12} \\ A_{12} & A_{22} & B_{12} & B_{22} \\ B_{11} & B_{12} & D_{11} & D_{12} \\ B_{12} & B_{22} & D_{12} & D_{22} \end{bmatrix} \begin{Bmatrix} \epsilon_{rr}^0 \\ \epsilon_{\theta\theta}^0 \\ \epsilon_{rr}^1 \\ \epsilon_{\theta\theta}^1 \end{Bmatrix}\tag{3.71}$$

$$\begin{Bmatrix} Q_r \end{Bmatrix} = \begin{bmatrix} A_{55} \end{bmatrix} \begin{Bmatrix} \epsilon_{rz} \end{Bmatrix}\tag{3.72}$$

The A_{ij} , B_{ij} , D_{ij} , and A_{mn} in (3.71) and (3.72) are determined precisely the same as in (3.44)-(3.47) using the corresponding \bar{Q}_{ij} and \bar{Q}_{mn} in equations (3.48)-(3.52).

The CPT partial differential equation of motion (3.55) in cylindrical coordinates is given by

$$D \left(\frac{\partial^2}{\partial r^2} + \frac{1}{r} \frac{\partial}{\partial r} + \frac{1}{r^2} \frac{\partial^2}{\partial \theta^2} \right) \left(\frac{\partial^2 w}{\partial r^2} + \frac{1}{r} \frac{\partial w}{\partial r} + \frac{1}{r^2} \frac{\partial^2 w}{\partial \theta^2} \right) + \rho h \frac{\partial^2 w}{\partial t^2} = p \quad (3.73)$$

Equation (3.73) can be simplified in the case of *axisymmetrical bending*, in which case the applied load and transverse deflection are assumed to be independent of the angle θ :

$$D \left(\frac{d^2}{dr^2} + \frac{1}{r} \frac{d}{dr} \right) \left(\frac{d^2 w}{dr^2} + \frac{1}{r} \frac{dw}{dr} \right) + \rho h \frac{\partial^2 w}{\partial t^2} = p \quad (3.74)$$

The governing equations, without derivation, for a circular plate subject to bending with the assumptions of FST are given as [119]:

$$\begin{aligned} -K_s G h \left[\frac{\partial}{\partial r} \left(r \frac{\partial w}{\partial r} \right) + \frac{\partial}{\partial \theta} \left(\frac{1}{r} \frac{\partial w}{\partial \theta} \right) + \frac{\partial}{\partial r} (r \phi_r + \phi_\theta) \right] \\ + r \rho h \frac{\partial^2 w_0}{\partial t^2} = r p \end{aligned} \quad (3.75)$$

$$\begin{aligned} D(1 - \nu) \left[(k_{11} - k_{22}) + \frac{1}{2} \frac{\partial k_{12}}{\partial \theta} + \frac{r}{1 - \nu} \left(\frac{\partial k_{11}}{\partial r} + \nu \frac{\partial k_{12}}{\partial r} \right) \right] \\ - K_s G h r \left(\frac{\partial w}{\partial r} + \phi_r \right) - r \frac{\rho h^3}{12} \frac{\partial^2 \phi_r}{\partial t^2} = 0 \end{aligned} \quad (3.76)$$

$$\begin{aligned} D(1 - \nu) \left[k_{12} + \frac{r}{2} \frac{\partial k_{12}}{\partial r} + \frac{1}{1 - \nu} \left(\frac{\partial k_{22}}{\partial \theta} + \nu \frac{\partial k_{11}}{\partial \theta} \right) \right] \\ - K_s G h r \left(\frac{1}{r} \frac{\partial w}{\partial \theta} + \phi_\theta \right) - r \frac{\rho h^3}{12} \frac{\partial^2 \phi_\theta}{\partial t^2} = 0 \end{aligned} \quad (3.77)$$

where

$$k_{11} = \frac{\partial \phi_r}{\partial r} \quad (3.78)$$

$$k_{22} = \frac{1}{r} \frac{\partial \phi_\theta}{\partial \theta} + \frac{\phi_r}{r} \quad (3.79)$$

$$k_{12} = r \frac{\partial}{\partial r} \left(\frac{\phi_\theta}{r} \right) + \frac{1}{r} \frac{\partial \phi_r}{\partial \theta} \quad (3.80)$$

Equation (3.75) accounts for the transverse deflection and equations (3.76) and (3.77) account for the rotations owing to shear. Once again, equations (3.75)-(3.77) simplify as a shear-deformable plate becomes sufficiently thin to allow the assumptions of CPT; that is:

$$\phi_r \rightarrow -\frac{\partial w_0}{\partial r} \quad , \quad \phi_\theta \rightarrow -\frac{\partial w_0}{\partial \theta}$$

The differential equations of motion governing CPT, (3.73), and FST, (3.75)-(3.77), can be solved once boundary conditions are applied. In the case of CPT, (3.73) is solved for w . In the case of FST, (3.75)-(3.77) are solved simultaneously for w , ϕ_r , and ϕ_θ . Equations (3.75)-(3.77) greatly simplify in the case of *axisymmetric bending* since all the contributions with respect to θ disappear and ϕ_θ disappears as well.

3.3 Closing

In this chapter, material models commonly used in FGM analyses have been discussed. A few of these models will be applied to analytical and computational models of the plate impact experiments discussed later in this dissertation. Basics in linear-elastic plate theory have also been presented to build a solid foundation from which the FGM plate impact problem can be further addressed, given that the FGM plates behaved in a nearly linear-elastic fashion during impact testing (discussed in Chapter V). The wave solution to the impact problem has not and will not be considered; the reasons for this will be made more clear in subsequent chapters. The theory presented here will be frequently referred to in the remaining chapters, and some of the plate theory concepts will be expanded in later chapters in order to effectively characterize the response of FGM plates under low-velocity, low- to medium-energy impact loads.

IV. Titanium-Titanium Boride FGM System

At this point, a literature review in FGM plate studies and the classic analysis methods for homogeneous and composite plates have been presented. The literature review demonstrated that deficiencies in the study of FGM composites exist in (1) experimental data to validate claims and (2) characterizing the response of graded plates and shells under impact loading. One of the key hallmarks of this study is an *experimental* method by which the impact response of FGM plates can be characterized. *The first step in this process was to obtain specimen FGM plates that could be tested in the laboratory.*

Perhaps the best reason that very little experimental work on FGMs has been performed is their limited availability. The short supply of FGMs can be attributed to the fact they are notoriously difficult to produce and thus can be extremely expensive compared to other available engineering materials. Polymer-based FGMs have been developed in the laboratory relatively inexpensively in the past for these very reasons; see Lambros et al. [64], [65] and Parameswaran and Shukla [91]. Metal-ceramic FGM systems are of greater interest here since a metal-ceramic FGM system would more likely be used as a thermal protection system than a polymer-based FGM. The technology for producing metal-ceramic FGM systems has emerged over the past two decades (see [122] and [63]), however, the technology to produce these composites needs to be enhanced before FGMs will be more readily available to design engineers.

The FGM system chosen for the experiments in this research was a titanium-titanium boride metal-ceramic material that is manufactured in industry. *The purpose of this chapter is to discuss the characteristics of this particular FGM system in detail.* Knowledge of the titanium (Ti) and titanium boride (TiB) constituents and the mixture of the two materials provides valuable insight as the FGM plates are subjected to impact loading.

4.1 Manufacturing Titanium-Titanium Boride FGMs

The FGM system that will be used in this research is a titanium-titanium boride system developed by BAE Systems-Advanced Ceramics in Vista, California. BAE Systems uses a proprietary “reaction sintering” process to produce the Ti-TiB FGMs. Titanium and titanium diboride (TiB_2) are combined in powder form in a graphite die according to the required volume fraction ratios through the FGM plate thickness. A catalyzing agent is applied to the construction, and the powders are subjected to extreme temperature (near the melting point of titanium) and pressure in a vacuum or inert gas environment. The catalyzing agent reacts with the titanium and titanium diboride powders to form titanium boride that crystalizes in a needle morphology. In the reaction process, almost no residual TiB_2 remains in the FGM. Through this process, the powders adhere together and the Ti-TiB FGM plate is the final product [4]. A microscopic view of a Ti-TiB plate can be seen in Figure 4.1. The process can be used to construct monolithic composites of constant volume fraction or composites graded along a given dimension. The change in composition of the constituents along a dimension is discrete and not truly continuous, although the length over which a discrete change occurs can be very small and can closely approximate a continuous function. In Figure 4.1, the grading from 100% Ti to 15% Ti-85% TiB occurred over seven discrete jumps in composition giving the plate a layered configuration.

4.2 Titanium, Titanium Boride Constituents

In this section, some material details associated with the Ti and TiB constituents are presented. With any multi-constituent FGM system, it is extremely important to understand well the individual constituent materials combined in the FGM construction. Knowledge about the individual constituents provides insight into the combination of materials and often allows conclusions to be drawn as the response of the mixture is studied.

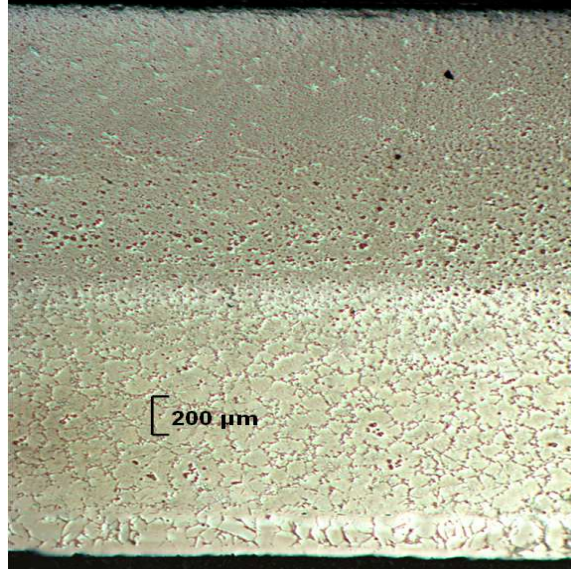


Figure 4.1: Microscopic view of Ti-TiB FGM [26]. TiB rich areas are near the top surface; Ti rich areas are near the bottom surface.

4.2.1 Titanium. Titanium is a metallic element that is arranged in a hexagonal-close-packed (HCP) crystal microstructure at room temperature (commonly called α -phase or α -Ti). The microstructure of Ti transforms to a body-centered-cubic (BCC) crystal structure at 883 °C (commonly called β -phase or β -Ti) [118]. It is known for its excellent corrosion resistance in many environments and is therefore a desirable material used frequently in the aerospace industry. Titanium is readily combined and commonly alloyed with various elements such as aluminum, vanadium, zirconium, and iron to improve mechanical properties for various applications [10]. For this research, we are primarily interested in commercially pure titanium (CP-Ti), generally considered composed of 99% Ti or better. CP-Ti is typically designated in three grades by the American Society for Testing and Materials (ASTM), specifically ASTM grades 1,2, and 7. The grade designation is assigned based on the level of impurities present in the material.

Table 4.1 gives typical properties for CP-Ti at room temperature. Mechanical properties for the three common ASTM grades do not vary greatly, and the values in the table are sufficient for most design purposes. As with most engineering materials,

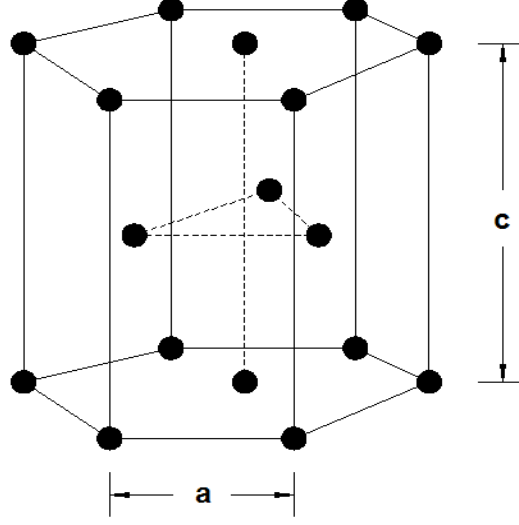


Figure 4.2: Hexagonal close-packed crystal structure of titanium at room-temperature. The dimensions of the crystal shown are $a = 295$ picometers and $c = 468$ picometers (1 picometer = 1×10^{-12} meters) [40].

however, the mechanical properties are a function of the operating temperature. Since the Ti-TiB FGMs were studied at room temperature in this work, all properties will be assumed as temperature-independent for simplification.

Where impact problems are concerned, the plastic region of the stress-strain curve is very important, especially given that even low-energy impacts can generate stresses high enough to induce permanent deformation local to the contact area. The

Table 4.1: Typical material property data for commercially pure titanium at room temperature [86], [4].

Property	Value	Units
Density, ρ	4512	kg/m ³
Young's Modulus, E	110.0	GPa
Poisson's Ratio, ν (minimum)	0.24	
Shear Modulus, G	41.37	GPa
Yield Stress, σ_y	379.2	MPa
Ultimate Stress, σ_{ult}	517.1	MPa
Coefficient of Thermal Expansion, α	9.18	$\mu\text{m}/(\text{m-K})$

temperature and strain-rate sensitivity of the plastic flow stress, ultimate stress, and material plastic modulus also become very important to impact studies, especially given applications of thermal protection in high-temperature environments. Effects such as these did not feature themselves in the plate impact experiments conducted in this work (discussed in Chapter V), however they must be considered in more general impact problems where higher velocity impacts potentially induce localized, strain-rate sensitive wave effects. In this context, a few studies into the high strain-rate response of Ti are worth mentioning briefly to give insight should the Ti constituent be used in a thermal protection FGM system. A study by Meyers et al. [79] in 1994 attempted to ascertain the strain-rate sensitivity and microstructure development of commercially pure α -Ti under plastic deformation. Strain-rate data was obtained in the regime between 2.0×10^{-4} and $7.6 \times 10^3 \text{ s}^{-1}$. The data collected indicated that the plastic flow stress of α -phase CP-Ti increased linearly on a logarithmic scale for the given strain rates below 10^3 s^{-1} . At very high strain rates, above 10^3 s^{-1} , the trend changes from linear increase to nearly parabolic increase (on a logarithmic scale) in plastic flow stress in qualitative form. Chichili et al. [27] in 1998 performed a highly comprehensive study of the strain-rate sensitivity of commercially pure titanium over the range of 10^{-5} to 10^5 s^{-1} with temperatures ranging between 77 and 298 K. These tests required use of a servohydraulic testing machine, a compression Hopkinson bar, and a pressure-shear flyer plate impact apparatus. The experimentally determined flow stress data matched well with the results obtained by Meyers et al. [79]. Constitutive modeling was performed using the Kocks-Mecking constitutive model (a highly complex physics-based constitutive model; see [78], [44], [43]) for strain rates up to 10^4 s^{-1} that captured the monotonic loading behavior of the α -Ti very well. Nemat-Nasser et al. [84] conducted an important experimental study into commercially pure titanium in 1999 where a large body of true stress-strain curves and data were generated for compression strain-rates up to 8000 s^{-1} and temperatures between 77 and 1000 K. The authors concluded that physics-based constitutive models must include contributions from crystal-microstructure effects to model the experimental data ef-

fectively. Two other similar studies in high-temperature, high strain-rate response of titanium alloys were conducted by Lee and Lin [70] and Rosen et al. [107].

4.2.2 Titanium Boride. Titanium boride (TiB) is the ceramic constituent used in the FGM system developed by BAE Systems. The development of titanium boride for use in titanium metal-matrix composites (MMCs) has only come about in recent years. TiB reinforcement can be produced *in situ* by solid state reaction using powder metallurgy techniques (BAE Systems uses the reaction sintering technique to produce their Ti-TiB MMCs and FGMs). Powders of commercially pure titanium and TiB₂ are combined in a die according to the volume ratio design configuration required. The powder construction is then subjected to extremely high pressures and temperatures (just below the melting point of titanium) in a vacuum or inert-gas environment. The powders in this high-temperature, compressed environment adhere together and the composite takes its final form and is cooled [4]. While the precise details of the manufacturing process are proprietary to BAE Systems, the novel technique of constructing Ti-TiB composites in this fashion has been documented in the literature (see Panda and Ravichandran [89] for a list of publications in this area). TiB₂ and TiB do not occur naturally and must be artificially processed. The following chemical reaction describes the process [89]:



Basic material properties for TiB are given in Table 4.2.

The crystal structure of TiB is B27 class orthorhombic, established by Decker and Kasper in 1954 [36]. The fundamental building block of TiB crystal structures is essentially a trigonal prism with titanium atoms at the corners of the prism and a boron atom at the center of the prism, shown in Figure 4.3. The trigonal prisms stack in columnar arrays connected at their edges only to form the orthorhombic crystal structure. An orthorhombic crystal structure is essentially a rectangular, right prism with unequal sides a , b , and c . A single unit cell contains four titanium atoms and

Table 4.2: Typical material property data for titanium boride at room temperature [4].

Property	Value	Units
Density, ρ	4630	kg/m ³
Young's Modulus, E	370.0	GPa
Poisson's Ratio, ν (minimum)	0.14	
Shear Modulus, G	162.3	GPa
Coefficient of Thermal Expansion, α	9.00	$\mu\text{m}/(\text{m-K})$

four boron atoms with dimensions $a = 612$ picometers, $b = 306$ picometers, and $c = 456$ picometers (1 picometer = 1×10^{-12} meters) [109]. The crystal structure formed during the solid state reaction contributes heavily to the needle morphology characteristic of TiB within MMCs. An extensive study of the microstructure and phases in Ti-TiB MMCs produced by the described reaction sintering was conducted by Sahay et al. [109] in 1999. In their study, Ti-TiB monolithic MMCs were constructed with various volume fraction ratios of Ti and TiB₂ powders. After the monolithic samples were manufactured, the authors used x-ray diffraction techniques to determine the volume fraction ratio of Ti and TiB formed through the process as well as the volume fraction of TiB₂ remaining untransformed into TiB. A sample of the results is shown in Table 4.3. A few important conclusions were made. At low volume fractions of TiB (up to $V^f = 0.30$), TiB whiskers are long, needle-shaped and randomly dispersed throughout the Ti matrix. At medium to high volume fractions of TiB (up to $V^f = 0.86$), colonies of densely-packed TiB whiskers formed. At very high volume fractions of TiB ($V^f > 0.86$), the TiB formed a very coarse, elongated structure with very few whiskers present. Finally, at the high volume fractions of TiB, residual TiB₂ was detected in the samples not present in samples with lower volume fractions of TiB.

The choice of TiB as reinforcement in Ti-MMCs has several distinct advantages over other possible titanium compounds [89], [97]. First, there is a dramatic increase in strength when TiB whiskers are added to titanium versus titanium by itself. Second, the coefficients of thermal expansion and mass densities of the two materials are very near in value, thus reducing localized thermal stresses from mismatching materials in

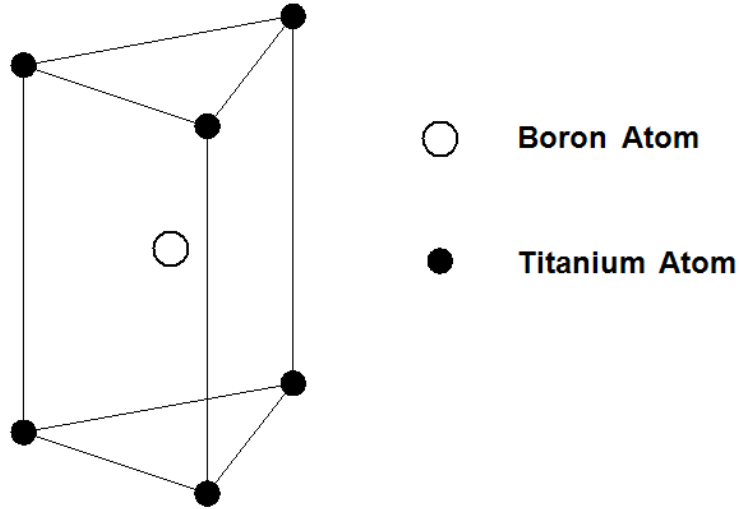


Figure 4.3: Trigonal prism building block for the orthorhombic crystal structure of TiB [109].

Table 4.3: Composition data for Ti-TiB monolithic composites manufactured by reaction sintering [109].

Initial Mixture		Manufactured Composite		
V^f Ti	V^f TiB ₂	V^f Ti	V^f TiB	V^f TiB ₂
0.882	0.118	0.70	0.30	0.00
0.763	0.237	0.45	0.55	0.00
0.645	0.355	0.27	0.73	0.00
0.526	0.474	0.08	0.86	0.06
0.408	0.592	0.00	0.92	0.08

an elevated thermal environment. Finally, the interface between Ti and TiB phases is clean with almost no residual reaction products remaining during TiB whisker formation. Other potential reinforcements, such as SiC, Al₂O₃, and Si₃N₄ do not have this property as reaction products can form at phase interfaces and have adverse effects on material properties.

TiB₂ and TiB are notoriously brittle materials that exhibit almost no plasticity. Properties for TiB are not easily obtained because of the fact that TiB is produced as a reaction product within the Ti-MMCs and is not easily isolated into stand-alone specimens that can be mechanically tested on a macroscopic scale. Efforts have been made by Atri et al. [9] and Ravichandran et al. [97] to isolate the elastic properties of TiB by testing monolithic Ti-MMC samples with various volume fraction ratios of titanium to titanium boride and inversely determining the necessary TiB material properties using various material mixture formulas. Also noteworthy is a report in 2006 by Panda and Ravichandran [90] where anisotropic elastic constants were determined for TiB using atomic physics with respect to a single crystal of TiB. Later, a polycrystal of Ti-TiB MMC was simulated using the same atomic model and elastic material data was obtained for various mixtures of Ti and TiB. It was found that the atomic theoretical models predicted elastic constants comparable to those obtained experimentally in [9].

4.3 Ti-TiB MMC and FGM Specimens

Ten plate specimens of various composition were obtained for the FGM plate impact experiments (discussed in more detail in Chapter V):

1. Two plates were monolithic, composed of 100% Ti - 0% TiB
2. Two plates were monolithic, composed of 85% Ti - 15% TiB
3. Two plates were monolithic, composed of 15% Ti - 85% TiB
4. Four plates were FGM, composed of Ti-TiB graded over seven layers

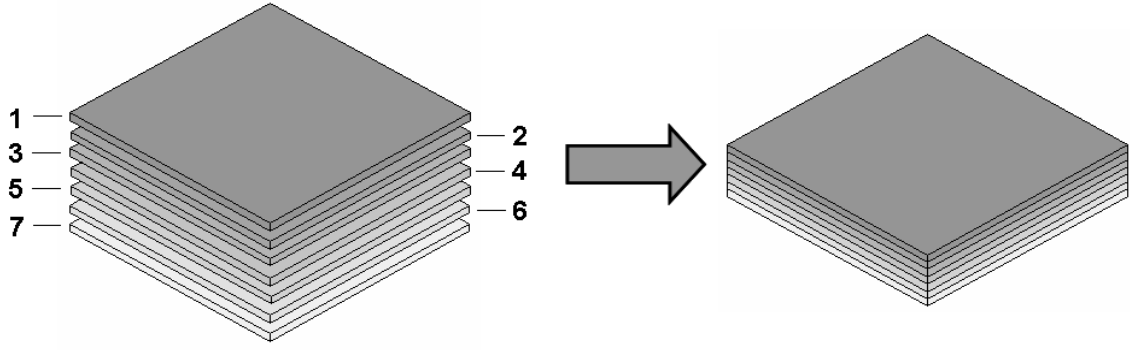


Figure 4.4: Illustration of layers in FGM plate specimens.

Table 4.4: BAE Systems Ti-TiB FGM through-the-thickness configuration of the plate specimens shown in Figure 4.4.

Layer	% Ti	% TiB	Thickness, cm
1	15	85	0.181
2	25	75	0.181
3	40	60	0.181
4	55	45	0.181
5	70	30	0.181
6	85	15	0.181
7	100	0	0.181

Each plate was 7.62 cm x 7.62 cm - 1.27 cm thick. The monolithic specimens were to be used to give baseline material data for specific volume fraction combinations of Ti and TiB that coincide with three of the seven compositional layers of the FGMs. The FGMs, with seven layers of different volume fraction ratios of Ti to TiB, are illustrated in Figure 4.4 with compositional data in Table 4.4. Scanning electron microscope (SEM) photographs of the individual layers are shown in Figures 4.5-4.11 (courtesy of Mr. Brett Hauber, Air Force Research Laboratory). Titanium appears as a light gray in the SEM photographs; titanium boride appears as a much darker shade of gray. The SEM photographs show starkly how at lower volume fractions the TiB constituent forms into needles embedded into a Ti matrix, while at higher volume fractions of TiB the needles are less distinguishable and the TiB constituent tends to coalesce into large colonies with coarse structure.

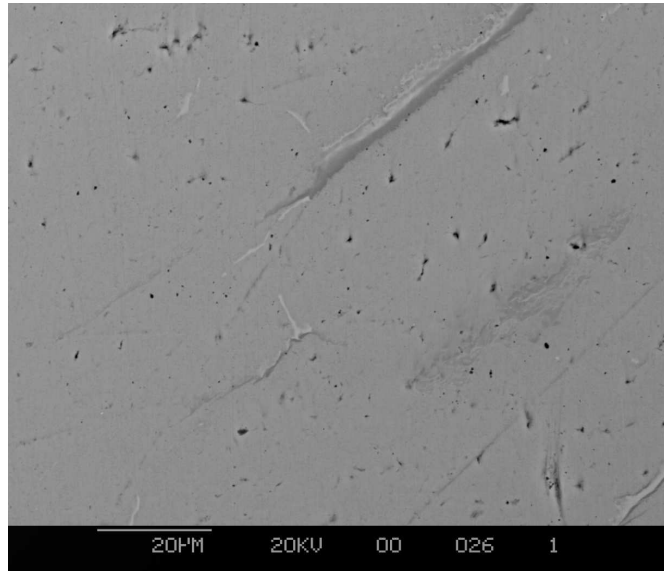


Figure 4.5: Scanning electron microscope image of 100% Ti (courtesy of Mr. Brett Hauber, AFRL).

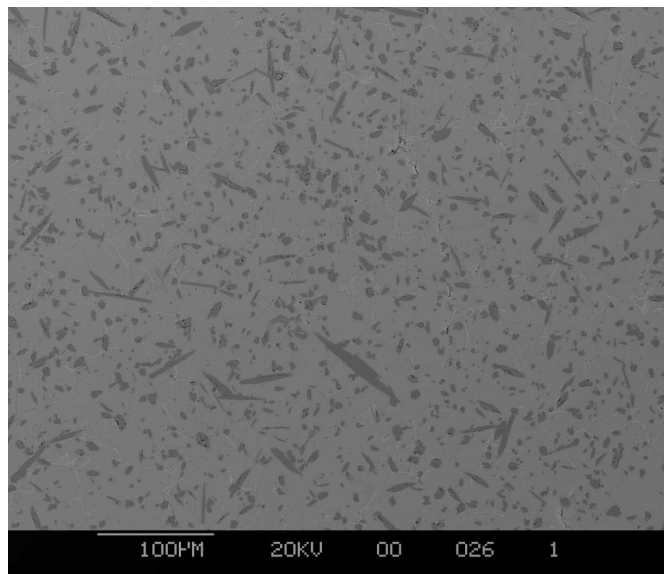


Figure 4.6: Scanning electron microscope image of 85% Ti, 15% TiB mixture (courtesy of Mr. Brett Hauber, AFRL).

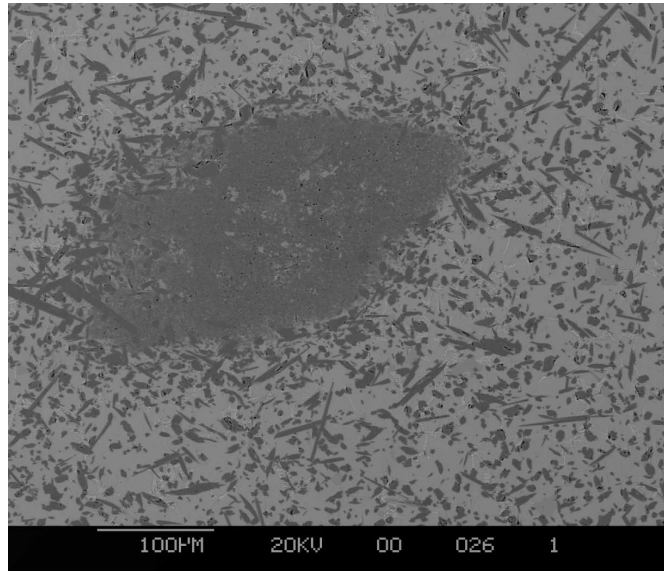


Figure 4.7: Scanning electron microscope image of 70% Ti, 30% TiB mixture (courtesy of Mr. Brett Hauber, AFRL).

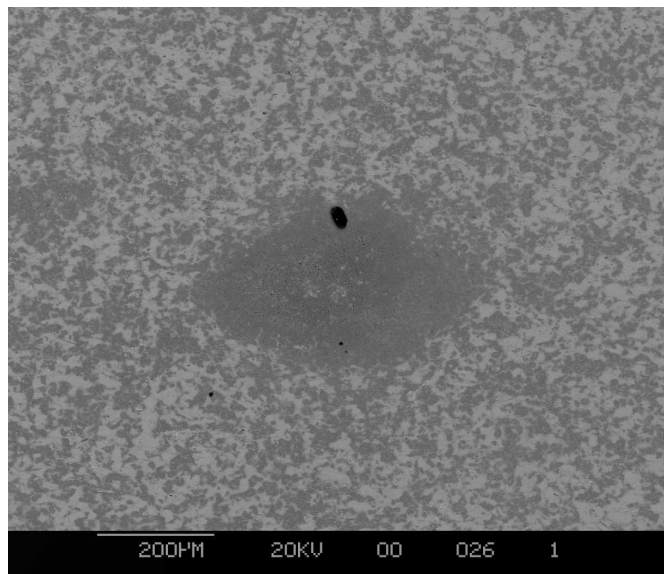


Figure 4.8: Scanning electron microscope image of 55% Ti, 45% TiB mixture (courtesy of Mr. Brett Hauber, AFRL).

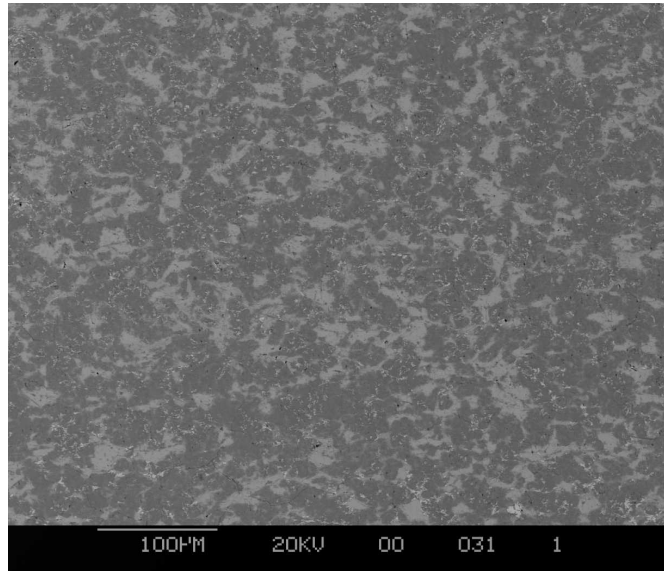


Figure 4.9: Scanning electron microscope image of 40% Ti, 60% TiB mixture (courtesy of Mr. Brett Hauber, AFRL).

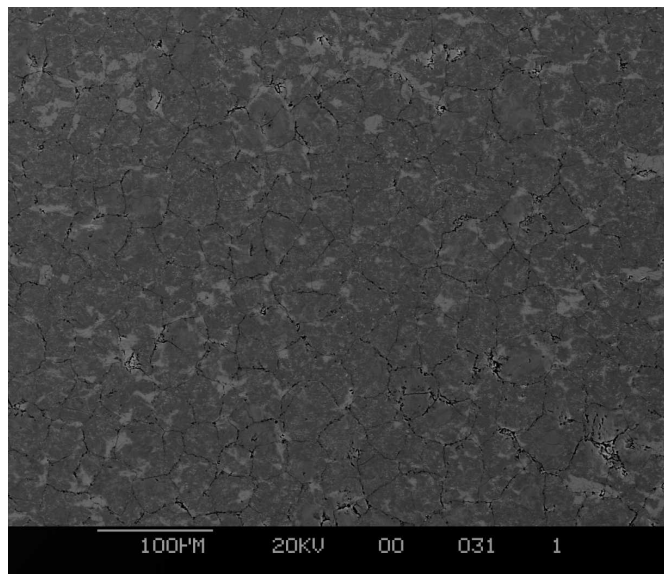


Figure 4.10: Scanning electron microscope image of 25% Ti, 75% TiB mixture (courtesy of Mr. Brett Hauber, AFRL).

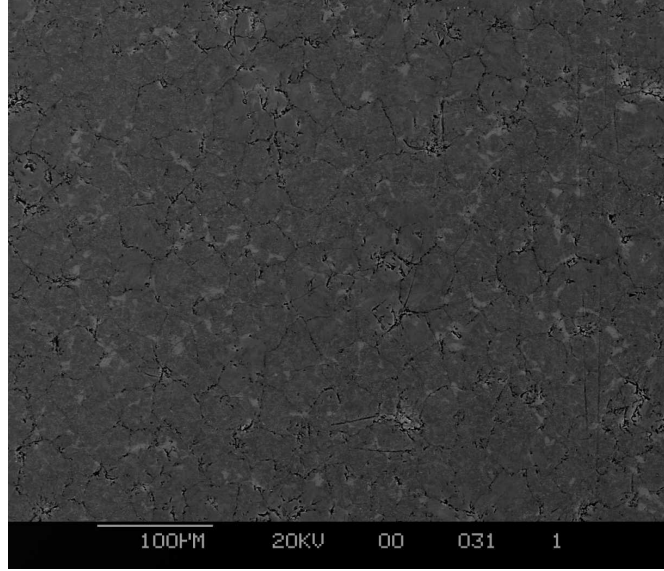


Figure 4.11: Scanning electron microscope image of 15% Ti, 85% TiB mixture (courtesy of Mr. Brett Hauber, AFRL).

A key part of this research will involve estimating the material properties of the individual Ti-TiB mixtures. The properties of Ti are well-established while the properties of TiB are not as well understood. Hill and Lin [55] compiled a table of experimentally determined material properties for individual layers within a Ti-TiB FGM where the volume fraction ratios of Ti to TiB are constant (based on the work of Carpenter et al. [25]). The elastic properties published by these authors and Atri et al. [9] are included with properties of Ti and TiB supplied by BAE Systems for their FGM system [4] in Table 4.5. Predicted values for the material properties are included in the tables using the classical rule-of-mixtures, the self-consistent material model, and the Mori-Tanaka estimates (presented in the previous chapter). Recall that the Mori-Tanaka estimates assumed that the TiB phase could assume either spherical or needle shape, although the needle morphology is more characteristic of the actual TiB phase in the MMCs and FGMs.

Table 4.5: Elastic property data for Ti-TiB volume ratios compared with predicted values from the classical rule-of-mixtures (ROM), self-consistent model (SC), and the Mori-Tanaka (MT) estimates assuming spherical (S) and needle (N) shaped TiB embedded in a titanium matrix. Data from [4] was used to calculate properties from the material models.

Configuration			Reported	ROM	SC	MT-S	MT-N
%Ti	%TiB	Source	E , GPa	E , GPa	E , GPa	E , GPa	E , GPa
100	0	[4]	110.0	110.0	110.0	110.0	110.0
100	0	[55]	106.9	110.0	110.0	110.0	110.0
100	0	[9]	117.7	110.0	110.0	110.0	110.0
85	15	[55]	120.1	149.0	131.6	138.8	137.4
70	30	[9]	163.0	188.0	159.0	170.2	167.6
68	32	[55]	139.4	193.2	163.1	174.6	171.9
53	47	[55]	162.2	232.2	198.1	209.7	206.2
46	54	[9]	211.0	250.4	216.8	227.3	223.7
38	62	[55]	193.7	271.2	239.9	248.5	244.9
31	69	[9]	269.0	289.4	261.6	268.2	264.7
21	79	[55]	247.6	315.4	294.6	298.2	295.3
15	85	[55]	274.3	331.0	315.4	317.4	315.0
0	100	[4]	370.0	370.0	370.0	370.0	370.0

Configuration			Reported	ROM	SC	MT-S	MT-N
%Ti	%TiB	Source	ν	ν	ν	ν	ν
100	0	[4]	0.340	0.340	0.340	0.340	0.340
100	0	[55]	0.340	0.340	0.340	0.340	0.340
100	0	[9]	0.335	0.340	0.340	0.340	0.340
85	15	[55]	0.310	0.310	0.319	0.310	0.312
70	30	[9]	0.290	0.280	0.294	0.281	0.284
68	32	[55]	0.276	0.276	0.291	0.278	0.281
53	47	[55]	0.246	0.246	0.261	0.249	0.252
46	54	[9]	0.250	0.232	0.246	0.235	0.239
38	62	[55]	0.216	0.216	0.228	0.219	0.223
31	69	[9]	0.220	0.202	0.212	0.205	0.209
21	79	[55]	0.182	0.182	0.188	0.185	0.188
15	85	[55]	0.170	0.170	0.174	0.173	0.175
0	100	[4]	0.140	0.140	0.140	0.140	0.140

The predicted values for material constants show some agreement for high volume fractions of titanium but tend to diverge for higher concentrations of TiB. This can be accounted for by one or more of the following points:

1. The properties for Ti and TiB shown in Table 4.5 and used to predict the properties of mixtures are inaccurate, especially the properties of TiB.
2. The sintering process used to construct the FGMs and MMCs does not produce a bond between constituent powders and whiskers sufficiently strong to assume the properties of the powders/whiskers are the same as the aggregate.
3. The mathematical models used to predict the properties are inadequate for this and possibly other metal-ceramic composites.

Also note that the data from Hill and Lin was found using layers from actual FGM specimens while the results by Atri et al. were from monolithic samples of constant volume fraction ratio. Byrd et al. [24] performed some static and dynamic bending tests using Ti-TiB monolithic and graded beam specimens and found that the monolithic beams had variability in properties that fit into a Gaussian distribution while the properties of the FGMs had significantly more variability that seemed to fit into a skewed distribution. The FGM experiments or the manufacturing process required to obtain the FGM configurations can perhaps play a role in the discrepancy between the estimates and the actual properties, although it is likely items 1-3 above play a greater role. Obtaining correct material properties for the Ti-TiB mixtures will be a central theme in later chapters.

4.4 Closing

Details associated with the Ti-TiB FGM system and its constituents have been presented in this chapter. The Ti-TiB FGM system was chosen primarily because it is one of the few metal-ceramic FGM systems available commercially. It is beyond the scope of this work to perform a material-science oriented study into the Ti-TiB metal-ceramic FGM system. Such studies must indeed be undertaken before any candidate

FGM system is integrated as part of an aerospace vehicle's TPS. *Understanding the basic properties and features of the FGM and its constituents is the first step in characterizing the impact response of an FGM plate or shell structure; this first step has been accomplished in this chapter for the Ti-TiB system studied in this work.*

V. FGM Plate Impact Experiments

The last three chapters presented important background information necessary to set the stage for the specific research of effectively characterizing the impact response of FGM plates. A pillar of this work was to devise and conduct a series of impact experiments that could be used as a baseline against analytical and computational predictions of FGM behavior under impact. *Given the lack of experimental data with functionally graded composites, the contribution of the experimental technique and the data collected cannot be understated.*

The first chief objective of this study (per the list of objectives in Chapter I) was to design and conduct impact tests on metal-ceramic FGM plates in order to record strain histories at various locations on the plate over the duration of the impact event. The requirements to meet this objective can be summarized as follows:

1. Utilize a test apparatus that can deliver a low- to medium-energy impact to a specimen under highly controlled, highly reproducible conditions.
2. Configure plate specimens such that analytical and computational comparisons of the impact event can readily be made.
3. Provide sufficient instrumentation to characterize the impact event along with the material response.

This chapter presents in detail how the FGM plate impact experiment was designed to meet these requirements and the method for collecting data for studying the impact response.

The experimental results from conducting these impact tests will also be presented. First, the plates were inspected using ultrasonic immersed through-transmission scanning to assess whether or not any damage or defects exist in the Ti-TiB plates prior to impact testing. Next, a series of ten impact tests using the Ti-TiB monolithic and FGM plates were conducted. The results from the monolithic specimens provide baseline tests for three of the seven individual mixtures of Ti-TiB that compose the seven-layer FGM specimens. The results from the FGM specimens provide baseline

results to test the validity of analytical and computational theories with respect to FGM plates. Strain histories were successfully collected in eight of the ten tests; two of the tests were unsuccessful due to specimen failure. The plates that survived the impact tests were once again inspected using ultrasonic immersed through-transmission scanning to assess whether or not significant damage was introduced after the plates were impacted in the Dynatup. *The data collected in these tests represents a significant contribution to the field of study given almost no available test data with FGMs and very little treatment of the impact response of FGMs.*

5.1 Plate Impact Experiments and Set-Up

5.1.1 Test Hardware. This section will discuss the selection and design of test hardware to meet the requirements in items 1 and 2 in the chapter introduction. The three primary hardware components are: (1) the Dynatup apparatus, (2) the plate specimen fixture, and (3) the plate specimens.

5.1.1.1 Dynatup Apparatus. Requirement 1 called to utilize a test apparatus that can deliver a low- to medium-energy impact to a specimen under highly controlled and reproducible conditions. The Dynatup apparatus is a device that can meet this requirement exceptionally well. The Dynatup apparatus was originally developed by General Research Corporation (Santa Barbara, CA), now Instron Corporation. A Dynatup apparatus (model GRC 8250) owned and operated by the Air Force Research Laboratory, Air Vehicles Directorate (office symbol AFRL/RB) at Wright-Patterson AFB, OH, is shown in Figure 5.1. The apparatus is designed to deliver a gravity-driven vertical impact of variable energy to a specimen placed in a fixture. The energy delivered to the test specimen is controlled by the height of the load cell and tup above the specimen and the mass attached to the tup assembly. Spring assists can be used to provide further potential energy to the system that is converted to kinetic energy prior to impact. Various load cell tups can be used to deliver the dynamic load to the specimen, depending on the needs of the test engineer.

The Dynatup apparatus can be configured to deliver impact energies up to 442 Joules. A set of pneumatic rebound brakes prevent a secondary impact from a rebound of the tup and crosshead. A schematic of the Dynatup components is shown in Figure 5.2.

The sequence of events that occur during an impact test with the Dynatup can be summarized as follows. A specific mass-velocity-impact energy is prescribed for an experiment. A tup geometry for transferring the impact load to the specimen is chosen. The impact test specimen is installed and secured at the base of the Dynatup using a fixture appropriate to the test conditions. The mass and tup are attached to the crosshead assembly, and this assembly is raised above the specimen to a specific height directly correlated to the required velocity-energy prescription for the test. If spring-assistance for additional velocity-energy above a gravity-driven impact is required, the springs are compressed against the crosshead assembly using a pneumatic press (the spring compression is dictated by a pneumatic pressure-velocity relationship that must be determined *a priori* to testing). The system is armed and the crosshead assembly is released from rest. The potential energy stored in the crosshead assembly is converted to kinetic energy and the assembly moves vertically downward along ideally frictionless guide rails. The guide rails control the trajectory of the crosshead and tup such that the tup impacts specimens at the same precise location over each test (compare this to a gas-gun or other such test where the impact site from a projectile can be highly variable). The tup impacts the specimen. A set of pneumatic rebound brakes prevent a secondary impact due to rebound. If a rebound does not occur due to specimen failure, the brakes simply stop the crosshead and tup from impacting the floor. The test is completed at this point.

In the FGM plate impact tests, a constant mass of 13.06 kg was applied to the crosshead for each test and a 2.54-cm diameter tup was used. The tup was composed of hardened steel and cylindrical in shape with a hemi-spherical tip (the exact alloy of steel is unknown and proprietary to Instron). The energy delivered at impact was controlled by the height of the crosshead. No spring assistance was used for any impact test in this research. The speed of the tup at impact was measured by a



Figure 5.1: Dynatup apparatus used for low- to medium-energy impact testing.

velocity photo-detector wired into the Dynatup data acquisition system. The Dynatup is additionally instrumented with a piezoelectric load-cell capable of capturing a force history over the contact duration between the tup and specimen during an impact test. This feature was not used during these tests due to a calibration error that prevented accurate force data collection. A picture of the Dynatup configuration is shown in Figure 5.3. More details associated with the actual tests will be presented later in this chapter.

5.1.1.2 Plate Specimen Fixture. The second requirement of the impact experiment was to configure plate specimens such that analytical and computational comparisons of the impact event can readily be made. A plate with a circular geometry is one that is very well-suited to studying impact events for a two specific reasons. First, stress waves generated from impact against a medium of general composition

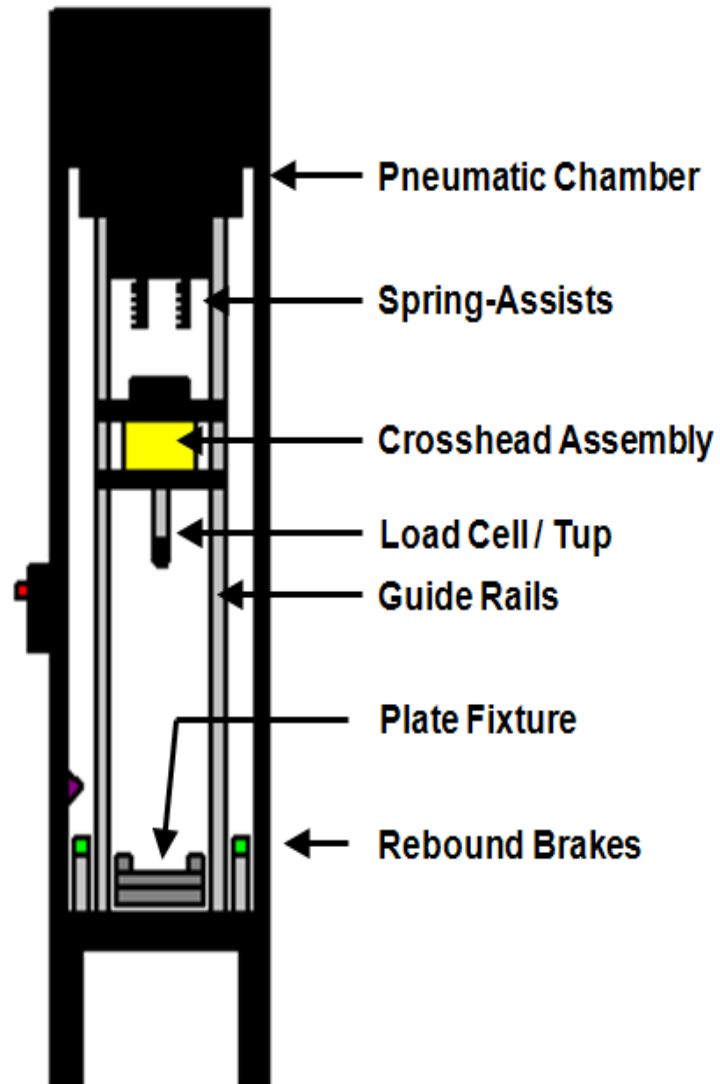


Figure 5.2: Schematic showing the major components of the Dynatup apparatus.

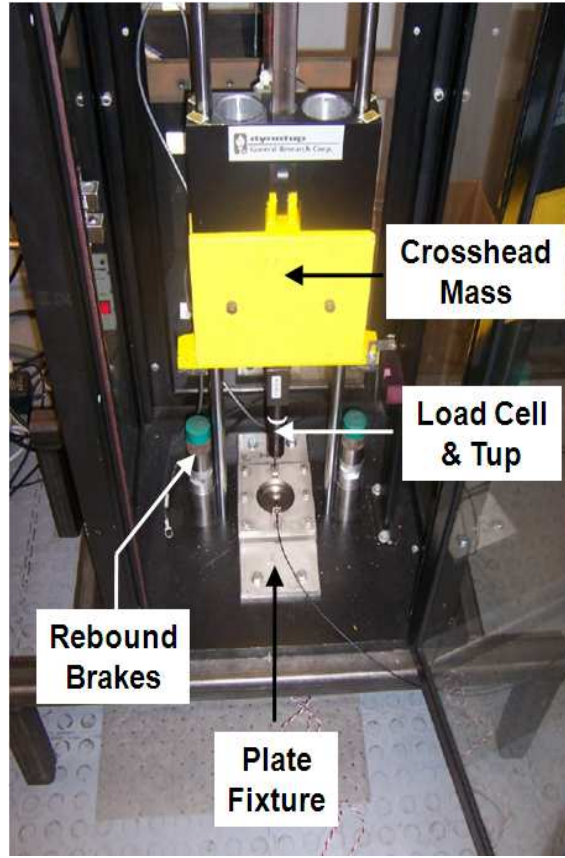


Figure 5.3: Dynatup apparatus with plate fixture installed.

and geometry will propagate radially prior to interaction effects from material and geometric boundaries. Secondly, flexural waves due to an impact that can be treated axisymmetrically will propagate only radially for a circular plate with a circular geometry and boundary. A response such as this greatly simplifies analysis, as was shown in Chapter III. Thus, configuring the Ti-TiB composite and FGM plate specimens as closely as possible to a circular plate is highly advantageous to subsequent analyses (although not always easily achieved).

Recall that the Ti-TiB composite and graded plate specimens constructed by BAE Systems were square in geometry (7.62 cm x 7.62 cm – 1.27 cm thick). BAE Systems constructs the FGM plates only in square and rectangular geometries without additional machining processes. Ti-TiB mixtures, even ones with low volume fraction of TiB, cannot be machined with conventional techniques. This fact makes

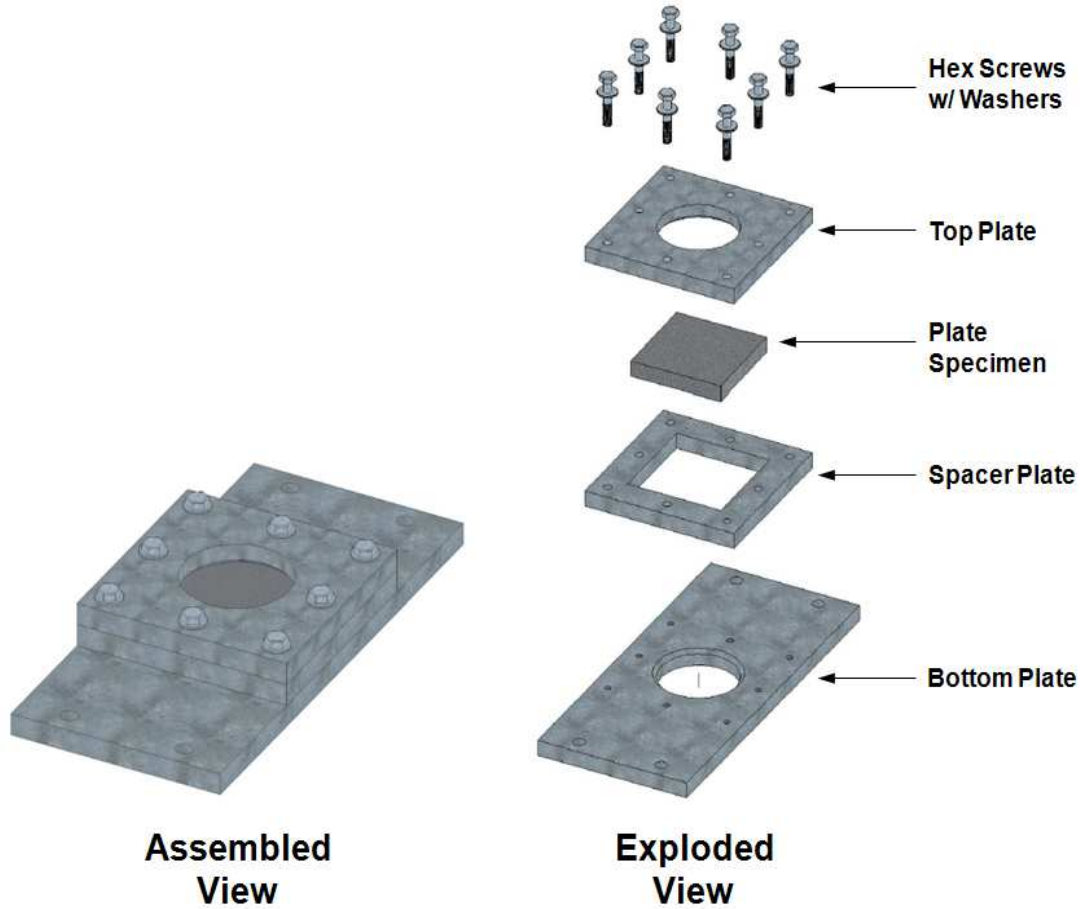


Figure 5.4: Assembled and exploded view of the plate specimen fixture used in the Dynatup apparatus.

additional processing of the specimens highly expensive, and the budget for this research would not allow for the plates to be machined into circular disks. It therefore became necessary to design a fixture that could configure the plates to have as close to a circular boundary condition as possible while simultaneously maintaining the as-processed square geometry of the plates. In addition to these requirements, the plate fixture must also fit into the space constraints of the Dynatup.

The plate fixture, as designed, is shown in Figure 5.4. *The fixture was specifically designed to configure the square plate as closely to a circular plate configuration as possible while additionally fitting within the spatial constraints of the Dynatup.* The fixture consists of three metal plate components: (1) a *top plate* with a circular

opening; (2) a *spacer plate* with an opening the same dimensions of the specimen; and (3) a *bottom plate* with a circular opening. The specimen plate fits into the opening provided for it in the spacer plate. The top and bottom plates sandwich the spacer plate and specimen and are secured by eight fasteners as shown. The fasteners are threaded into the bottom plate and tightened to secure the assembly together. The fixture and specimen plate assembly are then placed into the Dynatup. Four holes in the bottom plate of the fixture allow attachment to the Dynatup apparatus. The mechanical drawings for the bottom, spacer, and top plates of the specimen fixture are shown in Figures 5.5-5.7, and a photograph of the plate fixture installed in the Dynatup apparatus is shown in Figure 5.8.

The fixture components were all machined from 304 stainless steel. This grade of stainless steel is readily available and inexpensive and has favorable properties, including corrosion resistance, machinability, and strength. These properties make it an ideal material for use in impact tests where the fixture would require durability for use in multiple tests. The components were all machined from 1.27 cm plate stock according to the specifications in Figures 5.5-5.7. Note that these drawings have only nominal dimensions shown and do not include tolerances. Every attempt was made to hold the components as close to their nominal dimensions as possible during the machining process.

The bottom plate attaches to the base of the Dynatup via four hex-head 3/8-16 UNC (Unified Standard, American and English Standard) screws. The Dynatup base is 5.08 cm-thick steel with four tapped holes to receive these fasteners at the locations shown in Figure 5.5. The bottom plate additionally has eight holes tapped to receive 1/4-28 UNF fasteners to secure the three component plates together. The bottom plate had to be tapped because the bottom plate rests flat on the Dynatup base and protruding screws/fasteners would not fit-up properly. The spacer plate rests on top of the bottom plate. The spacer plate serves two purposes. First, its opening is only very slightly larger than the plate specimens, and thus it serves to properly position and center the specimen in the fixture and the Dynatup. Secondly, the spacer plate

is the same thickness as the specimen and prevents crushing of the plate specimen as the fasteners are tightened to secure the fixture and specimen in the Dynatup. The top plate then rests on top of the spacer plate. The top plate has eight through-holes for the hex-head 1/4-28 UNF fasteners. The eight 1/4-28 UNF fasteners were 3.81 cm long and partially threaded since they were only threaded into the bottom plate. Each fastener was composed of 18-8 grade stainless steel (note that 18-8 stainless steel is a broad category of stainless steel alloys containing 18% chromium and 8% nickel; 304-stainless steel alloy is a member of this category [86]). The four 3/8-16 UNC Dynatup attachment screws were 2.54 cm in length were also composed of this same common alloy. Washers were placed between all the fastener hex-heads and their contact sites on the fixture components to distribute the contact loads over larger areas.

The eight 1/4-28 UNF plate fastener screws were tightened to 20 Newton-meters (N-m) for each test. This value was determined based on a *trial-and-error process in the laboratory* with the fixture in the Dynatup. The key to finding an appropriate value was a compromise between securing the plate specimen adequately while simultaneously preventing crushing loads on the specimen plates. Based on experience in the laboratory, torque loadings in excess of 20 N-m increased the risk of crushing the plate specimens. Below 20 N-m, the specimen plates were found to not be well secured. The four 3/8-16 UNC Dynatup attachment screws were tightened to a bolt load of 35 N-m. This load was found to secure the plate fixture adequately without requiring re-tightening of the attachment bolts in between impact tests (although the bolt torque was verified for each test).

The top and bottom fixture plates each have a circular cutout 6.35 cm in diameter with a uniform 0.318 cm chamfer at an angle of 45° with the plate normal around the circumference on the face incident with the specimen plate. (The net opening, including the chamfer in each cutout was then 6.985 cm in diameter; see Figures 5.5 and 5.7). The circular cutouts configure the plate specimen as a circular plate with built-in edges. Upon impact from the tup at the center of the plate specimen top

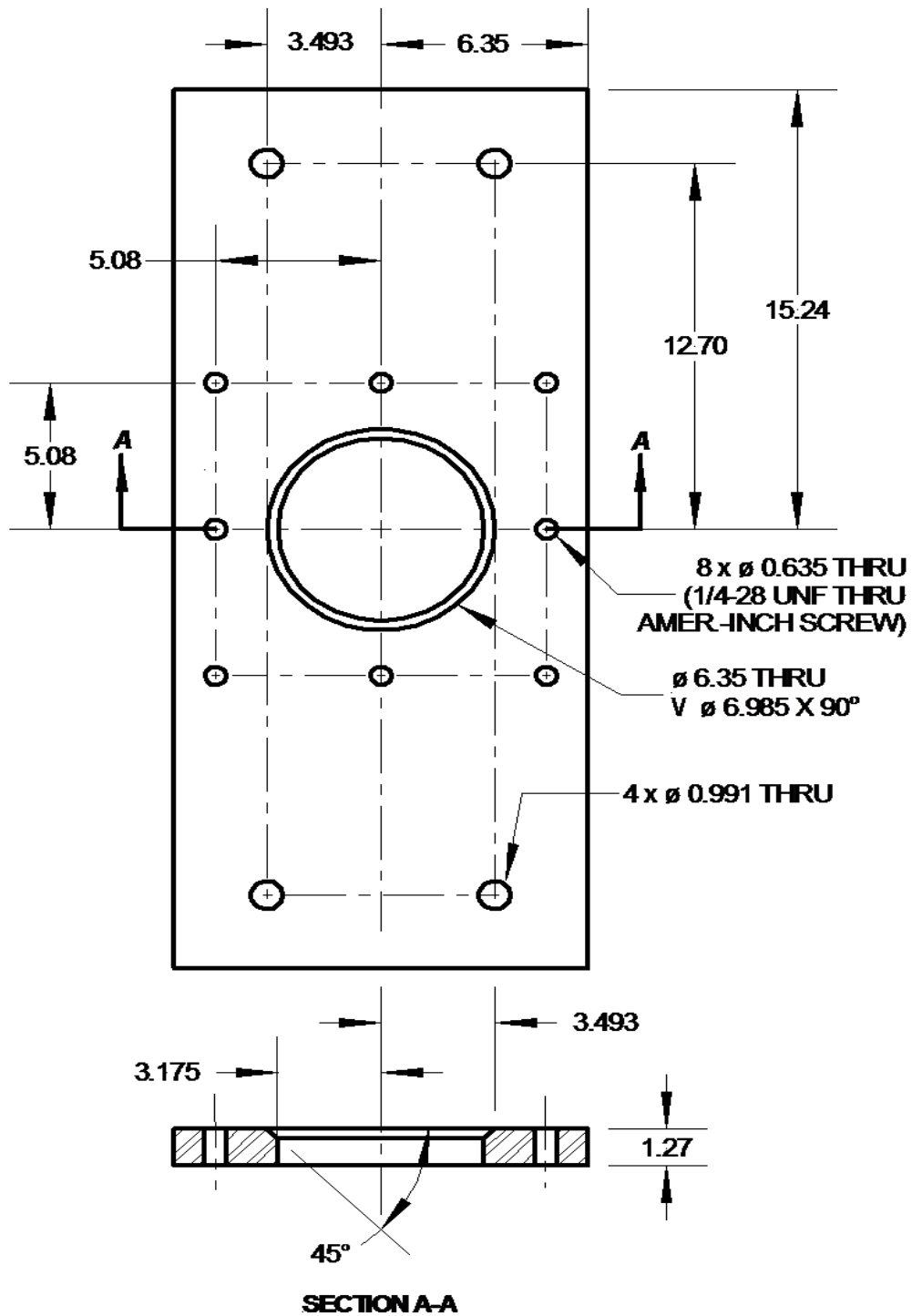


Figure 5.5: Bottom plate in the Dynatup plate specimen fixture assembly. The plate was machined from 304 stainless steel plate stock 1.27-cm thick. All dimensions are in *cm* unless otherwise specified.

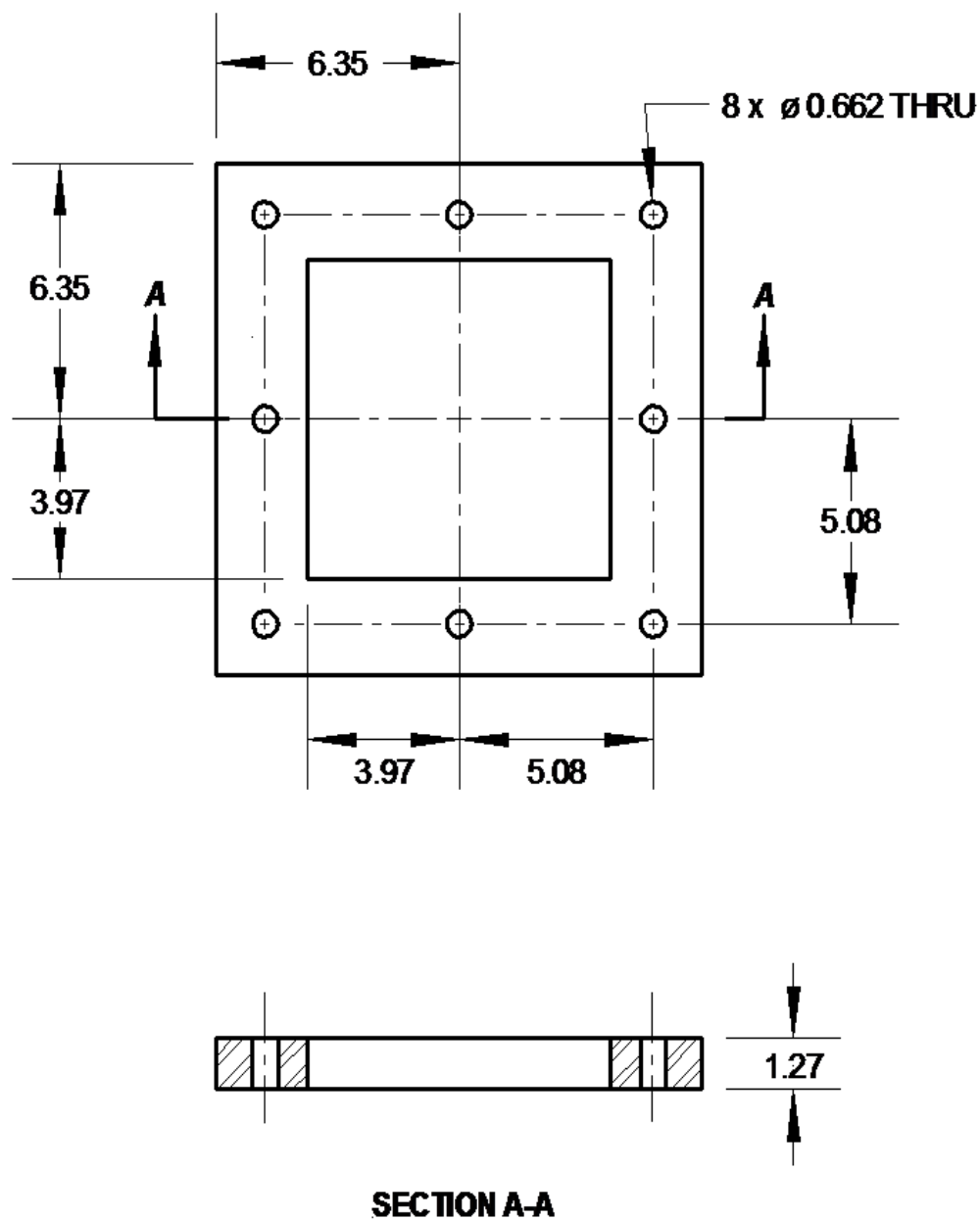


Figure 5.6: Spacer plate in the Dynatup plate specimen fixture assembly. The plate was machined from 304 stainless steel plate stock 1.27-cm thick. All dimensions are in *cm* unless otherwise specified.

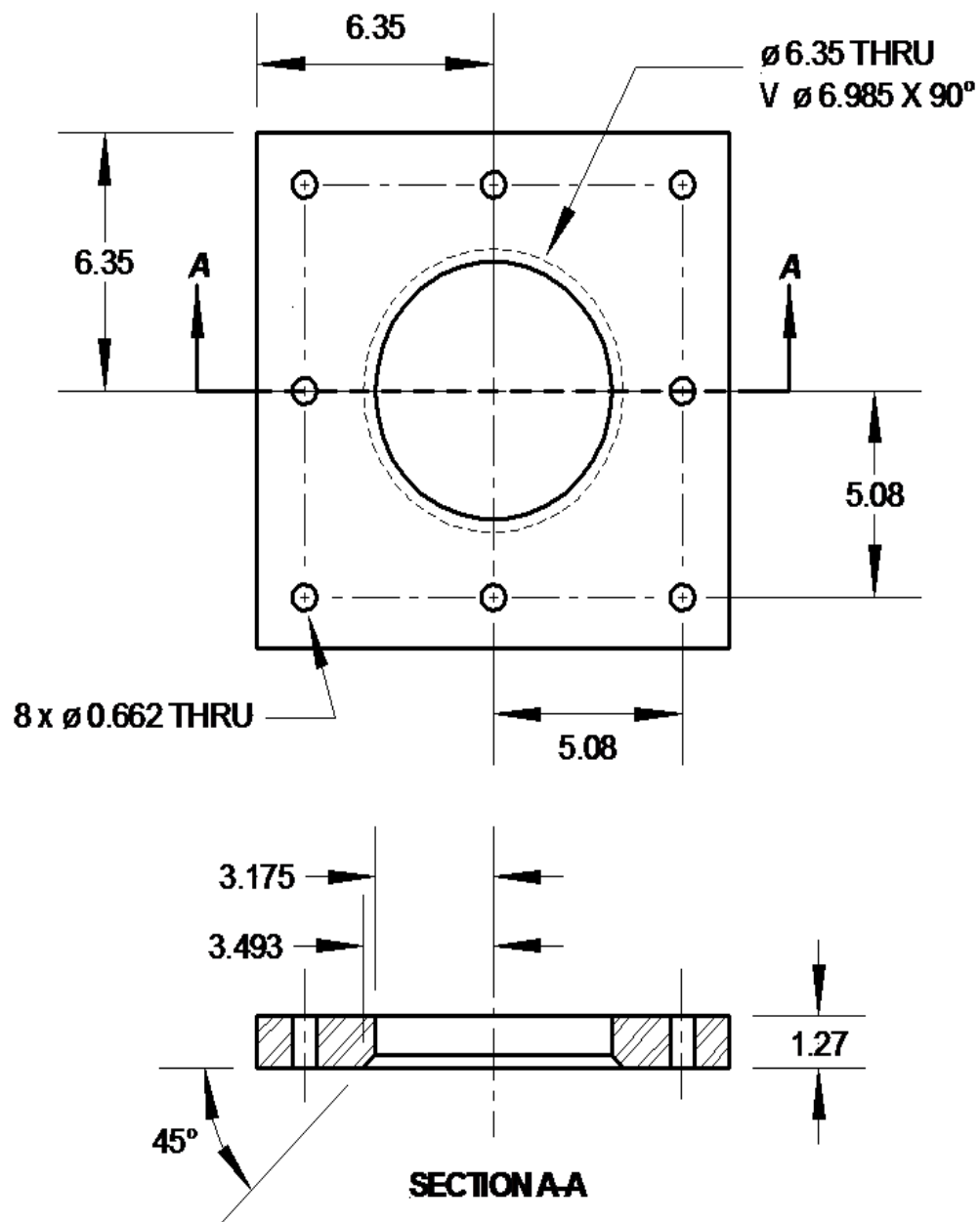


Figure 5.7: Top plate in the Dynatup plate specimen fixture assembly. The plate was machined from 304 stainless steel plate stock 1.27-cm thick. All dimensions are in *cm* unless otherwise specified.

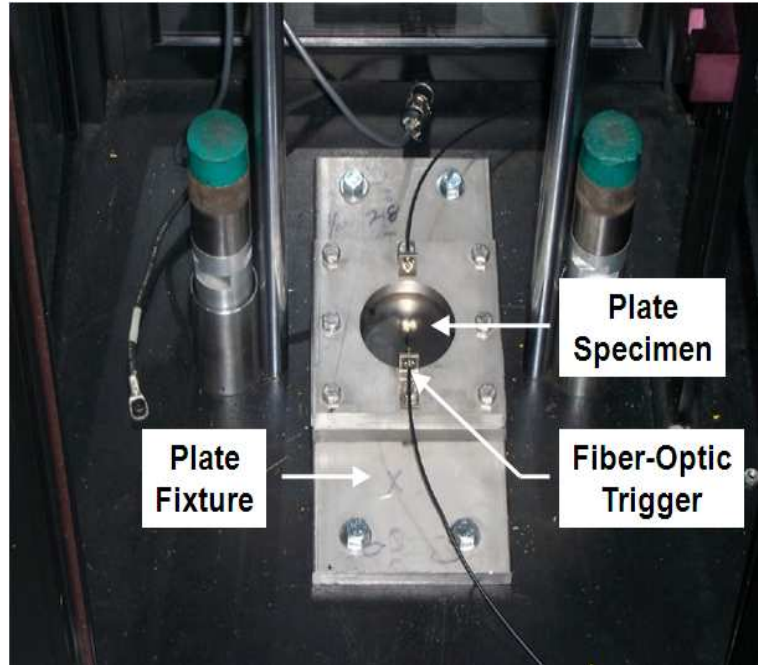


Figure 5.8: Plate fixture with FGM specimen plate installed in Dynatup.

surface, the transverse deformation of the plate will be very close to that of an ideal circular plate. The chamfers around the circumference of each cutout mitigate stress concentrations that would be present from an abrupt corner resisting deformation and bearing into the plate specimen. This has the added effect of allowing rotations of the plate at those locations where an abrupt corner could perhaps be much stiffer. In Chapter VII it will be shown that the plate follows closely the behavior of a simply-supported circular plate for transverse deflections.

5.1.1.3 Plate Specimens. Ten plate specimens of various composition were obtained for the FGM plate impact experiments:

1. Two plates were monolithic, composed of 100% Ti - 0% TiB
2. Two plates were monolithic, composed of 85% Ti - 15% TiB
3. Two plates were monolithic, composed of 15% Ti - 85% TiB
4. Four plates were FGM, composed of Ti-TiB graded over seven layers

Each plate was 7.62 cm x 7.62 cm - 1.27 cm thick. The monolithic specimens were to be used to give baseline material data for specific volume fraction combinations of Ti and TiB that coincide with three of the seven compositional layers of the FGMs. The FGMs, with seven layers of different volume fraction ratios of Ti to TiB, are illustrated in Figure 5.9 with compositional data in Table 5.1 (reproduced from Chapter IV for convenience). The expense of the Ti-TiB composites was the primary reason only ten specimens were obtained for testing.

A technical drawing of the plate specimens is given in Figure 5.10. The drawing shows the location of the four strain gages mounted to the bottom surface of each plate. The FGM plates were installed in the fixture such that the TiB-rich surface was the top surface and contact surface for the tup impact. *This was done to remain consistent with the aerospace vehicle TPS application where the FGM's ceramic-rich surface would likely be the exterior surface (resisting thermal loads) subject to impact from a foreign projectile.* The FGM's Ti-rich surface was the bottom surface where the strain gages were mounted. On monolithic samples, the choice of surface was arbitrary (since the material has the same monolithic composition through the thickness of the plate) but the strain gages were always placed on the surface opposite the tup impact surface. The plates are always centered underneath the tup impact site because of the design of the specimen fixture. The gages are shown numbered on an actual FGM specimen in order from the closest to the center of the plate to the most distant in Figure 5.11. Strain gages 1-3 were used to collect data, but gage 4 was left unconnected during the impact tests. The reason for this was a late improvement in the data collection triggering mechanism that required that a channel in the data acquisition oscilloscope be freed for this purpose. The details of the triggering mechanism will be discussed later in this chapter.

Note the gages were oriented along two axes on the surface of the plate. In the circular plate configuration, these gages are oriented along two perpendicular radial axes at different radial locations from the center of the plate. This allows the radial strain components to be measured during the entire impact event at three

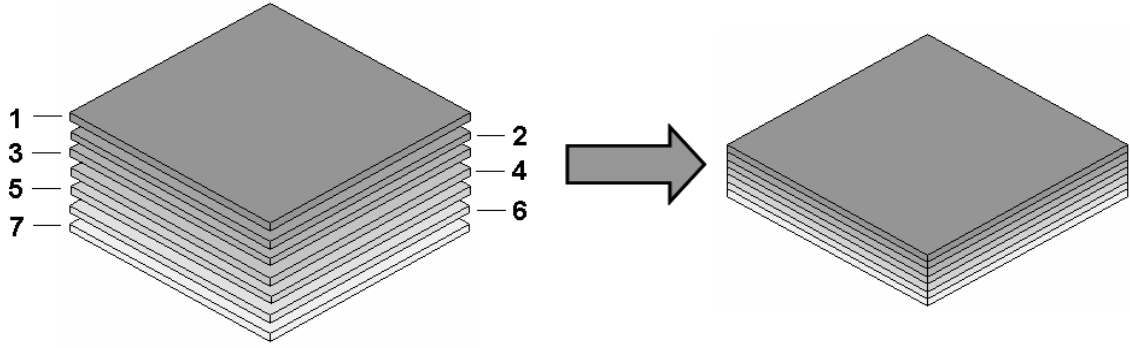


Figure 5.9: Illustration of layers in FGM plate specimens.

Table 5.1: BAE Systems Ti-TiB FGM through-the-thickness configuration of the plate specimens shown in Figure 5.9.

Layer	% Ti	% TiB	Thickness, cm
1	15	85	0.181
2	25	75	0.181
3	40	60	0.181
4	55	45	0.181
5	70	30	0.181
6	85	15	0.181
7	100	0	0.181

locations. Every attempt was made to orient the principal gage directions along these radial perpendicular axes, although admittedly very small deviations occurred during installation that could not be prevented because of the very close proximity of the gages to each other.

5.1.2 Instrumentation. The previous section detailed the hardware used in the plate impact tests and directly addressed requirements 1 and 2 of the test objective. Requirement 3 was to provide sufficient instrumentation to characterize the impact event along with the material response. In this section the instrumentation used to collect the strain histories during the impact events in the Dynatup apparatus will be briefly explained. The key components of the instrumentation system are the strain gages, the signal conditioning system, and the data acquisition system. Only

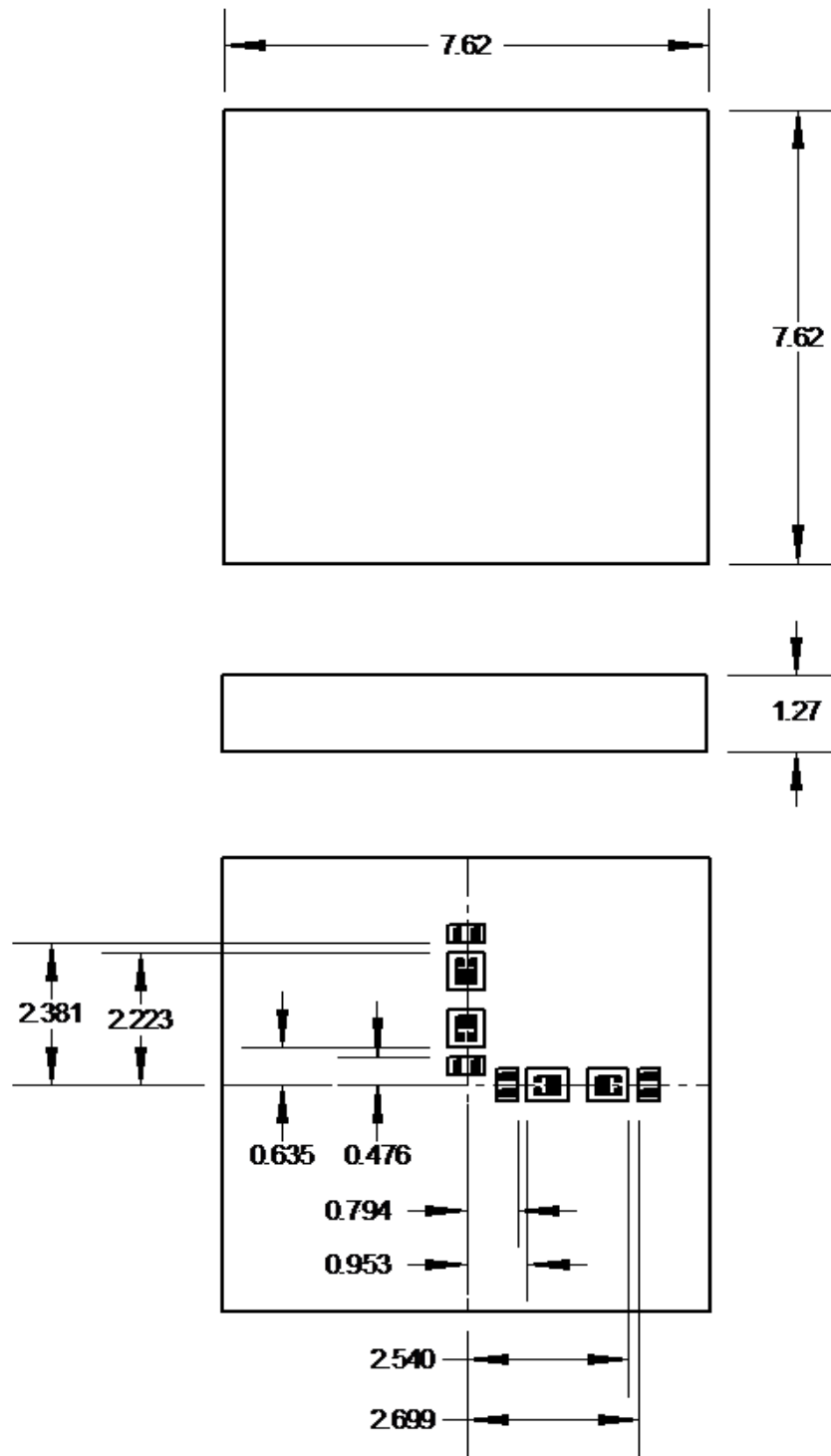


Figure 5.10: Plate specimen. Titanium, Ti-TiB monolithic, and Ti-TiB FGM specimens were machined using this specification. Placement of strain gages also shown. All dimensions are in *cm* unless otherwise specified.

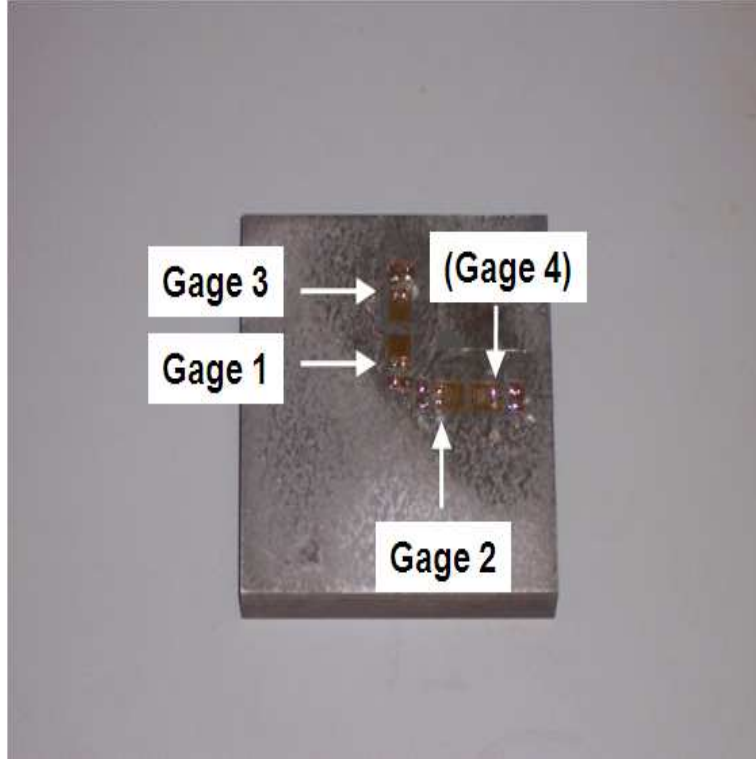


Figure 5.11: FGM plate specimen with strain gages installed.

information specific to the components used in the tests will be provided; a broad discussion of the components and how strain measurements are obtained is provided in Appendix A.

5.1.2.1 Strain Gages. Two types of foil strain gages were used for data collection (Vishay Micro-Measurements 125AC series gages; the gages are essentially the same and the only difference between the two types are the material used for wire in the gage). A photograph of the strain gage used is shown in Figure 5.12. Gage 1 (see Figures 5.10 and 5.11) is a linear foil gage composed of constantan wire (60% copper, 40% nickel) with a flexible polyimide backing and strain range of approximately $\pm 3\%$ (Vishay Micro-Measurements EA-13-125AC-350, see [127]). Gages 2-4 are linear foil gages composed of annealed constantan wire with flexible polyimide backing and a strain range of $\pm 10\%$ (Vishay Micro-Measurements EP-08-125AC-350, see [127]). Each gage has an unstrained resistance of 350 Ohms. The polyimide matrix width

and length are 5.6 mm and 10.2 mm, respectively, and the foil wire pattern has a length and width of 3.18 mm. The close proximity of the gages to each other on the plate required trimming of the polyimide matrix backing to near the wire patterns and solder tabs on each gage.

(Before continuing, a note on the choice of the different gages is in order. In the original design of this experiment, strain gage 1 was intended to be used as a sacrificial gage that would trigger the data collection system. It was felt that this gage being the closest to the impact site would not survive the duration of the test but would survive long enough to trace the initial strain in the plate to trigger data collection for the rest of the gages. For this reason, a less expensive strain gage was used for gage 1. The remaining gages 2-4 were large deformation gages intended to trace the strain histories in the plates at their respective locations. It was found during mock tests in the laboratory that the voltage signal from gage 1 was insufficient to trigger the data collection system in a reliable fashion. A different triggering mechanism was devised and is discussed in detail later in this section. The mock tests also proved that gage 1 would in fact survive impact testing and yielded very useful data. The new triggering mechanism did not allow all four gages to be used for data collection and therefore gage 4 was eliminated from the tests; only strain gages 1-3 were used.)

The gage strain sensitivity, which is also referred to as the gage factor (GF), is a dimensionless relationship expressed as

$$GF = \frac{\Delta R}{R} \frac{L}{\Delta L} \quad (5.1)$$

R is the resistance in the gage, ΔR is the change in resistance, L is the initial length of the foil wire gage section, and ΔL is the change in length of the foil wire gage section. *The gage factor for strain gage 1 was **2.135** and the gage factor for gages 2-4 was **2.100**.* The gage factor is usually pre-determined by the manufacturer and is reported with other gage specifications. These values and other specifications for

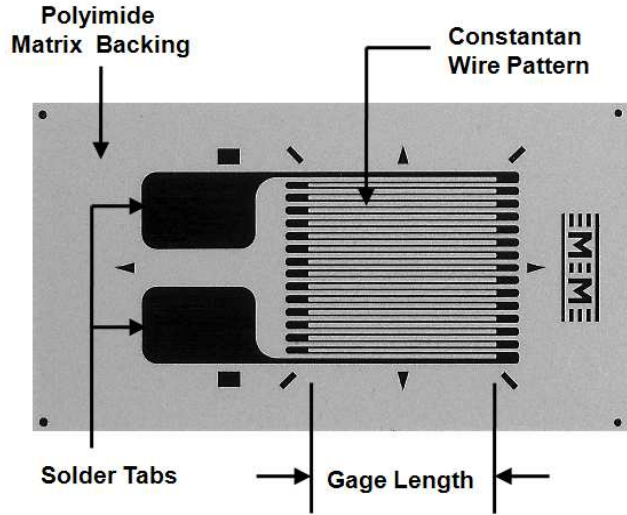


Figure 5.12: Vishay 125AC series strain gage used in impact tests for collecting strain histories [127].

the gages will be important when calculating the measured strain on each specimen over its impact response.

The strain gage configuration is shown in Figure 5.13. The strain gages were wired to the signal conditioner system using 3-conductor twisted, stranded copper wire with vinyl insulation (Vishay Micro-Measurements 326-DTV, see [131]). The bulk wires were soldered to terminals separate from the actual gages (Vishay Micro-Measurements CPF-75C, see [129]). Two single strands from the bulk wires were then soldered as jumper wires to the actual gages. This configuration was recommended by Vishay Micro-measurements to keep the mass of the wire and solder on the actual gage to a minimum to enhance survivability of the gages. The terminals and gages were bonded to the plate specimens using a special adhesive capable of nearly ideal adhesion to a test coupon undergoing large tensile deformations (Vishay Micro-Measurements M-Bond AE-15, see [128]).

5.1.2.2 Signal Conditioner. The strain gages, once installed on the plate specimens, were wired into a signal conditioning unit. The purpose of the signal conditioning unit is to convert the resistance change (due to plate straining) in

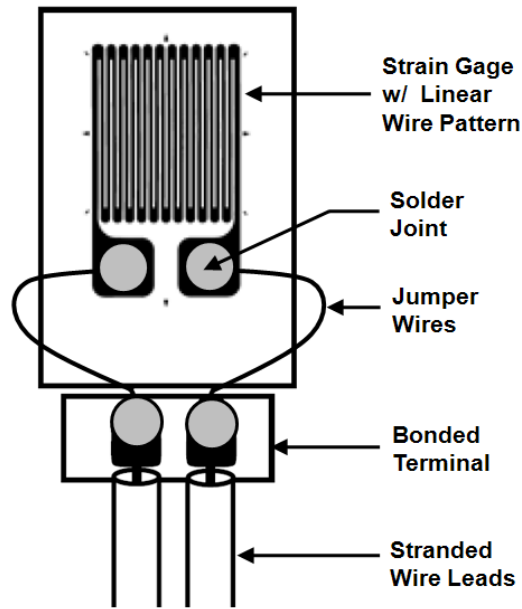


Figure 5.13: Illustration of strain gage configuration with separate bonded terminal for attachment of the wire leads to signal conditioner and two single-stranded jumper wires from the terminal soldered to the strain gages [130].

the strain gages into a meaningful quantity that can easily be measured. A separate signal conditioner was used for each strain gage. The signal conditioners used were manufactured by Ectron Corporation, Model 562, and owned by the University of Dayton Research Institute, Dayton, OH. The conditioners are composed of a Wheatstone bridge circuit and a DC differential operational amplifier (see Appendix A). The active arm of each Wheatstone bridge circuit was designed for 350 Ohm strain gages, the excitation voltage of each bridge circuit was 5.0 Volts, and the amplification gain was $G = 20$. The bridge circuit was balanced prior to each test to ensure accurate voltage readings. The signal conditioners used in the tests additionally had a shunt calibration feature that was used to correlate the output voltage from the signal conditioning unit to the strain in the plate specimens. This shunt resistance is a *known* quantity (49,000 Ohms for these units), and the system can be calibrated to correlate the output voltage to a known change in resistance. This is how the

mechanical strain from the strain gage is related to output voltage. The Ectron 562 conditioners have a (+) and (-) shunt calibration feature for calibration in tensile or compression gage loading.

5.1.2.3 Data Acquisition. The last component of the instrumentation is the data acquisition unit. The voltage signals output from the signal conditioner are useless if they cannot be deciphered. Thus, an instrument capable of detecting, deciphering, and conveying the signals to the test engineer becomes necessary to the overall experimental process. In theory, any device capable of measuring a voltage could be used including a voltmeter. In this case, the goal is to record strain histories over a finite length of time while the plate specimens respond to impact loading. It is important to capture the voltage changes over the entire length of the impact event in order to characterize the material response adequately. A voltmeter generally measures instantaneous voltages and cannot store a history of voltages over time. This makes such a device impractical for use in these tests. Further, the entire impact event can occur over a length of time on the order of a millisecond (1.0×10^{-3} sec). An oscilloscope, on the other hand, is capable of measuring voltages over time. Oscilloscopes vary widely in their capabilities, and therefore an oscilloscope with the capability to store a voltage-strain history over a brief period of time with sufficient resolution to capture strain effects on the order of microseconds (1.0×10^{-6} sec) is necessary.

The oscilloscope used in these tests was a Tektronix, Inc. TDS 3034 digital oscilloscope, owned by the University of Dayton Research Institute, Dayton, OH. The oscilloscope can measure separate voltages on up to four channels (i.e., four strain gages maximum) and can sample at a rate of 2.5×10^9 samples per second. Each channel stores a fixed number of data points (10,000 for this unit) over a finite period of time. Essentially, one sets the time window of interest and the oscilloscope collects 10,000 data points over that window. Thus, if one desires data over 2000 microsecond window, the oscilloscope measures voltages every 0.5 microseconds. The

10,000 data points are stored in memory and can be recovered as data files that can be read by a computer for data processing later. The key to collecting this important data is to automate the oscilloscope to begin collecting data as the impact event begins. This cannot be accomplished manually by a human since one could not react fast enough to consistently arm the oscilloscope for data collection over such a short period of time.

The digital oscilloscope used has a feature that allows one to automate data collection to begin (or “trigger”) once a voltage reading surpasses a given threshold. Further, since the unit collects 10,000 data points in continuous cycles, the oscilloscope can be programmed to store a finite amount of data before the voltage reaches a threshold value (or “pre-trigger”). This feature becomes important since voltage readings prior to reaching the triggering threshold are not lost; in fact, the entire strain history from the impact event can be captured. Thus, a history can have a zero voltage reading for a set percentage of the entire collection window, while the remaining window stores non-zero data.

The experiments were initially designed to use strain gage 1 as the gage to trigger the remaining gages to collect data. Initial mock tests with titanium plates demonstrated that a 2000 microsecond time window was adequate to capture the entire impact event from the plates with a 20% pre-trigger and 40 millivolt threshold. (In other words, 10,000 data points were continuously collected over a 2000 microsecond window but not stored to memory; once the voltage output from the signal conditioner reached 40 millivolts, the oscilloscope is triggered to store 20% of the 10,000 voltage readings before the threshold was reached into its memory while the remaining 80% of the 10,000 data points after the threshold was reached were also stored in memory. When the voltage threshold is reached on a gage (or sensor) designated as the trigger sensor, the other gages are ordered to immediately store to memory 20% of their data points before the trigger was initiated and 80% of the data points after the trigger was initiated.) While these settings worked well for collecting the strain histories, background noise in the facility and Dynatup apparatus

was found to prematurely trigger the data acquisition unit on some occasions and the histories of the impact events were lost. It was therefore deemed necessary to use a voltage signal much stronger than can be produced by a strain gage to trigger the oscilloscope.

A fiber optic sensor was chosen to successfully accomplish this task. A single sensor (Banner, Inc., Model FI22FP) was placed directly above each specimen plate to trigger the oscilloscope to begin data collection (see Figure 5.8). The sensor is essentially composed of a transmitter, receiver, and amplifier. The sensor was energized by a 10 Volt DC power supply (Hewlett-Packard Model 6023A) that caused the transmitter to emit a beam of red light. Provided the beam is detected by the receiver portion of the sensor, a signal is sent to the sensors amplifier and the output from that amplifier can be read by the oscilloscope. If the beam is not detected by the sensor, the output from the amplifier is essentially zero. Strain gages 1-3 in Figure 5.11 were kept for data collection and strain gage 4 was omitted. The fiber-optic sensor was then routed to the oscilloscope channel occupied by strain gage 4. The oscilloscope was programmed to begin data acquisition following this sequence: (1) the voltage reading from the fiber-optic sensor dropped below 5.0 Volts (one-half of the *uninterrupted* 10 Volt output from the fiber optic sensor—when the output drops sharply from the uninterrupted 10 Volt level, the sensor is indicating the beam is somehow interrupted), (2) followed by a short delay in the system to allow adequate time for the tup on the Dynatup crosshead to approach the plate specimen, (3) followed by the voltage reading from strain gage 1 surpassed a 40 millivolt threshold. With mock tests in the laboratory, this was found to eliminate premature triggering of the data acquisition system while resulting in extremely reliable collection of the impact events. The 2000 microsecond history window and 20% pre-trigger were maintained for the impact tests. The strain histories thus were collected such that 400 microseconds of data were stored prior to the 40 millivolt threshold being reached on strain gage 1, and 1600 microseconds of data were stored after the 40 millivolt threshold was

reached (this can be seen graphically in the raw data plots of the voltage histories in Appendix B.

5.1.3 Strain History Measurement. The goal of the impact tests was to obtain strain histories from the plate specimens that are generated over various impact events. These histories provide insight into the overall response of the plate specimens. The major hardware and instrument components of the impact experiment have been detailed. Before the test results are presented, a brief summary is provided here outlining the sequence of events that occur to obtain the strain histories from the plate specimens.

1. The plate specimen is placed in the plate fixture and the assembly is installed in the Dynatup apparatus. The four large machine screws that attach the fixture to the Dynatup base plate were torqued with a torque wrench to 35 N-m. The eight plate fixture screws were each torqued to 20 N-m.
2. The Dynatup is configured to deliver a prescribed impact to the plate. In the case of our tests, the crosshead mass was held constant at 13.06 kg and the height of the crosshead-load cell assembly above the plate impact site was varied. Only gravity mode impacts were carried out; pneumatic-assisted spring compression against the crosshead was not used in these tests.
3. The strain gages were wired to the signal conditioner and the fiber-optic sensor was aligned such that the infrared beam crossed directly in the path of the tup just above the impact site. The strain gages were balanced with shunt calibration before each test.
4. The Dynatup, with prescribed potential energy stored in the system, was released from rest and the potential energy was converted to kinetic energy as the crosshead-load cell assembly moves along the guide rails.
5. At the point where the tip of the tup moved directly into the path of the laser signal from the fiber-optic sensor, the beam signal is immediately broken and the

data acquisition in the oscilloscope is triggered to begin collecting data from the strain gages after a pre-determined time delay and minimum voltage threshold detected by the oscilloscope from the strain gages.

6. The tup impacts the plate specimen, immediately generating a stress wave that propagates through the plate specimen. Depending on the length of time that the tup remains in contact with the plate, significant global deformation of the plate may occur.
7. The initial and subsequent stress waves will eventually reach the bottom surface of the plate specimen. The waves and associated global deformation of the plate will strain the plate and these strains are measured by the strain gages mounted on the bottom surface of each plate. The data acquisition system in the oscilloscope records the strain history for each gage over the set time window.

A schematic showing the system components is shown in Figure 5.14.

5.2 Plate Impact Test Results

5.2.1 Pre-Test Inspection of the Ti-TiB Plates. Prior to impact testing, the graded and monolithic Ti-TiB plate specimens were evaluated using *non-destructive* ultrasonic scan tests to assess the level of damage that might exist in the specimens before more damage is potentially introduced in the Dynatup experiments. Such an assessment is important in the event the response of the structure is not what is expected from analysis. The literature related to the theory, equipment, and practices associated with ultrasonic non-destructive evaluation (NDE) of structures is extensive; for more details, including lists of relevant standards, the reader is referred to [77], [19], [54]. *These references will be used to summarize the ultrasonic scan tests performed for this work, specifically ultrasonic immersed through-transmission scanning discussed in the next paragraphs.*

Table 5.2: Strain gage and signal conditioner specifications common to all plate impact experiments. These values are necessary in order to convert voltage readings in the oscilloscope from the gages to physical strain.

Parameter	Value	Units
Gage Factor, GF , Strain Gage 1	2.135	
Gage Factor, GF , Strain Gages 2, 3	2.100	
Strain Gage Resistances, R_1	350	Ohms
Shunt Resistance, R_s	49,000	Ohms
Excitation Voltage, e_i	5.0	Volts
Gain, G	20	

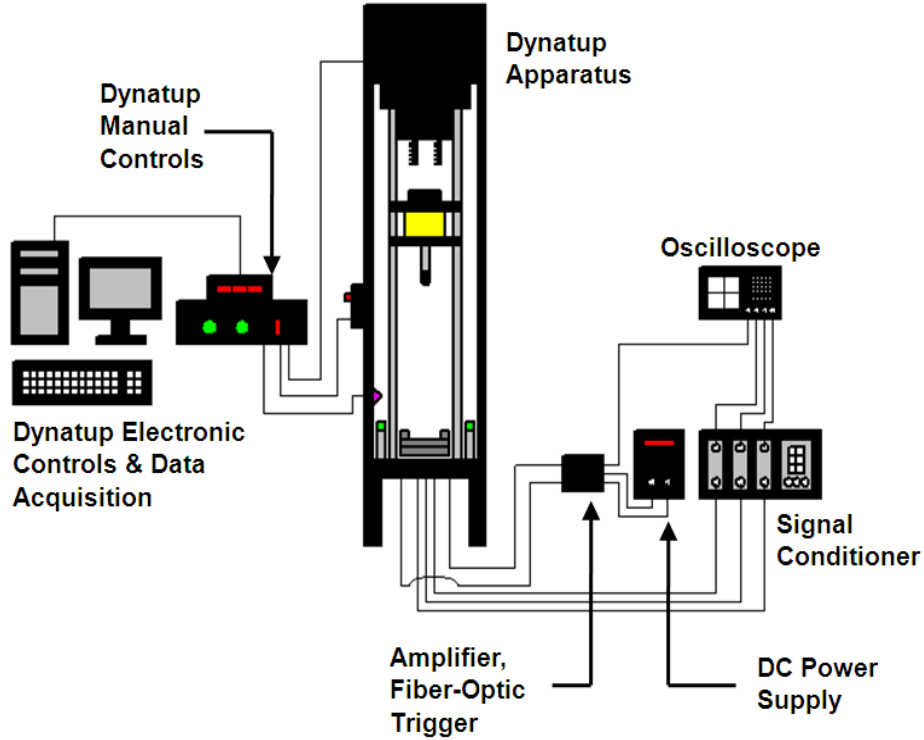


Figure 5.14: Schematic showing the sytem components for collecting strain histories from Dynatup impact events.

In ultrasonic immersed through-transmission scanning, the specimens are immersed in a tank of distilled water standing on their sides. The through-transmission scanning is accomplished by placing a piezoelectric emitter transducer on one side of the specimen and a piezoelectric receiver on the opposite side of the specimen, both immersed in the water tank with the specimens. The water serves as a coupling agent for sound waves to pass from the emitter to the specimen and receiver. Without the coupling agent, the disparity in acoustic impedance (material wave velocity multiplied by the density) between a solid and air can cause sound wave transmission problems for either the emitter or receiver if a gap exists between the specimen and one of the transducers. In through-transmission mode, a sound pulse is emitted from the emitter-transducer and the pulse propagates as a wave through the couplant (the water) until it reaches the material specimen. Some of the energy in the initial wave is transmitted into the specimen while some of the energy is reflected back toward the emitter. The transmitted energy propagates through the specimen as a mechanical wave. When the transmitted wave reaches the second material boundary, a portion of the wave energy transmits into the couplant while the remainder of the energy reflects back into the specimen. The wave that has passed through the specimen is then detected by the receiving transducer. A data acquisition system and digital readout then displays the results of the scan, typically as *a percentage of the wave amplitude that reaches the receiver with respect to either (1) the amplitude of the initial emitted pulse or (2) the peak amplitude detected by the receiver.*

So far, the immersed through-transmission ultrasonic NDE technique has been discussed under only ideal conditions. The ultimate purpose behind NDE is to determine if defects exist within the continuum of the specimen. Defects such as porosity, cracks, voids, inclusions, etc., all represent a material and/or geometric boundary within a specimen. When a wave traveling through a continuum encounters such a boundary, the wave is disrupted and scattered. Generally under these conditions, the receiver will detect a transmitted wave that is significantly lower in amplitude than the either the amplitude of the initial emitted pulse or the peak amplitude detected

by the receiver. When zones of this nature are found, it is assumed that some type of defect is present.

The inspection technique is termed “ultrasonic” because the sound waves are emitted at frequencies higher than what is perceivable by humans. The sound pulses in these tests usually vary between 0.1-15 Megahertz (1.0×10^6 cycles per second); young healthy humans can generally perceive sound frequencies up to 0.020 Megahertz [10]. The amplitude of sound waves is usually characterized by the measured pressure of a sound wave with respect to a reference pressure (which depends on a great number of factors but primarily material properties; reference pressure in air is usually taken to be 20 micropascals and in water is usually 1 micropascal [10]), measured in decibels:

$$Pressure\ Level = 20 \log_{10} \left(\frac{Sound\ Pressure}{Reference\ Pressure} \right) \text{ decibels} \quad (5.2)$$

With respect to sounds through air that humans are accustomed to, the sound waves in a radio broadcast can reach frequencies up to 5000 Hertz (0.005 Megahertz) and deafening sounds such as thunder or artillery reach amplitudes of 100-120 decibels [10].

It is important to note that the amplitude and frequency of the sound pulses play an important role in the ultrasonic NDE process. The piezoelectric emitter generates not merely a single pulse, but rather many pulses over a short period of time. As these pulses transmit into the specimen, the material undergoes low-amplitude cyclic loading. The cyclic loading generates internal friction that can attenuate some of the wave energy traveling through the specimen. Rigid materials are especially susceptible to this phenomenon, therefore lower frequency pulses are typically used with these specimens to ensure greater penetration of the waves. Sufficient amplitude, on the other hand, is important so that peaks from the emitted waves can be distinguished from system noise. Calibration specimens for specific materials and defects are constructed to aid NDE technicians in quickly determining optimal system settings and interpreting output from various tests.

The ultrasonic scans for this research were all performed at the Non-Destructive Evaluation Laboratory operated by the Air Force Research Laboratory, Materials & Manufacturing Directorate. Mr. Jeff Bennett, a certified NDE Specialist & Technician, performed the NDE for this work using the immersed through-transmission ultrasonic scan technique. The scan system is manufactured by WesDyne Corporation and is an AmData Model 100564, 4-Axis Ultrasonic System. The software used for readout is called IntraSpect and is developed by the same manufacturer. The emitter was set to generate sound wave pulses at a peak intensity of 51 decibels (dB) at a frequency of 2.25 Megahertz (MHz). The data was collected in “C-scan” mode (the designation given to scans that give a plan-view or “map-view” of the specimen characteristics), where the automated system used a raster scan pattern to move the transducers over the 7.62-cm x 7.62-cm plane of the plates such that the transmitted wave propagated through the 1.27-cm thickness direction of the plate. (Other ultrasonic inspection scan modes include “A-scan” mode, which provides depth information at a single point only, and “B-scan” mode, which provides cross-section information along a linear path. Neither of these scan techniques were used in this work.)

The results of the scans are shown in Figure 5.15. *No scans were taken of the 100% Ti plates.* The plates in Figure 5.15 are numbered based on the impact test in which they were used (see Table 5.3 in the next section). The two pure titanium plates that were not scanned were designated as specimens 1 and 2. Upon examining the results of the ultrasonic scans, some conclusions can be made with respect to the integrity of the composites. The two Ti-rich monolithic samples (85% Ti-15% TiB) allow 90%+ of the peak intensity of the sound wave to transmit through the plate, indicating that the plates likely have minimal internal defects that may be of consequence to the impact tests. The two TiB-rich monolithic samples (15% Ti-85% TiB), on the other hand, allow only 70%+ of the peak intensity to transmit through the specimens. The scans indicate for these specimens that the received intensity value is rather uniform throughout the plane of the specimens. The conclusion that

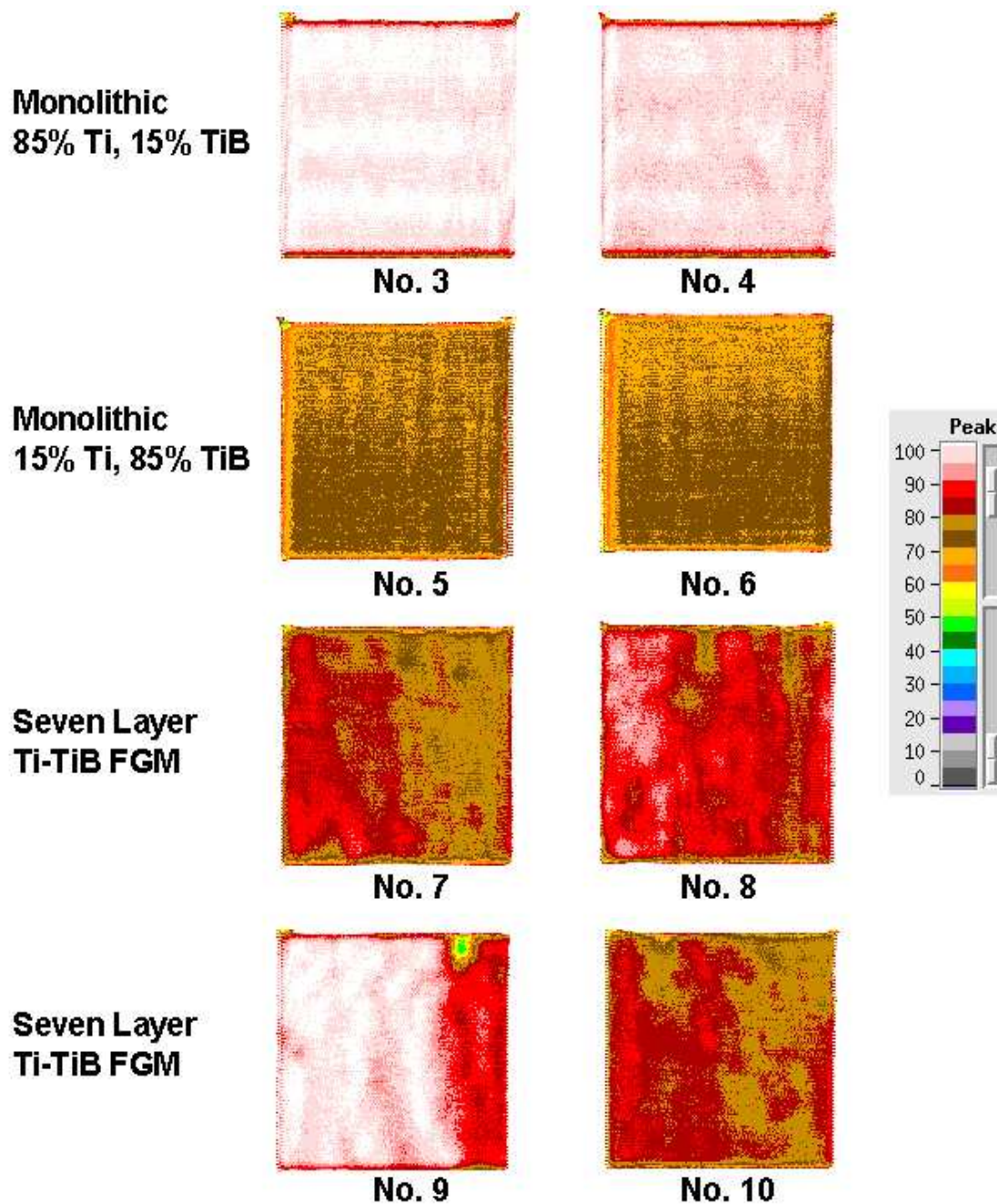


Figure 5.15: Through-transmission immersed ultrasonic C-scans of Ti-TiB monolithic and functionally graded plate specimens prior to impact testing. The color contours represent the percentage of the peak signal from the piezoelectric emitter (51 dB at 2.25 MHz frequency) detected by the piezoelectric receiver underneath the specimen according to the scale shown.

can be made is not necessarily that the TiB-rich specimens are greatly flawed but rather that the TiB-rich material attenuates the signal more dramatically than the Ti-rich material. It is easy to see that this may be the case when the fact that the elastic modulus for TiB is significantly larger than that for Ti by more than a factor of three even though the densities are comparable (recall the published elastic moduli from BAE Systems in [4] for Ti and TiB were 110 GPa and 370 GPa, respectively, in Table 4.5). Further, the amplitude and frequency of the sonic pulse were the same as for that of the Ti-rich monolithic samples, which can account for the difference in peak transmission. With regard to the functionally graded plates, specimen numbers 7 and 10 appear to allow an average of approximately 80% of the peak intensity to transmit. Specimen numbers 8 and 9, on the other hand, transmit closer to 90% of the peak intensity. Inspection seems to indicate that the contours lie between the two extreme volume fraction ratios of the monolithic samples. This is not an unexpected result when the compositions of the seven layers of the FGM are accounted for; the attenuation of the peak intensity should lie between the two extreme cases. It is noteworthy that the contours between the four FGM specimens appear to vary, implying that there may be significant variability in the reaction sintering process used to manufacture the FGMs. It is also important to note that FGM specimen 9 has a region near the outer edge of the plate where only 50% of the sound energy transmits through the plate. This is undoubtedly an area where there is potentially damage or another defect within the plate. The depth of the defect cannot be determined from an ultrasonic scan in C-scan mode, and no further scans were conducted to ascertain the depth or nature of the defect.

The main conclusion from the ultrasonic scans is that the plates, for the most part, appear to be free of macroscopic defects. FGM plate specimen 9 has a small defect near the edge of the plate but is otherwise free of any major defects. Microscopic defects (i.e., microcracks or microvoids) can be more difficult to trace with this inspection technique, but defects such as these cannot be easily detected without invasive measures. Since the plates needed to be intact for the impact tests, and since

Table 5.3: Summary of plate impact tests using Dynatup apparatus.

Test No.	Description	Crosshead/Tup		Velocity,	Impact
		Mass (kg)	Height (m)	Actual (m/s)	Energy (J)
1	100% Ti, 0% TiB Mono	13.06	0.508	3.040	60.35
2	100% Ti, 0% TiB Mono	13.06	0.635	3.476	78.90
3	85% Ti, 15% TiB Mono	13.06	0.508	3.050	60.75
4	85% Ti, 15% TiB Mono	13.06	0.635	3.479	79.04
5	15% Ti, 85% TiB Mono	13.06	0.381	2.585	43.63
6	15% Ti, 85% TiB Mono	13.06	0.508	3.050	60.75
7	7-Layer Ti-TiB FGM	13.06	0.508	3.040	60.35
8	7-Layer Ti-TiB FGM	13.06	0.635	3.412	76.02
9	7-Layer Ti-TiB FGM	13.06	0.762	3.765	92.56
10	7-Layer Ti-TiB FGM	13.06	0.889	4.078	108.6

the goal of this work is not to perform a material study on Ti-TiB, it was deemed appropriate to forgo such inspection of the plates.

5.2.2 Dynatup Plate Impacts. After pre-impact inspection of the Ti-TiB plate specimens yielded positive results, the plate specimens were then instrumented with strain gages and tested under impact conditions in the Dynatup apparatus. A summary of the Dynatup impact tests is shown in Table 5.3. The crosshead mass and height were chosen based on a laboratory trial-and-error process with extra 100% Ti plate samples. The mass, height, and impact energy were chosen sufficiently large to obtain measurable strain histories without permanently damaging the Dynatup system and plate fixture. The velocity was measured during the tests directly above the impact site using a velocity photo-detector that was part of the Dynatup apparatus [45]. The impact energy is assumed to be *kinetic energy* (KE) only, and is calculated by

$$KE = \frac{1}{2} m v^2 \quad (5.3)$$

where m is the mass of the crosshead and v is the velocity of the crosshead.

The actual impact velocity and impact energy in each test is compared to the ideal impact velocity and energy in Table 5.4. The ideal impact velocity assumes

that upon release of the crosshead from rest, all potential energy (PE) stored in the crosshead is converted to kinetic energy on impact with no work performed on the system or losses from external sources. The actual impact velocity is less than the ideal impact velocity because losses can occur in the system (such as friction in the guide rails) that slow the crosshead. Both the ideal and actual velocities of the crosshead and tup are computed from the energy relation:

$$KE_1 + PE_1 + W_{1 \rightarrow 2} = KE_2 + PE_2 \quad (5.4)$$

$$\frac{1}{2}mv_1^2 + mgH_1 + W_{1 \rightarrow 2} = \frac{1}{2}mv_2^2 + mgH_2 \quad (5.5)$$

KE and PE are the kinetic and potential energy of the crosshead assembly in states 1 and 2 in equation (5.4). $W_{1 \rightarrow 2}$ is the external work performed from state 1 to state 2. H is the height measured from the tip of the tup to the top surface of the specimen plate and g is the gravitational constant. State 1 is when the crosshead is at rest and raised above the plate at some height H_1 . State 2 is when the tup is at its maximum velocity and the height of the tup above the plate is zero. In state 1, all energy stored in the crosshead is in the form of potential energy; in state 2, all the energy stored in the crosshead is in the form of kinetic energy. In the ideal scenario, $W_{1 \rightarrow 2}$ is zero; in the actual tests, losses due to friction or other external sources are included in this term and thus $W_{1 \rightarrow 2}$ is non-zero. Assuming $W_{1 \rightarrow 2} = 0$ (ideal scenario), $v_1 = 0$, and $H_2 = 0$, the ideal impact velocity is calculated by rearranging terms in (5.5):

$$v_2 = \sqrt{2gH_1} \quad (5.6)$$

It is clear from the data that there are indeed losses in the system and $W_{1 \rightarrow 2}$ is non-zero. These losses could be attributed to any or multiple factors including friction/vibration in the guide rails and drag or uneven motion of the crosshead during a drop. The worst losses occurred in test 5, in which case the percent difference between the actual and ideal impact energies was 11.9%. The actual velocities and energies will be used for analytical and computational comparisons in subsequent chapters.

Table 5.4: Comparison of predicted and actual velocities and impact energies from Dynatup impact tests.

Test No.	Crosshead/Tup		Velocity		Impact Energy	
	Mass (kg)	Height (m)	Ideal (m/s)	Actual (m/s)	Ideal (J)	Actual (J)
1	13.06	0.508	3.157	3.040	65.08	60.35
2	13.06	0.635	3.530	3.476	81.37	78.90
3	13.06	0.508	3.157	3.050	65.08	60.75
4	13.06	0.635	3.530	3.479	81.37	79.04
5	13.06	0.381	2.734	2.585	48.81	43.63
6	13.06	0.508	3.157	3.050	65.08	60.75
7	13.06	0.508	3.157	3.040	65.08	60.35
8	13.06	0.635	3.530	3.412	81.37	76.02
9	13.06	0.762	3.867	3.765	97.65	92.56
10	13.06	0.889	4.176	4.078	113.9	108.6

Strain histories were successfully collected from eight of the ten tests. The tests involving the 15% Ti-85% TiB monolithic samples (tests 5 and 6) were the two unsuccessful tests. These specimens fractured severely immediately after impact and virtually no data was collected on these specimens as a result. The FGM specimen from test 10 also fractured, however, a significant portion of the strain history was collected prior to failure and this history has been included. Appendix B gives the raw strain histories for all tests and strain gages, successful and unsuccessful, in terms of their voltage signatures measured on the oscilloscope. These voltage readings were converted to strain by the process defined in Chapter V. Only the eight successful tests will be presented from this point forward.

The raw strain histories required some processing to clean up their respective data plots into something more meaningful. The data was processed using the commercial software Matlab® in three phases. Refer to Figure 5.16. The first phase was to truncate the strain gage signatures in the pre-trigger region. This region is the part of the history stored in memory before the voltage reading from strain gage 1 had reached its triggering threshold to order data acquisition on the remaining gages in the oscilloscope. The data where the strain readings were essentially zero were

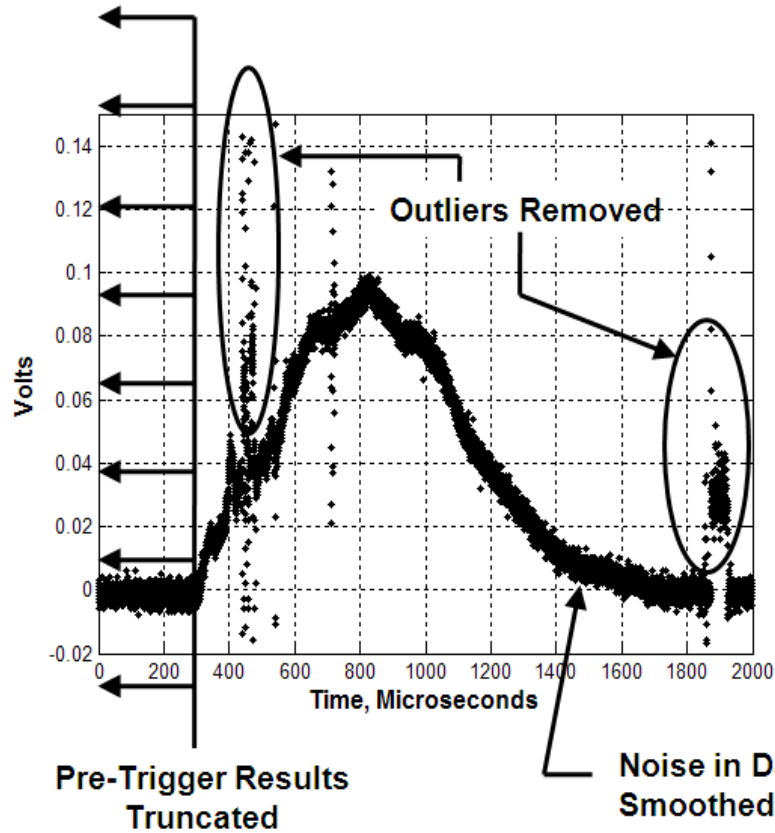


Figure 5.16: Illustration of areas requiring data processing from raw strain history.

deleted and the data where strain became significant were maintained. Furthermore, no impact event had significant strain data beyond 1500 microseconds after initial impact from the tup and thus data after this time was preserved but was not plotted. The second task was to remove significant outliers in the strain histories. The outliers generally occurred where a strain gage experienced an electrical disturbance (such as a short circuit or gage failure). Outliers were identified where it was clear that the strain readings were significantly different from the remaining trends that the reading could not be attributed to a physical behavior of the plate specimen. The outliers were removed subjectively and not by using a set mathematical criteria. Only very significant outliers were removed and the vast majority of the strain history was maintained.

The last task was to smooth the data in order to eliminate noise in the signal. The particular smoothing technique used is called *robust locally weighted regression*, or robust *loess*, a technique attributed to Cleveland [29], [30]. The data to be smoothed is *strain* (the “response” variable) as a function of *time* (the “predictor” or “explanatory” variable). The algorithm to perform this smoothing technique is included in **Matlab**[®] as a built-in function. Essentially robust loess fits a polynomial to a local subset of the data at each individual data point, with predictor variable values near the point whose response is being estimated. The polynomial is locally fit using weighted least squares, giving more weight to points near the data point whose response is being estimated and less weight to points further away. The value of the regression function for the point is then obtained by evaluating the local polynomial using the predictor variable values for that data point. The loess data fit is complete after regression function values have been computed for each of the data points (in this case, 10,000 data points minus any that were truncated or removed as outliers). The degree of the polynomial and the number of data points used in the weighted least squares are specified by the user. In this case, the smoothing was performed using quadratic (*second-order*) polynomial regression and weighted least-squares over a range of 40 data points (that is, weights were applied to 20 data points on either side of the data point whose response was being estimated). The choice of quadratic polynomial regression and weighted least-squares over 40 data points was so that potentially important oscillations in the plates were not lost while a significant portion of the noise present in the signals was eliminated. Further, the computational cost of this method is significant and the choice of higher-order polynomials over a greater number of data points did not significantly enhance the plots of the strain histories. The smoothed strain histories for the eight successful tests are shown in Figures 5.17-5.24. These histories can be compared to the raw voltage plots in Appendix B. The mathematics behind robust loess are quite extensive and will not be presented. Note that there is very little scatter in the raw data plots and the smoothing function merely enhanced

the general trend of the plot into something slightly more manageable. Arguably, the plots could potentially have been useful without smoothing on their own.

A few key results will be discussed regarding the strain histories. First, the general trend in most of the data is that strain gage 1 has the largest magnitudes of strain over the impact event, strain gage 2 the second largest, and strain gage 3 the smallest magnitudes. This is exactly what we should expect. In the circular plate configuration, the radial strain component measured by the strain gage would in fact be largest at the center and smaller as one approaches the boundary of the plate, given a circular plate with restrained boundary (whether clamped or simply-supported). Strain gage 1 was closest to the radial center, strain gage 2 slightly farther from the center, and strain gage 3 was closest to the boundary. The strains are tensile through the entire impact event, and the radial strain histories all follow a similar trajectory from zero strain prior to impact, maximum strain at the maximum load from the tup, followed by unloading to “zero” strain (this will be explained shortly).

Table 5.5 shows the maximum strains recorded from each gage in each test and the time that the maximum strain occurred. For plates of similar composition, the maximum strains are larger and the time to maximum strain occurs more quickly as the impact velocity increases. It is also clear that in some cases (very notably tests 1 & 2) that the magnitude separation between strain history curves from the same test are not always consistent. This is associated with deviations in the strain gage placement from the nominal positioning shown in Figure 5.10. In Chapter VI it will be shown the effects on recorded strain histories caused by slight variations in the gage location radially can be substantial.

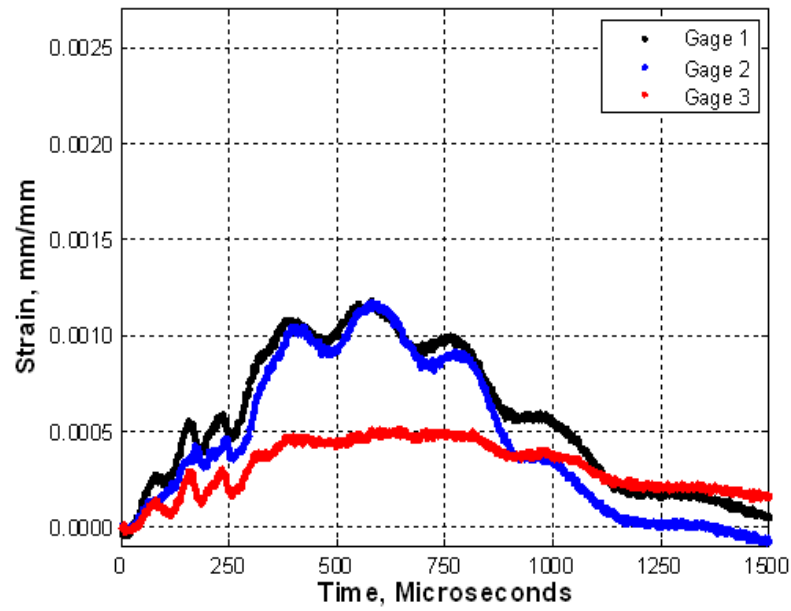


Figure 5.17: Strain histories for strain gages 1-3, 100% Ti monolithic plate, plate test no. 1.

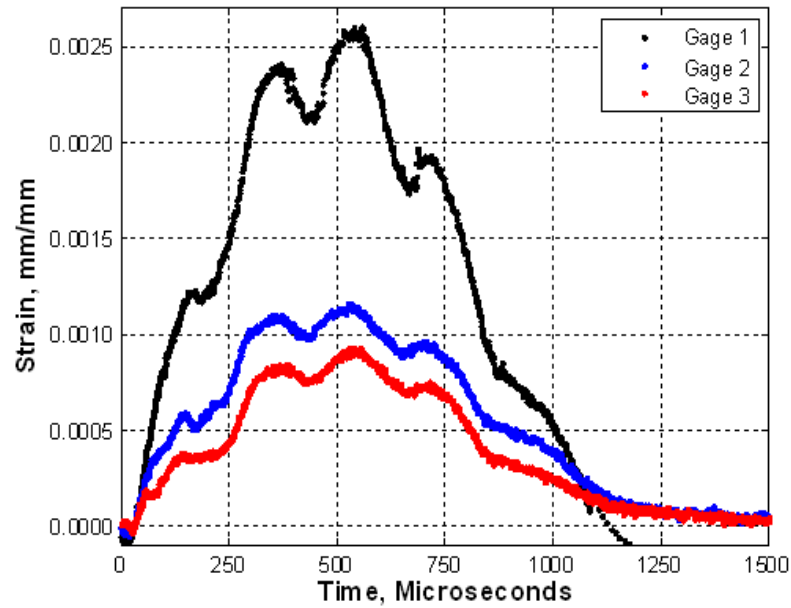


Figure 5.18: Strain histories for strain gages 1-3, 100% Ti monolithic plate, plate test no. 2.

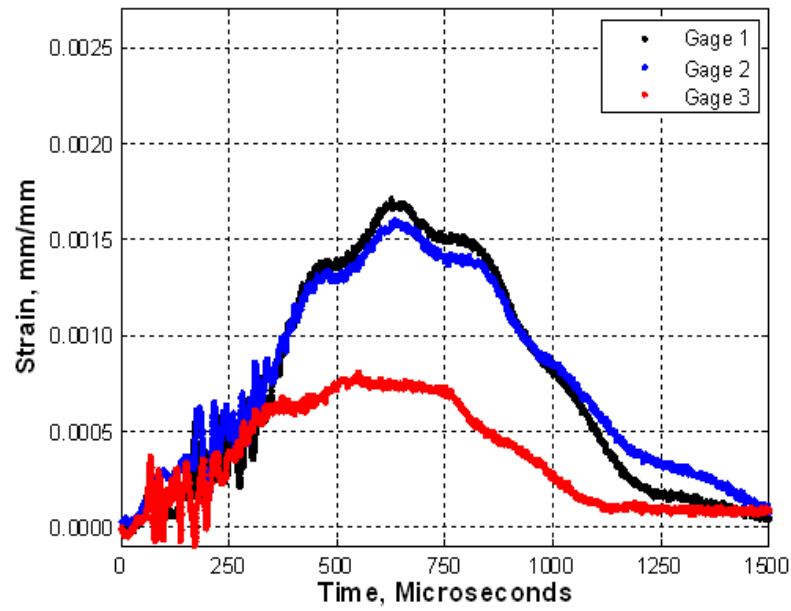


Figure 5.19: Strain histories for strain gages 1-3, 85% Ti-15% TiB monolithic plate, plate test no. 3.

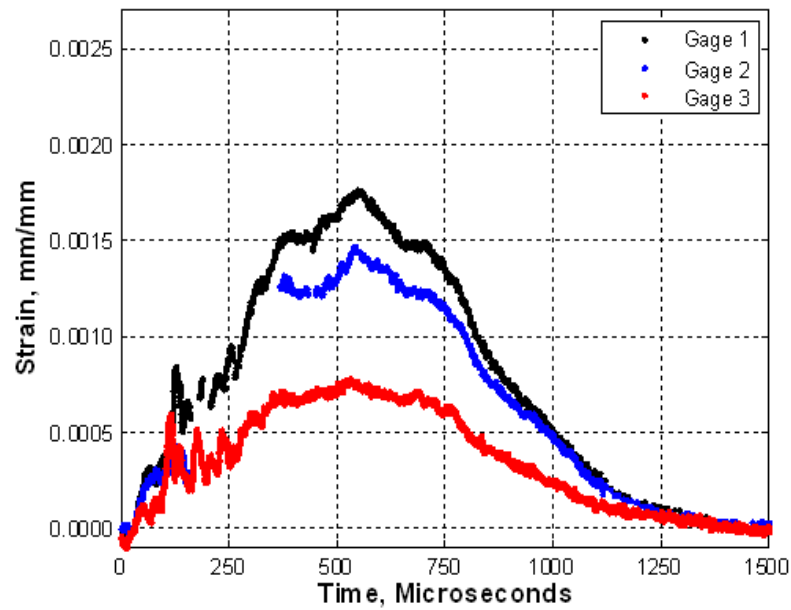


Figure 5.20: Strain histories for strain gages 1-3, 85% Ti-15% TiB monolithic plate, plate test no. 4.

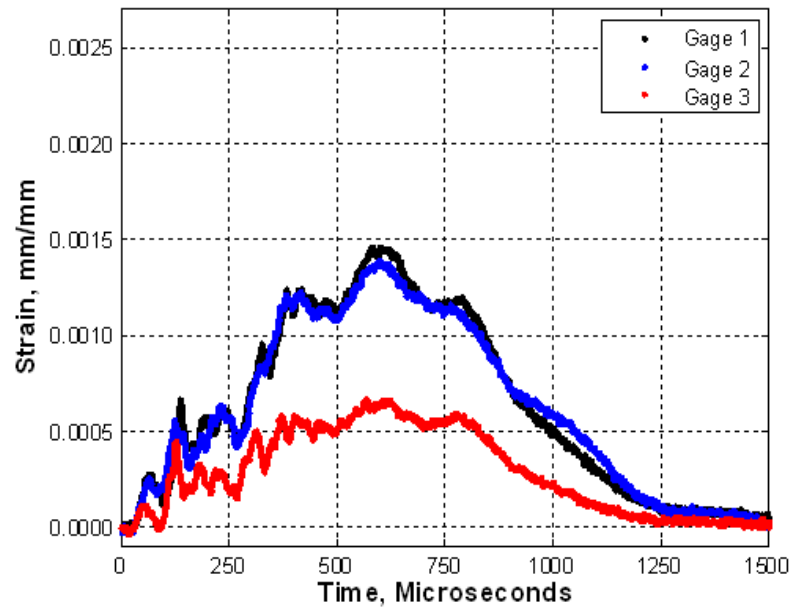


Figure 5.21: Strain histories for strain gages 1-3, Ti-TiB FGM plate, plate test no. 7.

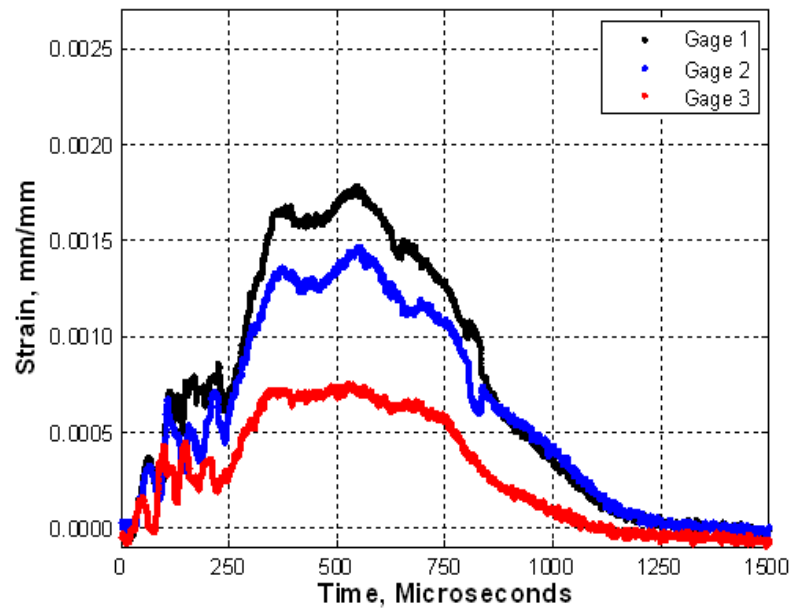


Figure 5.22: Strain histories for strain gages 1-3, Ti-TiB FGM plate, plate test no. 8.

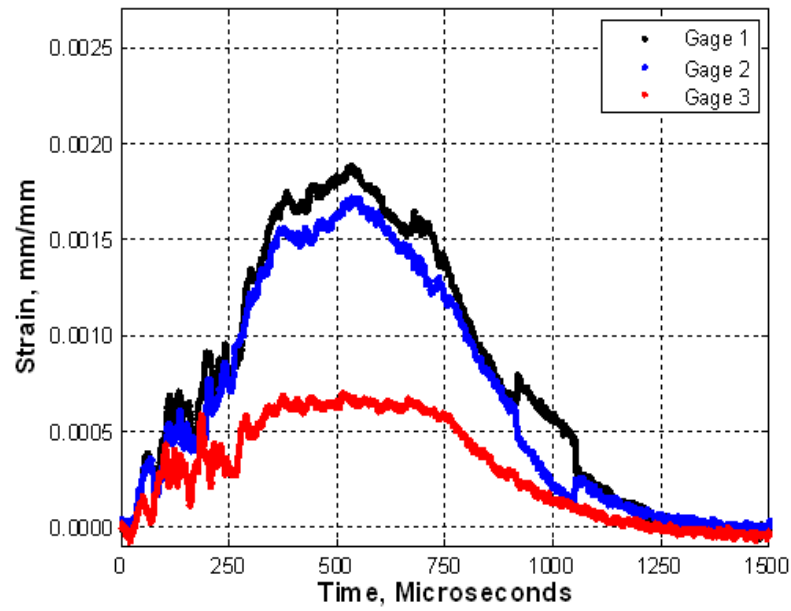


Figure 5.23: Strain histories for strain gages 1-3, Ti-TiB FGM plate, plate test no. 9.

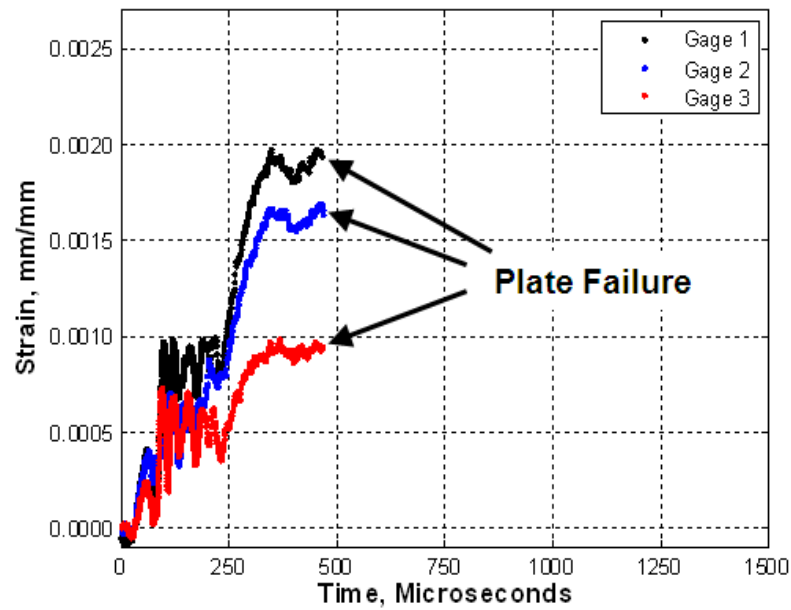


Figure 5.24: Strain histories for strain gages 1-3, Ti-TiB FGM plate, plate test no. 10.

Table 5.5: Maximum strains and associated time occurrence of maximum strains from impact tests.

Test	Description	Maximum Strains			@ Time μ -sec
		Gage 1	Gage 2	Gage 3	
1	100% Ti, 0% TiB Mono	0.0011837	0.0011728	0.0005157	579.4
2	100% Ti, 0% TiB Mono	0.0026020	0.0011612	0.0009269	528.4
3	85% Ti, 15% TiB Mono	0.0017115	0.0016030	0.0008058	629.5
4	85% Ti, 15% TiB Mono	0.0017644	0.0014692	0.0007834	542.0
5	15% Ti, 85% TiB Mono	Failed	Failed	Failed	
6	15% Ti, 85% TiB Mono	Failed	Failed	Failed	
7	7-Layer Ti-TiB FGM	0.0014595	0.0013910	0.0006638	599.9
8	7-Layer Ti-TiB FGM	0.0017830	0.0014677	0.0007573	545.9
9	7-Layer Ti-TiB FGM	0.0018890	0.0017203	0.0007016	534.6
10	7-Layer Ti-TiB FGM	Failed	Failed	Failed	

At the conclusion of some of the impact events, it is noteworthy that the strain values do not become zero as in other instances. This effect could be interpreted as residual plasticity in the specimens, but the evidence does not seem to support this. The plate specimens did not exhibit any visual indications of permanent deformation after impact except for tiny dimples on the surface of Ti-rich specimens (tests 1-4). The contact site on FGM plates could not be discerned. Further, during mock tests prior to formal testing, small impacts to the center of a dummy plate with a hammer would occasionally cause a measured voltage offset in the system after impact that needed to be corrected prior to subsequent testing. It is very probable that this is an effect associated with the adhesive system used to bond the strain gages to the plate specimens. This adhesive system is known for its resilience, especially in tension with large deformations, but the loading-unloading characteristics are not well understood.

Finally, a note on some of the observed oscillations in the strain histories is in order. The strains in the histories are tensile throughout the majority of the event, and the tensile strains in each gage appear to be moving in concert with each other over the length of the history. The significant strains in the histories occur over a 1000-1200 microsecond window. This would seem to indicate that the deformation of the plate is primarily a transverse global deformation as illustrated in Figure 5.25.

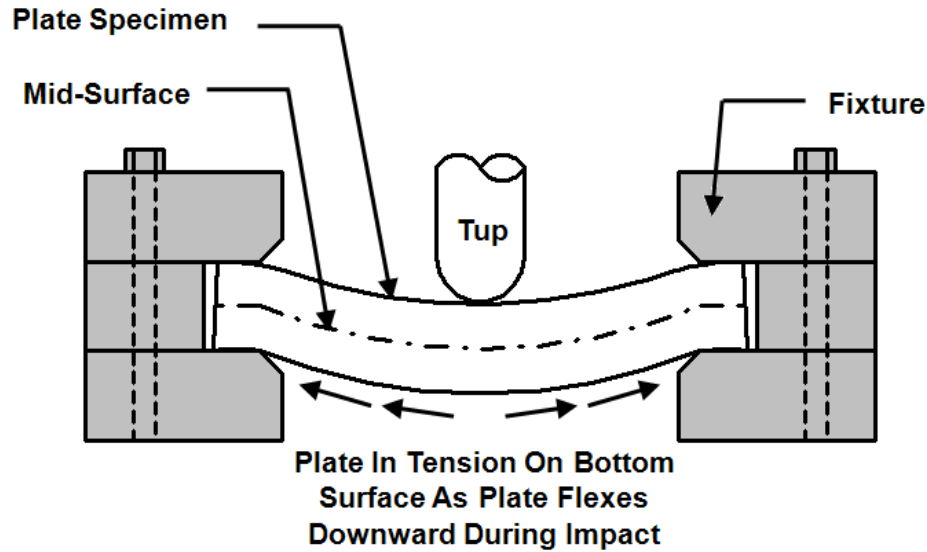


Figure 5.25: Apparent flexure of plate during impact events in Dynatup tests.

This assumption will be studied more in depth and verified in later chapters. Aside from sharp oscillations early in some of the histories (this will later be shown to be an electrical disturbance, not a plate behavior), there are only minor oscillations occurring through the majority of the history. Free vibration effects do not seem to be prevalent in the plate response; that is, oscillations between compressive and tensile strain on the bottom surface of the plate are not prevalent. The plates do not vibrate/oscillate significantly through the loading and unloading of the plate from the tup, nor do they oscillate at the end of the impact event as might be expected for an impulsive load. In Chapter VI, these and other oscillations in the strain histories will be studied in-depth. At this point it is difficult to draw any more meaningful conclusions without further study.

5.2.3 Post-Test Inspection of Plate Specimens. Ultrasonic immersed through-transmission scans were performed with the plate specimens after the impact tests with those plates that survived testing. The results are shown in Figure 5.26. The two monolithic 15% Ti-85% TiB plates did not survive their respective tests, and neither did FGM plate specimen 10. The C-scans of the post-impact plates were performed

at the same settings as before; sonic pulses were generated with amplitudes of 51 dB at a frequency of 2.25 MHz. The two monolithic 85% Ti - 15% TiB plates do not show appreciable damage after the impact events, although the location of the tup impact site can clearly be distinguished. The three surviving FGM plates for the most part did not incur additional damage, although plate 8 has two small areas along a straight line extending from the center of the plate to the boundary that appears to indicate some small damage accumulated in this area. *Overall, it would appear that the impacts to the surviving plates caused minimal damage and it is therefore likely that the impacts induced only elastic deformations to failure.*

5.3 Closing Remarks

In closing, the design of a novel test method for collecting strain histories in plate specimens subject to impact loading has been presented. The requirements of this test method were:

1. Utilize a test apparatus that can deliver a low- to medium-energy impact to a specimen under highly controlled, highly reproducible conditions.
2. Configure plate specimens such that analytical and computational comparisons of the impact event can readily be made.
3. Provide sufficient instrumentation to characterize the impact event along with the material response.

All of these requirements were met, the key results from the plate impact tests were presented. Ten plate impact tests were conducted. Six of the tests involved monolithic mixtures of Ti-TiB; four of the tests involved functionally graded Ti-TiB plates. Eight of the ten tests were successful, with strain histories collected throughout the duration of the impact events. A pre- and post-impact test inspection of the specimen plates seems to indicate minimal damage to the plates after impact, thus indicating that the impacts were primarily elastic in nature. Almost no visible plasticity was observed in any plate specimen after impact. The lack of visible plasticity and brittle fracture

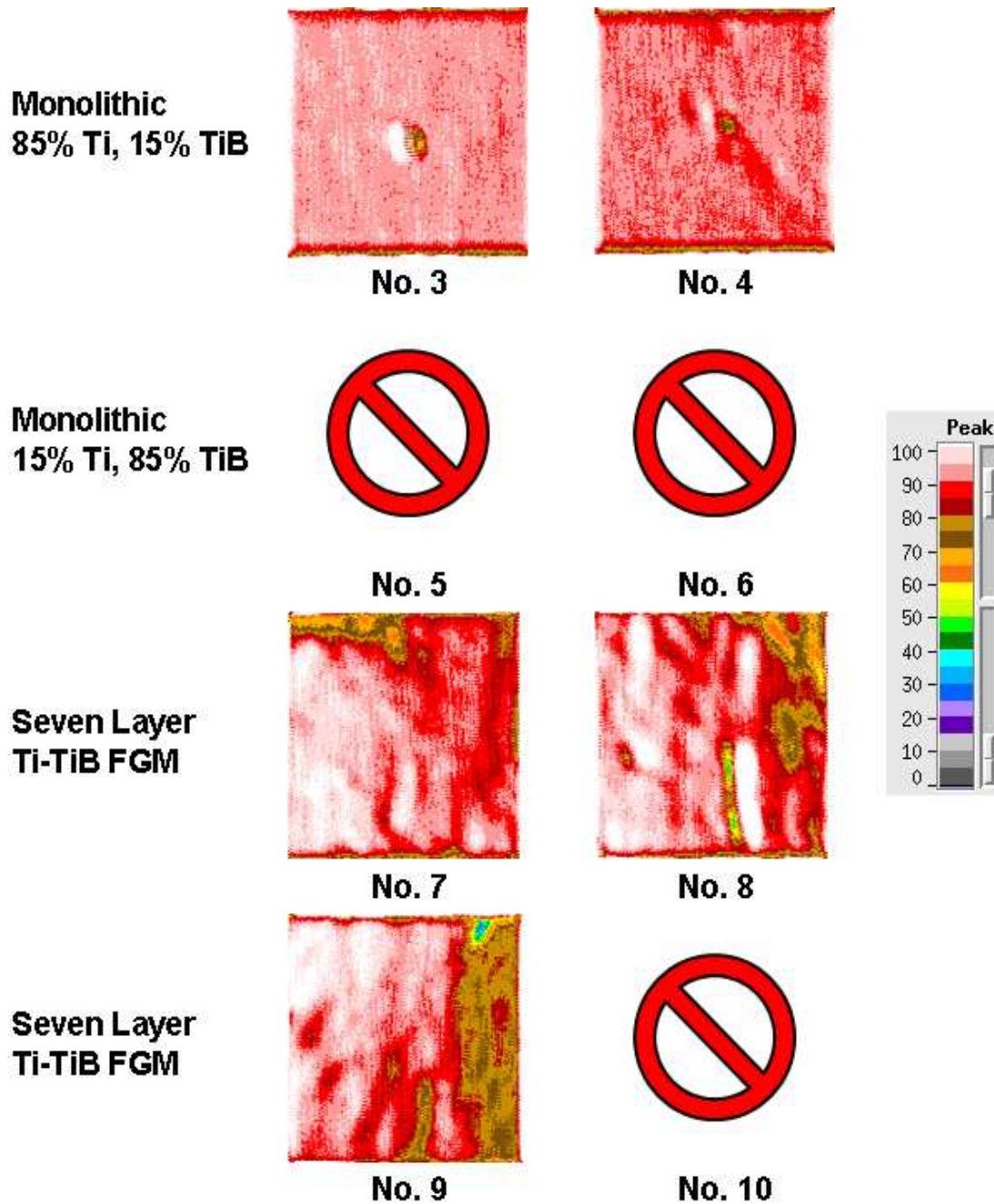


Figure 5.26: Through-transmission immersed ultrasonic C-scans of Ti-TiB monolithic and functionally graded plate specimens after impact testing. The color contours represent the percentage of the peak signal from the piezoelectric emitter (51 dB at 2.25 MHz frequency) detected by the piezoelectric receiver underneath the specimen according to the scale shown. Note that three specimens failed the initial impact tests.

occurring in three specimens indicates that the Ti-TiB mixture is very likely elastic to failure. The goal of these tests was not to perform a material study of the Ti-TiB system, but rather to obtain strain histories that can be compared to analytical and computational models applied to FGMs. In light of this, the experiments were highly successful. The design of this experimental technique and presentation of results in this chapter successfully accomplishes the first objective for this research (listed in Chapter I): *design and conduct impact experiments on metal-ceramic FGM plates to record strain histories at various locations on the plate over the duration of the impact event.*

The next chapter (Chapter VI) discusses a finite element model constructed to model these impact tests and takes the results from the finite element model and compares them to the experimental results of this chapter. A valid finite element model will allow the physics of the impacts to be analyzed in greater detail so that a fundamental understanding of the impact response of FGMs is obtained.

VI. Finite Element Modeling of Plate Impact Experiments

Finite element models (FEMs) were developed to study the impact experiments described in the previous chapter. The second objective of this research was *to construct a finite element simulation of the impact experiment that is sufficiently sophisticated to capture the dynamic effects of an impact load that is at the same time easily replicated by scientists and engineers in practice.* The manner in which the finite element models were constructed and this objective met are presented in this chapter. *These models are a very important part of this research in that if the finite element simulations match the observations and data collected during the experiment, it is possible to infer other behavior of the FGM in areas where data was not directly collected.* If the FEM does not effectively emulate the physical experiment, the computer simulation is of no value and no conclusions of consequence can be obtained from its use. This chapter will demonstrate that the FEM constructed to study the FGM plate impact experiments is indeed a valid simulation, and a wealth of information can be construed from the model related to the physics of the impact events. *This represents a significant contribution to the study of FGMs, namely, a simulation that has been validated based on correlation to experimental data.*

6.1 Finite Element Model Development

The finite element models were constructed in the commercial FEM software ABAQUS. The discussion here will concentrate on the high-level details of the FEM's *configuration only* and will not present many details of the associated theory; this will be left to Appendix C. A picture of the experiment FEM is shown in Figure 6.1 with all the major components labeled.

6.1.1 Plate Fixture Finite Element Model. The design and specifications of the plate fixture were described in detail in Chapter V. The nominal dimensions provided in the drawings (Figures 5.5-5.7) were used to construct the finite element models for the plate fixture components.

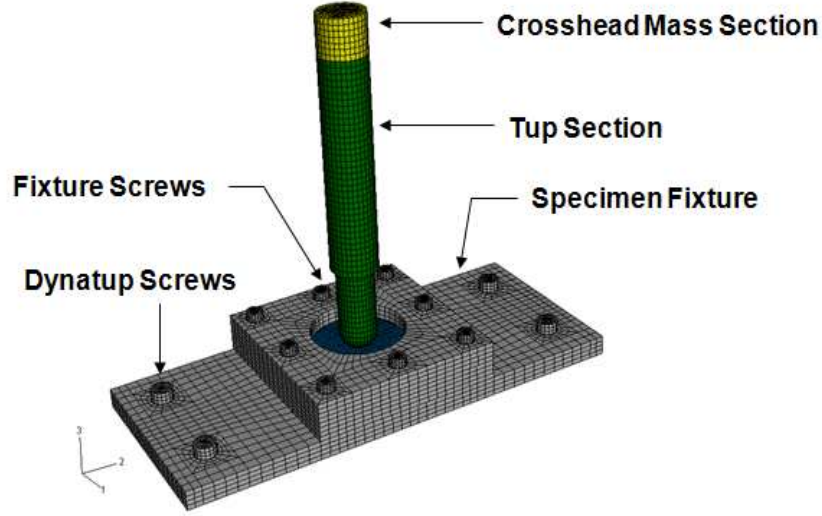


Figure 6.1: Finite element mesh and model for the plate impact experiments.

6.1.1.1 Top, Bottom, and Spacer Plate Components. The fixture components were visually inspected after testing and found to be virtually undeformed. The components are thus assumed to require only elastic material properties. The top, bottom, and spacer plate components of the fixture were machined from 304-stainless steel, as mentioned in Chapter V. Standard material properties for this grade of steel are shown in Table 6.1. Each component was meshed with *linear, isotropic, reduced-integration, eight-noded three-dimensional solid brick elements* (the theoretical details associated with these elements are included in Appendix C). An example element is shown in Figure 6.2. The part was manually meshed in order to maintain a consistent mesh and prevent formation of irregularly shaped elements that can cause numerical problems during solution. The finite element mesh for the bottom plate component is shown in Figure 6.3. The bottom plate contains 7935 nodes and 5656 elements. The spacer plate FEM is shown in Figure 6.4; the model contains 3800 nodes and 2560 elements. The finite element mesh for the top plate is shown in Figure 6.5; the model for this part contains 4280 nodes and 2944 elements.

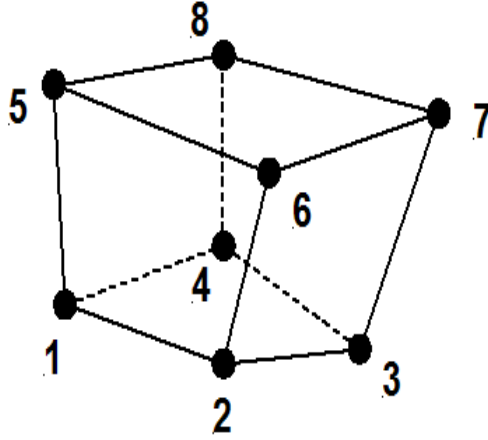


Figure 6.2: Eight-noded linear brick element as used in the finite element model.

Table 6.1: Material properties for 304 stainless steel applied to fixture plates and all screws in the FEM [10], [86].

Property	Value	Units
Density, ρ	8030	kg/m ³
Young's Modulus, E	193.0	GPa
Poisson's Ratio, ν (minimum)	0.29	
Shear Modulus, G	74.86	GPa
Yield Stress, σ_y	269	MPa
Ultimate Stress, σ_{ult}	600	MPa

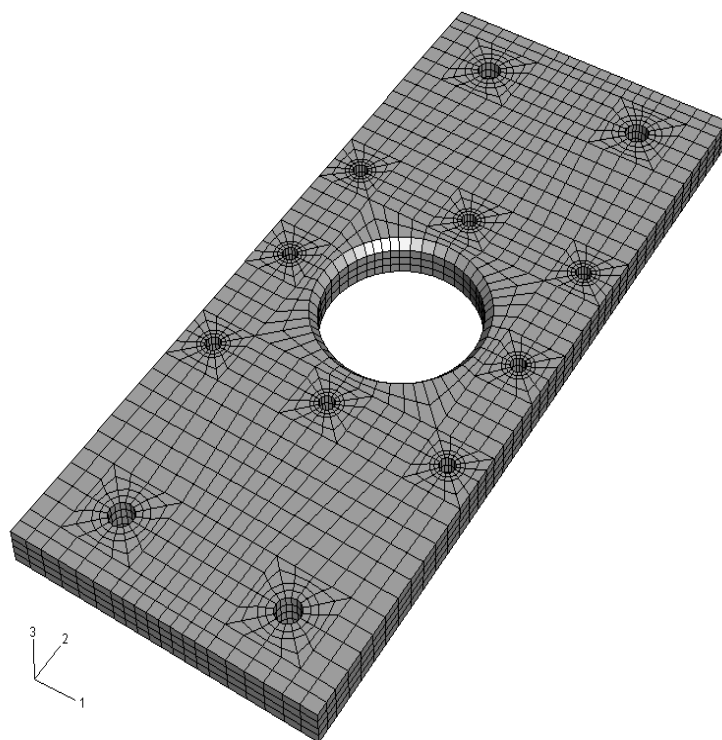


Figure 6.3: Plate specimen fixture; bottom plate component finite element mesh.

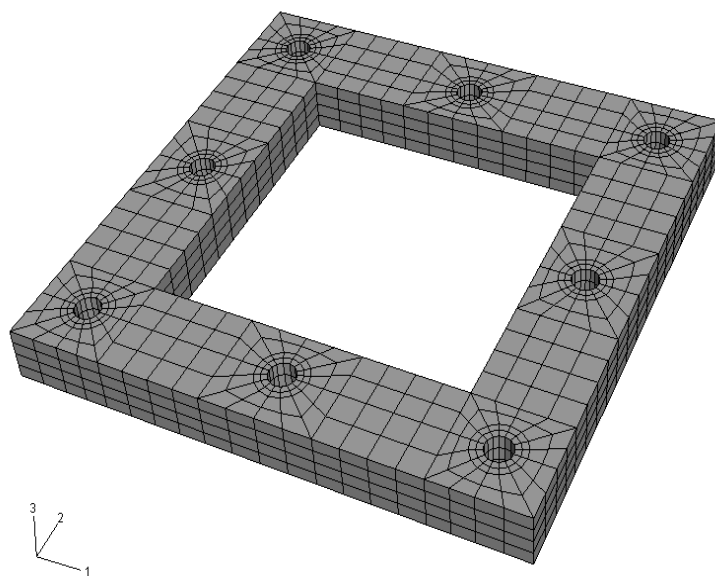


Figure 6.4: Plate specimen fixture; spacer plate component finite element mesh.

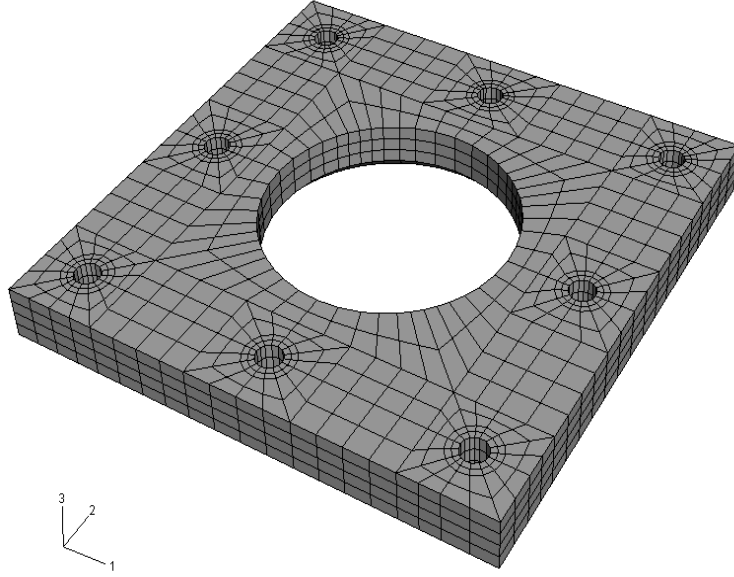


Figure 6.5: Plate specimen fixture; top plate component finite element mesh.

6.1.1.2 Plate Fastener Screws. The eight plate fastener screws were 0.635-cm stud diameter fine-threaded Unified hex cap screws (1/4-28 UNF; the Unified standard is nominally in units of inches, however, all units here are in cm to remain consistent with the metric units used throughout this work; see [86] for the specific dimensions of these screws) and were composed of 18-8 grade stainless steel. The simplified finite element model of the screws is shown in Figure 6.6. Note that “18-8” refers to stainless steels with a composition of 18% chromium and 8% nickel. Since 304-stainless steel falls within the more general 18-8 classification [86], the material properties for 304-stainless steel in Table 6.1 were used for the eight plate fastener screws for simplicity. The same screws were used in all impact tests and were virtually undeformed after testing; therefore only elastic properties were input into the finite element models. Each screw’s hexagonal head was 0.397-cm thick and the width across the flats was 1.111-cm. The round washers used in conjunction with the screws were the same 18-8 stainless steel as the screws and were 0.198-cm thick with an outside diameter slightly larger than the width across the flats of the hex-head. The simplified finite element model consists of a round cylinder for the head in lieu of the hex-head

geometry. The cylindrical head has a diameter equal to the width across the flats of the hex-head screw and the thickness is equal to the the hex-head plus the washer thickness (thus effectively combining the washer and head into one geometry). The stud length is equal to the thickness of all three fixture plates sandwiched together (3.81-cm). The screws were meshed with *linear, isotropic, reduced-integration, eight-noded three-dimensional solid brick elements*. Each screw contains 1300 nodes and 1040 elements. There are eight screws in the model and thus the total number of nodes and elements contained in the plate fastener screws are 10400 and 8320, respectively.

6.1.1.3 Dynatup Attachment Screws. The four Dynatup attachment screws were 0.9525-cm stud diameter coarse-threaded Unified hex cap screws (3/8-16 UNC; the Unified standard is nominally in units of inches, however, all units here are in cm to remain consistent with the metric units used throughout this work; see [86] for the specific dimensions of these screws) and were composed of 18-8 grade stainless steel (material properties in Table 6.1 apply). The simplified finite element model of the screws is shown in Figure 6.6. Each screw's head was 0.595-cm thick and the width across the flats was 1.429-cm. The round washers used in conjunction with the screws were the same 18-8 stainless steel as the screws and were 0.198-cm thick with an outside diameter slightly larger than the width across the flats of the hex-head. The simplified finite element model consists of a round cylinder for the head in lieu of the hex-head geometry. The cylindrical head has a diameter equal to the width across the flats of the hex-head screw and the thickness is equal to the the hex-head plus the washer thickness (thus effectively combining the washer and head into one geometry). The stud length is equal to the thickness of the bottom plate (the reason for this is discussed later) and the diameter of the stud is 0.9525-cm. Each screw was meshed with *linear, isotropic, reduced-integration, eight-noded three-dimensional solid brick elements*. Each screw contains 641 nodes and 480 elements. With four screws included in the model, the total number of nodes and elements for these components is 2564 and 1920, respectively.

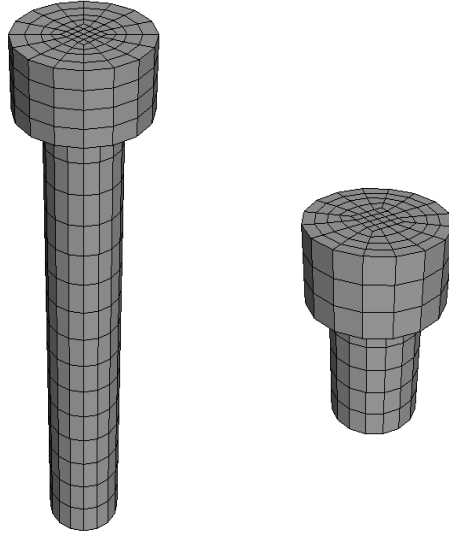


Figure 6.6: Simplified finite element models for the eight plate fastener screws (left) and four Dynatup attachment screws (right).

6.1.2 Tup and Load Cell Finite Element Model. The crosshead, load cell, and tup assembly in the Dynatup apparatus represent a very unique part of the FEM as a whole. The best scenario for modeling the Dynatup apparatus is to include nearly all the parts that make up the apparatus. This would not be a trivial undertaking in constructing the model and would further be computationally expensive. The primary function of the crosshead, load cell and tup assembly was to transfer energy and momentum to the target specimen through contact with the tup and specimen. A highly simplified model of this assembly was developed that would serve both of these purposes (referred to as simply the “tup FEM” or “tup model” from this point forward). The model is shown in Figure 6.7. It consists of two unique sections: (a) a tup section (shown in dark green in Figure 6.7) & (b) a crosshead-mass section (shown in yellow in Figure 6.7). The tup section is composed of two cylindrical pieces; one piece is 3.175-cm in diameter and 13.97-cm long and one piece is 2.54-cm in diameter and 4.445-cm long. At the end of the smaller cylinder is a hemispherical tip of radius 1.27-cm. The larger cylinder represents the load-cell and the smaller cylinder with hemispherical tip is the tup. The net length of this section is thus 19.69-cm. The

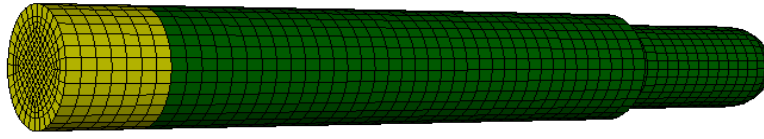


Figure 6.7: Simplified finite element model of mass, load cell, and tup in Dynatup apparatus.

crosshead-mass section is a cylinder 2.54-cm long and 3.175-cm in diameter. The net length of the entire tup model is thus 22.23-cm. The dimensions for the tup section in the FEM were chosen to be similar to those associated with the tup and load-cell on the Dynatup in the laboratory.

As stated in Chapter V, the actual composition of the tup was not known and was not provided by Instron. A set of material properties thus had to be assumed for the tup section, and 4340 hardened-alloy steel was chosen; material properties are found in Table 6.2. The crosshead-mass section was designated as a pseudo-material; essentially the purpose of this section was to store the entire mass of the crosshead. In Chapter V, it was explained that the mass of the crosshead assembly during testing was set at 13.06 kg. This mass included the crosshead, load cell, and tup and therefore represented the entire body of mass traveling down the guide rails once the crosshead assembly was released from rest. Knowing the dimensions of the components of the FEM tup model, this mass was distributed through the volume of the tup model. The mass contained in the tup section of this FEM was calculated based on the density of 4340 hardened steel (Table 6.2) and can be easily shown to be 1.072 kg. The remaining portion of the 13.06 kg not contained in the tup section is then 11.988 kg. A density for the pseudo-material in the crosshead-mass section can then be found to be 596,121 kg/m³ based on the dimensions of this section. The elastic modulus was set very high in comparison with the rest of the model components; essentially

Table 6.2: Material properties for 4340 hardened alloy steel applied to tup section of tup finite element model [21], [10], [86].

Property	Value	Units
Density, ρ	7800	kg/m ³
Young's Modulus, E	200.0	GPa
Poisson's Ratio, ν (minimum)	0.29	
Shear Modulus, G	77.52	GPa
Yield Stress, σ_y	860.0	MPa
Ultimate Stress, σ_{ult}	1310	MPa

Table 6.3: Material properties for the pseudo-material applied to the crosshead-mass section of tup finite element model.

Property	Value	Units
Density, ρ	596121	kg/m ³
Young's Modulus, E	5000	GPa
Poisson's Ratio, ν (minimum)	0.30	

the crosshead-mass section behaves like an rigid mass attached to a deformable tup. The properties of this pseudo-material are found in Table 6.3. The tup model was meshed with *linear, isotropic, reduced-integration, eight-noded three-dimensional solid brick elements*. The tup model contains 12190 nodes and 11008 elements total.

6.1.3 FGM Plate Specimen Models. Two distinct finite element models were developed to study the FGM plates. The first model is one that assumes that each individual layer in the FGM behaves as a *homogeneous, isotropic material*. The second model assumes that there are in fact *two distinct phases of material randomly distributed based on the volume fraction ratio of the constituents*. Each model is described in greater detail in the following subsections.

6.1.3.1 Homogenized-Layers Model. In Chapter III, several material models were presented where engineers and scientists used analytical formulas based on physical principles and underlying material assumptions to homogenize material

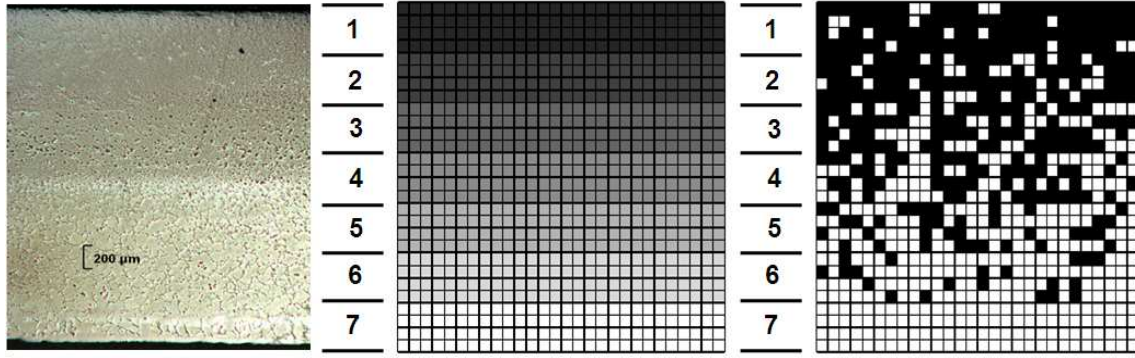


Figure 6.8: Comparison of actual seven-layer Ti-TiB FGM (left) and FEM representations: homogenized-layers model (middle) and two-phase model (right). In the FEM representations, Ti-rich areas are white and TiB-rich areas are black.

properties of a continuum with two or more constituents. Some of these models were formulated given an ordered distribution of the constituents that follow a repeating pattern of representative volume elements. Others assume random distributions of the constituent materials. In either case, the goal is to average the contributions of each material to a constitutive model governing the response of the continuum as a whole. This class of finite element model will do exactly this; that is, take known information of the distributions of Ti and TiB in the monolithic and functionally graded plates and compute homogenized material constitutive relations for each mixture of Ti-TiB. In Chapter V, it was hypothesized that the plates behave elastic to failure. Therefore, the constitutive relations in the FEM will be elastic. No failure model was incorporated in the constitutive relation. Typically strain rate-dependent plasticity and failure models are required to accurately model impact events, however, the strain-rates were relatively low in all the impact tests (this will be given a thorough treatment in Chapter IX) and only one FGM specimen failed. Strain rate-dependent effects are generally more important when incorporating yield, plasticity, and failure in simulation. None of these effects are included for reasons already discussed, so for now the elastic constitutive models will suffice.

The volume fraction and thickness data in Table 4.4 were used in conjunction with the material properties for Ti (Table 4.1) and TiB (Table 4.2). (While these baseline properties were used to initially assess the validity of the finite element model, in Chapter VIII the properties will be optimized to their actual values using a parameter estimation technique.) This information was then applied to one of the material models in Chapter III to calculate the elastic modulus, Poisson's ratio, and density of each individual layer. In the case of the monolithic Ti-TiB plates, only one layer of constant volume fraction exists so only one set of material properties is generated. In the case of the FGM specimens, seven sets of homogenized material properties are generated for each individual layer.

A **Matlab**[®] script was written to efficiently calculate the material properties for each monolithic and functionally graded plate configuration given a specific material model (classic rule-of-mixtures, self-consistent model, and Mori-Tanaka estimates). Given the 7.62 cm x 7.62 cm–1.27 cm thick plate geometry, the script was also designed to generate the finite element nodal grid and element mesh for each plate by assigning mesh densities along the three major dimensions of the plate. This script therefore allowed the plate mesh to be constructed very quickly and efficiently, and the plate geometry could be imported into ABAQUS to fit into the plate fixture model. This eliminated the need to calculate material properties for individual layers by hand and also eliminated the need to manually reconstruct the plate model if the plate mesh needed to be adjusted. The **Matlab**[®] script generates a text-based input file as its output, and this text-file is imported and read into ABAQUS.

The mesh for the specimen plates was determined based on an *informal* convergence study that considered the mesh that would be the most effective from both a computational and solution convergence standpoint. The plate mesh used, based on the study, was 14 elements through the thickness of the plate, and 42 element divisions along each side of the plate; thus the total number of nodes and elements for the plates were 27735 and 24696, respectively. The specimen plate model was meshed with *linear, isotropic, reduced-integration, eight-noded three-dimensional solid*

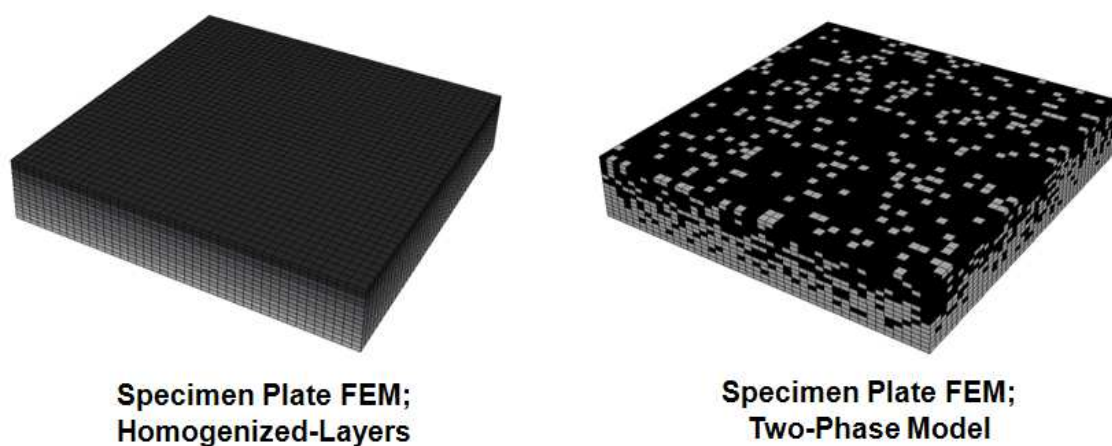


Figure 6.9: Comparison of homogenized-layers and two-phase plate specimen FEMs; see also Figure 6.8.

brick elements. For the seven-layer FGM plates, each layer was two elements thick (two elements thick per layer multiplied by seven layers gives the 14 element thickness of the plate). The monolithic plates used the same mesh as the FGM plates, however note again that each monolithic plate is a *single-layered construction*. Each layer of *elements* in the plate (14 in all) was assumed to adhere perfectly to the layers immediately above and below it. This was done to remain consistent with the assumption of perfect adhesion of layers in the composite plate theory of Chapter III. A note on the size of each element as compared to the size of a potential representative volume element of both constituents will be included momentarily. The plate FEM for the homogenized-layers model is shown in Figure 6.9.

6.1.3.2 Two-Phase Model. It can be seen in the SEM photographs of Ti-TiB mixtures in Chapter IV, Figures 4.5-4.11 the distribution of Ti and TiB in reaction-sintered composite systems is not well ordered and is random in nature. In fact, TiB clusters are very common even at very low volume fractions of TiB. To address this random distribution of materials, a second finite element model class was developed, the so-called “two-phase” finite element model. In this model, individual cells are distributed that contain only titanium and other cells that contain only ti-

tanium boride with no mixing of the two constituents. In Figure 6.8, this random mixing of cells (or “elements”) is illustrated, with white cells containing *strictly titanium material properties* and black cells containing *strictly titanium boride material properties*. In some respects, this model is more simple than the homogenized-layers model in that only two sets of material properties need to be known, that of the constituents. In other respects, the two-phase model can be more complicated in that the random distribution of constituents can result in clustering of the constituents that make it extremely difficult, if not impossible, to study analytically.

Similar to the homogenized-layers model, a **Matlab**[®] script was written to generate the nodal grid and element mesh for the specimen plate. No analytical material models are required since the two-phase model is simply constructed by randomly distributing the phases of each constituent. Once an element containing the properties of a specific constituent is defined, the script assigns the properties of the constituent to that element. The key advantage to running a script to generate the mesh is that **Matlab**[®] (or any other such program) can quickly and efficiently assign the element properties as opposed to manually accomplishing such a task in the ABAQUS graphical user interface one element at a time.

The script works as follows. First, the mesh densities along the major dimensions of the plate are assigned. The script then looks at the location of each layer of elements as compared to its analogous location in an actual plate specimen. The program then takes the volume fraction ratio of constituents at that location in the plate and applies it to the element layer in the FEM. Based on the volume fraction ratio at that element layer and the number of elements in the layer, the program assigns a set number of elements to be composed of one constituent and the remainder of elements to be composed of the second constituent.

As an example, suppose we have a seven-layer Ti-TiB FGM plate with 14 elements through the thickness; each of the seven FGM layers is two elements thick. Suppose now the FEM of the plate has 100 elements per element layer (1400 elements

in all). FGM layer 1 (Table 4.4) is composed of 85% TiB and 15% Ti. The two element layers in the FEM corresponding to actual FGM layer 1 would contain 85 elements of TiB and 15 elements of Ti *each* (170 elements of TiB and 30 elements of Ti *total*). The only remaining task is to then take these elements and distribute them randomly.

A random number generation feature in **Matlab**[®] was used to accomplish this. Note that the choice of a random number generator is not really important, provided that the constituents are truly distributed in a random fashion. Essentially, elements of TiB were assigned a designation of “1” and elements of Ti were assigned a designation of “2.” These designations were randomly mixed together and then applied to the list of elements in the given layer.

Continuing with the example, the top element layer corresponding to actual FGM layer 1 had 85 TiB elements and 15 Ti elements. 85 “1” designators and 15 “2” designators are placed into a 100 x 1 vector. The 85 “1” and 15 “2” designators are removed one at a time, from the initial vector and placed into a second 100 x 1 vector to a location (between 1 and 100) chosen without replacement by the random number generator. Eventually the entire vector is filled and this list is applied to the list of elements in that element layer. Another example of the output of this algorithm is illustrated in Figure 6.8, in which case the seven-layer FGM of Table 4.4 is modeled over a 28 layer x 28 wide grid. The program rounds up the number of elements required for TiB in each layer if the volume fraction of TiB multiplied by the number of elements in a layer is not an integer; the number of Ti elements is then determined after rounding occurs.

The mesh for the specimen plates using this model was the same as that used for the homogenized-layer model: 14 elements through the thickness of the plate, and 42 element divisions along each side of the plate. The total number of nodes and elements for the plates were 27735 and 24696, respectively. The specimen plate model was meshed with *linear, isotropic, reduced-integration, eight-noded three-dimensional*

solid brick elements. For the seven-layer FGM plates, each FGM layer was two elements thick. The monolithic plates used the same mesh as the FGM plates, however note again that each monolithic plate is a single-layered construction in which case the elements of constituents are randomly distributed under the same volume fraction throughout the entire plate. Each layer of *elements* in the plate (14 layers in all) was assumed to adhere perfectly to the layers immediately above and below it. Additionally, each element was assumed to adhere perfectly to each adjacent element, regardless of whether or not adjacent elements had mismatching properties. *Whether or not this assumption is valid for the Ti-TiB FGM or any other FGM system is very much dependent on the individual mixture and constituents.* Since it is not the goal of this work to focus on material science aspects, for now it will be assumed that this assumption is valid for elastic analyses as is the case here. The plate FEM for the two-phase model is shown in Figure 6.9.

One final comment on the choice of element size in the models, especially the two-phase model, is in order. According to the chosen mesh size, each element in the specimen plate FEMs has the dimensions 1.81 mm x 1.81 mm x 0.907 mm. In Figures 4.5-4.11, one could estimate a typical TiB whisker to be on the order of about 50 micrometers in length and 5 micrometers in maximum diameter. Comparing the largest dimensions of an individual element, 0.00181 m, to the largest dimension of a TiB whisker, 0.000050 m, the elements in the model are on the order of 36 times larger than that of an average TiB whisker. Further, the geometry of the element, essentially a 2 x 2 x 1 brick, is starkly different from that of the needle, which can have a length-to-diameter ratio of 10:1. The key assumption in the two-phase FEM then can be stated as *each element, composed of an individual constituent, contains a conglomerate of that constituent concentrated in the volume occupied by that element.* This is essentially a worst-case scenario on the micro-mechanics level that more or less can, but generally does not, occur in the mixture of materials. All of these facts are important to the analyst since the comparison between the actual FGM composite and the two-phase FEM is most definitely not one-to-one. However, if the goal is to follow

the *macro-mechanic behavior of the FGM*, the discrepancy between the geometries is less important than it is on a micro-mechanics scale.

6.1.4 FEM Loads and Constraints. To this point, the finite element construction and mesh of the individual components of the Dynatup experiments have been presented. The finite element model required thoughtfully applied loading and constraints throughout to ensure that the FEM behaved as close to the actual experiment as possible. In this section, the loads and constraints are discussed in depth.

6.1.4.1 FEM Boundary Conditions and Constraints. The following is a list of all the boundary conditions and constraints placed on the FEM. Note the coordinate system shown in Figure 6.1 and reference planes in Figure 6.10. The 1-axis runs parallel to the width of the fixture; the 2-axis runs parallel with the length of the bottom plate component; the 3-axis is parallel to the axis of the tup (this axis will be referred to occasionally as the “vertical axis” or “vertical direction;” reader take note).

1. The bottom surface of the bottom plate was constrained from vertical displacement only. This surface is in direct contact with the base of the Dynatup. The Dynatup base is made of 5.08-cm steel and is not easily deformable; thus this assumption was deemed prudent.
2. An imaginary plane parallel to the 13-plane passing through the center of the fixture assembly was constrained such that all nodes and element faces contained directly in this plane were not allowed translations parallel to the 2-axis direction. This included the bottom, spacer, and top plates of the fixture as well as the specimen plate; nodes or elements attached to the tup and plate fastener screws were not assigned this restriction.
3. An imaginary plane parallel to the 23-plane passing through the center of the fixture assembly was constrained such that all nodes and element faces contained directly in this plane were not allowed translations parallel to the 1-axis

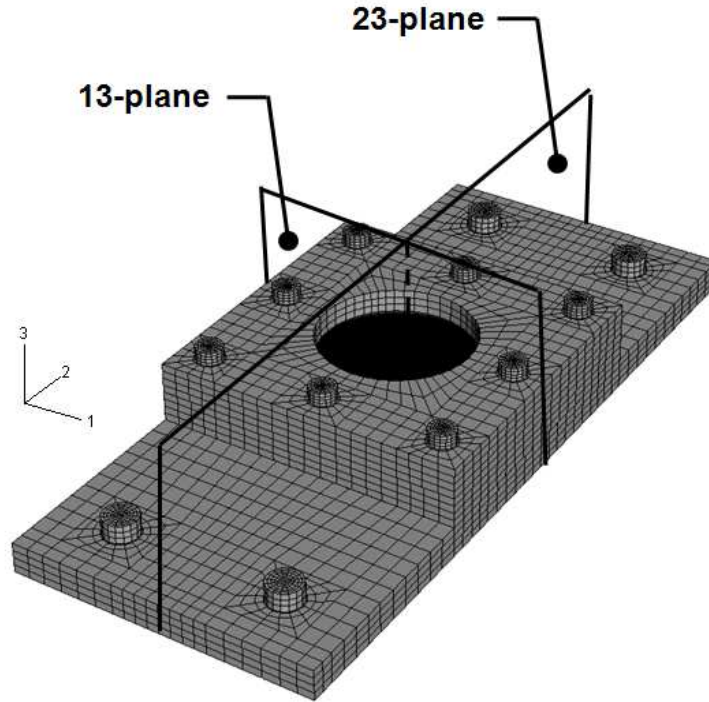


Figure 6.10: Reference planes used in FEM constraints.

direction. This included the bottom, spacer, and top plates of the fixture as well as the specimen plate; nodes or elements attached to the tup and plate fastener screws were not assigned this restriction.

4. The four Dynatup attachment screws were threaded into the Dynatup base. The stud length of these screws were shortened to a length equal to the thickness of the bottom plate of the fixture (1.27-cm). Once threaded and torqued to the required level, it is assumed that the screws could not be pulled out of the Dynatup base. Thus, the bottom surface of each Dynatup screw (that is, the surface contained in the same plane as the Dynatup base-fixture bottom plate interface) was constrained from vertical deflection only.
5. The axes of the four Dynatup attachment screws were constrained from motion in the 1 and 2-directions.
6. The axis of the tup was constrained from motion in the 1 and 2-directions.

7. Recall that the plate fastener screws were threaded into the bottom plate only. The holes in the spacer and top plates were through-holes only. In the FEM, the holes in the bottom plate were made to be the same diameter as the stud diameter of the plate fastener screws; the holes in the other two plates were made slightly larger. Therefore, a small portion of the outside surfaces of the screws along the stud length will coincide with the surfaces inside the holes of the bottom plate throughout the thickness of the plate. To simulate a tight, rigid connection between the fastener screws and the threaded holes of the bottom plate, the nodes attached to the coincident surfaces of the bottom plate and the screws in each hole were constrained to have identical displacements in all three principal directions. This constraint is assumed to model a threaded connection without requiring an actual model of the threads themselves.

6.1.4.2 Contact Interactions. The commercial finite element code ABAQUS has the capability of modeling contact interactions between various components of the model assembly. Contact in the realm of finite element theory is a highly nonlinear analysis and requires special treatment. It is important to note that there are many contact laws that can be applied, but the law used exclusively in this finite element model was that of *rigid-hard contact*. This contact law is the simplest contact law used by ABAQUS. The main feature of this law is that it is essentially an on-off law where the pressure applied from one object to another is zero when the objects are not in contact and positive when in contact; the magnitude of pressure is a function of the interpenetration of the two object surfaces in contact. Other more complex contact models incorporate pressure-deflection relations that are material-dependent and usually require empirical data to define the relation. Since empirical data relating pressure and displacement in the tup and Ti-TiB mixtures was not available, the hard contact law was used throughout the FEM (hard contact does not require a pressure-displacement relationship). Some of the more pertinent details associated with ABAQUS' treatment of contact interactions are presented in

Appendix C. The discussion here is limited to describing those locations in the model itself where contact laws were established.

The contact law is defined between the following surfaces (see Figure 6.11:

1. The interface of the bottom and spacer plates of the fixture.
2. The interface of the spacer and top plates of the fixture.
3. The interface of the specimen plate and the fixture bottom plate.
4. The interface of the specimen plate and the fixture top plate.
5. The top surface of the specimen plate and the surface near the tip of the tup.
6. The top surface of the fixture top plate and each surface underneath the head of each plate fastener screw.
7. The top surface of the fixture bottom plate and each surface underneath the head of each Dynatup attachment screw.

6.1.4.3 FEM Loads. In the *plate impact experiments*, the most important load delivered to the plates was the impact load from the tup when the potential energy stored in the crosshead assembly was converted to kinetic energy as the crosshead was released from rest. In the assembly of the FEM, the tup was placed above the specimen plate such that only 0.1-mm of separation existed initially between the tup and the top surface of the plate at the outset. The speed of the crosshead and tup just above the impact site on the specimen plate was measured in each test during the experiments. A *velocity field* was applied to the tup model in the FEM with a magnitude equal to the speed measured during the test. Incidentally, the velocity field has components in only the negative 3-direction (vertical) and thus the measured speed and the magnitude of the velocity field (through the vertical component) are identical. This velocity is applied to all volumes within the tup model and includes all nodes and elements contained in the volumes. This velocity is applied only as an *initial condition* within ABAQUS. The tup maintains this speed until contact is

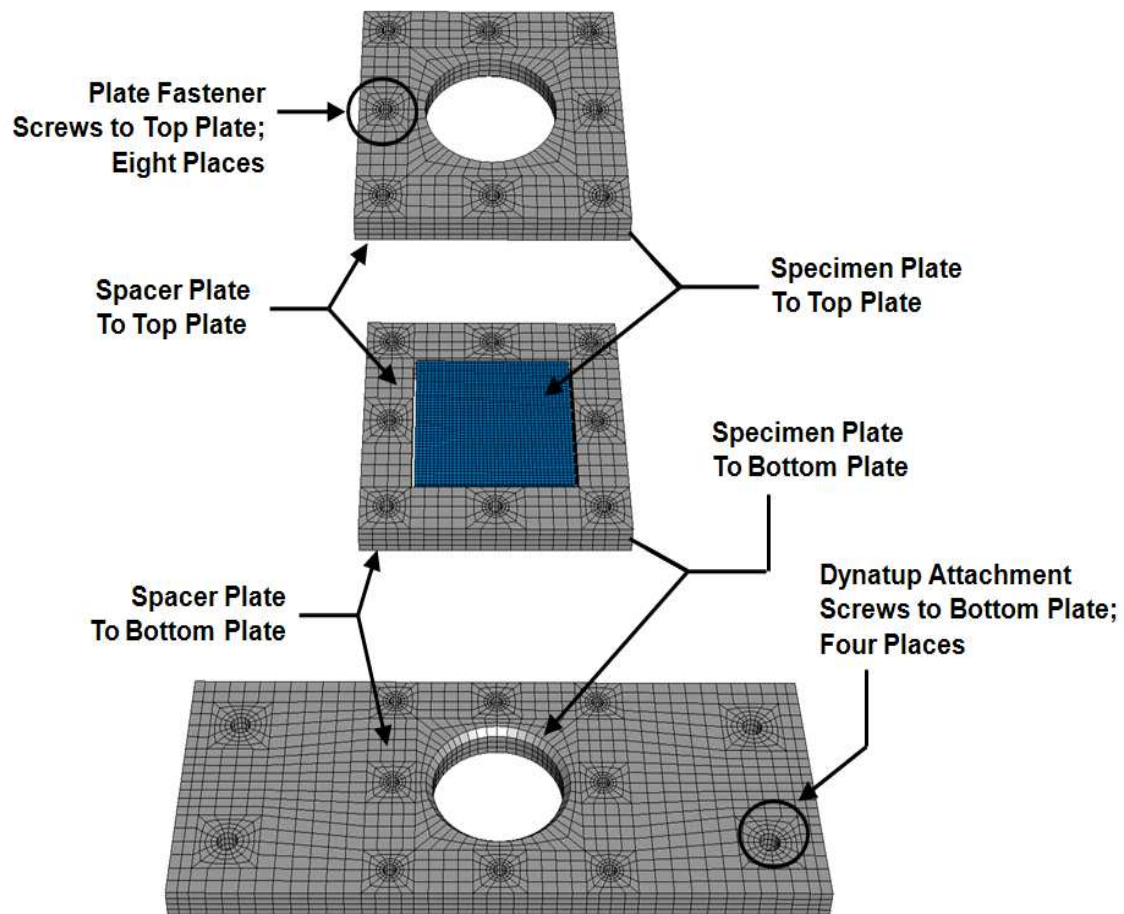


Figure 6.11: Illustration of selected contact areas between the plate fixture, specimen plates, and fastener screws.

established between the tup and the specimen plate. Once this occurs, the dynamics of the system take over and the instantaneous velocity of the tup must be determined based on the solution to the finite element model. The kinetic energy of the crosshead-/tup is maintained because the tup FEM has the same mass as the crosshead/tup assembly in the plate impact tests and the velocity is the same as that from the tests where it was measured just above the impact site. The initial separation between the tup and plate in the FEM was for convenience in tracing the response. In the FEM, the displacements, strain, and stress are zero until contact is initiated. Once contact is initiated, the displacement, strain, and stress are non-zero. Thus, when studying a history of the FEM's solution, it is clear where contact (impact) initiated and this can be correlated directly to the instant impact occurred in the experimental strain histories (recall that the oscilloscope stored strain data in pre-trigger mode just before the impact occurred). *Note that this velocity field is not the same as a gravitational acceleration field and the effects of gravity were not included in the FEM.* It was found that including a gravitational field in the model had a negligible effect on the strain histories. It is not difficult to see how this would be the case given (1) the short period of loading from the tup, (2) the very small deflections that occurred in the plate (that is, the potential energy stored in the system is primarily due to straining in the plate after impact and less a change in vertical height), and (3) the kinetic energy at the instant impact occurs is the same as in the test even though only the velocity field is included in the model.

It was also mentioned that the eight fixture attachment screws and the four Dynatup attachment screws were torqued to loads of 20 N-m and 35 N-m respectively during each test. These torque loads were applied to secure the specimen plate and secure the fixture in the Dynatup apparatus. It was observed that these torque loads did not appear to visually deform the fixture plates or the screws themselves during screw pre-loading or after impact tests occurred. Further the same screws were used in all tests without replacement. A subsequent analysis of the force loading on the screws using analytical and finite element techniques verified the hypothesis

that the deformation in the fixture component plates and screws was negligible during pre-loading of the screws. For this reason, the torque loading on the screws was left out of the finite element model. Analysis further showed that the deformation of the specimen plates during impact induced noticeable lifting and separation of the fixture plates from the specimen leveraging against the fixture. This action produced stresses in the plate fastener screws as they resisted the leveraging and fixture plate separation. With the screws in direct contact with the plates and threading accounted for in the constraints of the system, it was deemed that this was sufficient to emulate the behavior of the fixture plate fastening. The screws in the finite element model, especially the eight fixture attachment screws, merely serve to prevent separation of the fixture component plates as the specimen plate deforms on impact. The constraints on the attachment screws and the contact laws applied serve this purpose without applying an additional torque load to the fasteners.

6.2 Validation of Finite Element Model

6.2.1 Solution of the FEM. The commercial code ABAQUS was used to simulate the tests. Recall in the plate experiments, the data acquisition system was set to collect strain gage histories over a period of 2000 microseconds. It was therefore appropriate to analyze the FEM response over the same time window. Therefore, all simulations of the experiments were performed over 2000 microseconds of the event only. Explicit integration (via the solution module in ABAQUS called “ABAQUS/-Explicit”) was the numerical method used to solve the governing equations to take full advantage of its computational efficiency and its inherent effectiveness at solving dynamic, wave-oriented models (see Appendix C for more in-depth discussion on the explicit integration technique and the solution module ABAQUS/Explicit). The explicit integration technique is one that is *conditionally stable*, meaning that as the numerical integration is performed it is necessary to choose a time step that is sufficiently small to prevent the numerical calculations from becoming unbounded and therefore unrealistic. ABAQUS has internal algorithms for choosing time increments

that are not only small enough to prevent the solutions from becoming unbounded, but also ones that can vary the size of the time step to increase the computational efficiency of the algorithm. A variable time step was therefore chosen in the solution so that both of these ends could be simultaneously met. The output database generated from the solution of the FEM stored 1000 data points over the 2000 microsecond solution window. Thus, displacement, strain, and stress information was stored every two microseconds. Given the 2000 microsecond length of the event and the relatively small oscillations evident in the experimental strain histories, 1000 data points was sufficient to capture the physical dynamics of the impact event. FEMs that collected more data points over the solution window were found to produce insignificant improvements at the expense of larger output databases. As a final note, only solution data associated with the plate specimens were output to the solution database. The plate specimens were of primary interest and no data was collected in the experiments apart from them. This also helped keep the solution output databases to a more manageable size. *Note that damping was not included in the FEM simulations.* Values for damping coefficients were not available for the Ti-TiB system at the time of this study. An informal study of the matter showed that the addition of artificial values of damping into the FEM significantly increased the computational cost of running the simulations with negligible effect on the strain histories. While no viscous or structural damping was directly applied to the model, it is true that ABAQUS/Explicit incorporates bulk viscosity parameters to damp out high frequency ringing oscillations that can affect the solution. *Note that the bulk viscosity used in ABAQUS/Explicit is an effect introduced to assist the numerical implementation of the FEM solution and is not part of a material's constitutive response [3].*

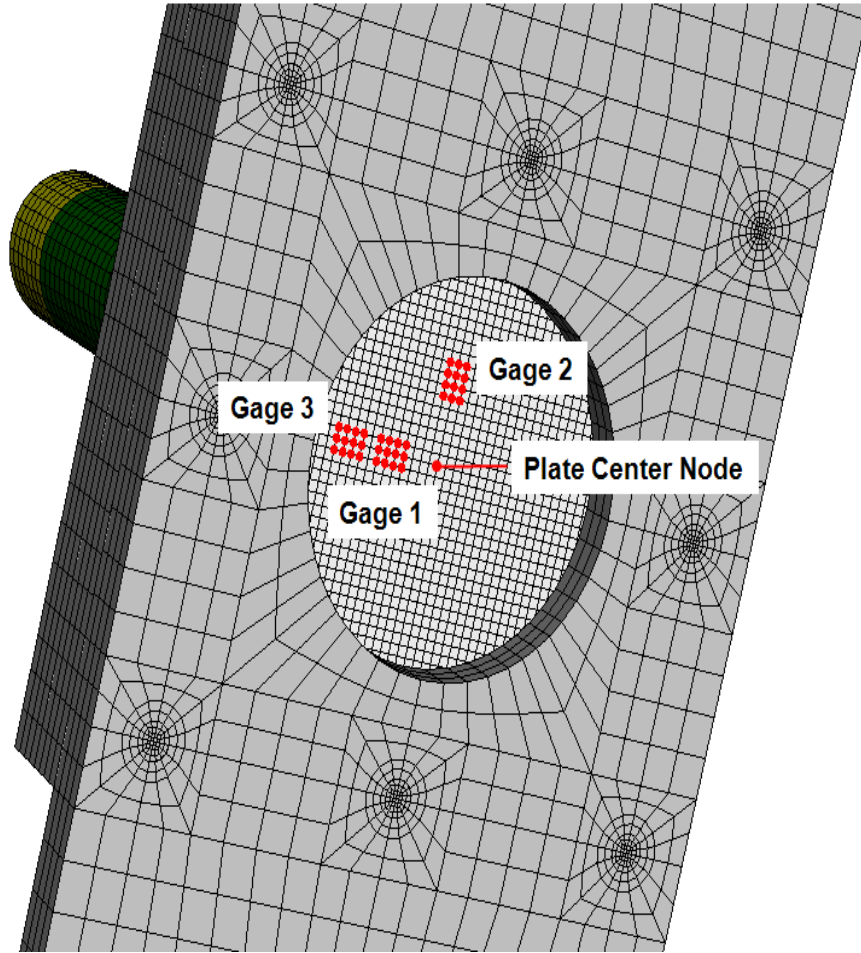


Figure 6.12: Bottom view of experiment FEM showing nodal locations corresponding to nominal location of strain gages 1-3; also node at center of plate on bottom surface of specimen.

Strain data was collected specifically from nodes directly under each strain gage and only strain outputs oriented along the principal direction of the strain gages were used to compare with the experimental strain histories. This is an important point to remember because the state of strain is a complex three-dimensional state at virtually all points in the plate during the impact event and the strain gage measures only the component of strain (directly) along the principal direction of the gage. Figure 6.12 shows the location and nodes used in the FEM strain history plots. Since strain gage 4 was not used in the tests, only strain gages 1-3 are shown in the figure.

6.2.2 *Strain Distribution Under Strain Gages.* Given the size of the elements in the plate specimen mesh, the nominal size and location of each strain gage encompasses 12 distinct nodes (arranged in a 4 node x 3 node array, shown in Figure 6.13). Note that these are the nodes under the *entire* gage, not just the nodes under the nominal location of the strain gage wire grid. This was done to look closely at the variations in the strain history at small distances away from the nominal location of the strain gage wire grid, noting that the *average* strain is measured by the data acquisition system. These variations are important to consider since placement of the gages was performed manually and could deviate very slightly from their nominal locations according to the drawing in Figure 5.10. As an example, consider the plots in Figure 6.14. These plots show the FEM radial strain distribution (assuming the plate is configured as a circular plate) along the axes containing strain gages 1-3 for both the two-phase and homogenized-layers model when the plate is at its maximum center deflection in test number 8 (see Table 6.4). The plots show the approximate nominal locations of each strain gage, the radial location of the fixture circular opening, and the portion of the distribution associated with the edge of the plate built-in to the fixture. It is very clear from Figure 6.14 how significantly the strain distribution can vary across a very small area. In Figure 6.15, the strain histories for each of the 12 nodes in strain gage 1 have been plotted over the entire impact event from test 8. The strain histories for nodes 1-3, 4-6, 7-9, and 10-12 are very close to each other and it is difficult to distinguish between their respective curves (see the nodal arrangement in Figure 6.13). This is further evidence that a significant difference in the strain distribution across the plate can occur over a very small area. While nothing has been said so far regarding the validity of the finite element models, it is acceptable to assume that these variations in strain do in fact occur and should be considered when comparing the experimental strain histories to the FEM simulation strain histories.

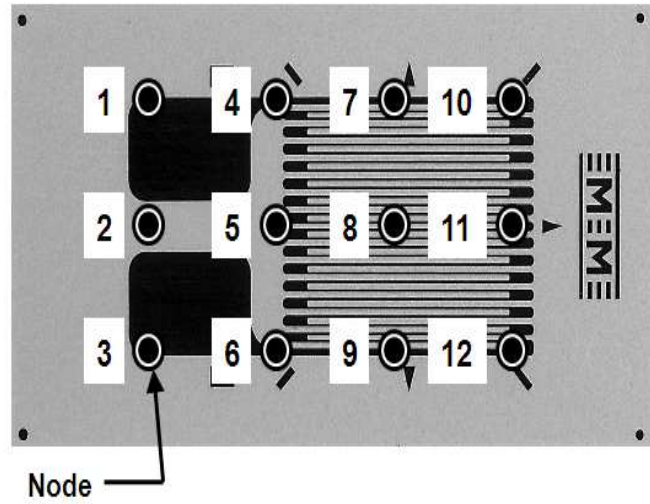


Figure 6.13: Strain gage used in impact tests for collecting strain histories [127], shown with the approximate location of the corresponding 12 nodes as arranged in the FEM analyses.

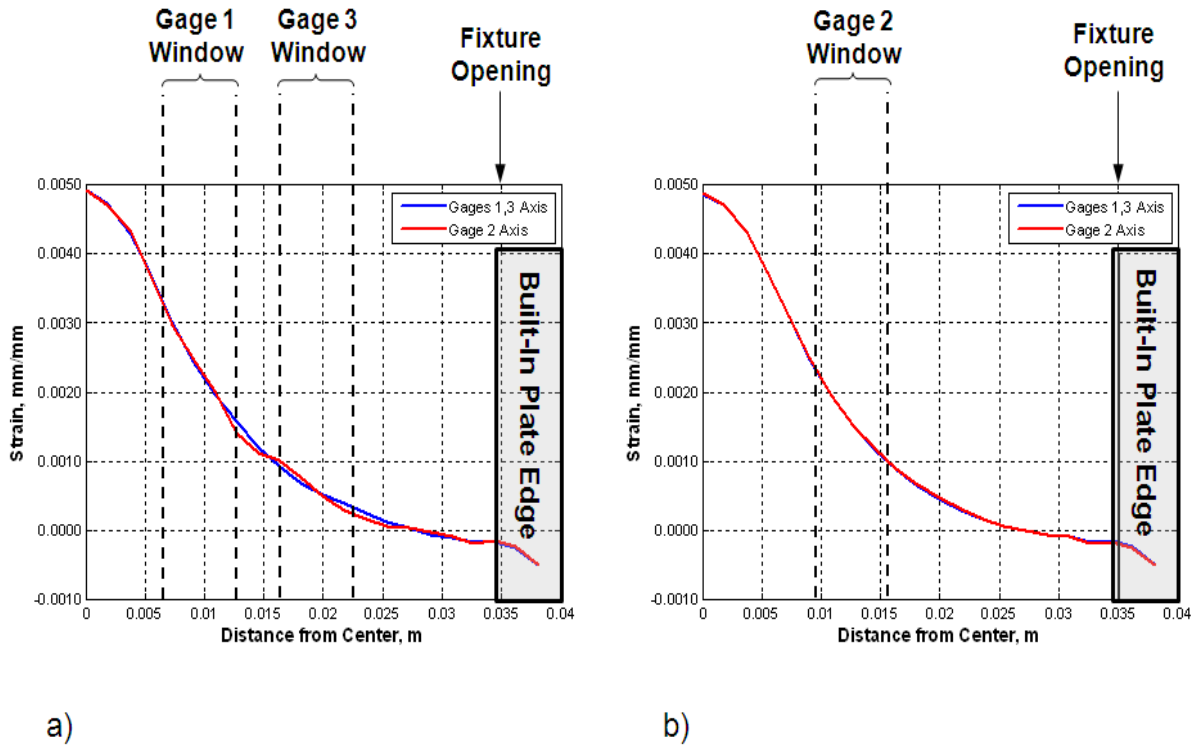


Figure 6.14: Strain variation that occurs along strain gage axes, for (a) two-phase model, (b) homogenized-layers model (Mori-Tanaka needles) in Dynatup test 8 at instant of maximum plate deflection.

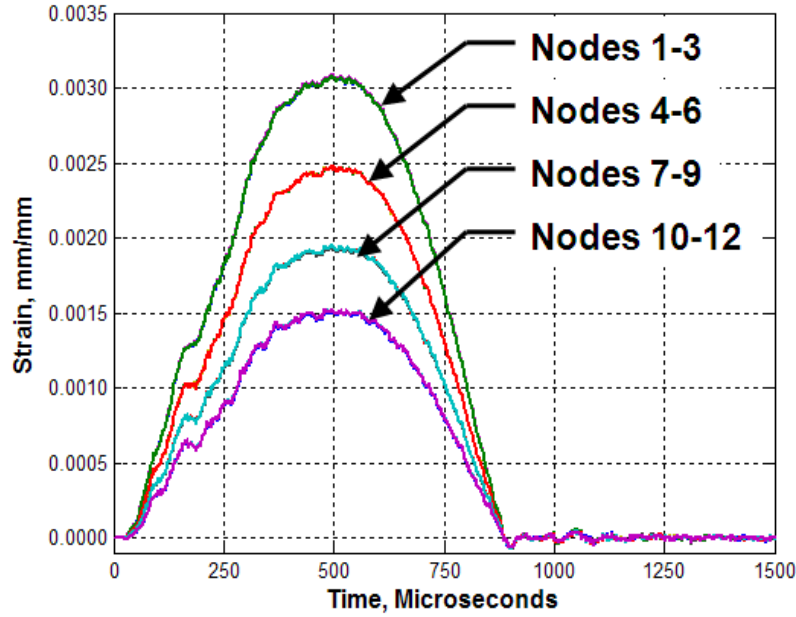


Figure 6.15: Test 8 FEM strain histories across strain gage 1; twelve in all, one plot for each node (Mori-Tanaka Needles FEM model) as shown in Figures 6.12 and 6.13. The histories of higher strain magnitude are closer to the center of the plate.

6.2.3 FEM vs. Experiment—Maximum Strains. The validity of the FEMs with the two-phase and homogenized-layers models of the plate specimens will be assessed. The two-phase material model will be wholly considered. Of the four material models (rule-of-mixtures, self-consistent method, Mori-Tanaka needles, and Mori-Tanaka spheres) used in the homogenized-layers plate models, only the results from the Mori-Tanaka needles (MT-N) material model will be discussed. This is primarily for purposes of brevity. The Mori-Tanaka needles model is conceptually the closest to the actual Ti-TiB composite model, and the material properties from different volume fraction combinations of Ti and TiB using different material models do not differ greatly (see Table 4.5). Therefore, the response of the homogenized-layers models should be roughly the same since the difference between models lies only in elastic material properties defined. Bottom line, if the FEM is valid using

MT-N in the homogenized-layers configuration, it should be valid using the other models as well.

Table 6.4 summarizes the tests as presented in Chapter V. This table will be used for reference purposes in this chapter. The maximum strains over the histories from each gage in each experimental test were first collected. The maximum strain in each test and in each gage corresponds to the moment of maximum transverse deflection at the center of the plate (refer back to Figure 5.25 in Chapter V for illustration and discussion associated with this point). At the point of maximum deflection during each test in the FEM, the strain distribution over the 12 nodes under each gage was also collected. Given the variation of strain across the gage area discussed earlier, it is possible to estimate some bounds within which the experimental strain should lie. These bounds correspond to the maximum and minimum strains from the 12 nodes at the point of maximum deflection in the FEM. Tables 6.5-6.7 detail the bounds from the FEM vs. the measured maximum strains in the histories over each test. Note that the time corresponding to the maximum strain in the experiments may not correspond directly to the time associated with the maximum strains in the FEMs. This point will be addressed later in this section.

Recall that the plate specimens failed in tests 5, 6, and 10. In tests 5 and 6, both of which used 15% TiB–85% Ti monolithic plates, no useful data was collected prior to plate failure. *The FEMs did not include failure criteria due to the lack of concrete experimental data from which to build such a criteria.* Without the criteria included, ABAQUS simply solves the FEM based on the material data input for its constitutive model (namely elastic modulus and Poisson’s ratio) and will predict an elastic response without failure. Thus, the FEM results for tests 5 and 6 cannot be assessed and must be assumed to be invalid given both tests induced failure of the plates. For this reason, no FEM bounds on the strain distributions for these tests will be presented. Test 10, and FGM plate test, is different. In this case, strain history data was collected over a significant portion of the impact event. *It cannot be assumed that the strain at which the plate failed is the maximum strain that would*

Table 6.4: Summary of plate impact tests using the Dynatup apparatus.

Test No.	Description	Crosshead/Tup		Velocity, Actual (m/s)	Impact Energy (J)
		Mass (kg)	Height (m)		
1	100% Ti, 0% TiB Mono	13.06	0.508	3.040	60.35
2	100% Ti, 0% TiB Mono	13.06	0.635	3.476	78.90
3	85% Ti, 15% TiB Mono	13.06	0.508	3.050	60.75
4	85% Ti, 15% TiB Mono	13.06	0.635	3.479	79.04
5	15% Ti, 85% TiB Mono	13.06	0.381	2.585	43.63
6	15% Ti, 85% TiB Mono	13.06	0.508	3.050	60.75
7	7-Layer Ti-TiB FGM	13.06	0.508	3.040	60.35
8	7-Layer Ti-TiB FGM	13.06	0.635	3.412	76.02
9	7-Layer Ti-TiB FGM	13.06	0.762	3.765	92.56
10	7-Layer Ti-TiB FGM	13.06	0.889	4.078	108.6

have occurred had the plate not failed. Since further tests were not conducted at the specific velocity and energy level, it can also not be assumed that the maximum strain that occurred during the test is also the strain that will always induce failure. For these reasons, test 10 will include FEM bounds but the experimental result will not be tested against these bounds.

Inspecting Tables 6.5-6.7, nearly all the experimental maximum strains fall within the bounds for the two-phase material model and the homogenized-layers material model. In all tests, the maximum experimental strains for strain gages 2 and 3 fell within the FEM bounds for both material models. For tests 1 and 7, the maximum experimental strains for strain gage 1 were outside the FEM bounds. In test 1, the maximum strain in the experiment is not close to the FEM bounds (the two-phase and Mori-Tanaka bounds for a 100% Ti plate will be the same since the equations for the Mori-Tanaka needles model yield Ti properties when the volume fraction of TiB is zero). In this instance, there was probably a serious issue with that particular gage since the results for gages 2 and 3 were within the FEM bounds as were all the gages used in test 2, a higher velocity test on the same material plate. In test 7, the maximum experimental strain was very close but just outside the bounds for the two-phase model, but was within the bounds for the Mori-Tanaka needles model.

Table 6.5: Maximum strain from experiments compared to upper and lower bound strains directly from strain gage area in FEM from two material models (two-phase and Mori-Tanaka-Needles); strain gage 1.

Test	Max Strain, Exper.	FEM Strains			
		Two-Phase		MT-Needles	
		Lower Bd.	Upper Bd.	Lower Bd.	Upper Bd.
1	0.001184	0.001678	0.003639	0.001678	0.003639
2	0.002602	0.001886	0.004067	0.001886	0.004067
3	0.001712	0.001632	0.002842	0.001456	0.003121
4	0.001764	0.001753	0.003141	0.001581	0.003427
5	Failed				
6	Failed				
7	0.001460	0.001467	0.002804	0.001419	0.002858
8	0.001783	0.001566	0.003032	0.001520	0.003086
9	0.001889	0.001685	0.003247	0.001654	0.003316
10	Failed	0.001844	0.003534	0.001802	0.003607

Table 6.6: Maximum strain from experiments compared to upper and lower bound strains directly from strain gage area in FEM from two material models (two-phase and Mori-Tanaka-Needles); strain gage 2.

Test	Max Strain, Exper.	FEM Strains			
		Two-Phase		MT-Needles	
		Lower Bd.	Upper Bd.	Lower Bd.	Upper Bd.
1	0.001173	0.0009628	0.002220	0.0009628	0.002220
2	0.001161	0.001045	0.002468	0.001045	0.002468
3	0.001603	0.0009078	0.002383	0.0008343	0.001906
4	0.001469	0.0009581	0.002609	0.0008930	0.002098
5	Failed				
6	Failed				
7	0.001391	0.0009047	0.001888	0.0008588	0.001829
8	0.001468	0.0009609	0.002029	0.0009141	0.001955
9	0.001720	0.001043	0.002176	0.0009999	0.002120
10	Failed	0.001142	0.002382	0.001086	0.002310

Table 6.7: Maximum strain from experiments compared to upper and lower bound strains directly from strain gage area in FEM from two material models (two-phase and Mori-Tanaka-Needles); strain gage 3.

Test	Max Strain, Exper.	FEM Strains			
		Two-Phase		MT-Needles	
		Lower Bd.	Upper Bd.	Lower Bd.	Upper Bd.
1	0.0005157	0.0003167	0.0009773	0.0003167	0.0009773
2	0.0009269	0.0003078	0.001078	0.0003078	0.001078
3	0.0008058	0.0003429	0.001085	0.0002790	0.0008473
4	0.0007834	0.0003475	0.001137	0.0002894	0.0009026
5	Failed				
6	Failed				
7	0.0006638	0.0004116	0.0009245	0.0003262	0.0008583
8	0.0007573	0.0004255	0.0009705	0.0003377	0.0009206
9	0.0007016	0.0004562	0.001053	0.0003723	0.001002
10	Failed	0.0004858	0.001145	0.0004108	0.001088

Strain gage 1 in test 7 can, for all intents and purposes, be considered within the FEM bounds for the maximum strain.

While the maximum experimental strains for strain gage 2 fell within the FEM bounds for both material models, one might note an inconsistency in the results for this gage between tests 3 and 4. In these tests, the maximum strain measured for gage 2 actually decreased from test 3 to 4 despite the fact that the velocity and energy in the plate impact actually increased. This is further evidence that the variation in strain over the small gage area needs to be considered. The measured strains fell within the bounds, but should not have decreased under ideal conditions. Further inspection of Tables 6.5- 6.7 show that a similar response was found in strain gage 2 between tests 1 and 2 and strain gage 3 between tests 8 and 9, although the decrease in strain was not as significant as in strain gage 2 between tests 3 and 4. *To reiterate, this is much more likely a consequence of strain gage placement slightly off the nominal location than a defect in the data acquisition unit or a large deviation in the plates' material properties.* Another potential for discrepancy between the FEM and the experiment is that the crosshead on the Dynatup was found to have some minor play

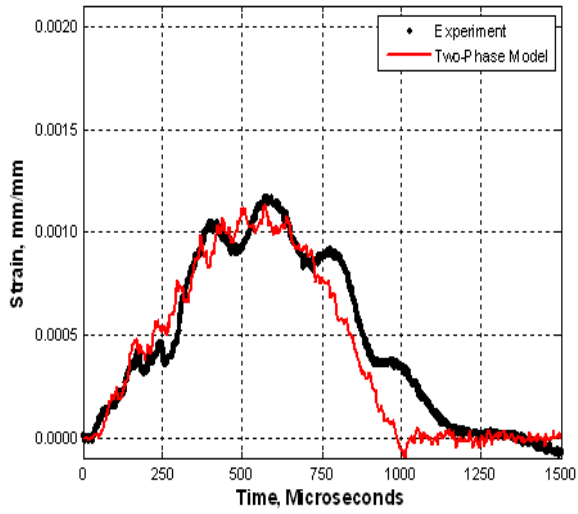
in the assembly due to mechanical fittings that have loosened with time. Thus, it is possible that the impact site for each experiment could vary slightly so as to not have a perfect central impact each test. This can account for some of the variance in experimental data compared to the FEM, which has a perfect central impact due to its ideal conditions. *Ultimately, these findings are extremely useful as a first step in validating the FEMs for the two-phase and homogenized-layers material models of the specimen plates.*

6.2.4 FEM vs. Experiment—Strain Histories. The next step in validating the FEM models is to look more closely at the individual strain histories themselves. Figures 6.16-6.23 show the FEM strain histories for the two-phase and homogenized-layers (MT-N) models compared to their experimental counterparts for strain gages 2 and 3. Strain gages 2 and 3 were chosen for plotting purposes for brevity only; the results from gages 1 and 2 are very close in magnitude (see the experimental plots in Chapter V, Figures 5.17-5.24) and gages 2 and 3 lie on perpendicular axes and provide good comparisons. Again, no plots or comparisons are made for tests 5 and 6.

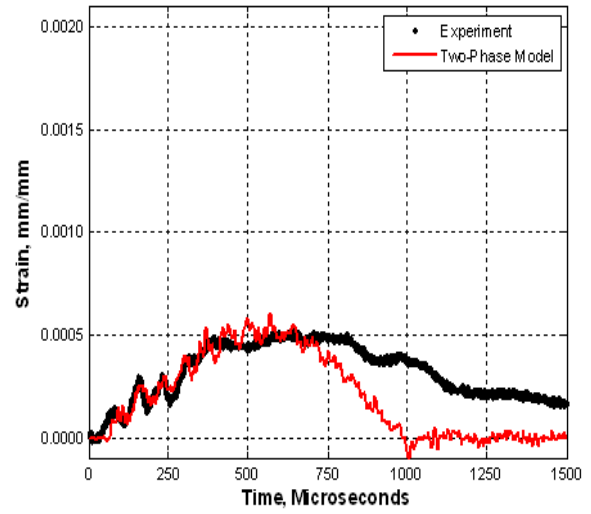
In the last section, we showed that for the most part, the maximum experimental strains were within bounds given by the FEM for the predicted strain distribution over the area nominally covered by the entire strain gage. In reality, the measured strains occur only over the area covered by the electrical wire grid on each gage, which covers only about half of the actual gage (see Figure 6.13). It is therefore not unreasonable to select a subset of the twelve nodes, namely a 2 node x 3 node subset of the 4 node x 3 node array, to use as the nodes most closely associated with the strain gage measurement of strain. The experimental strain history from an individual gage was compared to the strain histories from the corresponding 12 nodes in the FEM (such as plotted in the example from test 8 in Figure 6.15). *The 2 x 3 nodal array whose histories were most closely associated with the actual strain histories from the experiment were chosen from the 12 node array.* The strain histories from these six

nodes were averaged over time to produce a single strain history (we will term this averaged strain history as the “comparable strain history”, meaning it is comparable to the measured strain history over the experimental impact event). The resultant, or comparable, strain histories from this averaging are shown in Figures 6.16-6.23 for strain gages 2 and 3 for both the two-phase and MT-N finite element models. In nearly all cases, the 2 x 3 node array corresponded to the nodes directly over the nominal gage *grid* location (as visible in Figure 6.13). In a few cases, a 1 x 3 array of nodes almost nearly followed the experimental history, and in those few cases a 1 x 3 array of nodes were averaged to obtain the strain history. The averaging of nodal strain histories accounts for the fact that the gage grid measures the average strain under the grid, not merely the strain at a single point. Further, the choice of using a 1 x 3 versus a 2 x 3 array of nodes for averaging accounts for small variability in the gage placement, discussed at length earlier.

Inspecting Figures 6.16-6.23, it can be seen that there are many strong correlations between the FEMs and the test data, and there are also areas of discrepancy that need to be addressed. In the pure titanium plate tests 1 and 2, only the two-phase FEM strain history is plotted, but note that the MT-N material model and the two-phase model are identical with identical material properties for a monolithic mixture where one constituent has a volume fraction of zero. The FEMs in general can predict the maximum values of the strains for both gages at both locations very effectively. In most cases, both the two-phase model and the homogenized-layer models are within a reasonable error of the test results. In some cases, the two-phase and homogenized-layer models are nearly identical in response, and in other cases maximum strain predicted is slightly greater or less than the counterpart. The two-phase model is generated by randomly distributing cells of Ti and TiB, so it is not unexpected that this can and will occur. In fact, by the nature of the computer script used to generate the random distribution of Ti and TiB elements, it is entirely possible that one combination of the constituents would involve concentrating each material

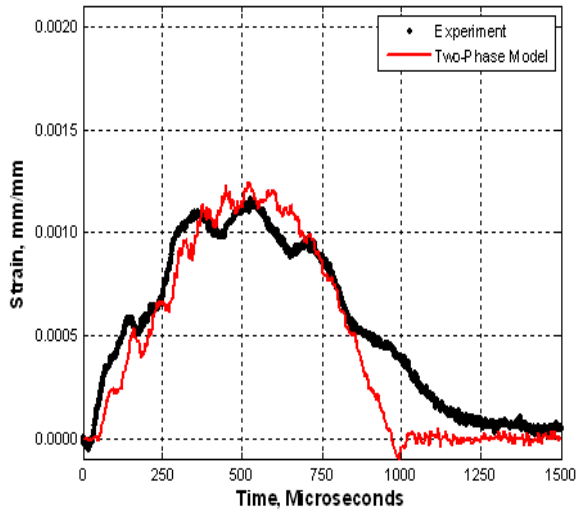


a)

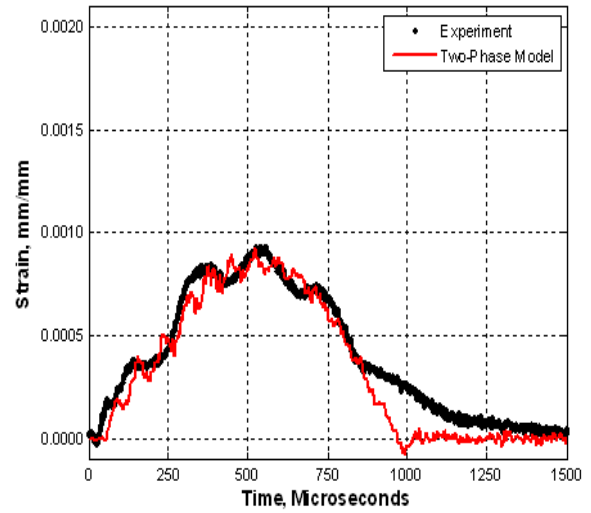


b)

Figure 6.16: Test 1 (monolithic) experimental strain histories & FEM comparison using two-phase plate model: a) strain gage 2, b) strain gage 3.

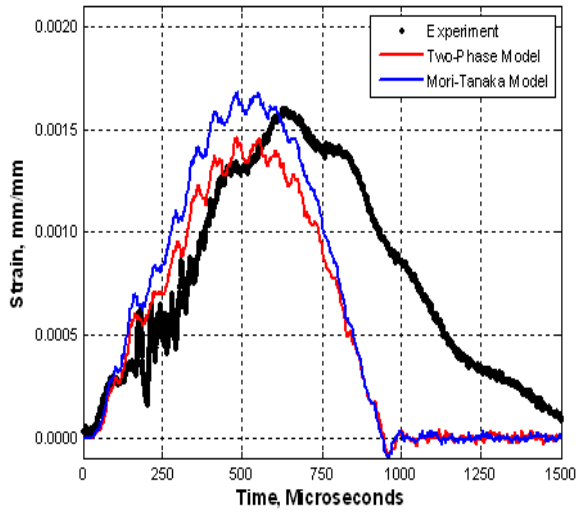


a)

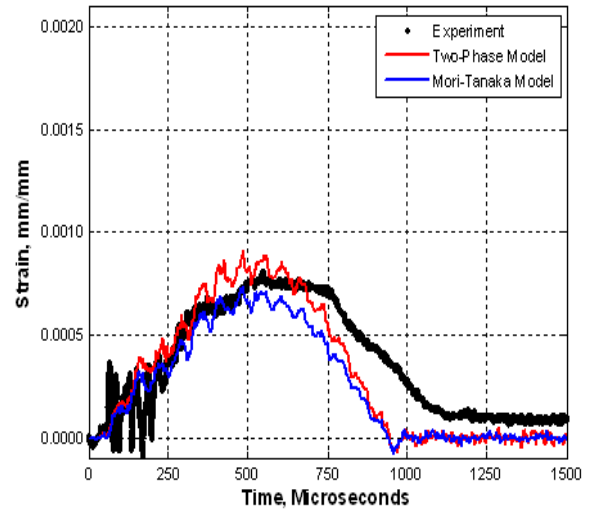


b)

Figure 6.17: Test 2 (monolithic) experimental strain histories & FEM comparison using two-phase plate models: a) strain gage 2, b) strain gage 3.

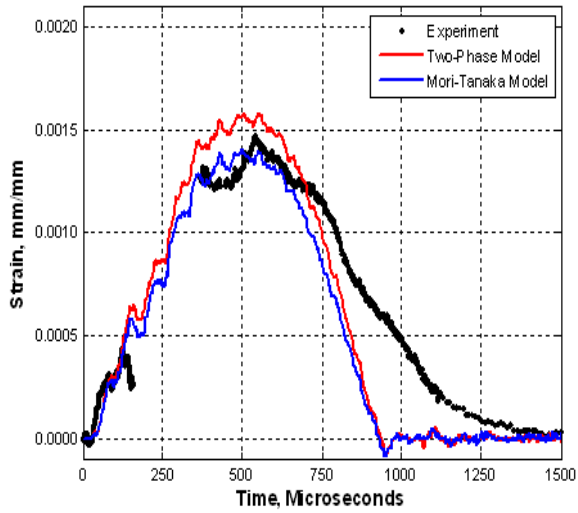


a)

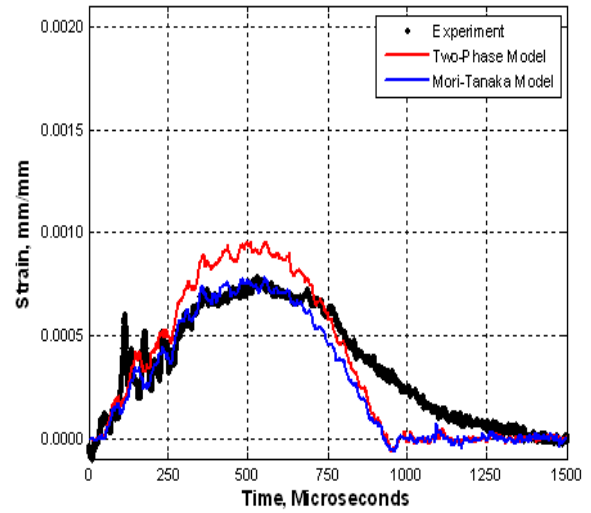


b)

Figure 6.18: Test 3 (monolithic) experimental strain histories & FEM comparison using two-phase and Mori-Tanaka Needles plate models: a) strain gage 2, b) strain gage 3.

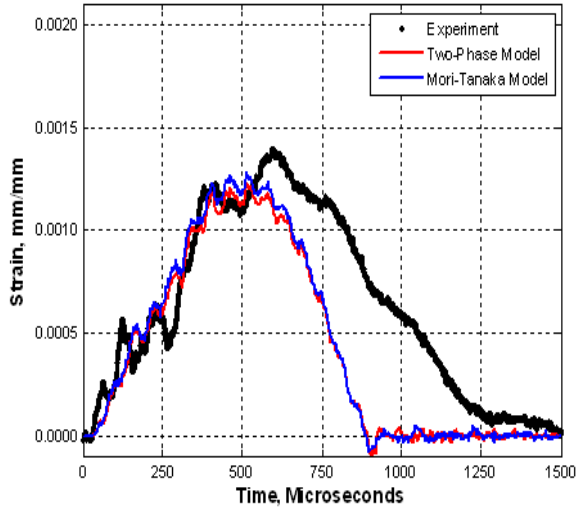


a)

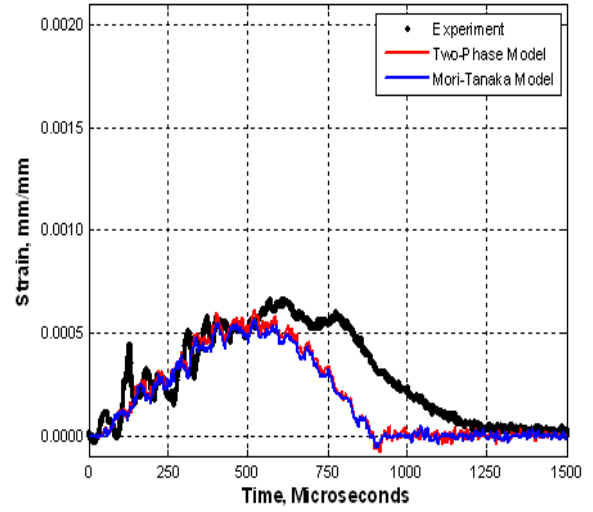


b)

Figure 6.19: Test 4 (monolithic) experimental strain histories & FEM comparison using two-phase and Mori-Tanaka Needles plate models: a) strain gage 2, b) strain gage 3.

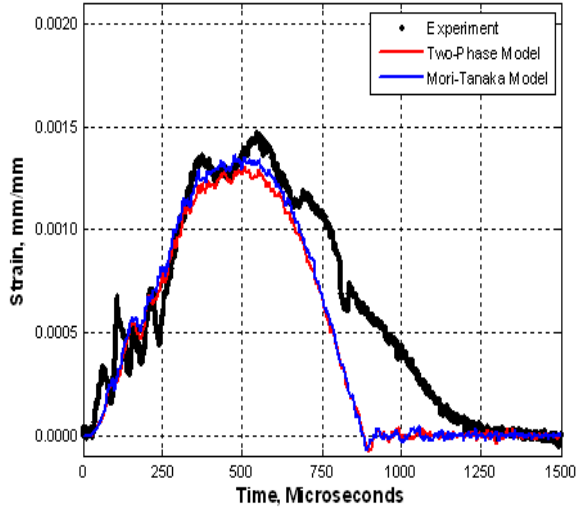


a)

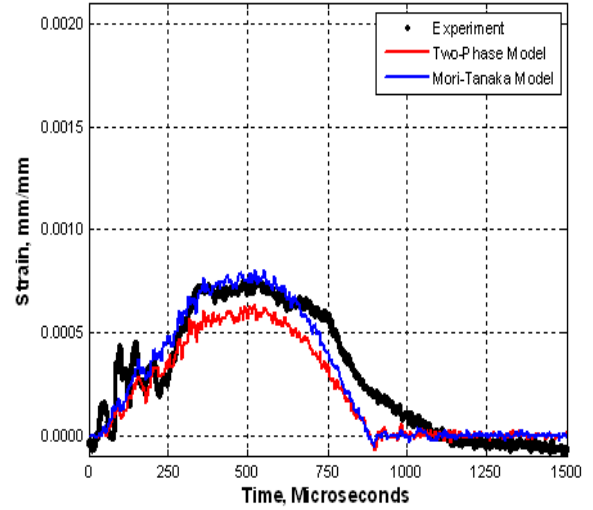


b)

Figure 6.20: Test 7 (FGM) experimental strain histories & FEM comparison using two-phase and Mori-Tanaka Needles plate models: a) strain gage 2, b) strain gage 3.

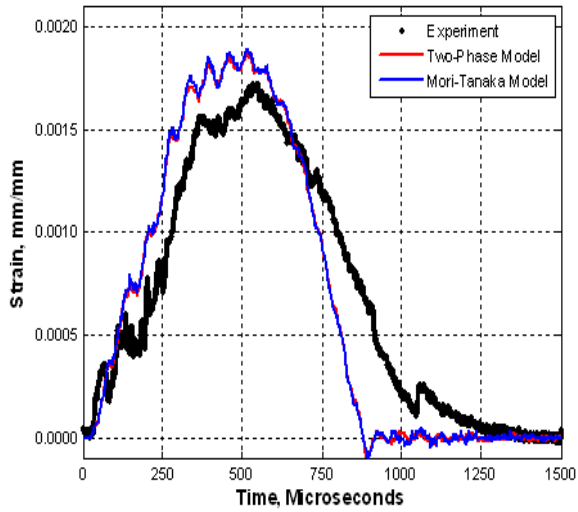


a)

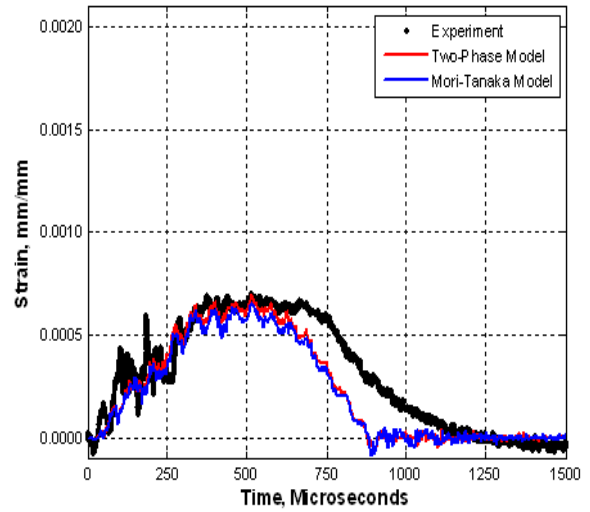


b)

Figure 6.21: Test 8 (FGM) experimental strain histories & FEM comparison using two-phase and Mori-Tanaka Needles plate models: a) strain gage 2, b) strain gage 3.

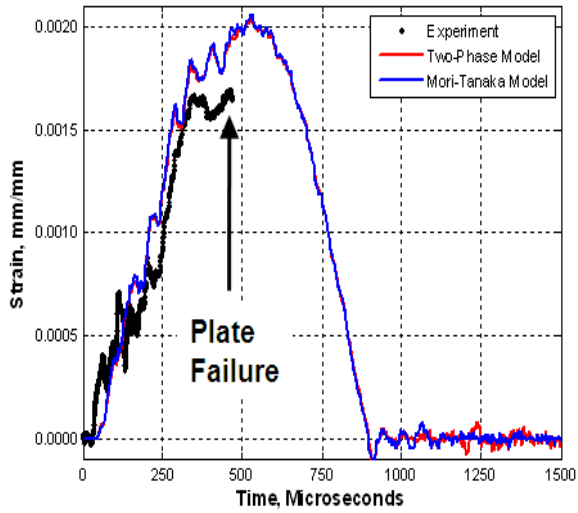


a)

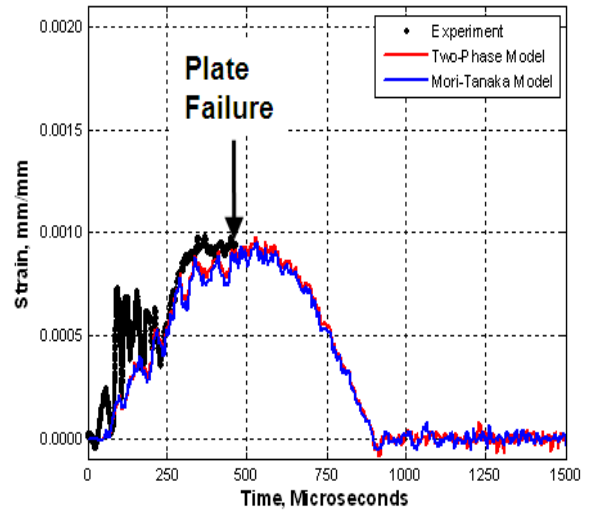


b)

Figure 6.22: Test 9 (FGM) experimental strain histories & FEM comparison using two-phase and Mori-Tanaka Needles plate models: a) strain gage 2, b) strain gage 3.



a)



b)

Figure 6.23: Test 10 (FGM) experimental strain histories & FEM comparison using two-phase and Mori-Tanaka Needles plate models: a) strain gage 2, b) strain gage 3.

in large masses opposite one another. The meshes were, however, inspected prior to solution to eliminate this possibility.

The FEMs predict loading slopes (that is, strain-rates) comparable to the experimental data for the gages up to the point of maximum strain. The time predicted for maximum deflection in the plate, and thus maximum strain in the histories, is correlated well on some tests and not as well on others. The error, however, seems to be reasonably well-within limits of what can be expected between an experiment and a simulation under ideal conditions. Some of the test data show highly distinct and sharp oscillations very early in the response that disappear as the deflections become larger through the course of the impact event. These oscillations are not reflected in the FEM, and are undoubtedly related to noise in the data or electrical shorting of the strain gages (fluttering of the single-stranded jumper wires during impact loading can account for this). It is immediately evident (especially for the plots of strain gage 2), that the slopes of the histories during the unloading portions of the curves do not correlate well. In fact, it appears that the rate the plate returns from maximum strain to “zero strain is significantly less than that of the FEM. It is not likely that this behavior is associated with the monolithic or FGM composites themselves—indicating an invalid material model or FEM. One possibility is that it is an effect of the response of the adhesive used for the strain gages unloading in a different manner than when it loads in tension to maximum strain. This would additionally explain why gages from the same specimen indicate larger or smaller windows for the total time over which the impact event occurs. A thick adhesive bond between the strain gage and plate could substantially magnify these effects.

The FEM clearly shows several vibration modes being excited upon impact from the tup. Some of these modes are not clearly discernable in the test results. On the other hand, it appears that there are some lower frequency modes being excited in the test data that are not reflected in the FEM, especially near the peaks of the response (especially gage 2). This could be attributed to many possibilities, but most likely a better material model or fixture model in the FEM would remedy portions of

the histories. Addressing the former, Hill and Lin [55] reported material properties while testing Ti-TiB FGM specimens that were significantly lower than the properties predicted by Mori-Tanaka estimates or other similar models (see Table 4.5). This is partially due to the difficulty in controlling the exact volume fractions of Ti to TiB given that a chemical reaction is required to produce the TiB *in-situ*, but may also be related to the sintering process itself. Additionally, the strain gage adhesive may inherently damp out some of the oscillations that occur in the plate and are thus not registered in the strain histories from the tests. The histories from the finite element models are obtained from strain recorded directly from nodes in the vicinity of the strain gage grids on the surface of the plate. Note again that damping was not included in the FEM simulations presented here.

The oscillations in the strain histories in both the experiments and the finite element models are potentially associated with wave propagation effects occurring in the plate as it is loaded by the tup during impact. In an infinite medium, dilatational waves (associated with volumetric change without change in shape) propagate at speed c while distortional or shear waves (associated with a change in shape without change in volume) propagate at speed c_s [50]:

$$c = \sqrt{\frac{E(1-\nu)}{\rho(1+\nu)(1-2\nu)}} \quad (6.1)$$

$$c_s = \sqrt{\frac{G}{\rho}} \quad (6.2)$$

The dilatational and distortional wave speeds for titanium are 6127.1 and 3016.8 m/s, respectively, and the dilatational and distortional wave speeds for titanium boride are 9150.4 and 5290.3 m/s, respectively, given the material properties for each in Tables 4.1 and 4.2. Given this information, the initial dilatational wavefront induced from the impact load from the tup will travel 1.27 cm through the plate thickness unimpeded in approximately two microseconds in the pure titanium plate. Surface waves, a third type of wave different than dilatational or distortional waves, travel along the surface

of a body and propagate at only a small fraction less than distortional waves and their wave speed is often approximated by that of distortional waves [50]. This is an important fact given that the strain gages and FEM data were taken directly from the surface of the plates. On the same titanium plate, a surface wavefront generated by impact from the tup at the center of the plate would travel 3.81 cm to the nearest boundary before reflecting at the boundary (the plates are 7.62 cm x 7.62 cm); the reflected wavefront would travel an additional 3.81 cm before returning to the center of the plate. If the surface wave travels at the same speed as a distortional wave, this journey would require approximately 25 microseconds. The period of the small oscillations in the FEM strain histories appear to be on the order of approximately 50 microseconds, or twice that of the period required for a surface wave to propagate to the boundary of a specimen plate and return. In the experimental strain histories, the few oscillations observed occur over an even longer period. Considering the fact that wave speeds for TiB-rich regions will be much faster than this, the estimates for wave propagation effects provided here tend to be a more conservative comparison. Thus, the high-frequency oscillations prevalent in the FEM and observed to a smaller degree in the experiments are more likely associated with excitation of specific structural modes than actual measured wave propagation effects.

The contact interactions applied throughout the finite element model did not incorporate the effects of friction; that is, all surfaces in contact with each other exhibit frictionless tangential behavior. Friction between the specimen plate and the fixture can potentially affect the measured strain profile in the experiments. The effects of friction can be seen in Figure 6.24. Here, the strain histories for two gage locations in the Mori-Tanaka Needles FEM for impact test 9 (FGM impact test) are plotted using sliding friction coefficients ranging from 0.00-1.00 for the locations of strain gages 2 and 3 (the responses of gages 1 and 2 are virtually the same). Recall that, in general, static and sliding friction forces are proportional to normal loads applied on a body against a surface [10]. The proportionality constant is the coefficient of friction which is dependent on the materials in contact with each other

and generally ranges from 0.00-1.00 for various materials. Also note that typically the coefficients of static friction and the coefficients of sliding friction are different for most materials; usually the coefficient of sliding friction is less than that of static friction [10]. Three effects of increasing coefficient of friction can be noticed from Figure 6.24. First, incorporating a friction coefficient damps out the high-frequency oscillations prevalent in the frictionless interaction model. Secondly, the maximum magnitude of strain decreases as the coefficient of friction increases. Lastly, especially in the response of strain gage 3, the histories tend to be less symmetric, meaning that the plate remains at or near the maximum magnitude of strain before dropping off very sharply as the tup unloads the plate. This is likely a leveraging effect near the boundary that is causing a stick-slip behavior that is not as pronounced for a frictionless model. It would seem that the stick-slip behavior with friction effects would tend to cause the length of the strain histories (where strains are significantly greater than zero) to increase, but this does not occur. The strains tend to return to zero for this test around 900 microseconds regardless of the friction coefficient. The frictionless FEMs tend to follow the experimental strain histories more closely and thus the frictionless models will be used throughout this work.

As another comparison to the maximum strains in the experiment, the maximum comparable strains in the FEM histories (as plotted) were determined and are tabulated based on test and gage number in Tables 6.8-6.10. With the exception of test 1 and gage 1 (already identified as one that is producing suspicious results), the comparable FEM maximum strains are within roughly 15% error of the experimental maximum strains. This is a key finding that gives further credence to the validity of both the two-phase material model and the homogenized-layers material model.

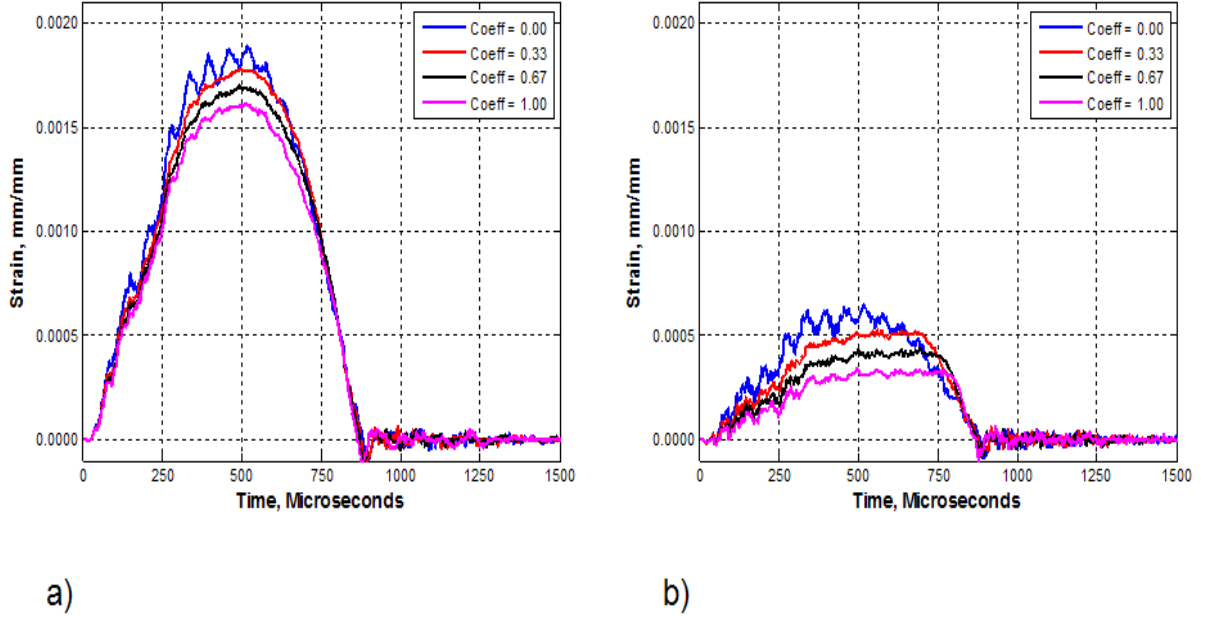


Figure 6.24: Test 9 (FGM) finite element strain histories using the Mori-Tanaka Needles plate model at the locations of: a) strain gage 2, b) strain gage 3. The histories are plotted for coefficients of sliding friction ranging from 0.00-1.00.

Table 6.8: Maximum strain comparison between experiment and FEM results, strain gage 1.

Test	Max Strain, Exper.	Max Comparable Strains		Max % Diff.
		Two-Phase FEM	MT-N FEM	
1	0.001184	0.001943	0.001943	64.1
2	0.002602	0.002845	0.002845	9.33
3	0.001712	0.001843	0.001684	7.70
4	0.001764	0.001998	0.001833	13.2
5	Failed			
6	Failed			
7	0.001460	0.001647	0.001621	12.8
8	0.001783	0.001763	0.001737	-2.56
9	0.001889	0.001894	0.001885	0.25
10	Failed	0.002071	0.002057	

Table 6.9: Maximum strain comparison between experiment and FEM results, strain gage 2.

Test	Max Strain, Exper.	Max Comparable Strains		Max % Diff.
		Two-Phase FEM	MT-N FEM	
1	0.001173	0.001131	0.001131	-3.54
2	0.001161	0.001239	0.001239	6.69
3	0.001603	0.001461	0.001679	-8.86
4	0.001469	0.001581	0.001401	7.60
5	Failed			
6	Failed			
7	0.001391	0.001227	0.001281	-11.8
8	0.001468	0.001307	0.001358	-11.0
9	0.001720	0.001867	0.001890	9.86
10	Failed	0.002045	0.002061	

Table 6.10: Maximum strain comparison between experiment and FEM results, strain gage 3.

Test	Max Strain, Exper.	Max Comparable Strains		Max % Diff.
		Two-Phase FEM	MT-N FEM	
1	0.0005157	0.0006026	0.0006026	16.9
2	0.0009269	0.0009241	0.0009241	-0.31
3	0.0008058	0.0009139	0.0007308	13.4
4	0.0007834	0.0009579	0.0007774	22.3
5	Failed			
6	Failed			
7	0.0006638	0.0006103	0.0005626	-15.2
8	0.0007573	0.0006394	0.0008032	-15.6
9	0.0007016	0.0006914	0.0006498	-7.39
10	Failed	0.0009787	0.0009522	

6.3 Closing Remarks

The key finding of this chapter is that the two-phase and homogenized-layers (via MT-N material model) FEMs produce strain histories very close to the strain histories from the experiments. This is an invaluable contribution the field of functionally graded material research; few have generated results comparable to any experimental data and no literature is currently available correlating impact tests to analytical or finite element analysis. The experiments traced strain histories at three locations on each plate along perpendicular radial axes on the circular plate configuration. The strong correlations given the idealized FEM and an experiment subject to some variability suggests that the FEMs as designed are indeed adequate for studying the behavior of Ti-TiB monolithic and functionally graded plates. Since the FEMs for the FGM plates matched very well to the experiment, these FEMs will be assumed to be valid, and the two-phase and homogenized-layers models will be assumed to be sufficient for studying the global behavior of Ti-TiB FGMs under low-velocity and low-to medium-energy impact loading conditions.

The construction and validation of the finite element models as discussed in this chapter meet the second objective of this work (listed in Chapter I): *construct a finite element simulation of the impact experiment that is sufficiently sophisticated to capture the dynamic effects of an impact load that is at the same time easily replicated by scientists and engineers in practice.* In the next chapter, an analytical treatment of the FGM plate impact problem will be presented that can be used to study the impacts conducted in the Dynatup experiments. This analytical treatment will be used extensively in a parameter estimation technique (presented in Chapter VIII) designed to enhance the material property predictions in the FGMs in order to further refine the finite element models discussed in this and the previous chapter.

VII. Analytical Treatment of the FGM Plate Impacts

This chapter will explore an analytical treatment of the FGM impact experiments. Thus far, a series of impact experiments were conducted to collect strain histories from monolithic and graded plates over the duration of the impact event. The strain histories were compared to the analogous histories from a finite element model of the experiment with different material models considered. The experiments and the finite element models showed a strong degree of correlation, although the simulations could potentially be improved with more accurate material properties for Ti-TiB mixtures. The material properties of the Ti-TiB mixtures were devised from published values for Ti and TiB and using common analytical models to average the composite properties based on volume fractions of one constituent to another constituent. In Chapter VIII, a parameter estimation technique will be devised that will allow more accurate material properties for Ti-TiB mixtures to be determined. These properties will attempt to minimize the error between the finite element model and analytical predictions of the plate based on experimental results. The result is a finite element model that is optimized to emulate the actual impact experiments and will allow the physics of the impacts to the FGM plates to be wholly captured. Before the parameter estimation technique is presented, it is necessary to discuss the analytical model used to study the experiments since this analytical model will play a crucial role in the formulation of the parameter estimation technique. The analytical technique presented expands on the concepts discussed in the plate theory sections of Chapter III and applies the concepts to the actual FGM experiments. This analytical model will be shown to be applicable to the plate impact tests and will be validated with results from both the experimental strain histories and the finite element models.

7.1 *Dynamic Considerations From Impact Loading*

While the detailed physics of the impact events have not been discussed at length, a few observations from the experiments and the associated finite element models can be made to assist in choosing a candidate analytical formulation to at-

tempt to describe the impact events. It is known and has been discussed that the tup makes a single impact to the plate specimens. The tup is pulled by gravity toward the plate specimen, the tup impacts the plate at the center of the top surface, and the tup loads the plate through its momentum until the tup is stopped when sufficient potential energy is stored in the plate (potential energy due to strain energy) to bleed off the kinetic energy of the tup and crosshead. At the point of maximum potential energy in the plate, the tup has exerted its maximum force on the plate specimen at the center of the plate. This portion of the impact event constitutes the *loading* portion of the impact event. After this point, the potential energy stored in the plate (which can be thought of as a compressed spring acting on a mass) begins to act on the tup/crosshead causing both the plate and tup/crosshead to rebound. As this rebounding effect occurs, the force between the tup and the plate begins to diminish. This is the *unloading* portion of the impact event. The loading and unloading of the plate can be seen in the strain histories in Chapter V where each strain gage shows a monotonic increase in strain up to a maximum value followed by a decrease in strain to some value nearly zero.

In Table 5.5, it was shown that for all the tests the elapsed time from the moment the tup came into contact with the plate specimen to the moment of maximum strain in the specimens was approximately 500 microseconds for any of the monolithic or functionally graded specimens. For the sake of argument in the remainder of this section we will simply say that the loading occurred over 500 microseconds. The unloading of the tup to the plate after maximum load is interesting as well, but at this point it is unclear when the tup is no longer in contact with the plate. It is impossible to tell if or how long the tup is exerting any type of force in the unloading portion of the event from the strain histories; for now the 500 microseconds will represent the entire period of loading by the tup. The unloading of the plate will be discussed at length in Chapter IX, but for now it is not necessary to know this dynamic.

In both the experimental and FEM strain histories, only small oscillations attributable to plate vibrations and waves were observed during the loading and unloading portions of the strain histories (recall most of the large oscillations were attributed to electrical disturbances). Further, after the unloading of the plate was completed, almost no free vibrations of the plate were traced in any of the strain histories. These observations would seem to indicate that the time-dependent motion of the plate is more or less secondary to the overall solution. *If this is the case, then assumptions associated with quasi-static analyses can be used.* There is precedent for modeling impacts analytically in this manner if time-dependent motions of the plate or structure are secondary to the overall solution, and it has been shown that such assumptions match experimental data (see [48], [142], [51]). However, *the key requirement to modeling impact under quasi-static conditions is that the period of impact loading must be much larger than the period of the first natural mode of the structure* [48], [142]. This requirement means that loading is sufficiently slow that it will not appreciably excite the first natural mode of the system or any higher modes in the system. Further, while it is recognized that there are indeed waves and vibrations propagating through the structure over increments in time during the load history, the magnitude of these vibrations is small compared to the global deformation of the structure. Finally, any localized wave or dynamic motions have been provided an ample amount of time to interact with the surrounding structure such that the waves have coalesced into global structural motions. Whether or not the actual loading from the tup occurs over a much larger period of time than the first mode of the plate in the plate fixture must be demonstrated in the case of the impact experiments before proceeding.

The validated finite element models discussed in the previous chapter were used in a modal analysis in ABAQUS to determine the first modal frequency of (a) a plate specimen in the fixture and (b) a free plate specimen. In the first case, the seven-layer Ti-TiB FGM with homogenized layers (Mori-Tanaka needles material model) in the specimen plate fixture was modeled in ABAQUS exactly as described in Chapter VI, including mesh, boundary conditions, constraints, and contact surfaces. The tup

was not included in the FEM since only modal contributions from the plate and fixture were necessary. In the second case, the same FGM plate was modeled in ABAQUS without any boundary conditions or constraints at all. Essentially the two modal analyses are the extreme cases under which the FGM plate is constrained; one with constraints (in the plate fixture) and the second without constraints (free). The periods of the first modes in both cases can be used for comparison against the experimentally-determined 500 microsecond loading period.

Essentially, ABAQUS performs modal analyses on a finite element model by solving the eigenvalue problem

$$([\mathbf{K} - \omega^2[\mathbf{M}]) \{\bar{\mathbf{D}}\} = \{\mathbf{0}\} \quad (7.1)$$

where $[\mathbf{K}]$ is the global stiffness matrix of the model, $[\mathbf{M}]$ is the mass matrix of the model, ω are the modal frequencies and $\{\bar{\mathbf{D}}\}$ are nodal displacements associated with solutions to (7.1) (or mode shapes). Equation (7.1) is the classic eigenvalue problem for determining *undamped* natural modes of free vibration. (Note that the modal analysis *was not performed in ABAQUS/Explicit but was solved in a different solution module in ABAQUS*. The details of this module will not be discussed here other than to note what the module is doing to determine the mode shapes and associated frequencies. *Damping was not directly included in these modal analyses despite the fact that ABAQUS includes a bulk viscosity term designed to damp out higher oscillations during the solution in ABAQUS/Explicit*; see Section 6.2.1 of Chapter VI. Application of bulk viscosity is a feature applied to assist numerical solution and is only used in the ABAQUS/Explicit module.) There are many ways to solve this problem numerically to determine the natural frequencies (eigenvalues) and associated mode shapes (non-trivial solutions, eigenvectors), but a treatment of this subject will not be provided. In particular, the models of the free plate and the plate in the fixture were solved with the Lanczos method and only the first 30 natural frequencies and mode shapes

were determined since only the first non-rigid body motion natural mode is needed (for further details see [3], [31], and [14]).

After solving these FEM models, it was determined that the first natural mode of the system for the FGM plate in the fixture occurs at a frequency 9805 cycles/sec and for the free FGM plate the first natural mode occurs at a frequency of 8270 cycles/sec. The period of each of these modes is the inverse of the frequency; thus the periods of each mode are 102 microseconds and 121 microseconds, respectively. The period of loading of the tup was 500 microseconds (as stated merely for the sake of argument), or about four times larger than the largest of the periods associated with the two natural frequencies. Thus the period of loading in the experiments was somewhat larger than that of the period of the first modes for the FGM plates.

As a second check on this concept, the same two FEM models (plate in a fixture and a free plate) were run using pure titanium specimen plates (100% Ti, 0% TiB). The first natural mode determined by ABAQUS for the titanium plate in the fixture occurs at a frequency 9103 cycles/sec. The first natural mode of the free Ti plate was found to be 6167 cycles/sec. The periods of these modal frequencies are 110 microseconds and 162 microseconds. In other words, for the titanium specimen plates, the period of loading in the impact experiments was over three times larger than the largest of the periods associated with the two natural frequencies. Thus the period of loading in the experiments was somewhat larger than that of the period of the first modes for the titanium plates.

The pure titanium plates are the softest of the plate specimens (elastic modulus 110 GPa). The 15% Ti-85% TiB monolithic specimens would be the stiffest of the plate specimens (recall the elastic modulus of TiB was estimated to be 370 GPa). Since we have consistently not studied these specimens due to their failure during experiments, it is fruitless to predict their natural modes. The FGM plates, thus, were the specimens that were the stiffest of all the *successful* tests and the 85% Ti-15% TiB monolithic specimens fell somewhere in between. By studying the periods

of the first modes of the Ti and FGM plates under these conditions, a set of bounds can be more or less set on what the extreme cases should be for the period of the first modes in comparison to the actual period of loading in the experiments. It has therefore been shown that the plates are indeed being loaded slower than the period of the first natural modes of the plates. This requirement for quasi-static analysis has been satisfied. Based on this observation and others discussed earlier, the impacts will be studied analytically using a quasi-static analysis technique.

7.2 Analytical Model for Estimating Plate Impact Response

It was shown in the last section that the time window over which the impact load from the Dynatup occurred was large compared to the period of the first natural frequencies of both the plates and the plate in the fixture. This finding is very important because even though the plate impact is a dynamic event, the *maximum global deformation* of the plate can be estimated assuming quasi-static force application. Thus, the time-dependent terms in the governing equations disappear. This greatly simplifies analysis. In this section, the concepts from plate theory given in Chapter III will be extended to study the plate experiments and FEMs presented in the previous chapters. This analytical model will additionally be used as part of a scheme to estimate the material properties of individual layers of the FGM in order to enhance the performance of the finite element models.

The theory presented in this section is summarized from works by J. N. Reddy [103], [132], [98], [99], and [100]. Of primary interest is the transverse deformation of a thick, composite (or functionally graded) circular plate with constrained boundary subject to a concentrated load at the center of the plate. The central concentrated load allows this plate to be studied assuming axisymmetry assumptions. Given the composite plate is thick, it was additionally assumed that transverse shear strains cannot be ignored. J.N. Reddy, along with some of his fellow colleagues through the references above, developed a link between the results for transverse deformation of an isotropic thin circular plate subject to a concentrated center load and the result for

a composite shear-deformable plate of same geometry and loading using first-order shear deformation theory (FST). This link is highly important to analyses such as these because the governing equations for shear deformable plates can be extremely complicated.

7.2.1 Formulation. Before proceeding, note that some aspects of the plate theory in Chapter III will be reproduced to assist the reader in this development, while some equations and concepts already thoroughly explained will not be included for brevity. To this point, and through the remainder of the dissertation, the behavior of the plates will be studied under the assumptions of linear-elastic deformation theory.

Given a circular plate in cylindrical coordinates (r, θ, z) of net thickness h and subject to an axisymmetric transverse load p , the displacement field for the plate is given as

$$\begin{aligned} u_r(r, z) &= u_0(r) - z \frac{dw_0}{dr} \\ u_z(r, z) &= w_0(r) \end{aligned} \tag{7.2}$$

according to Kirchhoff classical plate theory. u is the displacement along a given coordinate direction (subscripts r and z), $u_\theta = 0$, u_0 is the radial displacement and w_0 is the transverse displacement of the point $(r, 0)$ along the mid-plane of the plate ($z = 0$) as a function of the radial coordinate r . The plates used in this study are considered thick plates where the transverse shear effects generally neglected in CPT must be considered. First order shear-deformation plate theory will be used to account for this effect. The displacement field in (7.2) is modified to take the following form:

$$\begin{aligned} u_r(r, z) &= u_0(r) + z\phi(r) \\ u_z(r, z) &= w_0(r) \end{aligned} \tag{7.3}$$

ϕ is the rotation of a transverse normal in the plane $\theta = \text{constant}$.

Both CPT and FST are governed by the relations

$$\frac{d}{dr} (rN_{rr}) - N_{\theta\theta} = 0 \quad (7.4)$$

$$-\frac{d}{dr} (rQ_r) = rq \quad (7.5)$$

$$rQ_r = \frac{d}{dr} (rM_{rr}) - M_{\theta\theta} \quad (7.6)$$

N_{rr} and $N_{\theta\theta}$ are the radial and circumferential in-plane forces per unit length; M_{rr} and $M_{\theta\theta}$ are the radial and circumferential moments per unit length:

$$(N_{rr}, N_{\theta\theta}) = \int_{-\frac{h}{2}}^{\frac{h}{2}} (\sigma_{rr}, \sigma_{\theta\theta}) dz \quad (7.7)$$

$$(M_{rr}, M_{\theta\theta}) = \int_{-\frac{h}{2}}^{\frac{h}{2}} (\sigma_{rr}, \sigma_{\theta\theta}) z dz \quad (7.8)$$

and Q_r is the vertical shear force. The constitutive relations for the circular plates are given by:

1. CPT for an *isotropic* circular plate:

$$N_{rr}^C = A_{11} \frac{du_0^C}{dr} + A_{12} \frac{u_0^C}{r} \quad (7.9)$$

$$N_{\theta\theta}^C = A_{12} \frac{du_0^C}{dr} + A_{11} \frac{u_0^C}{r} \quad (7.10)$$

$$M_{rr}^C = -D_{11} \frac{d^2 w_0^C}{dr^2} - D_{12} \frac{1}{r} \frac{dw_0^C}{dr} \quad (7.11)$$

$$M_{\theta\theta}^C = -D_{12} \frac{d^2 w_0^C}{dr^2} - D_{11} \frac{1}{r} \frac{dw_0^C}{dr} \quad (7.12)$$

$$Q_r^C = \frac{1}{r} \left[\frac{d}{dr} (rM_{rr}^C) - M_{\theta\theta}^C \right] \quad (7.13)$$

2. FST for a non-symmetric composite or functionally graded circular plate:

$$N_{rr}^F = A_{11} \frac{du_0^F}{dr} + A_{12} \frac{u_0^F}{r} + B_{11} \frac{d\phi}{dr} + B_{12} \frac{\phi}{r} \quad (7.14)$$

$$N_{\theta\theta}^F = A_{12} \frac{du_0^F}{dr} + A_{11} \frac{u_0^F}{r} + B_{12} \frac{d\phi}{dr} + B_{11} \frac{\phi}{r} \quad (7.15)$$

$$M_{rr}^F = B_{11} \frac{du_0^F}{dr} + B_{12} \frac{u_0^F}{r} + D_{11} \frac{d\phi}{dr} + D_{12} \frac{\phi}{r} \quad (7.16)$$

$$M_{\theta\theta}^F = B_{12} \frac{du_0^F}{dr} + B_{11} \frac{u_0^F}{r} + D_{12} \frac{d\phi}{dr} + D_{11} \frac{\phi}{r} \quad (7.17)$$

$$Q_r^F = A_{55} \left(\phi + \frac{dw_0^F}{dr} \right) \quad (7.18)$$

Superscripts C and F denote association with the classical and first-order theories, respectively. A_{ij} , B_{ij} , and D_{ij} are the plate stiffness matrices (defined by equations (3.44)-(3.54) for the *axisymmetric case* as discussed in Chapter III). Note that for an isotropic plate, the B_{ij} matrix vanishes. (Compare (7.9)-(7.18) to the relations (3.65) and (3.71)-(3.72) in Chapter III.)

The relationship between CPT and FST as defined by Reddy is presented. Beginning with equation (7.4) and substituting the relations (7.14) and (7.15) results in the following expression (after mathematical manipulation):

$$\begin{aligned} 0 &= \frac{d}{dr} (rN_{rr}) - N_{\theta\theta} \\ &= A_{11} \left[r \frac{d}{dr} \left(\frac{1}{r} \frac{d}{dr} (ru_0^F) \right) \right] + B_{11} \left[r \frac{d}{dr} \left(\frac{1}{r} \frac{d}{dr} (r\phi) \right) \right] \end{aligned}$$

This expression is then rewritten in the following form:

$$\left[r \frac{d}{dr} \left(\frac{1}{r} \frac{d}{dr} (ru_0^F) \right) \right] = -\frac{B_{11}}{A_{11}} \left[r \frac{d}{dr} \left(\frac{1}{r} \frac{d}{dr} (r\phi) \right) \right] \quad (7.19)$$

Successive integrations of expression (7.19) gives

$$u_0^F = -\frac{B_{11}}{A_{11}} \phi + k_1 \frac{r}{2} + \frac{k_2}{r} \quad (7.20)$$

and differentiating (7.20) with respect to r produces

$$\frac{du_0^F}{dr} = -\frac{B_{11}}{A_{11}} \frac{d\phi}{dr} + \frac{k_1}{2} - \frac{k_2}{r^2} \quad (7.21)$$

Note that k_1 and k_2 are constants of integration that will be determined later. The equations for u_0^F and du_0^F/dr can be substituted into (7.14)-(7.17) and thus simplify the force and moment equations into functions of ϕ and r only.

$$M_{rr}^F = \Omega_1 \frac{d\phi}{dr} + \Omega_2 \frac{\phi}{r} + \frac{1}{2} \Omega_3 k_1 + \frac{1}{r^2} \Omega_4 k_2 \quad (7.22)$$

$$M_{\theta\theta}^F = \Omega_2 \frac{d\phi}{dr} + \Omega_1 \frac{\phi}{r} + \frac{1}{2} \Omega_3 k_1 - \frac{1}{r^2} \Omega_4 k_2 \quad (7.23)$$

$$N_{rr}^F = \Omega_5 \frac{\phi}{r} + \frac{1}{2} \Omega_6 k_1 + \frac{1}{r^2} \Omega_7 k_2 \quad (7.24)$$

$$N_{\theta\theta}^F = \Omega_5 \frac{\phi}{r} + \frac{1}{2} \Omega_6 k_1 - \frac{1}{r^2} \Omega_7 k_2 \quad (7.25)$$

The Ω_i 's are constants based on material properties and can be found to be

$$\Omega_1 = D_{11} - \frac{B_{11}^2}{A_{11}} \quad (7.26)$$

$$\Omega_2 = D_{12} - \frac{B_{11}B_{12}}{A_{11}} \quad (7.27)$$

$$\Omega_3 = B_{11} + B_{12} \quad (7.28)$$

$$\Omega_4 = B_{12} - B_{11} \quad (7.29)$$

$$\Omega_5 = B_{12} - \frac{A_{12}B_{11}}{A_{11}} \quad (7.30)$$

$$\Omega_6 = A_{11} + A_{12} \quad (7.31)$$

$$\Omega_7 = A_{12} - A_{11} \quad (7.32)$$

Now, load equivalence requires

$$\frac{d}{dr} (rQ_r^F) = \frac{d}{dr} (rQ_r^C) \quad (7.33)$$

and integration of this expression yields

$$rQ_r^F = rQ_r^C + c_1 \quad (7.34)$$

c_1 is a constant of integration. Substituting equations (7.22) and (7.23) into (7.6) gives

$$rQ_r^F = \frac{d}{dr} (rM_{rr}^F) - M_{\theta\theta}^F = \Omega_1 \left[r \frac{d}{dr} \left(\frac{1}{r} \frac{d}{dr} (r\phi) \right) \right] \quad (7.35)$$

and substituting equations (7.11) and (7.12) into (7.6) gives

$$rQ_r^C = \frac{d}{dr} (rM_{rr}^C) - M_{\theta\theta}^C = -D \left[r \frac{d}{dr} \left(\frac{1}{r} \frac{d}{dr} (r \frac{dw_0^C}{dr}) \right) \right] \quad (7.36)$$

where it is recognized that D_{11} and D_{12} in (7.11) and (7.12) are equal to D and νD , respectively. Substitution of (7.35) and (7.36) into equation (7.34) gives

$$\Omega_1 \left[r \frac{d}{dr} \left(\frac{1}{r} \frac{d}{dr} (r\phi) \right) \right] = -D \left[r \frac{d}{dr} \left(\frac{1}{r} \frac{d}{dr} (r \frac{dw_0^C}{dr}) \right) \right] + c_1 \quad (7.37)$$

successive integrations of this expression yields

$$\Omega_1 \frac{d}{dr} (r\phi) = -D \frac{d}{dr} \left(r \frac{dw_0^C}{dr} \right) + c_1 r \ln r + c_2 r \quad (7.38)$$

$$\Omega_1 \phi = -D \frac{dw_0^C}{dr} + \frac{1}{4} c_1 r (2 \ln r - 1) + \frac{1}{2} c_2 r + \frac{1}{r} c_3 \quad (7.39)$$

Defining the moment sum \mathcal{M}^C as

$$\mathcal{M}^C = \frac{M_{rr}^C + M_{\theta\theta}^C}{1 + \nu} \quad (7.40)$$

and combining equations (7.18) and (7.34) with some manipulation yields

$$A_{55} \left(\phi + \frac{dw_0^F}{dr} \right) = \frac{d\mathcal{M}^C}{dr} + \frac{1}{r} c_1 \quad (7.41)$$

The expression for ϕ in (7.39) is substituted into (7.41):

$$A_{55} \left[-\frac{D}{\Omega_1} \frac{dw_0^C}{dr} + \frac{c_1}{4\Omega_1} r(2 \ln r - 1) + \frac{c_2}{2\Omega_1} r + \frac{c_3}{\Omega_1 r} + \frac{dw_0^F}{dr} \right] = \frac{d\mathcal{M}^C}{dr} + \frac{1}{r} c_1 \quad (7.42)$$

Integrating this expression produces the important result

$$w_0^F(r) = \frac{D}{\Omega_1} w_0^C + \frac{c_1}{\Omega_1} \left[\frac{r^2}{4} (1 - \ln r) + \frac{\Omega_1}{A_{55}} \ln r \right] - \frac{c_2}{4\Omega_1} r^2 - \frac{c_3}{\Omega_1} \ln r - c_4 + \frac{\mathcal{M}^C}{A_{55}} \quad (7.43)$$

This equation thus relates the solution to the FST transverse displacement, w_0^F , to the solution for transverse displacement given by CPT for an isotropic plate, w_0^C . The constants of integration, c_i , are determined by the boundary conditions for the specific plate configuration of interest. Finally, the in-plane forces and moments will be determined based on the results to this point. Differentiation of (7.39) gives

$$\Omega_1 \frac{d\phi}{dr} = -D \frac{d^2 w_0^C}{dr^2} + \frac{c_1}{2} \left[\frac{1}{2} (2 \ln r - 1) + 1 \right] + \frac{c_2}{2} - \frac{c_3}{r^2} \quad (7.44)$$

The in-plane forces, N_{rr}^F and $N_{\theta\theta}^F$, are given by substituting (7.39) into (7.24) and (7.44) into (7.25), respectively:

$$\begin{aligned} N_{rr}^F &= \Omega_5 \left[-\frac{D}{\Omega_1} \frac{1}{r} \frac{dw_0^C}{dr} + \frac{c_1}{4\Omega_1} (2 \ln r - 1) + \frac{c_2}{2\Omega_1} + \frac{1}{r^2} \frac{c_3}{\Omega_1} \right] \\ &\quad + \Omega_6 \frac{k_1}{2} + \Omega_7 \frac{k_2}{r^2} \end{aligned} \quad (7.45)$$

$$\begin{aligned} N_{\theta\theta}^F &= \Omega_5 \left[-\frac{D}{\Omega_1} \frac{d^2 w_0^C}{dr^2} + \frac{c_1}{4\Omega_1} (2 \ln r + 1) + \frac{c_2}{2\Omega_1} - \frac{1}{r^2} \frac{c_3}{\Omega_1} \right] \\ &\quad + \Omega_6 \frac{k_1}{2} - \Omega_7 \frac{k_2}{r^2} \end{aligned} \quad (7.46)$$

The moments, M_{rr}^F and $M_{\theta\theta}^F$, are determined by substituting equations (7.39) and (7.44) into the moment relations (7.22) and (7.23), respectively, and employing alge-

braic manipulation (steps not shown for brevity):

$$\begin{aligned}
M_{rr}^F &= M_{rr}^C + \frac{D}{r} \frac{dw_0^C}{dr} \left(\nu - \frac{\Omega_2}{\Omega_1} \right) + \frac{c_1}{2} \left[\frac{1}{2} \left(1 - \frac{\Omega_2}{\Omega_1} \right) + \left(1 + \frac{\Omega_2}{\Omega_1} \right) \ln r \right] \\
&\quad + \frac{c_2}{2} \left(1 + \frac{\Omega_2}{\Omega_1} \right) - \frac{c_3}{r^2} \left(1 - \frac{\Omega_2}{\Omega_1} \right) + \Omega_3 \frac{k_1}{2} + \Omega_4 \frac{k_2}{r^2}
\end{aligned} \tag{7.47}$$

$$\begin{aligned}
M_{\theta\theta}^F &= M_{\theta\theta}^C + D \frac{d^2 w_0^C}{dr^2} \left(\nu - \frac{\Omega_2}{\Omega_1} \right) + \frac{c_1}{2} \left[-\frac{1}{2} \left(1 - \frac{\Omega_2}{\Omega_1} \right) + \left(1 + \frac{\Omega_2}{\Omega_1} \right) \ln r \right] \\
&\quad + \frac{c_2}{2} \left(1 + \frac{\Omega_2}{\Omega_1} \right) + \frac{c_3}{r^2} \left(1 - \frac{\Omega_2}{\Omega_1} \right) + \Omega_3 \frac{k_1}{2} - \Omega_4 \frac{k_2}{r^2}
\end{aligned} \tag{7.48}$$

This concludes the development for determining the transverse displacement, forces, and moments for a FST FGM circular plate under axisymmetric bending as related to the solution for an isotropic CPT circular plate with the same geometry and boundary conditions. These relations will now be applied to determine the transverse displacements of FST FGM circular plates for (1) a clamped boundary and (2) a simply-supported boundary. These common boundary conditions will be tested against the experimental and FEM results to assess which is closest to the actual impact events.

7.2.2 Clamped Boundary Condition. The boundary conditions for a plate clamped at the boundary (clamped at $r = a$) are:

1. $r = 0$

$$u = 0, \quad \phi = 0, \quad \frac{dw_0^C}{dr} = 0, \quad Q_r = 0 \tag{7.49}$$

2. $r = a$

$$u = 0, \quad w = 0, \quad \phi = 0, \quad \frac{dw_0^C}{dr} = 0 \tag{7.50}$$

Applying the boundary conditions for u to equation (7.20) shows the constants k_1, k_2 are both equal to zero. The boundary condition $Q_r = 0$ at $r = 0$ applied to equation (7.34) yields $c_1 = 0$. Additionally, we know $\phi = 0$ at both $r = 0$ and $r = a$. These conditions are applied to the expression for ϕ in (7.39) where the constants c_2 and c_3 are determined to be zero. Finally, c_4 is determined by applying the condition $w = 0$ at $r = a$ along with the known values of c_i and other conditions listed to equation

(7.43) to give $c_4 = \mathcal{M}^C(a)/A_{55}$. Noting the solution for a clamped, isotropic, CPT plate with a concentrated central load P is [125], [100]:

$$w_0^C(r) = \frac{P}{16\pi D} \left(2r^2 \ln \frac{r}{a} + a^2 - r^2 \right) \quad (7.51)$$

The solution $w_0^F(r)$ for the FST FGM clamped circular plate is then

$$w_0^F(r) = \frac{D}{\Omega_1} w_0^C(r) + \frac{\mathcal{M}^C(r) - \mathcal{M}^C(a)}{A_{55}} \quad (7.52)$$

Equations (7.34) and (7.45)-(7.48) reduce to the following expressions applicable to the clamped circular plate:

$$Q_r^F(r) = Q_r^C(r) \quad (7.53)$$

$$N_{rr}^F(r) = -\Omega_5 \frac{D}{\Omega_1} \left(\frac{1}{r} \frac{dw_0^C}{dr} \right) \quad (7.54)$$

$$N_{\theta\theta}^F(r) = -\Omega_5 \frac{D}{\Omega_1} \frac{d^2 w_0^C}{dr^2} \quad (7.55)$$

$$M_{rr}^F(r) = M_{rr}^C(r) + D \frac{1}{r} \frac{dw_0^C}{dr} \left(\nu - \frac{\Omega_2}{\Omega_1} \right) \quad (7.56)$$

$$M_{\theta\theta}^F(r) = M_{\theta\theta}^C(r) + D \frac{d^2 w_0^C}{dr^2} \left(\nu - \frac{\Omega_2}{\Omega_1} \right) \quad (7.57)$$

Using the linear-elastic strain-displacement relations in (3.64) and applying the solutions presented here to equations (7.20) and (7.39) to find u_r in (7.3), the radial strain in the plate can be shown to be

$$\epsilon_{rr}(r, z) = \frac{\partial u_r}{\partial r} = \frac{P}{4\pi\Omega_1} \left[\frac{B_{11}}{A_{11}} - z \right] \left(1 + \ln \frac{r}{a} \right) \quad (7.58)$$

This radial strain will be compared to the strain gage results from the plate tests shortly.

Given a FGM plate with two constituents, metal and ceramic, the choice of which isotropic plate (metal or ceramic) to use as the model plate solution w_0^C in (7.52) is arbitrary because the numerator of the coefficient D/Ω_1 will cancel out the

D in the denominator of the coefficient in (7.51), leaving only the Ω_1 term in the denominator of the FST solution. This term accounts for the composition of the actual FGM plate. Also note that the solution w_0^F can also be used with monolithic specimens since the $[A_{ij}]$, $[B_{ij}]$, and $[D_{ij}]$ matrices account for the plate composition through the thickness where a single, multiple, or infinite number of layers of varying composition can be accounted for.

A very important note on the vertical shear load Q_r is in order before proceeding. If the axisymmetric load applied to the plate is a *distributed* load, the condition $Q_r = 0$ is a condition applied at $r = 0$. This condition is important since through this boundary condition the constant c_1 in equation (7.34) is zero. Now, if the axisymmetric load applied to the plate is a *concentrated* load at the center, $Q_r = -P/2\pi r$ is required to hold for all r . This is somewhat problematic for two reasons. First, at the center of the plate, $r = 0$, Q_r is unbounded as are the deflections and stresses at the center of the plate. Westergaard [133] proposed that the problem can be alleviated by using an equivalent radius r_e in place of r in force, moment, and stress equations at the center of the plate, meaning the concentrated load is assumed to be applied over a very small area given by

$$r_e = \sqrt{1.6 r_c^2 + h^2} - 0.675 h, \quad r_c \leq 0.5 h \quad (7.59)$$

r_c is a small radius that defines a small circular area over which the concentrated load is assumed to be distributed. r_c can be set equal to zero for a concentrated load, if so desired, in which case the r_e is equal to $0.325h$. For r less than or equal to r_e , r_e is substituted for r as a constant in the equations for displacements, forces, moments, and stresses. This has the effect of bounding the solutions for these near the plate center, although it is an approximation to the exact solution. Westergaard [133] originally proposed this approximation and demonstrated its utility through rigorous theoretical analysis. Additionally, Westergaard demonstrated that the equation is applicable to a plate of any size and geometry. The result is used extensively in

practice (see [141], [125], and [100]). This equivalent radius will be used to produce bounded results for force, moments, and stresses when r is less than r_e given $r_e = 0$ and the plate thickness h in results documented later in the dissertation. The second problem associated with $Q_r = -P/2\pi r$ is that the solution for w_0^F was determined assuming that $Q_r = 0$ at the center of the plate yielding the result that the constant $c_1 = 0$. Note that the most significant contribution to the result for w_0^F is the solution w_0^C , which is solved in CPT assuming that $Q_r = -P/2\pi r$ applies across the plate for all r . The other terms in w_0^F more or less add corrections to account for the assumptions of FST. Now, since c_1 is a constant, assuming $c_1 = 0$ in the case of a concentrated load will still satisfy the load equivalence relation (7.33) and will not appreciably change the accuracy of the solution, especially in light of the justification and use of the equivalent radius described in this paragraph (meaning the concentrated load is assumed to be distributed over a small area).

7.2.3 Simply-Supported Boundary Condition. The boundary conditions for a plate simply-supported (or hinged) at the boundary (simply-supported/hinged at $r = a$) are:

1. $r = 0$

$$u = 0, \quad \phi = 0, \quad \frac{dw_0^C}{dr} = 0, \quad Q_r = 0 \quad (7.60)$$

2. $r = a$

$$u = 0, \quad w = 0, \quad M_{rr} = 0 \quad (7.61)$$

The boundary conditions for this case are applied in a very similar fashion to the procedure discussed for the clamped condition, but since the boundary conditions are different the results are also very different. As with the case of the clamped condition, this becomes a mathematical exercise in which only the results will be presented. The solution for a clamped, isotropic, CPT plate with a concentrated central load P and

simply-supported boundary is [125], [100]:

$$w_0^C(r) = \frac{P}{16\pi D} \left[2r^2 \ln \frac{r}{a} + \frac{3+\nu}{1+\nu} (a^2 - r^2) \right] \quad (7.62)$$

The constants from application of the boundary conditions are

$$\begin{aligned} k_1 &= \frac{2B_{11}}{aA_{11}} \left(-\frac{D}{\Omega_1} \frac{dw_0^C(a)}{dr} + \frac{c_2}{\Omega_1} \frac{a}{2} \right) \\ k_2 &= 0 \\ c_1 &= 0 \\ c_3 &= 0 \\ c_2 &= -\frac{2D}{a} \left(\frac{\nu - \frac{\Omega_2}{\Omega_1} - \Omega_9}{\nu + \frac{\Omega_2}{\Omega_1} + \Omega_9} \right) \frac{dw_0^C(a)}{dr} \\ c_4 &= \frac{\mathcal{M}^C(a)}{A_{55}} - \frac{c_2}{\Omega_1} \frac{a^2}{4} \\ \Omega_9 &= \frac{\Omega_3}{\Omega_1} \frac{B_{11}}{A_{11}} \end{aligned}$$

The solution $w_0^F(r)$ for the FST FGM simply-supported circular plate is then

$$w_0^F(r) = \frac{D}{\Omega_1} w_0^C(r) + \frac{\mathcal{M}^C(r) - \mathcal{M}^C(a)}{A_{55}} + \frac{1}{4} \frac{c_2}{\Omega_1} (a^2 - r^2) \quad (7.63)$$

Equations (7.34) and (7.45)-(7.48) reduce to the following expressions applicable to the simply-supported circular plate:

$$Q_r^F(r) = Q_r^C(r) \quad (7.64)$$

$$N_{rr}^F(r) = \Omega_5 \frac{D}{\Omega_1} \left(\frac{1}{a} \frac{dw_0^C(a)}{dr} - \frac{1}{r} \frac{dw_0^C}{dr} \right) \quad (7.65)$$

$$N_{\theta\theta}^F(r) = \Omega_5 \frac{D}{\Omega_1} \left(\frac{1}{a} \frac{dw_0^C(a)}{dr} - \frac{d^2 w_0^C}{dr^2} \right) \quad (7.66)$$

$$M_{rr}^F(r) = M_{rr}^C(r) + D \frac{1}{r} \frac{dw_0^C}{dr} \left(\nu - \frac{\Omega_2}{\Omega_1} \right) + \frac{1}{2} c_2 \left(1 + \frac{\Omega_2}{\Omega_1} \right) + \frac{1}{2} k_1 \Omega_3 \quad (7.67)$$

$$M_{\theta\theta}^F(r) = M_{\theta\theta}^C(r) + D \frac{d^2 w_0^C}{dr^2} \left(\nu - \frac{\Omega_2}{\Omega_1} \right) + \frac{1}{2} c_2 \left(1 + \frac{\Omega_2}{\Omega_1} \right) + \frac{1}{2} k_1 \Omega_3 \quad (7.68)$$

Using the linear-elastic strain-displacement relations in (3.64) and applying the solutions presented here to equations (7.20) and (7.39) to find u_r in (7.3), the radial strain in the plate can be shown to be

$$\epsilon_{rr}(r, z) = \left[z - \frac{B_{11}}{A_{11}} \right] \left\{ -\frac{P}{16\pi\Omega_1} \left[4 \ln \frac{r}{a} + 6 - 2 \left(\frac{3 + \nu}{1 + \nu} \right) \right] + \frac{c_2}{2\Omega_1} \right\} + \frac{k_1}{2} \quad (7.69)$$

This radial strain will be compared to the strain gage results from the plate tests in the next section. The use of the equivalent radius as well as the the considerations with respect to Q_r discussed for the clamped boundary condition are applicable to the simply-supported plate as well.

7.3 *Validation of Analytical Model*

The necessary theory for an analytical study of the impact events has been presented in the previous section. The formulas for strain and displacement will play a very prominent role in the parameter estimation scheme discussed in the next chapter. Two questions remain that must be answered before proceeding: (1) How will the formulation compare to the actual tests? and (2) What type of boundary condition is closest to the plate in the fixture? Both questions will be answered in the following discussion.

Formulas for determining radial strain and transverse displacements were developed for circular plates with a concentrated load at the center of the plate under the assumptions of axisymmetric bending for a clamped or simply-supported boundary. These formulas will be compared to the results for the 100% titanium plate of test 1 (see Table 5.3) in the experiments. The finite element solution for this test discussed in Chapter VI will be used as will the experimental results in Table 5.5 for comparison.

There are a few good reasons for using the titanium plate of test 1 as the verification test. First, the FST model of the last section is valid for a monolithic or graded plate, but the monolithic specimen provides the simplest solution because the

material properties are much simpler for an isotropic plate than a graded plate with varied composition through the thickness. Next, the material properties of titanium are very well known and not nearly as ambiguous as those for a Ti-TiB mixture. That is, while the 85% Ti-15% TiB specimens were also monolithic and (assumed) isotropic, one of the material models such as the rule-of-mixtures or Mori-Tanaka estimates would have to be applied and such is not the case with 100% Ti. Lastly, the Dynatup is able to measure contact force during impact events as mentioned in Chapter V. A few unused 100% Ti plates remained after testing in Chapter V was completed. The load cell for measuring contact force had a calibration problem during the initial tests that was later resolved. One unused 100% Ti plate was placed in the Dynatup and tested under the conditions of test 1 without strain gages (test 1: 13.06 kg crosshead mass, 0.508 m crosshead height, 3.040 m/s impact velocity, 60.35 J impact energy). The actual impact velocity of this second test was 3.086 m/s, with impact energy 62.19 J. This was deemed sufficiently close to assume the contact force measurement would be very close to that of test 1. The maximum contact force measured in the test was 87,380 Newtons. This force is used as the load P in the equations for transverse displacement (w_0^F) and radial strain (ϵ_{rr}). A subsequent test under the conditions of Test 2 with a pure titanium plate was also carried out, but this test was not fruitful as the maximum contact force was beyond the maximum detectable load (that is, the maximum load that the load cell is calibrated to accurately read—89,000 Newtons) for the load cell, and thus an accurate force was not collected for this test.

Figures 7.2 and 7.3 compare the analytical radial transverse displacements of the mid-surface of the plate (w_0^F) to the finite element solution for a 100% Ti-0% TiB monolithic plate under the conditions of Test 1. The finite element solutions are nodal displacements taken along axes as shown in Figure 7.1. Recall the original plate is a 7.62 cm x 7.62 cm – 1.27 cm thick square plate configured to a circular plate with a radius of 3.49 cm. The displacements are plotted only to the radial boundary (meaning the fixture’s circular opening) shown in Figure 7.1. The portions of the test plate that are covered and built into the fixture (shown in gray) are of interest, but

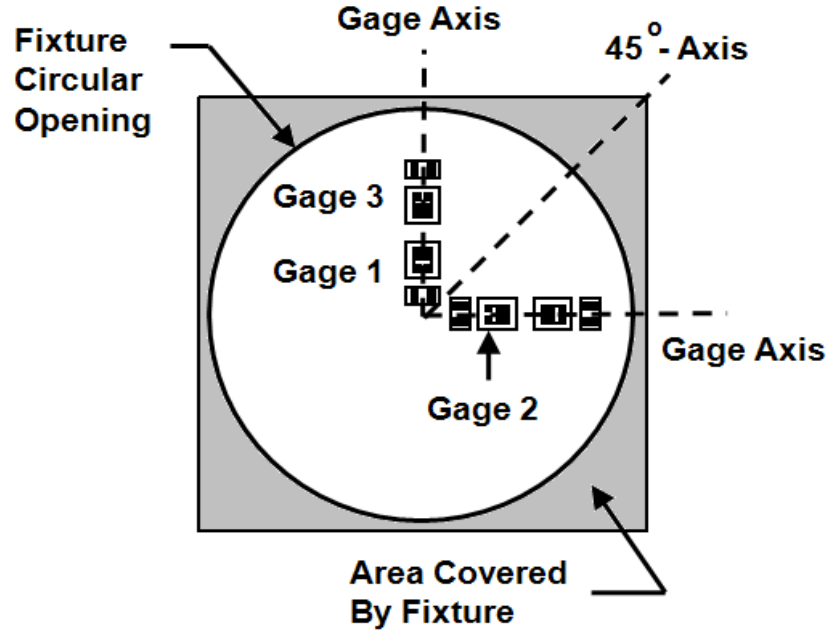


Figure 7.1: Specimen plate with gages, with key reference positions annotated.

the behavior of the plates in those sections will be discussed more in Chapter IX. By inspection, it can be seen from the displacement plots that the FEM solution is very close to the analytical FST solution for a simply-supported plate. The analytical displacement distribution for the clamped boundary condition (BC) does not match well with the finite element result. The radial strain distributions along the bottom surface of the plates along the axes in Figure 7.1 are plotted in Figures 7.4 and 7.5. The radial strain distributions from the FEM correlate well with the distribution predicted by analytical theory for the simply-supported case, but not well for the clamped BC. Further, the radial strains measured by the strain gages correlate well with the FEM and the simply-supported analytical solution. This indicates that the plate fixture acts much closer to a simply-supported BC than a clamped BC as one would believe knowing the fixture configuration.

A couple of notes on the displacement and strain distributions are in order. First, the analytical prediction has a “plateau” effect at the inner portions of the curve for the analytical theory. This is due to the use of the effective radius r_e used

in the equations in place of r for radii $\leq 0.325 h$, or 0.325 times the thickness of the plate (0.00413 m). Recall that without the use of the effective radius, the solutions for displacement and strain become unbounded due to the logarithmic terms. Clearly the solutions are not unbounded as is shown from the finite element results and from the fact that the plates did not instantly fail in the tests. This is merely an approximation to the actual behavior at that part of the plate. This effect introduces more error between the theory and the FEM in the strain distributions than in the displacement solutions for the simply-supported BC. Next, one can note two “kinks” in the displacement solutions (meaning a sharp change in the displacement solution away from the general trend of the curve) very near the fixture boundary for the FEM. This is undoubtedly attributable to a contact effect in the FEM where the sharp edge marking the boundary of the opening in the fixture contacts the plate specimen. This effect is propagated through the FEM solution along the entire boundary as is apparently visible along the gage axis and 45° axis of the plate. The next point involves the strain gage data plotted from test 1. Recall that gage 1, closest to the center, had a significant discrepancy between the measured strain and the FEM strain. This discrepancy is visible in Figures 7.4 and 7.5. However, the other gages follow the FEM result well and the analytical prediction for the radial strain distribution for the simply-supported BC also passes through the strain gage measurements. These are important observations in that now there is strong evidence that the fixture is indeed acting very much like a simple-support to the plate specimens. Finally, the gage axes provide the best comparison for radial strain distribution to the strain gage results and the analytical predictions. The 45° axis of the plate has some radial strain discrepancy associated with it. This undoubtedly implies that the material built into the fixture plays a role in the difference between the actual tests and the ideal conditions of a simple-support under plate theory. Even in light of this discrepancy, the displacement results match reasonably well along the 45° axis as well as along the gage axis and the strain distributions are not far removed from one another along either axis. More will be said regarding these concepts in later chapters.

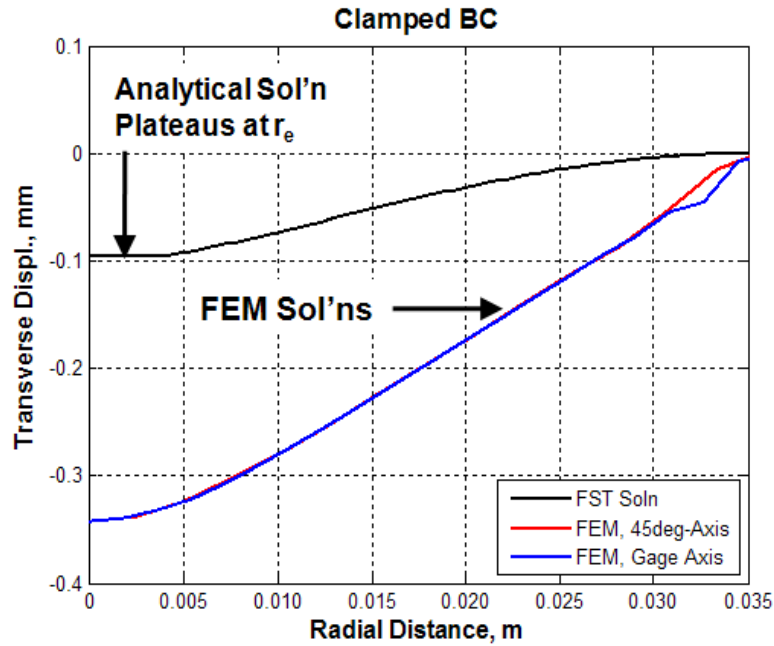


Figure 7.2: Transverse displacement of the plate in test 1 at maximum center displacement given the FEM and analytical predictions with clamped BC.

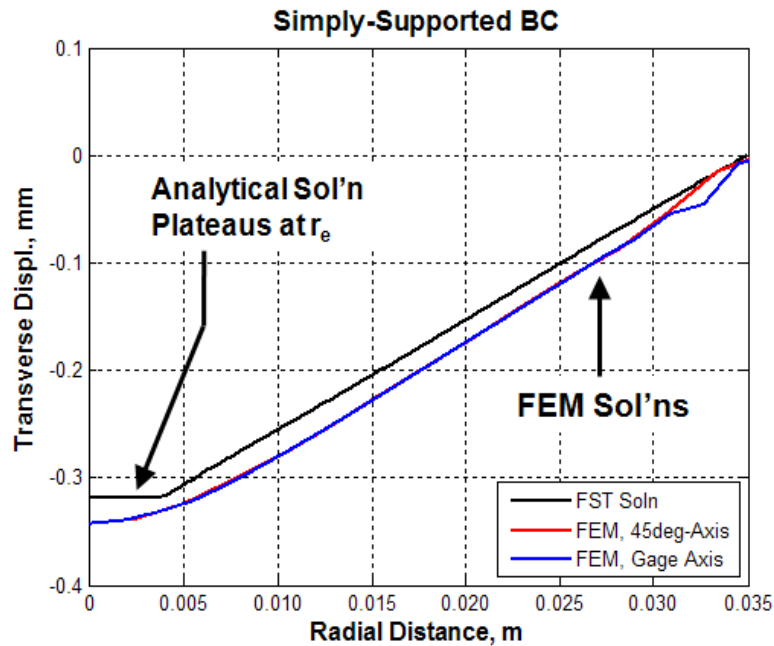


Figure 7.3: Transverse displacement of the plate in test 1 at maximum center displacement given the FEM and analytical predictions with simply-supported BC.

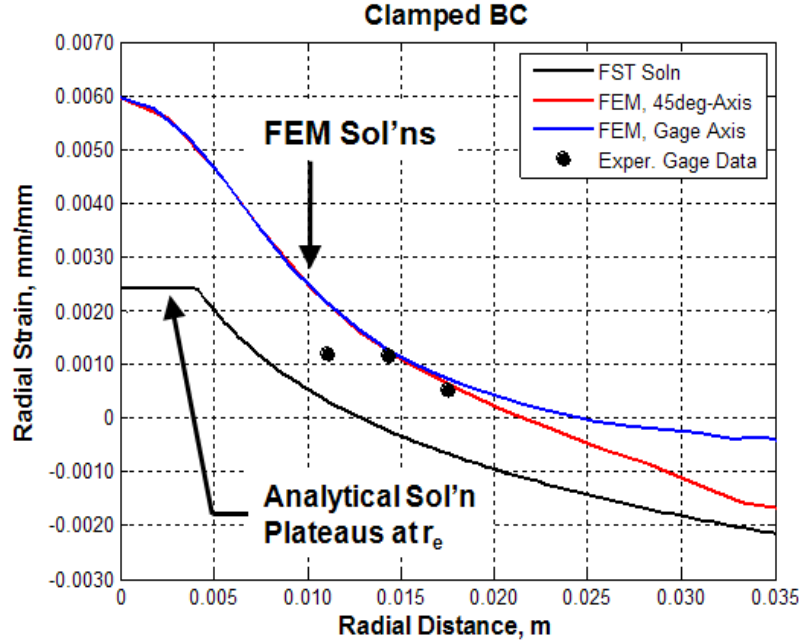


Figure 7.4: Radial strain distributions on the bottom surface of the plate (experiment, FEM, and analytical) in test 1 at maximum center displacement with clamped BC.

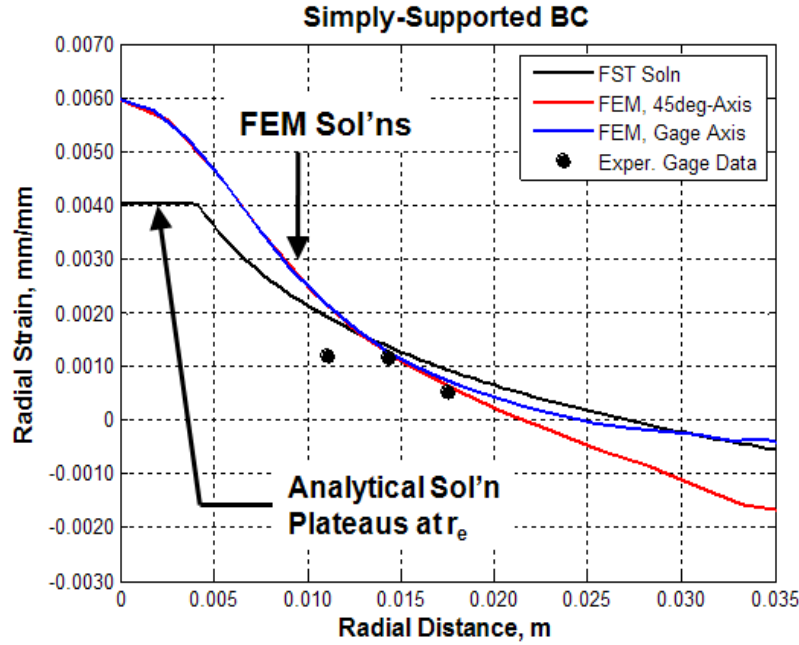


Figure 7.5: Radial strain distributions on the bottom surface of the plate (experiment, FEM, and analytical) in test 1 at maximum center displacement with simply-supported BC.

7.4 *Closing*

In closing, an analytical model to estimate the maximum deformation of the plate specimens in the impact experiments has been developed under quasi-static loading assumptions and first-order shear deformable plate theory. The analytical treatment of the plate was tested against experimental data and finite element solutions from a previous experiment at the instant of maximum deformation. It was found that the plate impact experiments correlate well to a circular plate in a simple-support (hinge) under a central concentrated load given axisymmetric bending assumptions. This analytical model will play a crucial role in the parameter estimation algorithm discussed in the next chapter and will provide a direct link between theory, the FEMs, and the experiments that will allow the material models for the FGM to be more effectively determined. *These improved material models will enhance the FEMs such that impacts against FGM specimens can be completely characterized.*

VIII. Estimation of Ti-TiB Material Parameters

Chapter VII outlined an analytical technique for estimating the response of a FGM plate under the conditions of the FGM plate experiments. *It was shown that an axisymmetric plate with a simply-supported boundary condition most closely modeled the impact tests through experimental and finite element validation.* The analytical technique will now be applied to a parameter estimation scheme that characterizes the material properties for the Ti-TiB mixtures through the graded layers of the FGM. The formulation and implementation of the parameter estimation technique will simultaneously satisfy the next two objectives in this research: (1) *correlate the results from the experiments and finite element models to available analytical theory* and (2) *refine the finite element material models using parameter estimation techniques to more effectively and accurately simulate the FGM plate impact experiments.*

To this point, the material properties in each layer in the FGM were estimated using mathematical models that related *known* properties for the constituents to their volume fractions locally in the FGM. In this chapter, a parameter estimation technique will be demonstrated where material properties of a single constituent are varied to minimize the error between the analytical model of the impact tests (from the previous chapter) and another tailored mathematical model fit to data points from a series of simulations with the two-phase finite element model of the tests. This parameter estimation scheme will allow the material properties to be compared against published values of the constituents and will further provide material data that will enhance the current finite element models being used. The parameter estimation scheme, once implemented, will be the final step in generating a finite element simulation that can be used to study the physics of low-velocity, low- to medium-energy impact events with functionally graded materials. *This parameter estimation scheme is a valuable contribution to the study of two-phase FGMs because it allows basic material properties of two-phase mixtures to be estimated if either: (a) the material properties of one constituent are not well known but the properties of the composite mixture are believed to follow available material models, or (b) the properties of the constituents*

are well known but material models relating the volume fractions and properties of the constituents to the average properties of the composite are not well known.

This chapter begins with an overview of the parameter estimation sequence. The problem is posed to minimize the error between the analytical model of the impact experiments and a mathematical model of the two-phase FEM by varying the material properties of the TiB constituent while holding the properties of the Ti constituent constant. Next, the mathematical model constructed to predict the maximum transverse deflection in the FGM plates from impact loading in the two-phase FEM is presented. Next, the techniques necessary to acquire the numerical solution of the minimization problem designed to estimate the FGM material properties is provided along with the steps required to implement the techniques in practice. The chapter concludes with results from the parameter estimation sequence compared to data collected from the FGM impact experiments.

8.1 Problem Formulation & Overview

In this section, the parameter estimation problem will be posed as an *optimization problem* where the error between the finite element model of the impact experiments and the analytical predictions will be minimized by varying the material properties of the Ti-TiB mixtures. The discussion will begin by defining how the material properties will be varied. First, the material properties and behavior of the titanium constituent are well documented in the literature and it is assumed that the material properties for this constituent are accurate. The TiB constituent, on the other hand, is not well-understood and the limited available literature shows a wide range of estimated properties (see Chapter IV). However, it can be assumed that the properties of TiB, notably elastic modulus, Poisson's ratio, and density, are more or less the properties (\mathcal{P}_i) of Ti multiplied by some coefficient C_i . In other words:

$$\begin{aligned} \text{FGM Constituent 1 (Ti):} & \quad \mathcal{P}_1, \mathcal{P}_2, \dots, \mathcal{P}_n \\ \text{FGM Constituent 2 (TiB):} & \quad (C_1*\mathcal{P}_1), (C_2*\mathcal{P}_2), \dots, (C_n*\mathcal{P}_n) \end{aligned}$$

Since we are only interested in three properties, $n = 3$ for the Ti-TiB system. C_1 will be associated with the elastic modulus of TiB; C_2 will be associated with the Poisson's ratio of TiB; and C_3 will be associated with the density of TiB. The choice of these three properties is simply based on the fact that these properties were the only ones required for the FGM in both the analytical model and the finite element model. As discussed earlier, the FGM plates behaved elastically in the room temperature environment and therefore restricting the study to these three parameters is valid.

The finite element models in both the two-phase and homogenized-layers cases were shown to model the impact experiments reasonably well in Chapter VI. The two-phase model had an advantage over the homogenized-layers model in that the individual constituents were randomly dispersed based on local volume fraction ratio of the constituents. As discussed earlier, there are features of this model that can capture some effects that the homogenized-layers model cannot capture due to the random distribution of the constituents. One feature of particular interest is the local distribution of constituents is highly statistical in nature in those FEMs. The homogenized-layers FEM on the other hand, is the most commonly used in analysis due to the convenience in assuming averaged properties for local volume fraction ratios of the constituents. The analytical model in the previous chapter assumes the materials are averaged using a mathematical relation as well. The ideal scenario is to bridge the gap between the two-phase and homogenized-layers models so that the features of both can be used to estimate the average material properties of individual layers and simultaneously estimating the properties of the individual constituents.

The parameter estimation problem will be posed as follows:

$$\begin{aligned}
\min f &= (w_0^{FST} - w_0^{FEM})^2 \\
\text{Subject to} \quad &C_1^{min} \leq C_1 \leq C_1^{max} \\
&C_2^{min} \leq C_2 \leq C_2^{max} \\
&C_3^{min} \leq C_3 \leq C_3^{max}
\end{aligned} \tag{8.1}$$

w_0^{FST} is the transverse displacement of the center of the FGM plate using the FST plate formulation in the previous chapter (called w_0^F earlier but the full acronym “FST” is used here to clearly separate the nomenclature from the transverse displacement of the FEM). w_0^{FEM} is the transverse displacement of the same FGM plate taken from the two-phase finite element model. C_i are the constant coefficients that are used to determine the material properties of constituent 2 (TiB). Essentially the problem can be stated in words as follows: minimize the difference, or error, in center transverse displacements between the analytical model and the two-phase FEM subject to limits on the values that the material properties of TiB can attain. The transverse displacements from the analytical model and the FEM can be used to estimate the material properties of the constituents by noting that *the displacements are both functions of the elastic moduli, Poisson’s ratios, and densities of the constituent materials*. The material properties of Ti are assumed fixed, and the properties of TiB are varied by changing the values of the coefficients C_1 , C_2 , and C_3 . The values for C_i are altered iteratively until the two-phase FEM response matches the response from the analytical model using (a) the same values for C_i , (b) the same volume fraction distribution of constituents, and (c) a chosen material model such as the rule-of-mixtures or the Mori-Tanaka estimates.

A few notes on the estimation problem. A series of tests with the two-phase FEM will be conducted to determine a mathematical model for w_0^{FEM} based on the material properties of Ti and TiB as inputs. Another input to the mathematical model will be impact velocity, a variable that is associated with the contact force in the FEM that will have an effect on the net displacement of the FGM plate. The method for accomplishing this will be presented in the following section. Developing such a mathematical model allows the parameter estimation problem to be solved off-line apart from ABAQUS, increasing the efficiency of the numerical solution. The numerical solution to equation (8.1) will be discussed later in this chapter.

With regard to w_0^{FST} , this displacement was solved analytically in Chapter VII. The displacements from classical theory & first-order shear deformable theory and

the radial strain in the plate for a circular simply-supported plate were shown to be (reprinted here for convenience):

$$w_0^C(r) = \frac{P}{16\pi D} \left[2r^2 \ln \frac{r}{a} + \frac{3+\nu}{1+\nu} (a^2 - r^2) \right] \quad (8.2)$$

$$w_0^{FST}(r) = \frac{D}{\Omega_1} w_0^C(r) + \frac{\mathcal{M}^C(r) - \mathcal{M}^C(a)}{A_{55}} + \frac{1}{4} \frac{c_2}{\Omega_1} (a^2 - r^2) \quad (8.3)$$

$$\epsilon_{rr}(r, z) = \left[z - \frac{B_{11}}{A_{11}} \right] \left\{ -\frac{P}{16\pi\Omega_1} \left[4 \ln \frac{r}{a} + 6 - 2 \left(\frac{3+\nu}{1+\nu} \right) \right] + \frac{c_2}{2\Omega_1} \right\} + \frac{k_1}{2} \quad (8.4)$$

As can be seen from equations (8.2) and (8.3), solving for the transverse displacement of a simply-supported circular plate requires knowledge of the magnitude of the concentrated force applied at the center of the plate P . In the plate tests, this force was not known due to the calibration problem in the Dynatup. However, the magnitude of force P is also a term in the radial strain equation (7.69). The maximum strains were measured at the nominal gage positions during the impact tests. Using this equation, the force applied at the center of the plate from the tup can be estimated by solving equation (7.69) for P given the maximum strain in the gage and the assumed material properties of the plate. The values for all three gages in the plate should yield roughly the same value in each test through the equation, and the average of the three P estimates provides a good estimate of the actual maximum force exerted on the plate by the tup. Later it will be shown that solving for the force in the plate through the experimental strains works very well. Also note that the solution for P is directly affected by the material properties of Ti and TiB; therefore as the properties of TiB are varied through C_1 , C_2 , and C_3 , the predicted magnitude of the force P will also vary. This is an extremely useful fact since it ties the analytical solution directly to the experiments as the error between the FEM and analytical model is minimized. More will be said about this later as the solution and implementation of the parameter estimation is presented.

Finally, w_0^{FST} requires a choice of mathematical material model (rule-of-mixtures, self-consistent model, Mori-Tanaka estimates, etc.) to average the contributions of Ti and TiB based on the local volume fraction ratio of the constituents. (*The assumed distribution of Ti-TiB will not vary from the values in Table 4.4 during the parameter estimation sequence.*) The choice of material model can affect the solution during the minimization process, however, it will be shown later in this chapter that the choice of material model very nearly predicts the same material properties in each layer of the FGM; further, for some of the models, the predictions for TiB material properties are very close to the same for each material model.

8.2 *Estimating Transverse Deflection from the Two-Phase FEM*

The two-phase finite element material model was shown to agree relatively well with both the experimental results as well as the homogenized material model results in Chapter VI. The goal is to estimate the maximum transverse deflection of functionally graded plates due to the Dynatup impact events as a function of the material properties of titanium and titanium boride as well as the velocity of the tup. The two-phase FEM provides a degree of uncertainty in the response due to the random distribution of constituents from one FEM test to the next; this is not the case with the homogenized-layers model since the material properties in each layer are the same. To account for the random distribution of constituents, the two-phase FEM provides a vehicle through which the homogenized-layers material models can be assessed further.

A series of simulations with the two-phase FEM (*seven-layer Ti-TiB functionally graded model only*) were run in order to estimate the maximum deflection of the plate by fitting a second-order polynomial to the FEM results using the method of *least squares* (such techniques are well-documented in the literature; Myers & Montgomery [82] and Lawson & Erjavec [69] were referenced in the documentation of this

section). The second-order polynomial has the form

$$\hat{y} = b_0 + \sum_{i=1}^k b_i x_i + \sum_{i=1}^k \sum_{j=i}^k b_{ij} x_i x_j \quad (8.5)$$

where \hat{y} is the dependent variable being estimated, x_i ($i = 1, \dots, k$) are the independent variables or “factors” of the second-order polynomial, and b_0 , b_{ii} , and b_{ij} are the coefficients of the independent variables.

The process to construct the second-order mathematical model in the context of the FGM plate impact problem can be described as follows. Four factors ($k = 4$) were chosen as independent variables whose values directly affect the response of the plate deflection on impact: (1) the elastic moduli of the constituents, (2) the Poisson’s ratio of the constituents, (3) the densities of the constituents, and (4) the velocity of the tup at impact. The variables (1)–(3) are all material property parameters. Since the material properties of Ti were assumed to be constant, the material properties of TiB will be variable in the mathematical model. Thus, factors x_1 , x_2 , and x_3 will represent the material property coefficients C_1 , C_2 , and C_3 that are associated with the elastic modulus, Poisson’s ratio, and density of TiB, respectively. The fourth factor, x_4 , will represent the velocity of the tup v_{tup} . The dependent variable \hat{y} , the maximum center deflection of the FGM plate on impact w_0^{FEM} , is thus assumed to be a function of all four variables in the form of equation (8.5). Each of the x_i independent variables is assigned an upper and lower bound on values that each variable might attain in practice. A series of tests is then run by choosing distinct values for each x_i variable over their respective regions of interest and then measuring the response of the system associated with those values, \hat{y} . Each set of settings x_i for individual tests are then correlated to their measured responses \hat{y} by fitting equation (8.5) to the test results using the method of least squares. Generally the number of tests that can be feasibly conducted to determine \hat{y} over a range of x_i values is limited. Therefore, when attempting to fit test data to a quadratic mathematical model, three equally spaced values for each x_i are chosen over the region of interest for each variable

Table 8.1: Factors used in Box-Behnken designed experiment.

Variable		Equivalent To	Values	
Coded	Actual		Coded	Actual
x_1	C_1	Elastic Modulus Coeff.	+1	4.20
			0	3.40
			-1	2.60
x_2	C_2	Poisson's Ratio Coeff.	+1	0.50
			0	0.40
			-1	0.30
x_3	C_3	Density Coeff.	+1	1.10
			0	1.00
			-1	0.90
x_4	v_{tup}	Tup Velocity	+1	4.128 m/s
			0	3.493 m/s
			-1	2.858 m/s

and a series of tests based on combinations of the three values for each variable is conducted. The three equally spaced values for each variable will be termed “levels” from this point forward. The choice of three levels for each x_i is based on the need to find intermediate curvature points in the test data when fitting test data to the second-order mathematical model (8.5).

Refer to Table 8.1. The four independent variables chosen to measure the maximum center deflection of the two-phase FEM on impact are shown along with their respective test levels. The variables and their values are shown as either actual values or coded values. Unitless coded variables and values (shown as $-1 \leq x_i \leq +1$) are often applied when fitting an empirical model to the form (8.5) because actual values can at times be cumbersome to work with if the independent variables are not of the same order of magnitude or if the variables have drastically different units (more will be said of this point later). The uncoded (or actual) independent variables and values can in some instances have values and units that are similar in nature in which case the advantages with applying unitless coded variables no longer exist. Using actual values of variables (C_i and v_{tup} with their associated values) can be advantageous

in that the mathematical model (8.5) is easier to relate to physical numbers. It is valid to use either actual variables or coded variables in practice, and it is possible to translate between actual and coded values provided some assumptions are applied. Whether coded or actual variables are used, generally \hat{y} is measured as an actual value and is not coded even when coded variables are used. More will be said of this in subsequent paragraphs and examples associated with the two-phase FEM will be provided.

It was stated earlier that fitting a second-order polynomial requires each x_i factor (coded or uncoded) to be tested at three different levels to define the curvature in the response \hat{y} . A standard series of experiments that would be used to determine the complete response surface \hat{y} for k factors at three levels for each factor would require 3^k experiments. A study involving $k = 3$ factors would thus require 27 experiments and $k = 4$ would require 81 experiments for a complete response surface. It is easy to see that the more variables that are associated with the response \hat{y} , the more tests are required to wholly capture the complete second-order response surface of \hat{y} .

An efficient method for generating the coefficients in equation (8.5) has been developed by Box and Behnken [22]. In this study, the second-order polynomial model consists of four independent variables, three of which are associated with the material properties of Ti and TiB and the fourth is the velocity of the tup. These variables were shown in Table 8.1 within the context of equation (8.5). The series of tests necessary to determine the b -coefficients (15 in all for the four factors x_i) in equation (8.5) are shown in Table 8.2. According to the Box-Behnken designed experiments, 27 tests must be conducted where \hat{y} is measured (again, \hat{y} is the maximum center deflection of the FGM plate denoted w_0^{FEM}) using the combination of variables and associated levels shown in Table 8.2. The series of 27 tests necessary to accomplish this is shown for coded variables and values as well as actual variables and values for reference.

Some explanation into the factors and series of experiments is in order. First, each variable is subject to change in each test according to the order of experiments in Table 8.2. The variables are tested at three points to check for curvatures when fitting the model into the form of equation (8.5). The three levels are chosen beforehand based on some range of interest. In this instance, the levels for each of the three material coefficients were chosen based on a range of material data from various authors (see Chapter IV, Section 4.3 for the references and discussion). The three levels for each velocity were chosen based on the Dynatup tests in order to encompass the full range of tup velocities (these are velocities in metric units associated with 6750 in/min, 8250 in/min, and 9750 in/min, respectively). The two-phase FEM was constructed according to the prescribed material properties and velocity levels in Table 8.2. Aside from these alterations, the two-phase FEM was exactly the same as described in Chapter VI. Once each FEM had been solved (27 models total), the maximum transverse deflection of the mid-surface, w_0 , was extracted from the model solution. The result of each test is shown in Table 8.2 along with the test settings in coded and uncoded form.

The next step in the process is to construct the mathematical model (8.5) using the common least-squares approach. The model is constructed by determining the b -coefficients. Without derivation, the equations for doing so can be posed in matrix and vector form by setting:

$$\mathbf{X} = \begin{bmatrix} 1 & \mathbf{x}_1 & \mathbf{x}_2 & \mathbf{x}_3 & \mathbf{x}_4 & \mathbf{x}_1^2 & \mathbf{x}_2^2 & \mathbf{x}_3^2 & \mathbf{x}_4^2 & \mathbf{x}_1\mathbf{x}_2 & \mathbf{x}_1\mathbf{x}_3 & \mathbf{x}_1\mathbf{x}_4 & \mathbf{x}_2\mathbf{x}_3 & \mathbf{x}_2\mathbf{x}_4 & \mathbf{x}_3\mathbf{x}_4 \end{bmatrix} \quad (8.6)$$

where in coded form \mathbf{X} is tabulated in Table 8.3. A similar array for the actual variables and values can be tabulated, but second-order terms (that is, terms that are squared or cross-multiplied) must use the actual values and associated units. For brevity, only the coded form is shown. There were 27 tests and 15 b -coefficients to be determined in this math model of the two-phase FEM. Therefore \mathbf{X} is a 27 x 15 matrix as shown in Table 8.3. The response variable \hat{y} corresponds to the transverse

Table 8.2: Box-Behnken designed experiment for four factors (TiB material coefficients and tup velocity) with results from FEM (maximum transverse displacement at center of plate w_0^{FEM}) using coded and actual variables.

Test	Coded Variables				Actual Variables				Result w_0^{FEM} , mm
	x_1	x_2	x_3	x_4	C_1	C_2	C_3	v_{tup} , m/s	
1	-1	-1	0	0	2.60	0.30	1.00	3.493	0.2849
2	+1	-1	0	0	4.20	0.30	1.00	3.493	0.2401
3	-1	+1	0	0	2.60	0.50	1.00	3.493	0.2827
4	+1	+1	0	0	4.20	0.50	1.00	3.493	0.2374
5	0	0	-1	-1	3.40	0.40	0.90	2.858	0.2250
6	0	0	+1	-1	3.40	0.40	1.10	2.858	0.2248
7	0	0	-1	+1	3.40	0.40	0.90	4.128	0.3003
8	0	0	+1	+1	3.40	0.40	1.10	4.128	0.3003
9	0	0	0	0	3.40	0.40	1.00	3.493	0.2583
10	-1	0	0	-1	2.60	0.40	1.00	2.858	0.2466
11	+1	0	0	-1	4.20	0.40	1.00	2.858	0.2084
12	-1	0	0	+1	2.60	0.40	1.00	4.128	0.3310
13	+1	0	0	+1	4.20	0.40	1.00	4.128	0.2784
14	0	-1	-1	0	3.40	0.30	0.90	3.493	0.2592
15	0	+1	-1	0	3.40	0.50	0.90	3.493	0.2564
16	0	-1	+1	0	3.40	0.30	1.10	3.493	0.2597
17	0	+1	+1	0	3.40	0.50	1.10	3.493	0.2570
18	0	0	0	0	3.40	0.40	1.00	3.493	0.2583
19	0	-1	0	-1	3.40	0.30	1.00	2.858	0.2262
20	0	+1	0	-1	3.40	0.50	1.00	2.858	0.2240
21	0	-1	0	+1	3.40	0.30	1.00	4.128	0.3001
22	0	+1	0	+1	3.40	0.50	1.00	4.128	0.2981
23	-1	0	-1	0	2.60	0.40	0.90	3.493	0.2845
24	+1	0	-1	0	4.20	0.40	0.90	3.493	0.2393
25	-1	0	+1	0	2.60	0.40	1.10	3.493	0.2838
26	+1	0	+1	0	4.20	0.40	1.10	3.493	0.2391
27	0	0	0	0	3.40	0.40	1.00	3.493	0.2583

deflection w_0^{FEM} collected in each test. The results of the tests are assembled into a 27 x 1 vector and denoted \mathbf{Y} . The vector of coefficients \mathbf{b} corresponding to each of the 15 elements in \mathbf{X} is given by:

$$\mathbf{b} = (\mathbf{X}^T \mathbf{X})^{-1} \mathbf{X}^T \mathbf{Y} \quad (8.7)$$

The mathematical model for the two-phase FEM's maximum center transverse displacement was found to be, using this process with *unitless coded* variables:

$$\begin{aligned} \hat{y} &= (-258.34 * 10^{-6}) \\ &+ (22.57 * 10^{-6})x_1 + (1.21 * 10^{-6})x_2 + (9.25 * 10^{-9})x_3 + (-37.77 * 10^{-6})x_4 \\ &+ (-3.39 * 10^{-6})x_1^2 + (420.46 * 10^{-9})x_2^2 + (-42.04 * 10^{-9})x_3^2 + (-4.26 * 10^{-6})x_4^2 \\ &+ (142.00 * 10^{-9})x_1x_2 + (-148.50 * 10^{-9})x_1x_3 + (3.60 * 10^{-6})x_1x_4 \\ &+ (-55.50 * 10^{-9})x_2x_3 + (-90.75 * 10^{-9})x_2x_4 + (-45.25 * 10^{-9})x_3x_4 \\ &= w_0^{FEM} \end{aligned} \quad (8.8)$$

where $-1 \leq x_i \leq +1$. The units of w_0^{FEM} are *meters*. Since the coded variables for the TiB property coefficients and tup velocity are unitless, all the *b*-coefficients in equation 8.8 are in units of meters as well. If uncoded actual variables and values are used, the two-phase FEM mathematical model can be shown to be, based on the results in Table 8.2:

$$\begin{aligned} \hat{y} &= (-265.42 * 10^{-6}) \\ &+ (40.60 * 10^{-6})C_1 + (-17.00 * 10^{-6})C_2 + (19.52 * 10^{-6})C_3 + (-8.50 * 10^{-6})v_{tup} \\ &+ (-5.30 * 10^{-6})C_1^2 + (42.05 * 10^{-6})C_2^2 + (-4.20 * 10^{-6})C_3^2 + (-10.57 * 10^{-6})v_{tup}^2 \\ &+ (1.77 * 10^{-6})C_1C_2 + (-1.86 * 10^{-6})C_1C_3 + (7.09 * 10^{-6})C_1v_{tup} \\ &+ (-5.55 * 10^{-6})C_2C_3 + (-1.43 * 10^{-6})C_2v_{tup} + (-712.60 * 10^{-9})C_3v_{tup} \\ &= w_0^{FEM} \end{aligned} \quad (8.9)$$

Table 8.3: Box-Behnken [22] designed experiment for four factors with effects and interactions in coded form. The \mathbf{X} 27 x 15 array is tabulated here for the *coded* variables.

Test	1	x_1	x_2	x_3	x_4	x_1^2	x_2^2	x_3^2	x_4^2	x_1x_2	x_1x_3	x_1x_4	x_2x_3	x_2x_4	x_3x_4
1	1	-1	-1	0	0	+1	+1	0	0	+1	0	0	0	0	0
2	1	+1	-1	0	0	+1	+1	0	0	-1	0	0	0	0	0
3	1	-1	+1	0	0	+1	+1	0	0	-1	0	0	0	0	0
4	1	+1	+1	0	0	+1	+1	0	0	+1	0	0	0	0	0
5	1	0	0	-1	-1	0	0	+1	+1	0	0	0	0	0	+1
6	1	0	0	+1	-1	0	0	+1	+1	0	0	0	0	0	-1
7	1	0	0	-1	+1	0	0	+1	+1	0	0	0	0	0	-1
8	1	0	0	+1	+1	0	0	+1	+1	0	0	0	0	0	+1
9	1	0	0	0	0	0	0	0	0	0	0	0	0	0	0
10	1	-1	0	0	-1	+1	0	0	+1	0	0	+1	0	0	0
11	1	+1	0	0	-1	+1	0	0	+1	0	0	-1	0	0	0
12	1	-1	0	0	+1	+1	0	0	+1	0	0	-1	0	0	0
13	1	+1	0	0	+1	+1	0	0	+1	0	0	+1	0	0	0
14	1	0	-1	-1	0	0	+1	+1	0	0	0	0	+1	0	0
15	1	0	+1	-1	0	0	+1	+1	0	0	0	0	-1	0	0
16	1	0	-1	+1	0	0	+1	+1	0	0	0	0	-1	0	0
17	1	0	+1	+1	0	0	+1	+1	0	0	0	0	+1	0	0
18	1	0	0	0	0	0	0	0	0	0	0	0	0	0	0
19	1	0	-1	0	-1	0	+1	0	+1	0	0	0	0	+1	0
20	1	0	+1	0	-1	0	+1	0	+1	0	0	0	0	-1	0
21	1	0	-1	0	+1	0	+1	0	+1	0	0	0	0	-1	0
22	1	0	+1	0	+1	0	+1	0	+1	0	0	0	0	+1	0
23	1	-1	0	-1	0	+1	0	+1	0	0	+1	0	0	0	0
24	1	+1	0	-1	0	+1	0	+1	0	0	-1	0	0	0	0
25	1	-1	0	+1	0	+1	0	+1	0	0	-1	0	0	0	0
26	1	+1	0	+1	0	+1	0	+1	0	0	+1	0	0	0	0
27	1	0	0	0	0	0	0	0	0	0	0	0	0	0	0

Here, the actual variables are substituted in place of x_i to distinguish from the coded counterpart equation (8.8). Units associated with each b -coefficient are not shown because they can be complex and not physically meaningful based on the matrix-vector multiplication in 8.7.

The coded mathematical model in (8.8) was used in the parameter estimation sequence. *Thus, a coded value of C_1 , C_2 , C_3 , and v_{tup} must be used in equation (8.8).* The relations for a general uncoded value (C_i , v_{tup}) of a parameter and its associated

coded value (x_i) are:

$$\begin{aligned} x_1 &= \frac{C_1 - C_1^0}{C_1^{+1} - C_1^0} \\ x_2 &= \frac{C_2 - C_2^0}{C_2^{+1} - C_2^0} \\ x_3 &= \frac{C_3 - C_3^0}{C_3^{+1} - C_3^0} \\ x_4 &= \frac{v_{tup} - v_{tup}^0}{v_{tup}^{+1} - v_{tup}^0} \end{aligned}$$

where a superscript of +1 or 0 refers to the coded level of that parameter (see Table 8.1). In the relations C_i is the actual value of the parameter. Any value of C_i or v_{tup} can be used in (8.8) provided it is converted to a coded value and it within the limits of the +1 level and -1 level of the parameter (usually the +1 and -1 levels are taken at the upper and lower bounds for the variable, but not always so). The mathematical model should in general not be assumed reliable outside the limits of the tests, although it may be applicable to points in the set just outside the constraints (this is more of a judgment call based on subsequent tests and experience with the model).

The order of the tests were conducted in the order of Table 8.2 and the order itself was not randomized. Physical experiments should be randomized to account for effects that may affect test results (for instance, environmental conditions or different material lots), however in the computer simulation environment these factors really do not come into play and the order of the tests will not directly affect results.

The mathematical model (8.8) could have been refined by removing terms with coefficients that are sufficiently small that their contributions to the overall solution are very minor. In particular, some of the coefficients associated with the density parameter are small compared to the other coefficients. This is not unexpected since the density of Ti and TiB are close and the FST predictions do not require density for calculation since quasi-static assumptions were made. There are methods for

determining which terms of this nature can be removed without appreciably affecting results, however this was not done in this case.

In Table 8.4, the predictions from the mathematical model (8.8) are compared to those collected in the FEM tests (Table 8.2 is reproduced here). Just by inspecting the data, it is clear the mathematical model predicts the actual FEM test data *at the values of the variables where data was collected* very well. In fact, the sum of the squared errors for the model (SSE) is calculated by:

$$SSE = \sum (y_i - \hat{y}_i)^2 = 6.179 * 10^{-12} \approx 0 \quad (8.10)$$

and the sum of the squared totals (SST)

$$SST = \sum (y_i - \bar{y})^2 = 23.47 * 10^{-9} \approx 0 \quad (8.11)$$

where y_i are the individual test results and \hat{y}_i are the corresponding predictions for y_i using equation (8.8). \bar{y} is the mean of the 27 FEM tests. Low values of SSE are desired; the higher the value, the less the data corresponds with the mathematical model. SST is the sum of the square deviations of \mathbf{Y} data from the average. A metric associated with SSE and SST is called the R^2 metric:

$$R^2 = 1 - \frac{SSE}{SST} = 0.9997 \quad (8.12)$$

where $0 < R^2 < 1$. A value close to one is desired and is interpreted as a high correlation between the mathematical model and the data. The high degree of correlation, despite the random distribution of constituents, is likely due to the very fine mesh in the plate FEMs. *In other words, the small element size minimizes the probability that elements of a single constituent will be clustered together to affect the global response.* This is an important conclusion that will be addressed again at a later time. There are other mathematical metrics that could be considered, but given the demonstrated high degree of correlation between the math model of the FEM and the two-phase

Table 8.4: Box-Behnken designed experiment for four factors (TiB material coefficients and tup velocity) with results from FEM (maximum transverse displacement at center of plate w_0) in coded form.

Test	Coded Variable				Result	Predicted
	x_1	x_2	x_3	x_4	w_0^{FEM} , mm	w_0^{FEM} , mm
1	-1	-1	0	0	0.2849	0.2849
2	+1	-1	0	0	0.2401	0.2401
3	-1	+1	0	0	0.2827	0.2828
4	+1	+1	0	0	0.2374	0.2374
5	0	0	-1	-1	0.2250	0.2249
6	0	0	+1	-1	0.2248	0.2248
7	0	0	-1	+1	0.3003	0.3004
8	0	0	+1	+1	0.3003	0.3004
9	0	0	0	0	0.2583	0.2583
10	-1	0	0	-1	0.2466	0.2472
11	+1	0	0	-1	0.2084	0.2093
12	-1	0	0	+1	0.3310	0.3299
13	+1	0	0	+1	0.2784	0.2776
14	0	-1	-1	0	0.2592	0.2592
15	0	+1	-1	0	0.2564	0.2567
16	0	-1	+1	0	0.2597	0.2591
17	0	+1	+1	0	0.2570	0.2568
18	0	0	0	0	0.2583	0.2583
19	0	-1	0	-1	0.2262	0.2257
20	0	+1	0	-1	0.2240	0.2231
21	0	-1	0	+1	0.3001	0.3011
22	0	+1	0	+1	0.2981	0.2988
23	-1	0	-1	0	0.2845	0.2845
24	+1	0	-1	0	0.2393	0.2391
25	-1	0	+1	0	0.2838	0.2842
26	+1	0	+1	0	0.2391	0.2393
27	0	0	0	0	0.2583	0.2583

FEM itself, no more demonstration of the applicability is necessary. The mathematical model w_0^{FEM} will be used as part of the parameter estimation sequence in the remainder of the chapter.

8.3 Solution to the Minimization Problem

As a recap, estimation of the FGM properties has been posed such that the difference between the transverse deflection at the center of the FGM plate in the two-phase finite element model and analytical model of the impact tests is minimized. The difference in solutions is minimized by varying the set of material property estimates for TiB given constant properties of Ti and the properties of TiB are the properties of Ti multiplied by a constant. The properties are varied until the square of the differences converges to a minimum. The same properties are used in the two-phase FEM as in the analytical model. To this point, it has been shown how to obtain the center displacement from the two-phase FEM and from analytical theory. Nothing has been said regarding how the minimization problem is solved; this will be done in this section. The implementation of the parameter estimation sequence will be outlined in the following section.

The literature dedicated to minimization problems of one or more variables is very rich, and numerous excellent textbooks and papers can be found in mathematics, engineering, and sciences where minimization problems are solved for countless applications. The theory will not be derived in this section, however the necessary concepts required to solve and implement the minimization will be presented in the context of this application. The theory presented in this section is summarized wholly from the textbooks by Arora [8], Haftka et al. [52], and Dennis & Schnabel [37].

8.3.1 *General Constrained Minimization Problem.* The constrained minimization problem is generally defined as:

$$\begin{aligned} \min f(\mathbf{x}) &= f(x_1, \dots, x_n) \\ \text{Subject to } \mathbf{h}(\mathbf{x}) &= 0 \\ \mathbf{g}(\mathbf{x}) &\leq 0 \end{aligned} \tag{8.13}$$

where f is termed the objective function, a mathematical function of design variable $\mathbf{x} = (x_1, \dots, x_n)$; $\mathbf{h} = h_i$ are a set of $i = 1, \dots, p$ *equality* constraint equations, and $\mathbf{g} = g_i$ are a set of $i = 1, \dots, m$ *inequality* constraint equations. (Regarding notation, h_i in this section should not be confused with plate thickness h used in other chapters. Additionally, x was used in the previous section as notation for coded variables in the second-order math model of the FGM plate deflection; in this section it is merely a general design variable.)

The objective function, equality constraints, and inequality constraints can be combined into a new, single equation called the Lagrange function \mathcal{L} , defined as:

$$\mathcal{L}(\mathbf{x}, \lambda, \mu) = f(\mathbf{x}) + \lambda^T \mathbf{h}(\mathbf{x}) + \mu^T \mathbf{g}(\mathbf{x}) \tag{8.14}$$

λ and μ are two vectors of Lagrange multipliers, one vector for the p equality constraints and one vector for the m inequality constraints, respectively. The Lagrange multipliers are not functions of the design variable \mathbf{x} . The Lagrange function will be used to minimize the objective function $f(\mathbf{x})$ momentarily.

A couple notes from multivariable calculus are in order. First, for a general function $F(\mathbf{x})$, the gradient of F (denoted as ∇F) at some arbitrary point \mathbf{x}^* is given by:

$$\nabla F(\mathbf{x}^*) = \left[\frac{\partial F(\mathbf{x}^*)}{\partial x_1}, \frac{\partial F(\mathbf{x}^*)}{\partial x_2}, \dots, \frac{\partial F(\mathbf{x}^*)}{\partial x_n} \right]^T \tag{8.15}$$

The Hessian \mathbf{H} of F is determined by differentiating the gradient vector and is given by:

$$\mathbf{H} = \frac{\partial^2 F}{\partial \mathbf{x} \partial \mathbf{x}} = \begin{bmatrix} \frac{\partial^2 F}{\partial x_1 \partial x_1} & \frac{\partial^2 F}{\partial x_1 \partial x_2} & \cdots & \frac{\partial^2 F}{\partial x_1 \partial x_n} \\ \frac{\partial^2 F}{\partial x_2 \partial x_1} & \frac{\partial^2 F}{\partial x_2 \partial x_2} & \cdots & \frac{\partial^2 F}{\partial x_2 \partial x_n} \\ \vdots & \vdots & & \vdots \\ \frac{\partial^2 F}{\partial x_n \partial x_1} & \frac{\partial^2 F}{\partial x_n \partial x_2} & \cdots & \frac{\partial^2 F}{\partial x_n \partial x_n} \end{bmatrix} \quad (8.16)$$

The Hessian matrix is a symmetric matrix where each element of the matrix is a function of \mathbf{x} . Without derivation, a *necessary* condition for a local extremum, maximum or minimum, at \mathbf{x}^* is that the gradient of F is zero:

$$\nabla F(\mathbf{x}^*) = \mathbf{0} \quad (8.17)$$

A *sufficient* condition for a local *minimum* of F at \mathbf{x}^* is the Hessian matrix evaluated at \mathbf{x}^* must be positive definite, meaning all eigenvalues of $\mathbf{H}(\mathbf{x}^*)$ are greater than zero. Note that it is also *necessary* that the Hessian of F be at least positive semi-definite for $F(\mathbf{x}^*)$ to be a minimum, meaning that all eigenvalues of $\mathbf{H}(\mathbf{x}^*)$ are greater than or equal to zero. These concepts can be thought of in another way. First, the gradient vector points in the direction of maximum increase in a function. At a minimum or maximum point, the gradient equaling zero more or less says that the function does not necessarily increase or decrease initially in any one direction. The requirement of \mathbf{H} to be positive definite for a minimum simply means that F curves upward at \mathbf{x}^* . The “necessary” and “sufficient” conditions are simply what their names imply. It is necessary that the gradient of a function at its minimum be equal to zero, but that does not tell us for sure if we are actually looking at a minimum or a maximum point. It is necessary for the Hessian of F to be positive semi-definite at a minimum point, but without knowing if the gradient is zero at that point it is not clear if the point is indeed a minimizer. However, if $\mathbf{H}(\mathbf{x}^*)$ is positive-definite, then \mathbf{x}^* is a

minimizer of F without requiring a check on the gradient at that point...that is, it is sufficient information to make the judgment that \mathbf{x}^* is a minimizer without knowing anything else about F . On the other hand, if it is desired to maximize a function rather than minimize, the necessary conditions for a maximum of F at \mathbf{x}^* is that the gradient is equal to zero and the Hessian is negative semi-definite at the point \mathbf{x}^* . A sufficient condition for maximization of F at \mathbf{x}^* is that the Hessian at that point is negative-definite. An indefinite Hessian implies neither a maximum or minimum of F at \mathbf{x}^* .

Returning to the Lagrange function (8.14), the minimization of f subject to the equality and inequality constraints is accomplished by finding a point \mathbf{x}^* and associated Lagrange multipliers λ^* & μ^* that minimize the Lagrange function. The necessary conditions for minimizing \mathcal{L} such that f is minimized and satisfies the equality and inequality constraints are as follows, known as the Kuhn-Tucker (K-T) necessary conditions:

$$\begin{aligned}
\frac{\partial \mathcal{L}}{\partial x_j} &\equiv \frac{\partial f}{\partial x_j} + \sum_{i=1}^p \lambda_i * \frac{\partial h_i}{\partial x_j} + \sum_{i=1}^m \mu_i * \frac{\partial g_i}{\partial x_j} = 0; \quad j = 1 \text{ to } n \\
h_i(\mathbf{x}^*) &= 0; \quad i = 1 \text{ to } p \\
g_i(\mathbf{x}^*) &\leq 0; \quad i = 1 \text{ to } m \\
\mu_i * g_i(\mathbf{x}^*) &= 0; \quad i = 1 \text{ to } m \\
\mu_i^* &\geq 0; \quad i = 1 \text{ to } m
\end{aligned} \tag{8.18}$$

Since \mathcal{L} is a function of the design variable and two sets of Lagrange multipliers, the gradient of \mathcal{L} involves partial derivatives of the individual elements of the design variable and Lagrange multiplier vectors. If the gradient of \mathcal{L} is evaluated at a minimum point, its gradient will be zero (a necessary condition). The first condition of the K-T conditions is merely stating that the first partial derivatives of \mathcal{L} with respect to the design variable elements x_j must be zero. These equations represent a portion of the total gradient vector for \mathcal{L} . The next condition on the Lagrange function is that

the equality constraints h_i at the minimum point must be satisfied. This satisfies the conditions on the objective function f (equation (8.13)), but this K-T condition really comes from taking the partial derivative of \mathcal{L} with respect to each of the first set of Lagrange multipliers in λ and requiring these partial derivatives to be zero to meet the condition that all elements of the gradient equal zero at the minimum point. The next two of the five conditions must be treated simultaneously. The third condition, requiring g_i to be less than or equal to zero, is a similar consequence of taking the partial derivative of \mathcal{L} with respect to each of the second set of Lagrange multipliers in μ and requiring these partial derivatives to be zero to meet the condition that all elements of the gradient equal zero at the minimum point. However, the inequality constraints do not require that g_i be zero but rather less than or equal to zero. The fourth and fifth conditions, $\mu_i^* g_i(\mathbf{x}^*) = 0$ and $\mu_i^* \geq 0$, address the inequality portion of the third requirement. In the fourth condition, if g_i is non-zero, μ_i^* is required to be zero. If g_i is zero, μ_i^* is required to be non-zero. If μ_i^* is zero, meaning the constraint is satisfied as an inequality constraint, the constraint can be thought of as inconsequential to \mathcal{L} and is more or less not included, meaning there is one less partial derivative to assess in μ . If μ_i^* is non-zero, the partial derivative must be accounted for and g_i behaves more like an equality constraint. In either case, the terms involving μ^* and g_i do not contribute to the value of \mathcal{L} at the minimum point \mathbf{x}^* . The same can be said of h_i at the candidate minimum point. This is how a Lagrange function can be used to satisfy the requirements of equation (8.13) using a completely different function \mathcal{L} . Lastly, the fifth requirement that $\mu_i^* \geq 0$ must be satisfied is associated with the interpretation of the Lagrange multipliers. Without getting into the mathematical details associated with the multipliers, the physical interpretation of them in the context of the minimization problem is the amount of effort (or “force”) required mathematically to enforce the constraint equations (both equality and inequality) while searching for a minimum of \mathcal{L} over the region of interest. At the minimum point, $\mu_i^* \geq 0$ ensures that the gradients of the objective

and constraint equations point in opposite directions so that f cannot be reduced further in a negative gradient direction without violating constraints.

Another point regarding the Kuhn-Tucker conditions is worth mentioning. If the K-T conditions are satisfied, it is true that an extremum has been reached in \mathcal{L} . However, it does not necessarily imply that the point is a minimum. To verify that the candidate point is indeed a minimum, the Hessian of \mathcal{L} must be at least positive semi-definite (to satisfy the necessary second-order condition) or at best positive-definite (a sufficient condition for a minimum point). The Hessian of \mathcal{L} consists of second partial derivative terms including all the design variables and Lagrange multipliers (in essentially the same form as equation (8.16)).

Now that a little general knowledge of the minimization problem is understood, it will be applied directly to the problem at hand in the following paragraphs.

8.3.2 FGM Plate Parameter Estimation Problem. The minimization problem from (8.1) is copied here for reference:

$$\begin{aligned}
\min f &= (w_0^{FST} - w_0^{FEM})^2 \\
\text{Subject to} \quad &C_1^{min} \leq C_1 \leq C_1^{max} \\
&C_2^{min} \leq C_2 \leq C_2^{max} \\
&C_3^{min} \leq C_3 \leq C_3^{max}
\end{aligned} \tag{8.19}$$

(8.1) is termed a constrained minimization problem due to the minimum and maximum constraints on the $\mathbf{C} = C_i$ ($i = 1, 2, 3$) values. The constrained minimization

problem can be rewritten in the following fashion:

$$\begin{aligned}
f(\mathbf{C}) &= (w_0^{FST}(C_1, C_2) - w_0^{FEM}(C_1, C_2, C_3))^2 \\
g_1(\mathbf{C}) &= C_1^{min} - C_1 \leq 0 \\
g_2(\mathbf{C}) &= C_1 - C_1^{max} \leq 0 \\
g_3(\mathbf{C}) &= C_2^{min} - C_2 \leq 0 \\
g_4(\mathbf{C}) &= C_2 - C_2^{max} \leq 0 \\
g_5(\mathbf{C}) &= C_3^{min} - C_3 \leq 0 \\
g_6(\mathbf{C}) &= C_3 - C_3^{max} \leq 0
\end{aligned} \tag{8.20}$$

$f(\mathbf{C})$ is termed the objective function and the equations $g_i(\mathbf{C})$ in (8.20) are the *inequality* constraint equations. The objective function and the constraint equations are combined into a Lagrange equation, as follows:

$$\mathcal{L} = f(\mathbf{C}) + \mu^T \mathbf{g}(\mathbf{C}) \tag{8.21}$$

μ is a vector of Lagrange multipliers, one for each inequality constraint equation. $\mathbf{g}(\mathbf{C})$ is the vector of constraint equations g_i . In our case, we have six Lagrange multipliers and six constraint equations. The minimum point of $\mathcal{L}(\mathbf{C})$ occurs at $[\mathbf{C}^*, \mu^*]$, subject to the Kuhn-Tucker necessary conditions. If the point \mathbf{C}^*, μ^* is truly a minimizer of \mathcal{L} , then the Hessian of \mathcal{L} will be at least positive semi-definite and at best positive-definite to satisfy the necessary and sufficient conditions for a minimum point.

The minimization problem will be solved numerically. The mathematical model for the two-phase FEM is rather straightforward, however the analytical prediction for w_0^{FST} is very difficult to evaluate into a simple closed-form relationship. All partial derivatives will be evaluated numerically and the solution to find the minimizer of \mathcal{L} will be conducted using a modified Newton's method. These will be explained in the following paragraphs.

8.3.3 *Numerical Solution.* The concepts of this discussion are summarized primarily from the numerical analysis text by Dennis & Schnabel [37], with some additional inputs from [8], [52], and [143]. The minimization problem in equation (8.1) in terms of the Lagrange equation (8.21) was solved using a *modified form of Newton's method*. The choice of Newton's method versus other numerical techniques was based in its simplicity and ease of implementation, although almost any similar technique could in theory be used. A derivation of Newton's method will not be provided, but the reader can refer to the references above for additional details.

Newton's method is designed to solve the following problem:

$$\text{Given } F : \mathbb{R}^n \rightarrow \mathbb{R}^n, \quad \text{find } \mathbf{x}^* \in \mathbb{R}^n \text{ such that } F(\mathbf{x}^*) = 0 \quad (8.22)$$

where F is a system of nonlinear equations f_1, f_2, \dots, f_m (m here is not the same number as the number of m inequality constraints) that are continuously differentiable. The Newton's Method algorithm to solve the series of nonlinear equations $F = 0$ is to solve the following at each iteration $k = 0, 1, \dots$:

$$\begin{aligned} J(\mathbf{x}_k) \mathbf{s}_k &= -F(\mathbf{x}_k) \\ \mathbf{x}_{k+1} &= \mathbf{x}_k + \mathbf{s}_k \end{aligned} \quad (8.23)$$

where the initial guess for \mathbf{x}_k is $\mathbf{x}_0 \in \mathbb{R}^n$. $J(\mathbf{x})$ is the Jacobian ($m \times n$) matrix

$$J(\mathbf{x}) = F'(\mathbf{x})_{ij} = \frac{\partial F_i}{\partial x_j}(\mathbf{x}) = \nabla F^T(\mathbf{x}) \quad (8.24)$$

The algorithm terminates when \mathbf{x} has converged acceptably (usually by some user-determined convergence criteria) to a solution \mathbf{x}^* . Depending on the nature of F , the initial guess \mathbf{x}_0 for the solution \mathbf{x}^* can be important. If F has multiple solutions, potentially Newton's method could converge to a local minimum that is less optimal than another local minimum or even a global minimum. Another important point is

that convergence can be slow if the solution to F is near a “plateau” where local \mathbf{x} in the vicinity of \mathbf{x}^* produce F results that are very close to $F = 0$.

In the case of the minimization problem, we want to satisfy the necessary condition that the gradients of the Lagrange equation are equal to zero under the Kuhn-Tucker conditions. In the context of this problem, Newton’s method solves:

$$\text{Given } \mathcal{L} : \mathbb{R}^n \rightarrow \mathbb{R}, \quad \text{find } \bar{\mathbf{x}}^* \in \mathbb{R}^n \text{ such that } \nabla \mathcal{L}(\bar{\mathbf{x}}^*) = 0 \quad (8.25)$$

and the algorithm is given by

$$\begin{aligned} \nabla^2 \mathcal{L}(\bar{\mathbf{x}}_k) \mathbf{s}_k &= -\nabla \mathcal{L}(\bar{\mathbf{x}}_k) \\ \bar{\mathbf{x}}_{k+1} &= \bar{\mathbf{x}}_k + \mathbf{s}_k \end{aligned} \quad (8.26)$$

where $\nabla^2 \mathcal{L}(\mathbf{x})$ is the Hessian of \mathcal{L} as described in equation (8.16). $\bar{\mathbf{x}}$ is, for the general optimization problem, $[\mathbf{x}, \lambda, \mu]$. *In the FGM plate parameter estimation problem, there were no equality constraints so $\bar{\mathbf{x}} = [\mathbf{x}, \mu]$.*

A few problems can arise in the implementation of the general Newton’s method. First, the solution can tend to become unbounded if the Hessian is nearly singular at one or more iterations. This problem is inherent in Newton’s method algorithms. Also, there is no guarantee that the algorithm will not converge to a maximum point instead of a minimum point. The second problem is addressed by employing a modified Newton’s method. This algorithm was used to solve this particular minimization problem. In the modified Newton’s method, solve the following [47], [37]:

$$\text{Given } \mathcal{L} : \mathbb{R}^n \rightarrow \mathbb{R}, \quad \text{find } \bar{\mathbf{x}}^* \in \mathbb{R}^n \text{ such that } \nabla \mathcal{L}(\bar{\mathbf{x}}^*) = 0 \quad (8.27)$$

and the algorithm is

$$\begin{aligned}
H_k &= \nabla^2 \mathcal{L}(\bar{\mathbf{x}}_k) + \Gamma_k I \\
H_k \mathbf{s}_k &= -\nabla \mathcal{L}(\bar{\mathbf{x}}_k) \\
\bar{\mathbf{x}}_{k+1} &= \bar{\mathbf{x}}_k + \mathbf{s}_k
\end{aligned} \tag{8.28}$$

Γ_k is a coefficient at each iteration and I is the identity matrix. $\nabla^2 \mathcal{L}(\bar{\mathbf{x}}_k)$ is tested for positive definiteness at each iteration. If $\nabla^2 \mathcal{L}(\bar{\mathbf{x}}_k)$ is positive definite at iteration k , Γ_k is set equal to zero. If $\nabla^2 \mathcal{L}(\bar{\mathbf{x}}_k)$ is not positive definite, Γ_k is set sufficiently large so that when multiplied by the identity matrix and added to $\nabla^2 \mathcal{L}(\bar{\mathbf{x}}_k)$, the new matrix H_k is positive definite. There are many ways to accomplish this, but in this work Γ_k was programmed to be larger than the magnitude of the most negative eigenvalue of $\nabla^2 \mathcal{L}(\bar{\mathbf{x}}_k)$; a technique proposed by Dennis and Schnabel [37]. If $\nabla^2 \mathcal{L}(\bar{\mathbf{x}}_k)$ was at least positive semi-definite, Γ_k was set to zero. By forcing the Hessian (or modified Hessian) to be positive semi-definite at each iteration, the method is forced to move toward a minimizing direction.

The complexity of evaluating w_0^{FST} is such that analytical formulas for the gradient and Hessian of \mathcal{L} are extremely difficult to obtain. Numerical partial derivatives were used to estimate the gradient and the Hessian at each iteration [37]. To estimate the gradients and Hessians, the following equations were used at each iteration:

$$\nabla \mathcal{L}_i = \frac{\mathcal{L}(\bar{\mathbf{x}} + \tau \mathbf{e}_i) - \mathcal{L}(\bar{\mathbf{x}} - \tau \mathbf{e}_i)}{2\tau} \tag{8.29}$$

$$\nabla^2 \mathcal{L}_{ij} = \frac{\mathcal{L}(\bar{\mathbf{x}} + \tau \mathbf{e}_i + \tau \mathbf{e}_j) - \mathcal{L}(\bar{\mathbf{x}} + \tau \mathbf{e}_i) - \mathcal{L}(\bar{\mathbf{x}} + \tau \mathbf{e}_j) + \mathcal{L}(\bar{\mathbf{x}})}{\tau^2} \tag{8.30}$$

where τ is the step size for incrementation (not to be confused with the equality constraints) and \mathbf{e}_i is the i -th unit vector (a value of one at element i and zeros everywhere else). The estimates work well provided the step-size is kept small since both numerical estimates have error of order $\mathcal{O}(\tau)$. These estimates were chosen because of their simplicity in implementation, although note that there are other

numerical estimates for both the gradient and Hessian available in the literature with significantly less error associated with them that allow larger choices of τ .

The modified Newton's method solution was terminated once the changes in the gradient of \mathcal{L} from one iteration to the next were very small. This was done by evaluating the vector norm of the gradient at the current iteration and comparing it to the vector norm of the previous iteration. If the change in the value of the norm was sufficiently small (that is, the norm did not change by more than 0.0001), the solution was terminated. The gradient of \mathcal{L} was checked to make sure the final iteration brought the solution to within numerical error of zero. The Hessian was also evaluated at the final iteration to ensure that the matrix was positive definite. The results, presented in the next section, were all found to satisfy the necessary and sufficient conditions for a minimum of \mathcal{L} in all cases.

One last note regarding the solution to a minimum. It has not and will not be proved in this chapter that our Lagrange function is a convex function. Convex functions are functions defined on convex sets (that is, a set S in \Re^n is called convex if, for every pair of \mathbf{x} and \mathbf{y} in S and every real θ that satisfies $0 < \theta < 1$, $\theta\mathbf{x} + (1 - \theta)\mathbf{y} \in S$ [7]; geometrically this means a line segment drawn between two points contained in S is contained wholly in S), but not all functions defined on convex sets are convex functions. A function defined on a convex set is convex if its Hessian is positive semi-definite or positive definite for all points in the convex set. Convex functions have a nice property that a local minimum of the function in the convex set is also a global minimum [8]. In terms of the optimization problem, the set of design variables \mathbf{C} is convex because the inequality constraints are convex functions themselves (due to their linearity and our definition of a convex function) [8]. If equality constraints were present, they would need to be linear for the set to be convex [8]. Whether or not the Lagrange function is convex is difficult to prove since analytical gradients and Hessians are not determined. It is much easier to prove convexity with analytical functions. At this time, it will be assumed that the Lagrange function is not convex and care will be taken with the numerical solutions presented in the following pages.

8.4 Implementation

The following is a summary of the steps to implement this parameter estimation sequence. This sequence is demonstrated using the Ti-TiB FGM, but the steps to carry out the estimation can be used with any two-constituent material system evaluated in the manner the Ti-TiB FGM plates have been in this dissertation. It will be assumed that a mathematical model for the finite element response of the FGM has already been determined.

1. Set the material properties of one constituent to be held constant, named constituent 1 here (Ti for this study). (This choice should be based on strong knowledge of the properties of this constituent from extensive published data; if this is not available, one must use best engineering judgment in choosing the constituent whose properties should be set constant). The properties of constituent 2 (TiB) will be a set of constants multiplied by the set of material properties for the first constituent:

$$\text{FGM Constituent 1: } \mathcal{P}_1, \mathcal{P}_2, \dots, \mathcal{P}_n$$

$$\text{FGM Constituent 2: } C_1*\mathcal{P}_1, C_2*\mathcal{P}_2, \dots, C_n*\mathcal{P}_n$$

2. Determine limits for the constants as constraints on the solution.
3. Assemble the objective function and constraints into the minimization problem (8.20). Form the Lagrange function by augmenting the objective function with the constraint relations multiplied by the set of Lagrange multipliers.
4. Choose a set of constants C_1, \dots, C_n as an initial estimate for the properties of constituent 2 within the constraints of the set. Set the vectors of Lagrange multipliers to zero. Assemble the vector $\bar{\mathbf{C}}_k = [\mathbf{C}_k, \mu_k]$. At this initial estimate, $k = 0$. Choose numerical step-size τ (a fixed step-size was used here but a variable step-size could potentially be used to increase fidelity) and convergence tolerance criteria to terminate the numerical solution.
5. Evaluate the gradient and Hessian of \mathcal{L} at $\bar{\mathbf{C}}_k$.

6. Use the current properties for constituents 1 and 2 to solve for the transverse displacement of the FGM plate at the center with the mathematical model for the finite element tests, w_0^{FEM} .
7. Using the strain gage data (maximum radial strains) from the nominal radial plate locations and the current estimate for the material properties of constituents 1 and 2, solve for the maximum impact load P from the impact event through equation (7.69). Use this P load and the current estimate for the material properties of constituents 1 and 2 to solve for the maximum transverse displacement w_0^{FST} at the center of the plate through equation (7.63).
8. Solve for the current estimate of \mathcal{L} using the solutions of w_0^{FST} , w_0^{FEM} , and the current estimate for $\bar{\mathbf{C}}_k$.
9. Perform the modified Newton's method iteration (8.28) to solve for $\bar{\mathbf{C}}_{k+1}$.
10. Evaluate the gradient and Hessian of \mathcal{L} at the updated $\bar{\mathbf{C}}_{k+1}$.
11. Compare the norm of $\nabla\mathcal{L}(\bar{\mathbf{C}}_k)$ to the norm of $\nabla\mathcal{L}(\bar{\mathbf{C}}_{k+1})$. If the absolute value of the difference of the two norms is less than a pre-defined tolerance, terminate solution and go to the next step. Else, set $k+1 = k$ and go to step 6.
12. If $\nabla^2\mathcal{L}$ (Hessian) at the updated $\bar{\mathbf{C}}_{k+1}$ is positive definite and $\nabla\mathcal{L}$ at the updated $\bar{\mathbf{C}}_{k+1}$ is sufficiently close to zero (determined by a user-defined metric), terminate solution and analyze minimum point. If minimum point is determined to be not acceptable, adjust initial choice of $\bar{\mathbf{C}}_0$ and repeat process.

8.5 Results

Here the results of the parameter estimation sequence will be evaluated. Only the FGM plate impact experiments will be discussed, since the parameter estimation sequence was designed to study these plates and not the monolithic plates. Additionally, this work is primarily interested in characterizing the response of FGM plates and not monolithic plates.

Table 8.5: Summary of FGM plate impact tests using Dynatup apparatus.

Test No.	Description	Crosshead Mass (kg)	Crosshead Height (m)	Velocity, Actual (m/s)	Impact Energy (J)
7	7-Layer Ti-TiB FGM	13.06	0.508	3.040	60.35
8	7-Layer Ti-TiB FGM	13.06	0.635	3.412	76.02
9	7-Layer Ti-TiB FGM	13.06	0.762	3.765	92.56
10	7-Layer Ti-TiB FGM	13.06	0.889	4.078	108.6

The test results related to the FGM plate experiments are recopied in Table 8.5 for reference throughout this section. The parameter estimation sequence was conducted as described in this chapter using four material models to estimate the analytical prediction of w_0^{FST} . These models were the classic rule-of-mixtures (ROM), the self-consistent model (SC), the Mori-Tanaka needles estimate (MT-N), and the Mori-Tanaka spheres estimate (MT-S). Refer back to Chapter III for detailed information on these models. The initial estimates for the material parameters published in this section were $C_1 = 3.40$, $C_2 = 0.40$, and $C_3 = 1.00$; essentially the center points from the Box-Behnken tests in Table 8.1. The choice of these initial values here was merely for conceptual convenience only and the choice of initial values is more or less arbitrary in the region of interest. The minimum and maximum constraints on the parameters are the minimum and maximum levels for each parameter shown in Table 8.1 relaxed by 20% in each direction. Given the high degree of correlation in the second-order math model for the two-phase FEM, it was felt that this range would be accurate to the two-phase FEM without running further tests in the Box-Behnken FEM tests. Note that while the results published in this section may not represent global minimums of \mathcal{L} (recall that analytically the convexity of the objective function was not evaluated) for the region of interest here, various initial estimates were taken throughout the region, including points on the boundary from the inequality constraints, and in all cases the algorithm converged to a very similar solution for the material parameters. The solutions found for these parameters are shown in Table 8.6 as tested for the four material models and experimental tests 7-9 (recall that the FGM

Table 8.6: Comparison of predicted coefficients for TiB material properties using the parameter estimation technique and four different material models. Initial estimates for the material parameters were $C_1 = 3.40$, $C_2 = 0.40$, and $C_3 = 1.00$.

Test	Coeff.	Material Model			
		ROM	SC	MT-S	MT-N
7	C_1	2.549	2.468	2.494	2.486
	C_2	0.3478	0.3583	0.3594	0.3602
	C_3	0.9458	0.9414	0.9409	0.9408
8	C_1	2.309	2.239	2.256	2.250
	C_2	0.3468	0.3551	0.3573	0.3572
	C_3	0.9325	0.9298	0.9277	0.9281
9	C_1	2.442	2.367	2.389	2.381
	C_2	0.3355	0.3424	0.3439	0.3441
	C_3	0.9540	0.9508	0.9501	0.9501

Table 8.7: Comparison of predicted coefficients for TiB material properties based on average from results shown in Table 8.6.

Coeff.	Material Model			
	ROM	SC	MT-S	MT-N
C_1	2.433	2.358	2.380	2.372
C_2	0.3434	0.3519	0.3535	0.3538
C_3	0.9441	0.9407	0.9396	0.9397

plate in Test 10 failed so data was not used in the estimation sequence from that test). When the FEM mathematical model was used to estimate w_0^{FEM} for iterations of the parameter estimation sequence, the velocity from the Dynatup experiment was used for v_{tup} and held constant. Thus, w_0^{FEM} for each estimation sequence was reduced to a function of C_1 , C_2 , and C_3 .

The estimates for the coefficients C_1 , C_2 , and C_3 in Table 8.6 show that in general all models estimated similar results for the three parameters. The difference in results is associated directly with the material models themselves and their estimates for material properties in each layer of the FGM. To illustrate this, consider the transverse displacements at the center of the plates at the minimization of \mathcal{L} summarized in Table

Table 8.8: Predicted maximum center displacement of plate at center of bottom surface using the predicted TiB coefficients in Table 8.6. All units in millimeters.

Test	Method	Material Model			
		ROM	SC	MT-S	MT-N
7	Plate Theory	0.25926	0.26197	0.26107	0.26136
	FEM Math Model	0.25927	0.26198	0.26108	0.26137
8	Plate Theory	0.29064	0.29336	0.29268	0.29291
	FEM Math Model	0.29065	0.29337	0.29269	0.29292
9	Plate Theory	0.30959	0.31261	0.31170	0.31199
	FEM Math Model	0.30960	0.31262	0.31171	0.31200

8.8. In all cases the parameter estimation sequence virtually estimated the same plate deflections at the center regardless of material model. Recall the estimation sequence was tied directly to the results of the plate experiments for all material models. Since the Ti-TiB plates should ideally have the same composition through the thickness and the plates should have the same average behavior in each layer regardless of the material model chosen, it should be expected that the parameter estimation sequence would converge to very similar material properties for each layer and adjust C_i so that the material model reflects this. In Table 8.9, it is evident that this is indeed the case. The material property estimates (E and ν only) in each layer, based on the average results for C_i in Table 8.7 show a very strong degree of correlation between the layers. Further, the estimates for these layers based on C_i correlate well with the published results determined experimentally. The correlation between the published results is strongest at low-medium volume fractions of TiB and weakest (but still pretty good) at higher volume fractions of TiB. This is very likely associated with residual titanium diboride known to be present at higher volume fractions of TiB (see Chapter IV) affecting the predictions from the estimation sequence.

In Chapter VII, it was shown that the maximum impact force P in each test could be related to the maximum radial strains at points on the plate. Since the force data was not collected during the tests, the strain histories from the plates were

Table 8.9: Elastic property data from parameter estimation scheme for Ti-TiB volume ratios using the (averaged) predicted values from the four material models in the estimation sequence, compared to properties determined experimentally in the literature.

Configuration		Ref. [55]	ROM	SC	MT-S	MT-N
%Ti	%TiB	E , GPa	E , GPa	E , GPa	E , GPa	E , GPa
15	85	274.3	244.0	231.7	234.3	232.7
25	75	247.6	228.2	213.9	217.0	215.2
40	60	193.7	204.6	188.4	192.6	190.8
55	45	162.2	180.9	165.1	169.9	168.2
70	30	139.4	157.3	144.1	148.6	147.4
85	15	120.1	133.6	125.8	128.7	128.0
100	0	106.9	110.0	110.0	110.0	110.0

Configuration		Ref. [55]	ROM	SC	MT-S	MT-N
%Ti	%TiB	ν	ν	ν	ν	ν
15	85	0.170	0.150	0.161	0.160	0.161
25	75	0.182	0.173	0.187	0.185	0.187
40	60	0.216	0.206	0.225	0.220	0.222
55	45	0.246	0.240	0.259	0.253	0.255
70	30	0.276	0.273	0.290	0.284	0.286
85	15	0.310	0.307	0.317	0.313	0.314
100	0	0.340	0.340	0.340	0.340	0.340

Table 8.10: Predicted maximum force applied to the plate at instant of maximum center displacement using the predicted TiB coefficients in Table 8.6. All units are in kilonewtons.

Test	Method	Material Model			
		ROM	SC	MT-S	MT-N
7	Strain Gage 1	96.24	92.57	93.61	93.22
	Strain Gage 2	131.75	126.82	128.16	127.61
	Strain Gage 3	96.35	92.88	93.73	93.32
	<i>Average Load</i>	108.11	104.09	105.16	104.72
8	Strain Gage 1	111.15	107.91	108.81	108.46
	Strain Gage 2	130.31	126.58	127.58	127.16
	Strain Gage 3	101.52	98.72	99.42	99.09
	<i>Average Load</i>	114.33	111.07	111.94	111.57
9	Strain Gage 1	121.29	117.18	118.36	117.91
	Strain Gage 2	157.87	152.63	154.07	153.47
	Strain Gage 3	97.924	94.78	95.57	95.19
	<i>Average Load</i>	125.70	121.53	122.67	122.19

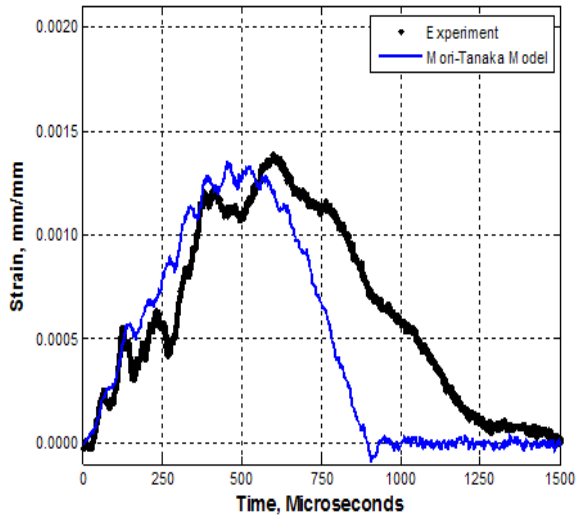
used to estimate P . The predictions of load P are affected by the material properties through the FGM plates. In Table 8.10, the estimated force P based on the strain histories in each test at each location are compared with the different material models used to predict C_i . The average predicted load was calculated at each iteration of the parameter estimation sequence. The data in table yields some interesting results. First, the average P for each test matches very well regardless of material model. This is another verification of the statement that the estimation sequence attempts to match the properties in each layer to the actual FGM within the framework of the material model used in the sequence. Secondly, the results show the trend that the force increases as the velocity/energy increases for each test. Lastly, the P loads individually calculated at each position vary somewhat in each test, adding verification to the claim of the variability that occurred in strain gage placement on each plate (due to human error).

Table 8.11: Maximum strains from the three strain gages for the tests, the Mori-Tanaka needles estimates (MT-N, reproduced from Chapter VI) and the Mori-Tanaka needles estimates using the parameter estimation scheme (MT-N/PE).

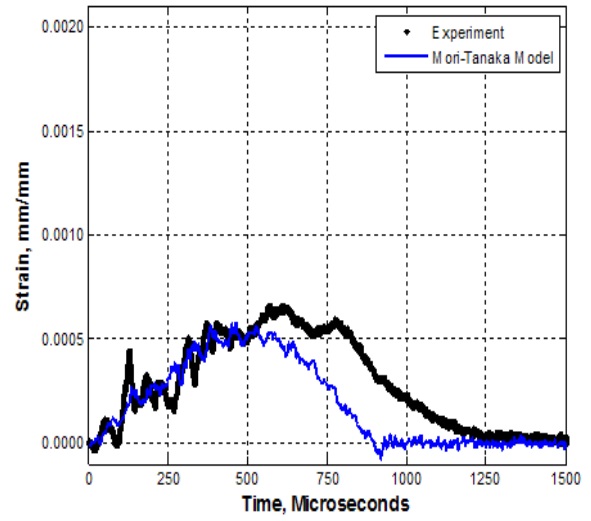
Test	Description	Maximum Strains (Gage 1)		
		Test	MT-N	MT-N/PE
7	7-Layer Ti-TiB FGM	0.001460	0.001621	0.001741
8	7-Layer Ti-TiB FGM	0.001783	0.001737	0.001858
9	7-Layer Ti-TiB FGM	0.001889	0.001885	0.002016
10	7-Layer Ti-TiB FGM	Failed	0.002057	0.002199

Test	Description	Maximum Strains (Gage 2)		
		Test	MT-N	MT-N/PE
7	7-Layer Ti-TiB FGM	0.001391	0.001281	0.001337
8	7-Layer Ti-TiB FGM	0.001468	0.001358	0.001449
9	7-Layer Ti-TiB FGM	0.001720	0.001890	0.001558
10	7-Layer Ti-TiB FGM	Failed	0.002061	0.001724

Test	Description	Maximum Strains (Gage 3)		
		Test	MT-N	MT-N/PE
7	7-Layer Ti-TiB FGM	0.0006638	0.0005626	0.0005797
8	7-Layer Ti-TiB FGM	0.0007573	0.0008032	0.0008284
9	7-Layer Ti-TiB FGM	0.0007016	0.0006498	0.0006564
10	7-Layer Ti-TiB FGM	Failed	0.0009522	0.0009839

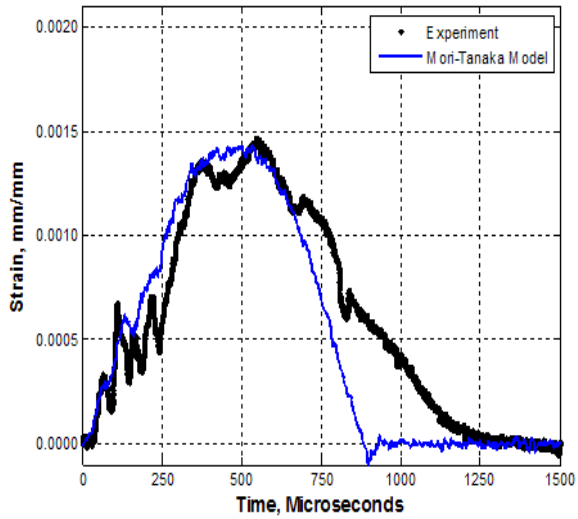


a)

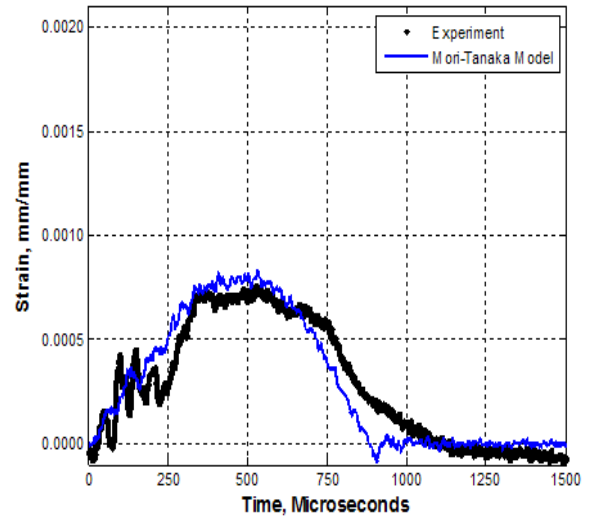


b)

Figure 8.1: Test 7 experimental strain histories & FEM comparison using optimized Mori-Tanaka Needles plate models: a) strain gage 2, b) strain gage 3.

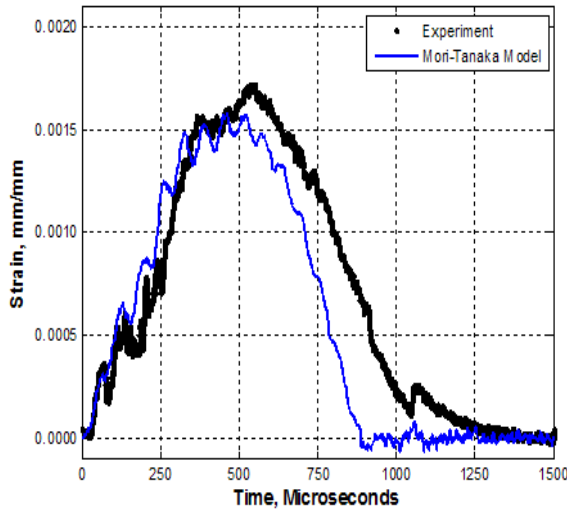


a)

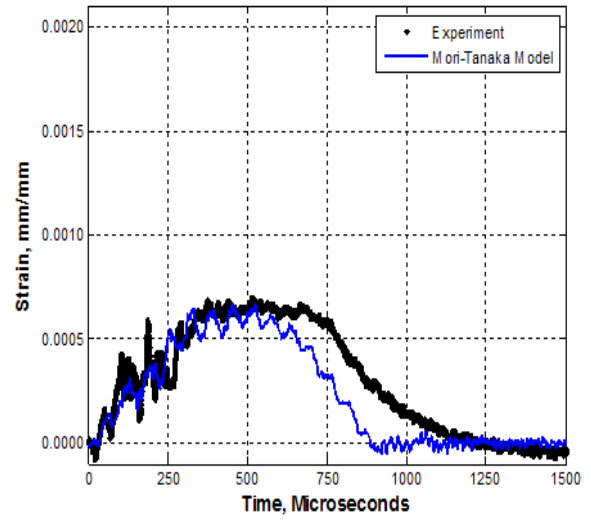


b)

Figure 8.2: Test 8 experimental strain histories & FEM comparison using optimized Mori-Tanaka Needles plate models: a) strain gage 2, b) strain gage 3.

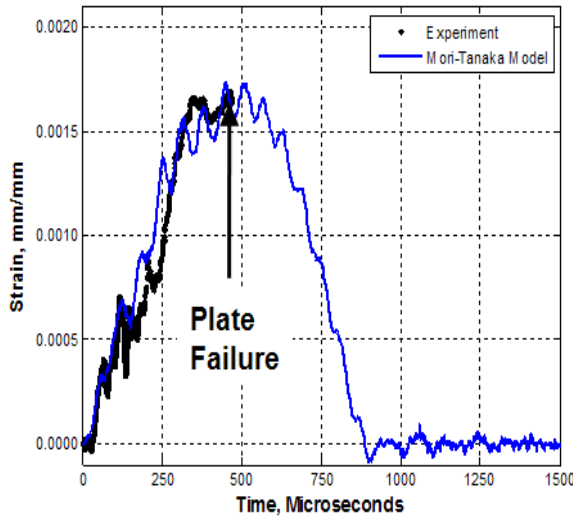


a)

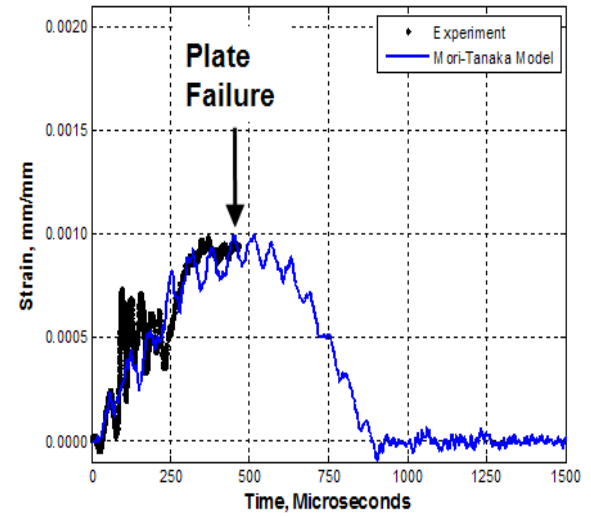


b)

Figure 8.3: Test 9 experimental strain histories & FEM comparison using optimized Mori-Tanaka Needles plate models: a) strain gage 2, b) strain gage 3.



a)



b)

Figure 8.4: Test 10 experimental strain histories & FEM comparison using optimized Mori-Tanaka Needles plate models: a) strain gage 2, b) strain gage 3.

Lastly, Figures 8.1-8.4 show the strain histories from the homogenized-layers FEMs using the Mori-Tanaka needles material model results compared to the experimental strain histories for FGM plate tests 7-10 (C_i per Table 8.7). The other models were not plotted simply because the results were virtually the same (as demonstrated through the correlation of layer-by-layer material properties). The FEM results match the test data very well for the most part, but it appears that little improvement of the overall histories was gained through the parameter estimation process (compare with the plots of Chapter VI). Most of the peculiarities observed in the experimental strain histories (discussed in Chapter V) are still not captured with the optimized FEMs and therefore more investigation needs to be conducted into the FGM plates and the Dynatup plate-tup interactions in the laboratory. The FEM determined through this process, however, correlates much better with published results and was developed through a process more directly tied to the physics and results of the Dynatup impact tests. For this reason, the model for the FGM plates developed in this chapter will be used exclusively through the remainder of this work.

8.6 Closing

This chapter described a parameter estimation sequence that can be used to estimate the material properties of FGM plates. The sequence ties experimental, analytical, and computational data from FGM plate impact events together and poses the estimation sequence as a sophisticated minimization problem. The results of the sequence were shown to correlate well with published material data available in the literature and matched trends observed and expected from the FGM plate impact experiments. The optimized model of the FEM was shown to emulate the plate experiments well, but little improvement was obtained over and above the models discussed in previous chapters where material properties of the Ti-TiB constituents and the material models relating the properties and volume fractions of the constituents were assumed to be known. The parameter estimation sequence nevertheless simultaneously satisfied two objectives in this research: (1) *correlate the results from the*

experiments and finite element models to available analytical theory and (2) refine the finite element material models using parameter estimation techniques to more effectively and accurately simulate the FGM plate impact experiments. The parameter estimation sequence is a valuable contribution to the field of FGMs given that the method has been demonstrated to effectively link analytical theory, computer simulations, and experimental data for a metal-ceramic FGM system, and the sequence is theoretically applicable to other FGM systems as well.

Before concluding this chapter, a couple of notes with respect to the monolithic plates are in order. First, the 100% Ti plates are not affected by the study since (a) the two-phase and homogenized-layers FEM models are the same, (b) the properties of TiB were varied during the optimization and the properties of Ti remained constant. The 15% Ti-85% TiB plates did not yield test results and really have not been studied in this dissertation due to lack of information on these specimens. Lastly, monolithic 85% Ti-15% TiB specimens can only be studied after the parameter estimation sequence has yielded acceptable results; that is, since a math model for the monolithic two-phase FEMs was not constructed, their test results cannot be used to predict material properties. However, the same estimation sequence could have been used to estimate the properties of the monolithic specimens using more or less the same steps as detailed in this chapter. The predicted material properties and material models from the FGM parameter estimates will be applied to the monolithic specimens and some of the results will be discussed in Chapter IX.

IX. Study of the Impact Response of the FGM Plates

Many of the interesting features associated with the physics of the impact events with FGMs have not yet been discussed. This fact is attributed to the need to validate a FEM that can properly characterize the behavior of an actual metal-ceramic FGM system. Having accomplished this, the FEM can be used to study the physics of the impact events. The optimized FEM of the previous chapter has been shown to be a good model of the actual Dynatup experiments. *This optimized finite element model will be used to study the interesting features of the impact events in this chapter.* This chapter will be wholly dedicated to studying a few of the behaviors associated with the impact experiments and will demonstrate the utility of using these FEMs in studying the impact response of metal-ceramic FGM plates. *This is precisely the chief objective of this work: characterizing the impact response of FGM plates.* Four aspects of the impact response of FGM plates will be studied in this chapter. First, the contact interaction between the tup and plate will be addressed. Next, the loading and unloading characteristics of the FGM plate will be studied through the strain histories in both the experiment and the FEM. Next, the stress distributions in the FGM plates will be studied using both the two-phase and homogenized-layers FEMs as they develop throughout the impact event and the distributions will be compared to those in monolithic specimens. Lastly, the effects of an impact from the tup slightly away from the center of the plate will be presented.

9.1 Tup and Plate Interaction

The rebound of the tup after the maximum force has been applied to the plates is a dynamic that was not addressed earlier in the dissertation. In this section, the FEM will be used to better understand this interaction between the plate and tup. To study this, the displacements and velocities of two nodes in the model will be checked. The first node is at the very tip of the tup, precisely at the point of contact between the tup and the plate. The second node was located at the center of the plate at the bottom surface. This node in the plate was selected so that it was away from the tup

tip to prevent looking at results that are directly coupled through the contact forces in the FEM. Figure 9.1 shows the displacement and velocities of the two nodes. The tup was initially separated with a small gap just above the plate impact site. Thus, some of the displacement of the tup would account for the movement to close this gap, introducing displacement bias in the results. To account for this, the displacement was removed from the FEM output and the displacement for the tup was set to zero at the instant contact between the tup and plate initiated.

The key question here is: How long does the tup actually remain in contact with the plate specimen? In Figure 9.1 (a), the transverse displacements of the two nodes are plotted from FGM plate test 9 (crosshead mass 13.06 kg, impact velocity 3.765 m/s, impact energy 92.56 J, FGM plate). The nodes show a negative displacement as the tup bears downward and the plate flexes downward. (Recall the FEM coordinate system; a negative displacement from the FEM implies displacement downward.) The tup actually has a larger displacement downward than the plate. This would indicate local indentation at the contact point is occurring (0.07 mm at its maximum); recall that local dimpling of the specimens at the impact site on the FGM monolithic and functionally graded specimens was observed experimentally. When both nodes return to zero displacement, the nodes are at the same position as the instant contact was initiated. The time between initiation of contact and returning to the zero displacement is approximately 900 microseconds. This is about the same as the length of the significant portions of the strain histories in the experiments. This indicates that the tup and plate remained in contact over that entire period of time. After the 900 microsecond period of contact, the node remains very close to zero displacement while the tup displaces upward at a nearly uniform rate. This is the point where the two bodies separate and can clearly be viewed in Figure 9.1 (a). Recall that gravity was not included in the FEMs. The uniform displacement rate upward is a result of this truth; had gravity been included the tup would displace upward until its kinetic energy was converted completely to gravitational potential energy. Gravity was found to have virtually no effect on the results during the impact event itself

and since secondary impacts did not occur it did not contribute much to the overall result. Also note that the velocity at the impact site (the tup's maximum kinetic energy) was known and the small displacements from initiation of impact to maximum plate transverse deflection were sufficiently small that gravity did not contribute significantly to the potential energy of the system.

The velocities of the two nodes can be viewed in Figure 9.1 (b). (Positive velocities from the FEM indicate upward motion; negative velocities indicate downward motion.) At the initiation of contact, the tup node shows sharp (accelerations) oscillations at the beginning of the history. This is attributable to the abrupt shock to the tup at the plate interface. The node on the bottom surface of the plate does not undergo the dramatic accelerations that the tup node undergoes, but this is in part because the node is separated from the tup by seven graded layers of metal-ceramic mixtures and not directly at the interface. After about 100 microseconds, the velocity profiles for the nodes tend to converge together such that their profiles are nearly identical. The nodal velocities are in concert with each other with some gradual oscillations that trend upward. The velocities are negative early in the impact event but trend toward positive velocities later. This shows the plate (1) moving downward at impact, (2) reaches some maximum displacement where the tup and plate are basically at rest (only instantaneously), and (3) moves upward as the potential energy stored in the plate converts to kinetic energy and pushes the tup upward. This interaction is illustrated visually in Figure 9.2. As the plate moves upward, it pushes the tup upward until the plate reaches some maximum velocity (approximately 900 microseconds). The instant the upward velocity reaches its maximum, the tup separates (or ejects) from the plate. In the absence of gravity, the tup will not slow as it moves upward. After the initial ejection, the tup accelerates upward initially but then moves with more or less a "constant" velocity upward. It is true there are oscillations (accelerations) present in the node here but these are merely associated with local vibrations in the tup. The crosshead/tup assembly is at this point moving upward at constant velocity.

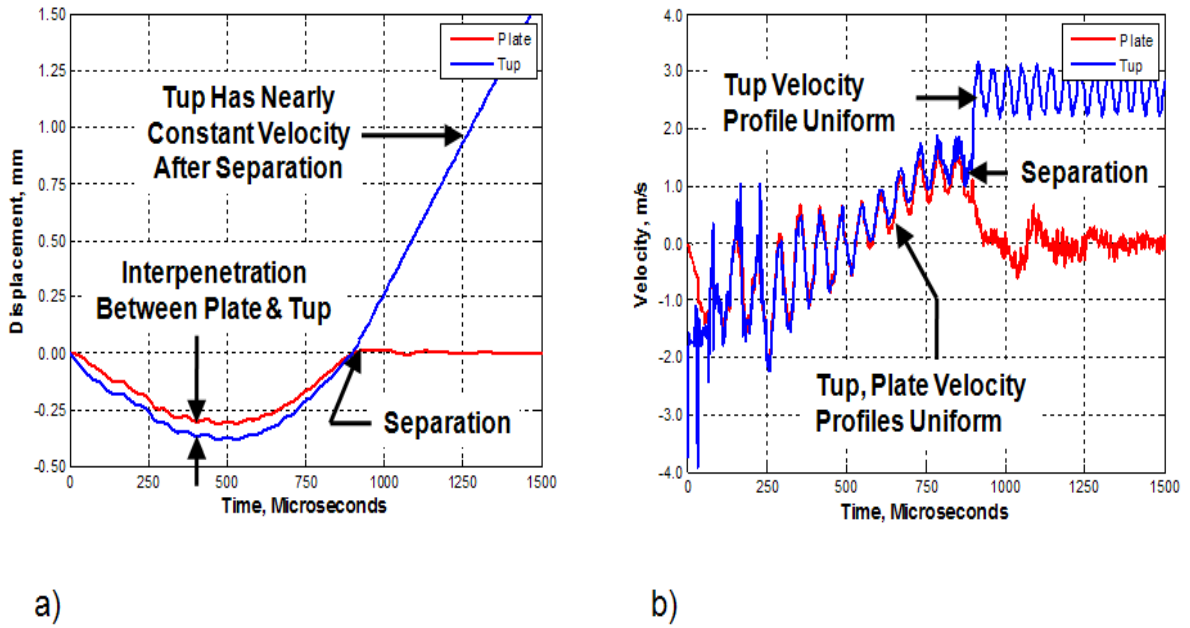


Figure 9.1: Transverse (a) displacement and (b) velocity profiles for the node at the tip of the tup (in contact with the plate) and the node on the bottom surface of the FGM plate at the center for the optimized FEM of test 9.

9.2 Loading and Unloading of the FGM Plates

The interaction between the tup and plate was characterized in the previous section. It was shown that the tup and plate remain in contact together for virtually the entire length of the significant strain histories in the plates. The impact between the plates occurs over two significant periods of time: (1) the “loading” portion of the impact that occurs between 1-2 in Figure 9.2; and (2) the “unloading” of the plate that occurs between 2-3 in Figure 9.2. In this section, the loading-unloading regions of the impacts will be studied.

Chapter VII showed that the analytical treatment of the FGM plates could be simplified to a quasi-static analysis given the length of time over which the tup applied loading to the FGM plates. However, this assumption does not imply that the response of the FGM plate is not dynamic. In fact, there are many interesting dynamic features that occur over the duration of the impact events.

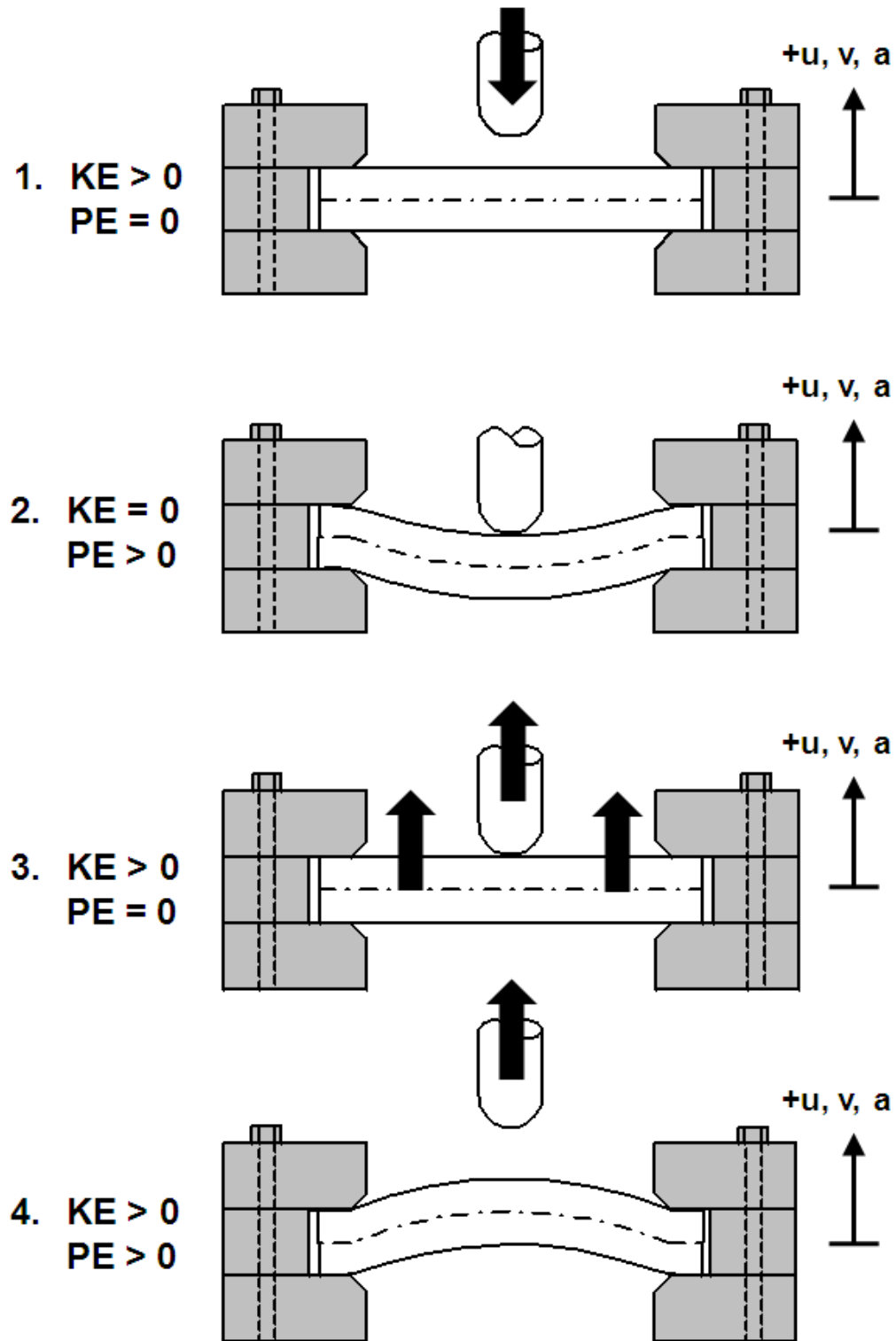


Figure 9.2: Four stages of the tup-plate interaction. Coordinate systems for positive deflections (u), velocities (v), and accelerations (a) are shown.

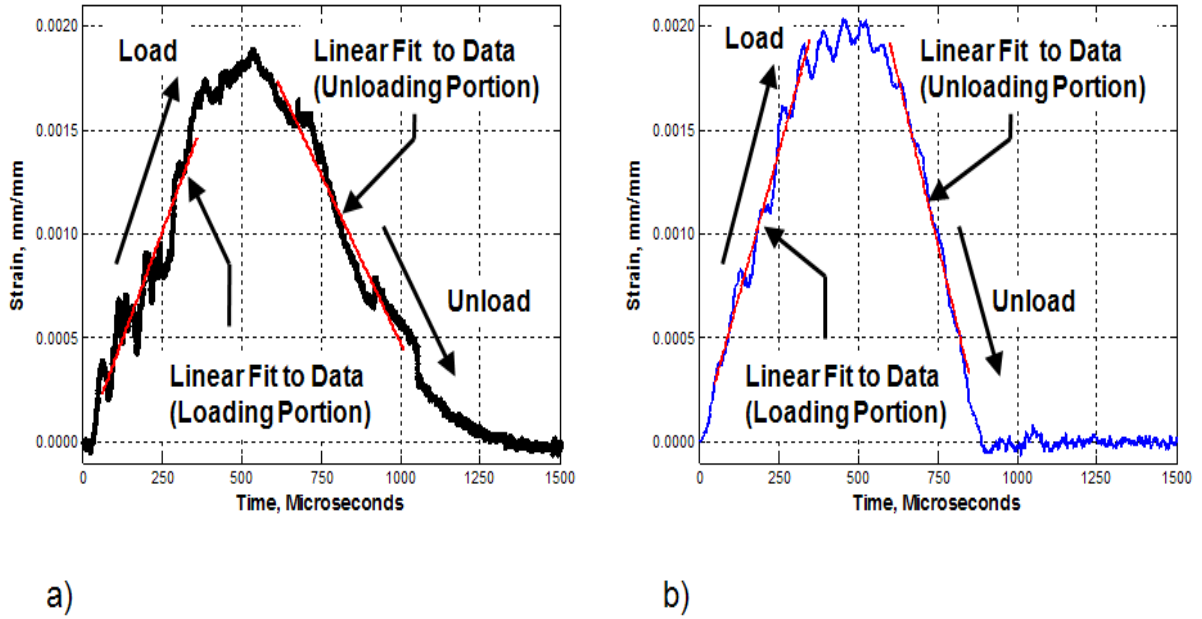


Figure 9.3: A straight line was fit to the data in the loading and unloading portions of the strain history curves to determine the strain rates in each respective part of the curve. Shown are the data from FGM plate test 9, strain gage 2: (a) experimental and (b) optimized FEM with homogenized-layers MT-N model.

Strain rates are important to the discussion of nearly all impact events. Here the strain rates in the plate from both the experiments and the FEMs will be compared using the homogenized-layers FGM models from Chapter VIII. Figure 9.3 shows how the strain rates in the experiments and FEMs is determined. A linear curve fit to the data in the loading and unloading portions of the strain histories was applied. The linear data fit was used to determine a general slope to the line through the data. The slope of that line is the strain rate for that part of the curve. The strain rate is not, in general, a constant through the duration of the impact events. For each oscillation in the history, the strain rate is changing dynamically. However, the linear fit to the data in the loading and unloading portions of the curve allow the general trend to be assessed. The linear fit is merely a least squares fit to the data (see [82], [69]) using a polynomial of degree one (a line). The linear fit was performed

by an internal function in the commercial software **Matlab**[®]. The line fit was taken so that the peak at maximum strain from each gage was not included in the strain rate calculation. The duration of the experimental histories was slightly longer than that of the FEMs (shown in Chapters VI and VIII) and so the time over which the strain rates were assessed in the loading and unloading portions of the curves had to be adjusted accordingly. The linear fit, in general, was taken between 50-350 microseconds for loading and 600-850 microseconds for unloading in the FEMs. The linear fit, in general, was taken between 50-350 microseconds for loading and 600-1000 microseconds for unloading in the experiments. These windows had to be adjusted slightly at times for the experimental data if the trendlines did not match the data in instances where electrical disturbances strongly affected the measured strain histories.

Tables 9.1-9.4 show tabulated strain rates for the Dynatup impact tests and the FEM impact tests for both loading and unloading at the three gage locations. Also shown are the tup impact velocities for each of the tests for reference. In general, the strain rates show a trend where increasing tup velocity results in increasing magnitude of strain rate. This trend is not followed in all instances, but this can be attributed to positioning of gages in the experiments that can have a profound effect on the strain histories. Further, the FEM was used to match the experimental strain histories as close as possible and accounted for this potential variation in gage placement. Note that the magnitudes of strain rates for the most part are lower the farther away the gages are from the center. This is due to the fact that the plates deform globally downward in a “bowl-shaped” fashion (demonstrated in Figure 7.3 assuming a simply-supported boundary condition at the fixture opening; see also Figure 9.2). The strains are lower near the edges of the fixture’s circular opening and highest near the center of the plate. This bowl-shaped deformation throughout the impact event causes the strains in the plate to occur mostly in concert together. The strain histories at the

Table 9.1: Summary of loading strain rates from plate impact tests using Dynatup apparatus. Strain rate is in units of strain/sec = (mm/mm)/sec.

Test No.	Description	Tup Velocity, Actual (m/s)	Strain Rates, Loading		
			Gage 1	Gage 2	Gage 3
1	100% Ti, 0% TiB Mono	3.040	2.324	2.184	0.967
2	100% Ti, 0% TiB Mono	3.476	6.175	2.754	2.161
3	85% Ti, 15% TiB Mono	3.050	3.979	3.302	1.800
4	85% Ti, 15% TiB Mono	3.479	3.759	3.367	1.781
5	15% Ti, 85% TiB Mono	2.585	Failed	Failed	Failed
6	15% Ti, 85% TiB Mono	3.050	Failed	Failed	Failed
7	7-Layer Ti-TiB FGM	3.040	2.509	2.467	1.110
8	7-Layer Ti-TiB FGM	3.412	3.927	3.389	1.643
9	7-Layer Ti-TiB FGM	3.765	4.135	4.091	1.379
10	7-Layer Ti-TiB FGM	4.078	5.167	4.678	2.140

Table 9.2: Summary of loading strain rates from optimized finite element models with homogenized-layers and Mori-Tanaka-needles material model. Strain rate is in units of strain/sec = (mm/mm)/sec.

Test No.	Description	Tup Velocity, Actual (m/s)	Strain Rates, Loading		
			Gage 1	Gage 2	Gage 3
1	100% Ti, 0% TiB Mono	3.040	4.295	2.374	1.162
2	100% Ti, 0% TiB Mono	3.476	6.738	2.821	2.032
3	85% Ti, 15% TiB Mono	3.050	4.035	4.055	1.640
4	85% Ti, 15% TiB Mono	3.479	4.964	3.756	2.038
5	15% Ti, 85% TiB Mono	2.585	Failed	Failed	Failed
6	15% Ti, 85% TiB Mono	3.050	Failed	Failed	Failed
7	7-Layer Ti-TiB FGM	3.040	4.099	3.152	1.272
8	7-Layer Ti-TiB FGM	3.412	4.850	3.726	2.077
9	7-Layer Ti-TiB FGM	3.765	5.527	4.261	1.724
10	7-Layer Ti-TiB FGM	4.078	5.852	4.507	2.508

Table 9.3: Summary of unloading strain rates from plate impact tests using Dynatup apparatus. Strain rate is in units of strain/sec = (mm/mm)/sec.

Test No.	Description	Tup Velocity, Actual (m/s)	Strain Rates, Unloading		
			Gage 1	Gage 2	Gage 3
1	100% Ti, 0% TiB Mono	3.040	-1.540	-2.111	-0.363
2	100% Ti, 0% TiB Mono	3.476	-4.463	-1.746	-1.589
3	85% Ti, 15% TiB Mono	3.050	-2.966	-2.393	-1.331
4	85% Ti, 15% TiB Mono	3.479	-3.207	-2.580	-1.350
5	15% Ti, 85% TiB Mono	2.585	Failed	Failed	Failed
6	15% Ti, 85% TiB Mono	3.050	Failed	Failed	Failed
7	7-Layer Ti-TiB FGM	3.040	-2.449	-2.074	-1.096
8	7-Layer Ti-TiB FGM	3.412	-3.522	-2.432	-1.723
9	7-Layer Ti-TiB FGM	3.765	-3.245	-3.599	-1.477
10	7-Layer Ti-TiB FGM	4.078	Failed	Failed	Failed

Table 9.4: Summary of unloading strain rates from optimized finite element models with homogenized-layers and Mori-Tanaka-needles material model. Strain rate is in units of strain/sec = (mm/mm)/sec

Test No.	Description	Tup Velocity, Actual (m/s)	Strain Rates, Unloading		
			Gage 1	Gage 2	Gage 3
1	100% Ti, 0% TiB Mono	3.040	-5.862	-3.283	-1.604
2	100% Ti, 0% TiB Mono	3.476	-8.847	-3.764	-2.682
3	85% Ti, 15% TiB Mono	3.050	-4.879	-4.904	-1.975
4	85% Ti, 15% TiB Mono	3.479	-5.498	-4.164	-2.231
5	15% Ti, 85% TiB Mono	2.585	Failed	Failed	Failed
6	15% Ti, 85% TiB Mono	3.050	Failed	Failed	Failed
7	7-Layer Ti-TiB FGM	3.040	-5.368	-4.119	-1.608
8	7-Layer Ti-TiB FGM	3.412	-6.006	-4.620	-2.548
9	7-Layer Ti-TiB FGM	3.765	-6.397	-4.906	-1.898
10	7-Layer Ti-TiB FGM	4.078	Failed	Failed	Failed

gauge locations all reach maximum values at the same time, and the strain magnitude is dictated by the location of the gauge with respect to the center of the plate. Thus, gauges farther away from the center reach a lower magnitude of maximum strain at the same time instant as gauges closer to the center reach a larger magnitude of maximum strain. Since the strain rate is more or less the difference in strain divided by the time period the difference is measured, it is easy to see how the rates near the circular opening of the fixture would be less than those near the center of the plates (assuming the simply-supported boundary condition around the circumference of the fixture's opening and global deformation as in Figure 9.2).

The maximum *magnitude* of strain rate for any of the impact tests is 8.847 (mm/mm)/sec in the unloading of the pure titanium plate in test 2, predicted by the FEM. These rates of strain, as tabulated for these tests, are very low compared to what would be experienced from a high-speed impact, such as occurring from a projectile in space [142]. In applications such as these, the rates of strain can be in excess of 10^3 - 10^5 . Given rates as high as these, localized wave response and the effects of rate-sensitive constitutive models need to be included [142]. The rates experienced by the FGM plates here in these tests are low enough that the global effects dominate the solution and the local wave effects are so dominated by the global response of the structure that they are virtually indistinguishable.

Another interesting trend is that the magnitude of strain rate in the experiments is greater in the loading of the plate and lower in the unloading of the plate. Just the opposite is true with the FEMs. In the FEMs, the magnitude of strain rate is greater in unloading than in loading. As mentioned, the effects of gravity were found to not contribute to this response, and thus another physical characteristic of the tests is causing this to occur. The strain rates with respect to the loading of the plates experimentally and through the FEM show good correlation. During the loading of the plate, there is a certain amount of “pulling” on the plate as the tup tries to push the plate through the circular opening of the fixture. One can picture what might occur if a thin piece of sheet metal were placed in the fixture in place of the thick

specimen plate. The tup, on impact, would very likely push the sheet through the bottom opening of the fixture and the sheet would be pulled right out of the fixture through its large deformations. The thick plates undergo a similar deformation, but the tup cannot push the plate through the opening and out of the fixture because the plate is too thick and too strong for the tup to do so. However, the tup will try push the specimen plate through the bottom circular opening in the fixture as much as possible during the loading phase of the plate. During the unloading phase, the plate is relaxing as it and the tup rebound from the impact and the potential energy stored in the plate is reconverted to kinetic energy. As the plate relaxes, there is likely a large amount of friction that may be resisting the specimen plates from returning to their original configuration, especially near the chamfered edges of the fixture’s circular openings. This resistance may be slowing the response during unloading in the actual fixture and can account for the fact it returns very slowly back to zero strain. In the FEM, this effect may not be as pronounced given the frictionless contact model used in the FEMs (see Appendix C for details). Also, the friction may still be just as prevalent in the fixture during the loading phase but the friction forces may not be as pronounced as the plate is “pulled” out of the fixture during loading as they are as the plate “pushes” itself back to its original configuration.

9.3 Stresses in the FGM Plates

The discussion will now switch gears slightly to look at the stress distribution through the FGM plates over the course of the impact events. The stresses in the two-phase and homogenized-layers FGMs will be studied under the conditions of FGM plate test 9 (crosshead mass 13.06 kg, impact velocity 3.765 m/s, impact energy 92.56 J, FGM plate). Also included in the study is a homogenized-layers model of one of the 85% Ti-15% TiB monolithic plates for comparison. The homogenized-layers monolithic specimen provides a baseline from which the results from the graded composites can be compared.

Figures 9.4-9.12 provide von Mises stress contours of the homogenized-layers FGM (Figures 9.4-9.6) , the two-phase FEM (Figures 9.7-9.9), and the monolithic FGM (Figures 9.10-9.12). The von Mises stress σ_e is given by the following relationship [31]:

$$\sigma_e = \frac{1}{\sqrt{2}} \left[(\sigma_{xx} - \sigma_{yy})^2 + (\sigma_{yy} - \sigma_{zz})^2 + (\sigma_{zz} - \sigma_{xx})^2 + 6(\sigma_{xy}^2 + \sigma_{yz}^2 + \sigma_{xz}^2) \right]^{1/2} \quad (9.1)$$

This stress is termed an equivalent stress because it generates a scalar stress that encompasses the contributions of the entire stress tensor, both normal and shear components. The von Mises stress is non-negative due to its squared terms in (9.1).

Before discussing some of the interesting features due to the impact of the FGM specimens, some explanation of the figures is in order. Figures 9.4-9.6 will be presented first (the homogenized-layers Ti-TiB FGM) and the remaining six Figures 9.7-9.12 follow suit for their respective FGM models. Figure 9.4 shows a top view of the von Mises stress contours during the response of the FGM at six snapshots in time. The first snapshot, $t = 0$, *merely shows the finite element model of the plate with no contours for reference purposes*. The next five snapshots are taken at five different equally spaced intervals so the reader can get a feel for the stresses developing in the plate as the tup interacts with the plates. Figure 9.5 shows the von Mises stress contours at four snapshots in time with a section cut through the middle of the plate, slightly different from the first figure. The snapshots in this figure include a reference snapshot at $t = 0$, one at $t = 250$ microseconds, one at $t = 524$ microseconds, and one at $t = 1000$ microseconds. The snapshot at $t = 524$ microseconds represents the time at which the center deflection of the FGM plate was at a maximum. Figure 9.6 shows the same stress contours at the same snapshots in time, however the section cut through the middle of the plate is now made at a 45° angle through the center. The section cuts give good representations of how the plate behaves near the corners where the fixture fastener screws are farthest from the circular opening in the plate fixture.

A simulation of an 85% Ti-15% TiB monolithic plate under the impact conditions of experimental test 9 was run for comparison of the FGM results to a homogenized, isotropic plate. The von Mises stress distributions for the monolithic plates are shown in Figures 9.10-9.12.

The von Mises stress contours were all plotted on the same scale in ABAQUS. This was done so that a one-to-one comparison of the stress distributions could be made. *As we study the contours, the distribution of stress will be the focus, and not the magnitudes of the stresses themselves.* There are a couple of reasons for this. First, with the exception of the monolithic plate, the FGM finite element models have many elements that are bound to other elements with mismatching material properties. The stress contours are averaged across the elements for smooth transitions in plotting, but the stress state at mismatching material boundaries can be much more complex. Secondly, the stresses at the impact site on the plate are very high due to a force concentrated over a very small area. The magnitudes of these stresses in that local area can be sufficiently high that the elastic constitutive model applied throughout the plate is no longer valid (for instance, localized plasticity or crushing at or near the impact site may be occurring). Without better material data for the Ti-TiB specimens, these behaviors cannot be captured without an appropriate constitutive model. Finally, the monolithic plate behaves slightly different than the FGM plates with a slightly different response (owing to the fact that it is homogeneous in composition where the FGM has more or less an unbalanced material configuration through the thickness). It is not the goal to compare the magnitudes of stresses between the FGM and this plate since their composition and constitutive models are not the same. Note that the maximum deflection in the monolithic plate does not occur at 524 microseconds, but this snapshot was used in the plots for consistency purposes.

First, the stress contours in the full plate views in Figures 9.4, 9.7, 9.10 will be interpreted. Recall that for the FGM, the maximum displacement in test 9 occurred at 524 microseconds and the plate and tup separate around 900 microseconds. Between

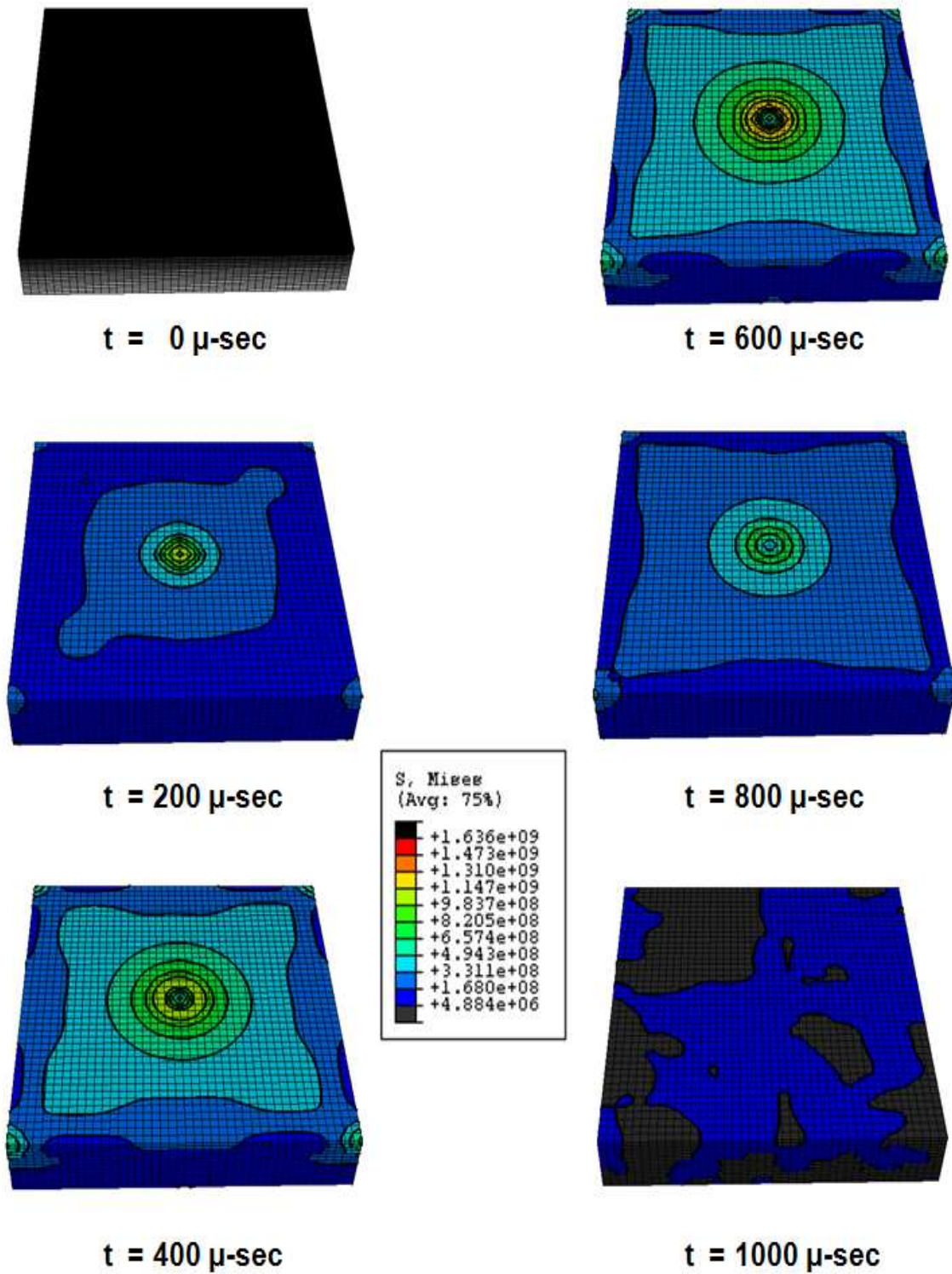


Figure 9.4: Top view of homogenized-layers FGM plate (plate impact test 9) subject to stresses at six snapshots in time. Contours of von Mises stress, in Pascals, are plotted.

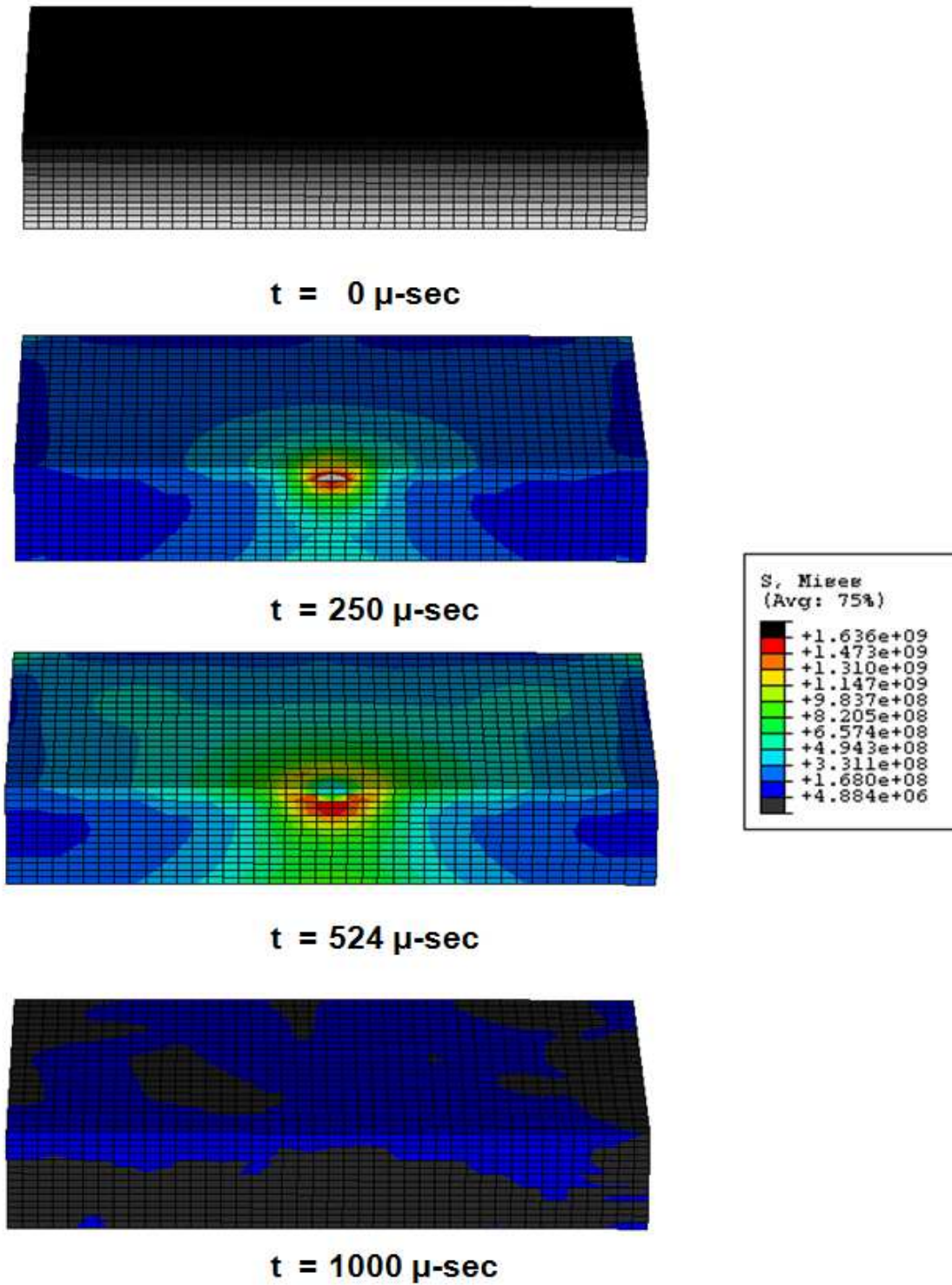


Figure 9.5: Top view with section cut through middle of homogenized-layers FGM plate (plate impact test 9) subject to stresses at four snapshots in time. Contours of von Mises stress, in Pascals, are plotted.

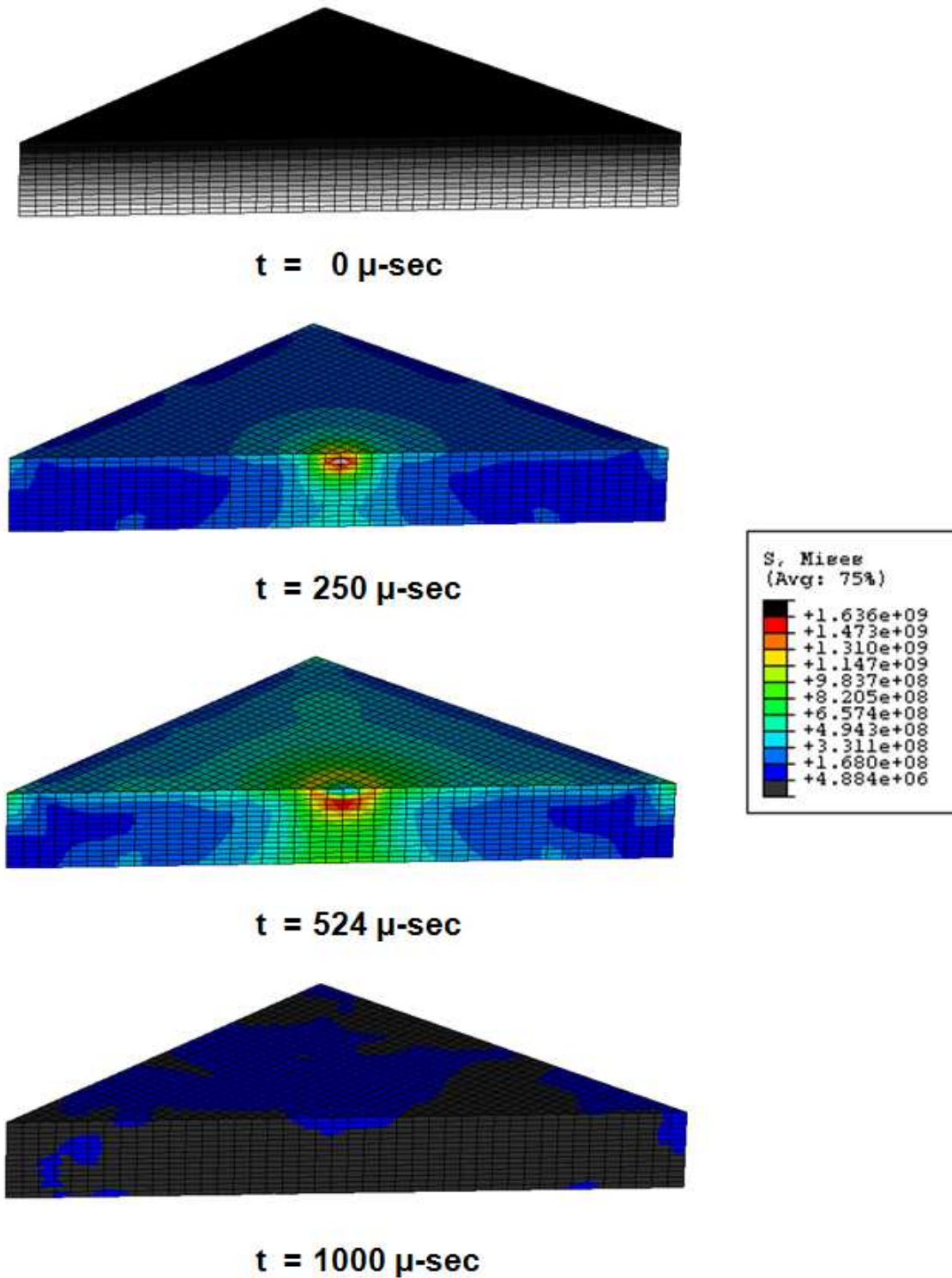


Figure 9.6: Top view with 45° section cut through middle of homogenized-layers FGM plate (plate impact test 9) subject to stresses at four snapshots in time. Contours of von Mises stress, in Pascals, are plotted.

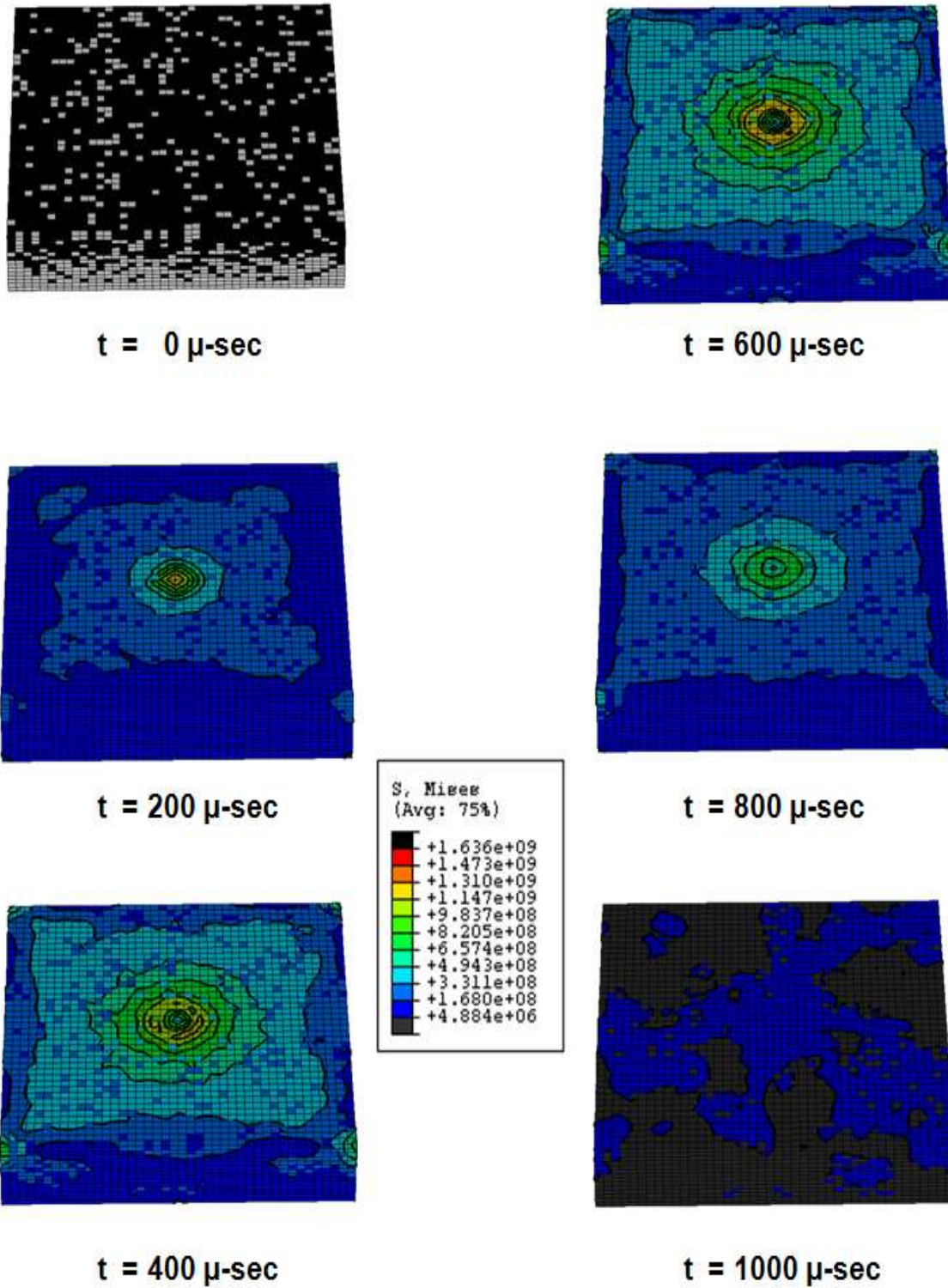


Figure 9.7: Top view of two-phase FGM plate (plate impact test 9) subject to stresses at six snapshots in time. Contours of von Mises stress, in Pascals, are plotted.

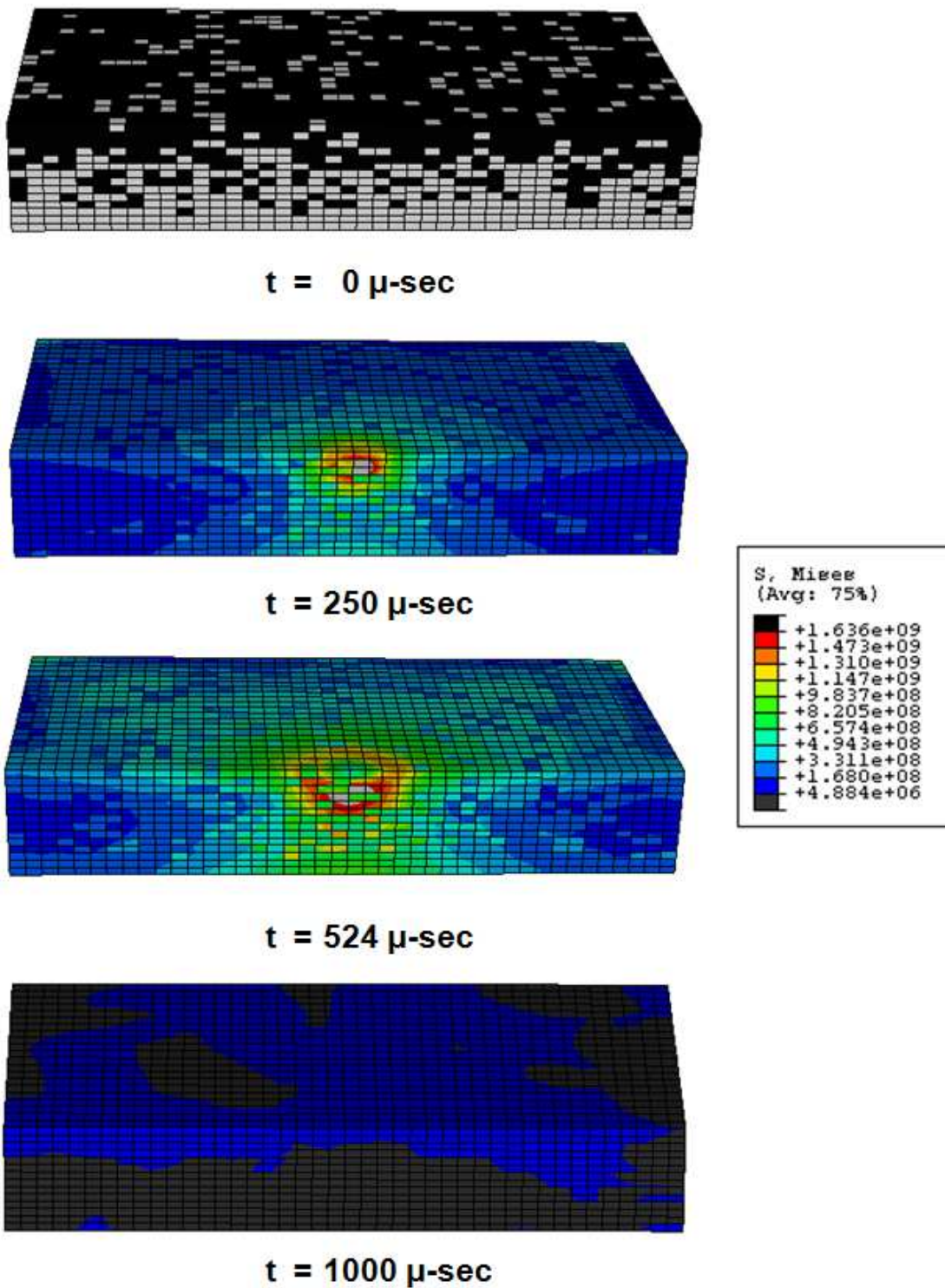


Figure 9.8: Top view with section cut through middle of two-phase FGM plate (plate impact test 9) subject to stresses at four snapshots in time. Contours of von Mises stress, in Pascals, are plotted.

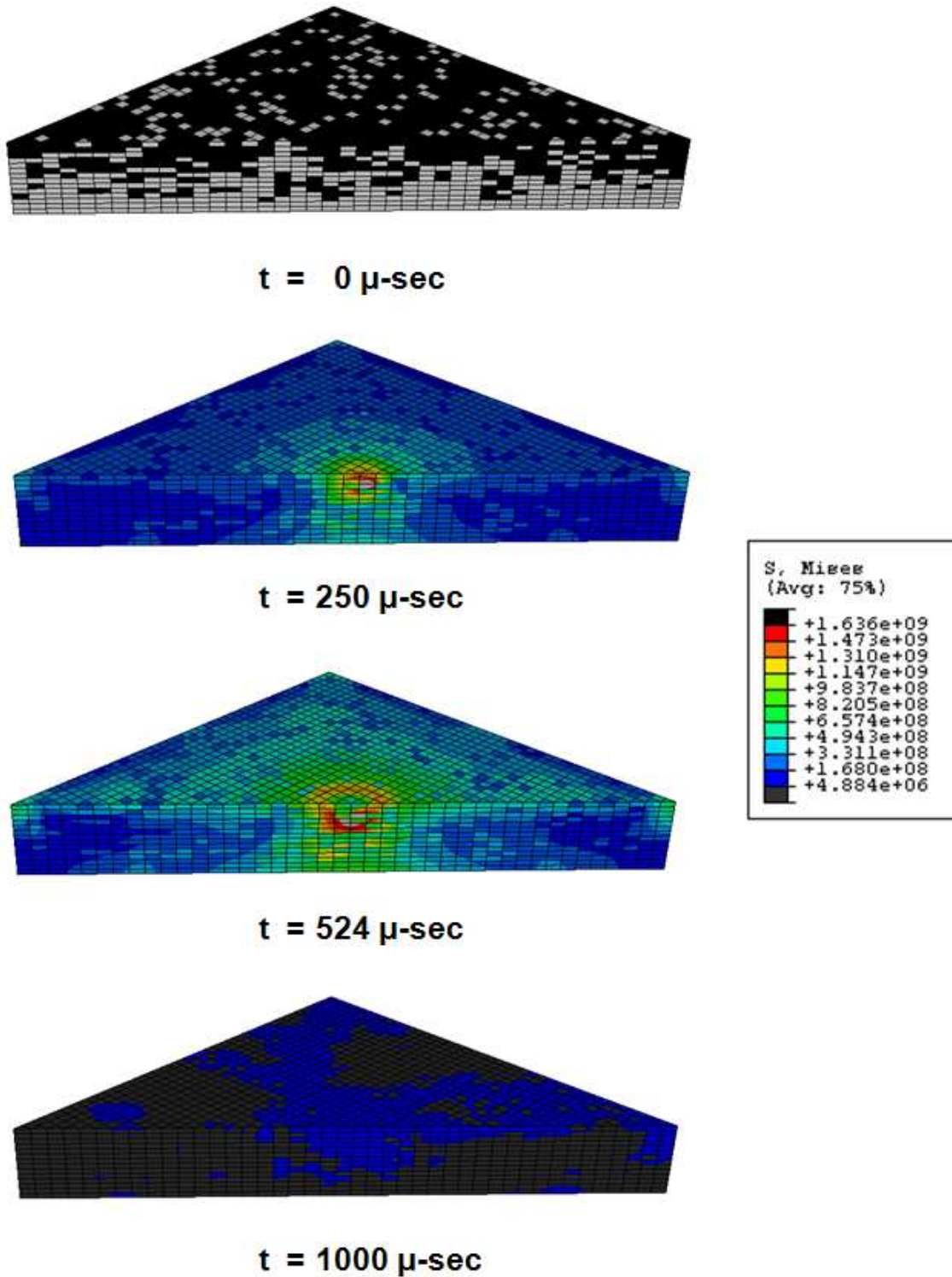


Figure 9.9: Top view with 45° section cut through middle of two-phase FGM plate (plate impact test 9) subject to stresses at four snapshots in time. Contours of von Mises stress, in Pascals, are plotted.

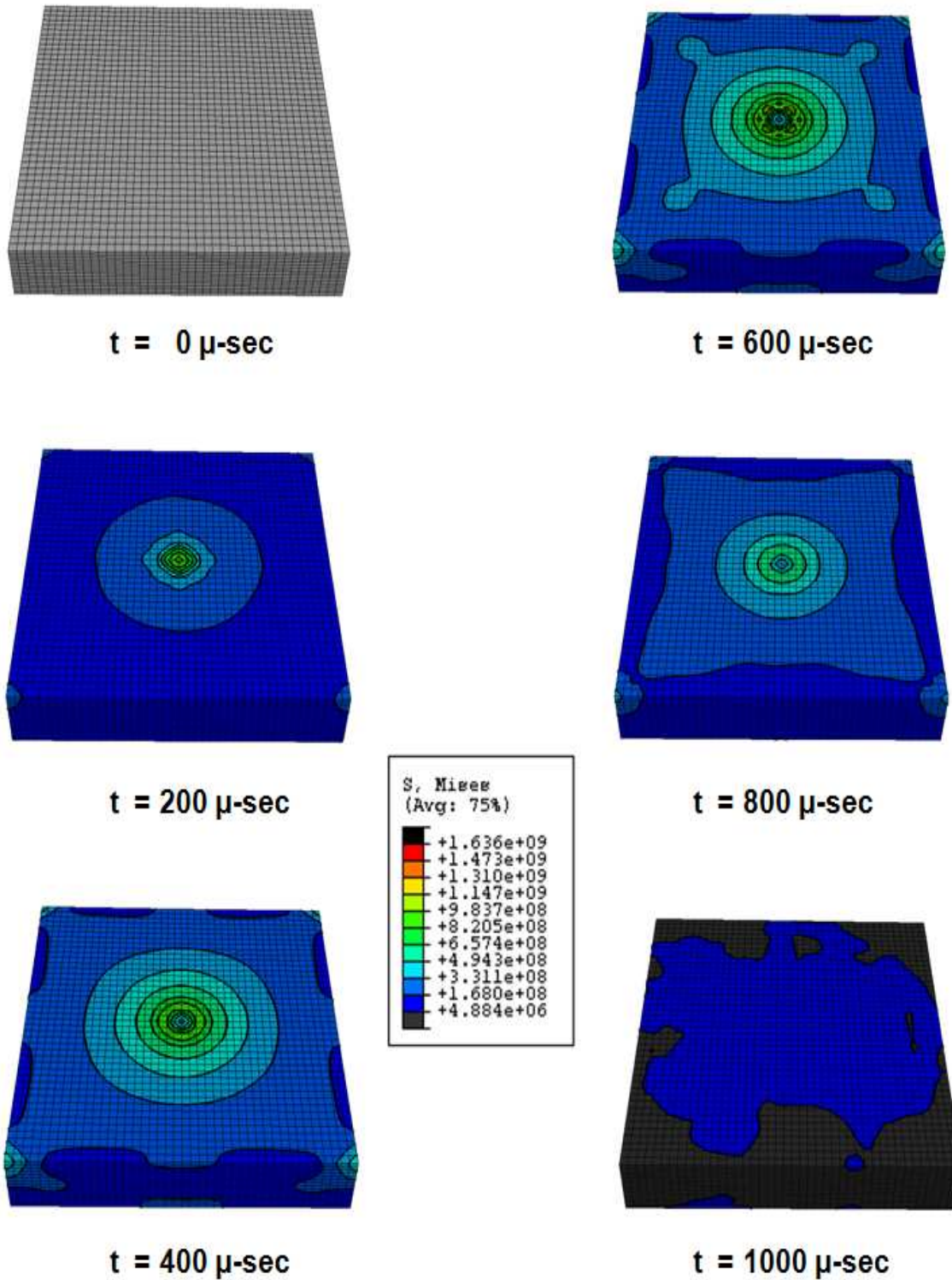


Figure 9.10: Top view of homogenized-layers 85% Ti-15% TiB monolithic (comparable to plate impact test 9) subject to stresses at six snapshots in time. Contours of von Mises stress, in Pascals, are plotted.

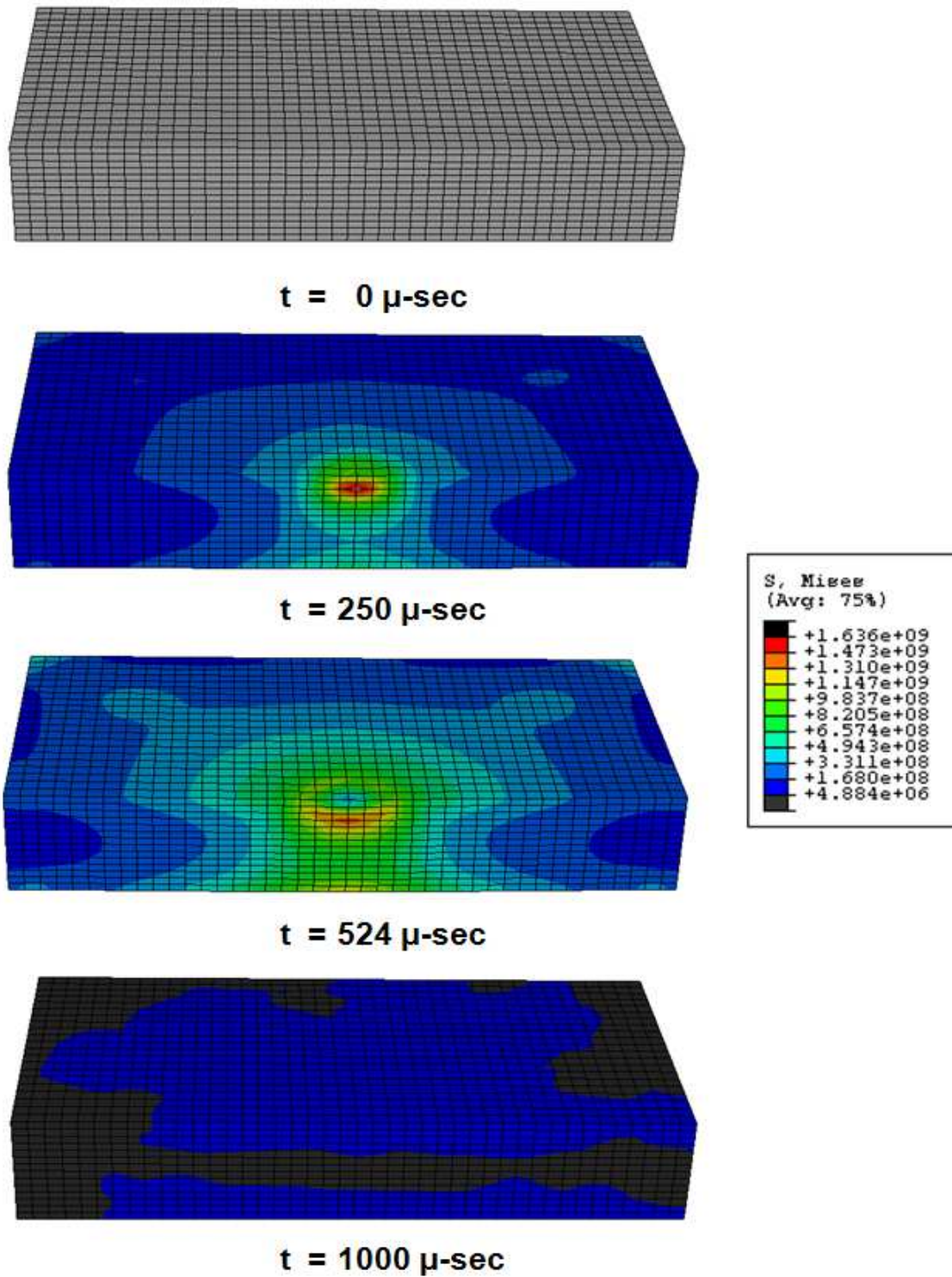


Figure 9.11: Top view with section cut through middle of homogenized-layers 85% Ti-15% TiB monolithic (comparable to plate impact test 9) subject to stresses at four snapshots in time. Contours of von Mises stress, in Pascals, are plotted.

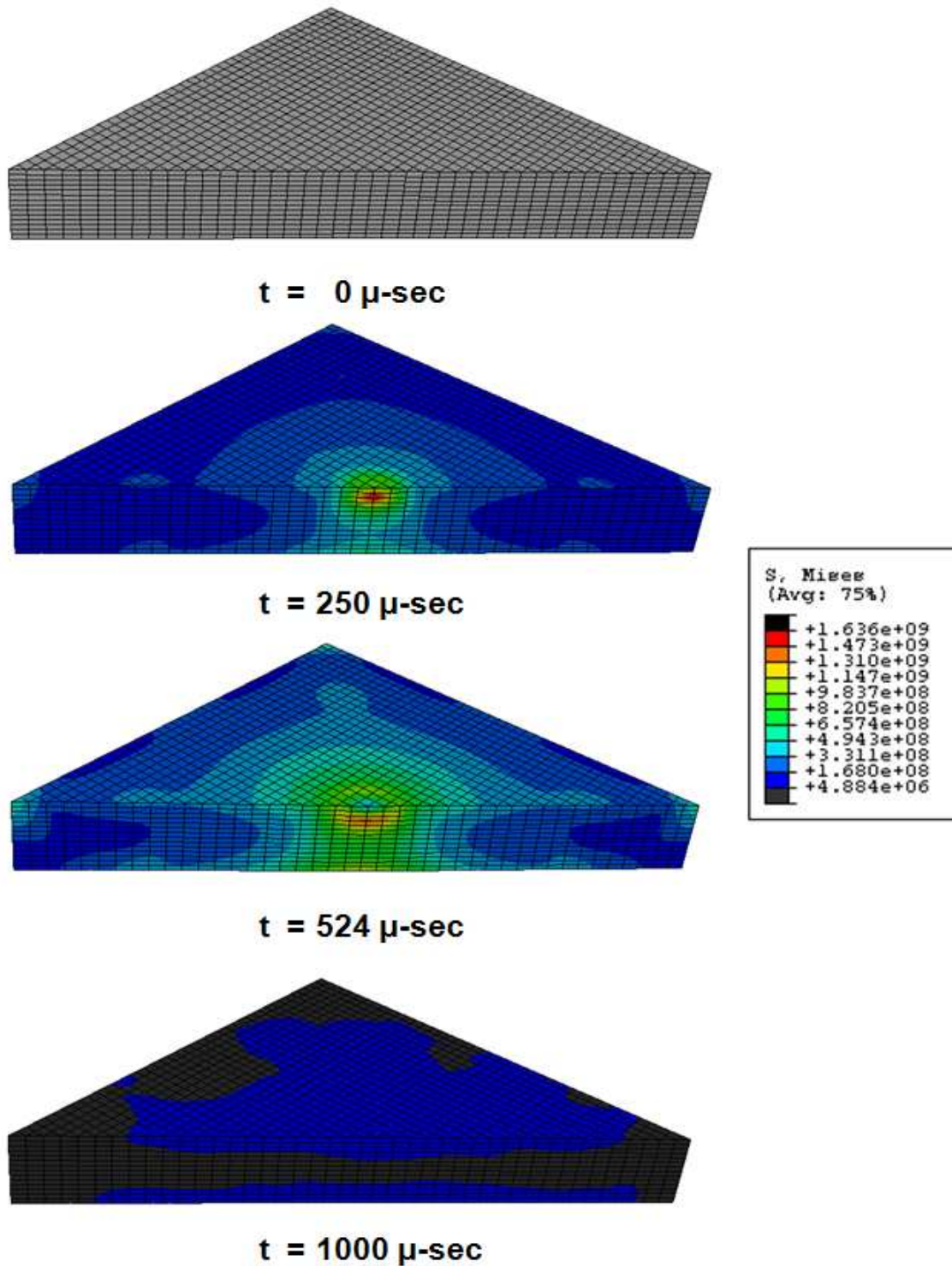


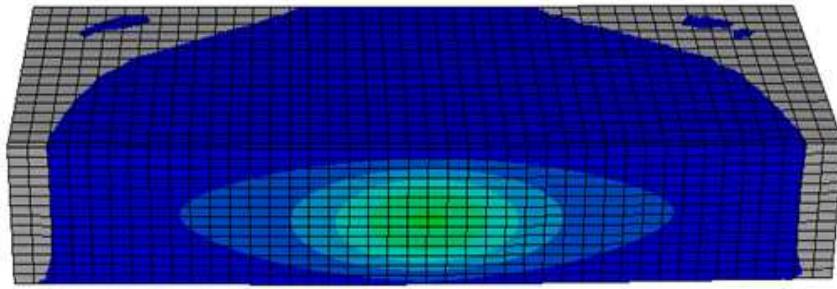
Figure 9.12: Top view with 45° section cut through middle of homogenized-layers 85% Ti-15% TiB monolithic (comparable to plate impact test 9) subject to stresses at four snapshots in time. Contours of von Mises stress, in Pascals, are plotted.

0-524 microseconds, the tup induces a target-bullseye stress distribution on the top surface that carries through to the bottom surface. The maximum stresses are at the center and decrease as the radial distance from the center increases. Toward the outer edges of the plate, the stress distribution changes from the target-bullseye pattern to another pattern that is more square-shaped. With a geometrically circular plate, the target-bullseye pattern would continue out to the boundary. The plate studied here is square and thus the pattern changes from the target pattern to one that reflects the square geometry *and additionally the restraints on the plate imposed by the plate fixture*. This is especially noticeable in the plate corners where the stress increases locally at these points. This is due to a leveraging effect with the square plate against the fixture during the impact event where the corners come into contact with the top plate component of the plate fixture. Lastly, at time $t = 1000$ microseconds, the tup and plate have separated for some time and the only stresses left are due to minor oscillations that occur. There is no discernable pattern to these low-magnitude stresses that occur as waves from the impact merely propagate throughout the plate after the impact event. An important point here is also that the two-phase model shows many of these same patterns, but the pattern is somewhat distorted due to the mis-matching of material properties throughout the element mesh that distorts the stress state across the elements. This is a behavior that we should expect from a FGM (or any other such material) that exhibits two-phase distributions of constituents.

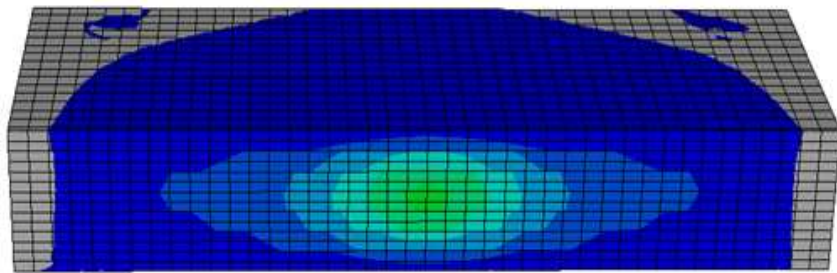
Next, the section cuts through the plates in Figures 9.5, 9.6, 9.8, 9.9, 9.11, and 9.12 are explained. In the monolithic specimens (Figures 9.11, 9.12), the von Mises stress distributions exhibit nearly symmetric distributions where the von Mises stresses for a line normal to the plate surface at a point through the thickness have nearly identical stresses on the top and bottom surfaces with a variation through the thickness owing to both the shear components in the plate and the primarily tensile stresses on the bottom surface transitioning to primarily compressive stresses on the top surface. This is the behavior that should be expected for a homogeneous plate of uniform composition subject to bending. On the other hand, the FGM plates

in Figures 9.5 and 9.6 do not exhibit this behavior. In fact, the stresses compared at the same position through the thickness show a shape that is not necessarily symmetric and is somewhat jagged at the interface of each material layer and the magnitude of the von Mises stresses on the top surface are not the same as that toward the bottom surface. This is expected and is consistent with composite plate theory where the strains through the thickness are continuous (due to the assumption the layers are perfectly bonded) but the stresses are not necessarily continuous if the constitutive model changes. This same pattern and observation can be seen in the two-phase model although the symmetric shape of the contours is highly distorted with some localized patches of high-intensity stress surrounded by patches of low-intensity stresses (Figures 9.8, 9.9). Lastly, the highest intensity of stresses are at and very near the position of the impact site. As stated earlier, the constitutive behavior of the FGM constituents and mixtures must be very well understood to effectively model the behavior and response of the plates at those positions.

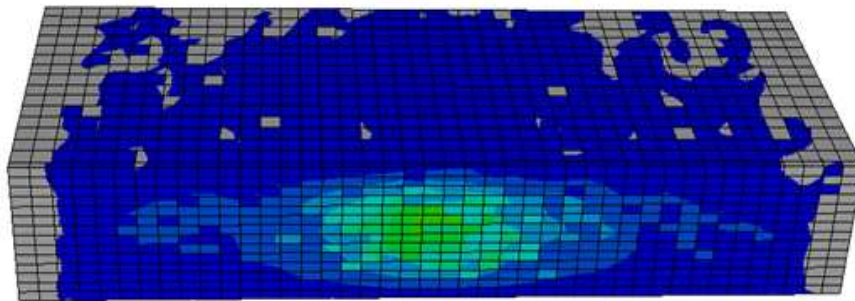
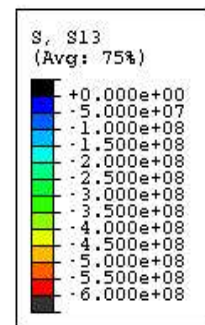
Before concluding this section, a note on the transverse shear in the plates is in order. Figure 9.13 shows the distribution of shear stress through the thickness of each of the three plate models at the time of maximum center deflection of the FGM plates. Taking the 15 through-the-thickness nodes at the center of the plane cross-sections in Figure 9.13, the transverse shear distributions are plotted in Figures 9.14-9.16 for three different snapshots in time. Note that the shear stress plotted is not von Mises equivalent stress, but is the actual shear stress acting directly on the plane of the cross-sectional cut (σ_{13} in ABAQUS, corresponding to σ_{xz} in the Cartesian coordinate system of the model). The section cut is taken 1.0 cm away from the center of the plate so that the shear stresses from the concentrated load on the tup do not distort the distributions. In the monolithic plate, a very clearly parabolic stress distribution is evident through the thickness of the plate as is expected under bending of thick plates (much the same as in beam theory). In the FGM plates, a parabolic distribution of stress is also evident however the distribution is clearly affected by the changing material properties in each layer. The distribution tends to have sharp discontinuities



85% Ti—15% TiB Monolithic



Layered Ti-TiB FGM



Two-Phase Ti-TiB FGM

Figure 9.13: Top view with section cut through middle of homogenized-layers 85% Ti-15% TiB monolithic, homogenized-layers Ti-TiB FGM, and two-phase Ti-TiB FGM (comparable to plate impact test 9) subject to transverse shear stresses at snapshot of maximum deflection. Section cut taken 1.0 cm from the center plane of plate. Contours of transverse shear stress on plane in section cut, in Pascals, are plotted.

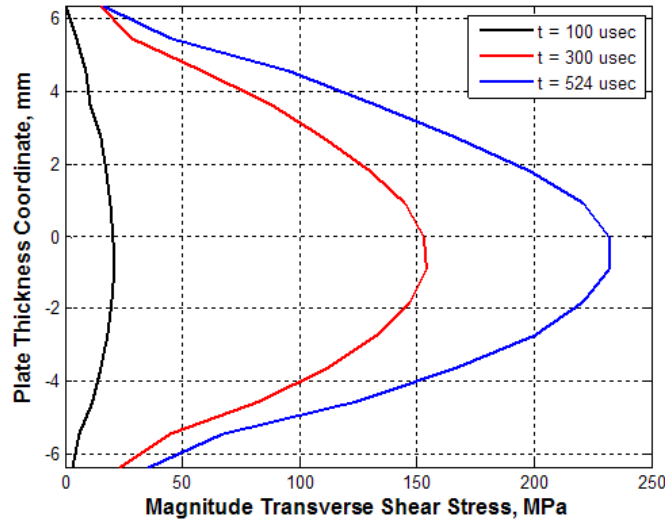


Figure 9.14: Transverse shear distribution through thickness of the 85% Ti-15% TiB monolithic homogenized-layers plate (MT-Needles material model) at three snapshots in time under conditions of impact test 9. Distribution is taken from 15 nodes through thickness of the plate at center of cross-section in Figure 9.13.

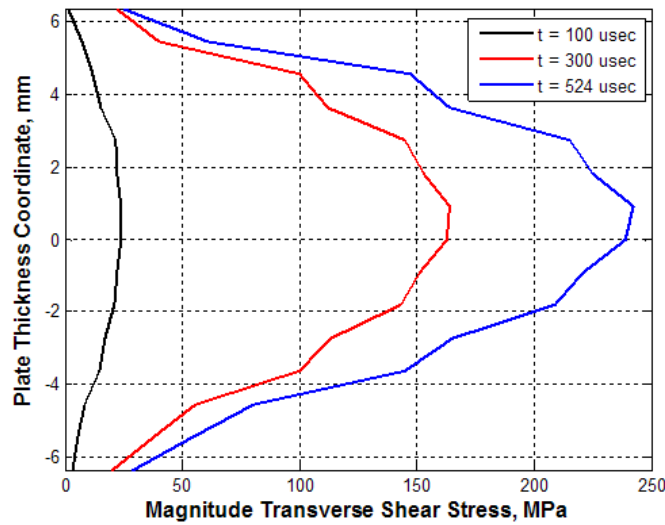


Figure 9.15: Transverse shear distribution through thickness of the FGM homogenized layers plate (MT-Needles material model) at three snapshots in time under conditions of impact test 9. Distribution is taken from 15 nodes through thickness of the plate at center of cross-section in Figure 9.13.

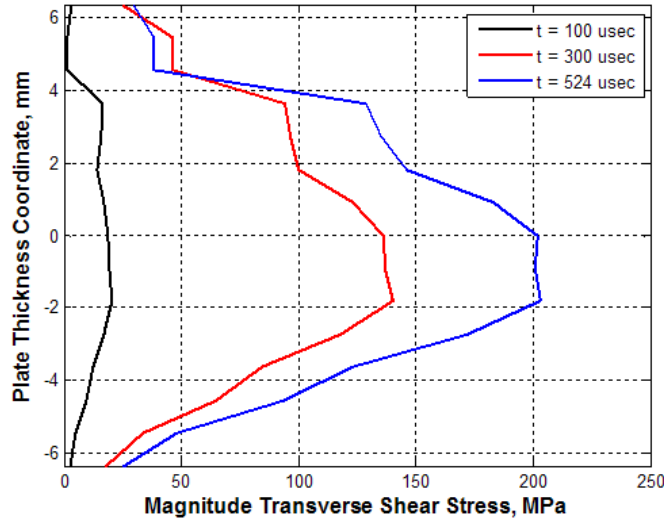


Figure 9.16: Transverse shear distribution through thickness of the FGM two-phase plate at three snapshots in time under conditions of impact test 9. Distribution is taken from 15 nodes through thickness of the plate at center of cross-section in Figure 9.13.

at each of the material interfaces through the seven individual layers. A somewhat similar distribution can be seen in the two-phase FGM model, but once again the distribution is heavily distorted due to the random mixture of elements of individual Ti and TiB constituents. Recall in the analytical treatment of the FGM plates in Chapter VII, the transverse shear stress through the idealized circular plate was assumed to be constant for a given radial coordinate and independent of the thickness coordinate of the plate (FST assumption). This assumption increased the accuracy of the analytical model but simplified the equations from requiring a higher-order shear deformable theory where the transverse shear is dependent on both the radial and thickness coordinates of the plate. However, the transverse shear distributions from the FEM indicate that incorporating a higher-order shear deformable theory when analytically studying the FGM plates would be highly justified and appropriate.

9.4 *Effects of Non-Central Impact Load*

The last topic in the impact characterization involves the effects of a non-centered impact load on the FGM plates. The Dynatup tests were assumed to deliver an impact perfectly centered on the plate specimen for each test. For the most part, this was observed to be a pretty good assumption. Each specimen plate was carefully marked and positioned in the fixture to make sure that the Dynatup would impact the center of each plate (see Chapter V). However, as mentioned in Chapter V, the Dynatup crosshead had a small amount of play due to fittings that have loosened over use. Most of the looseness in the apparatus was primarily between the crosshead and the guide rails and little could be done to correct the problem. Inspection of the plates after the tests showed that the impacts were very close to the center point of the plate, but a few tests showed impacts sites slightly perturbed away from the center point. The FEM simulations conducted up to now all involved a perfectly centered impact. Here the strain histories at the strain gage locations will be compared with those at the same locations assuming the tup model in the FEM is positioned slightly off-center.

Continuing with the optimized homogenized-layers MT-N model of FGM plate test 9, the tup was re-positioned in the FEM to impact at two different locations off-of-center as shown in Figure 9.17. The tup was moved to two positions at 0.898 cm along the 45° axis of the plate ($0.898 \text{ cm} = [(0.635 \text{ cm})^2 + (0.635 \text{ cm})^2]^{1/2}$). This distance was arbitrarily chosen for illustration purposes. The influence of the perturbed location of the tup impact site on strain gages 2 and 3 are shown in Figure 9.18. The histories from the experiment, the nominal FEM results from a central impact, and the histories from the two perturbed impact sites are all included for comparison.

It can be seen in Figure 9.18 that the greatest effect in the strain histories occurred as the tup was placed at impact site 1 (Figure 9.17). The strain histories changed very little when the tup impacted the plate at impact site 2. (Note that the

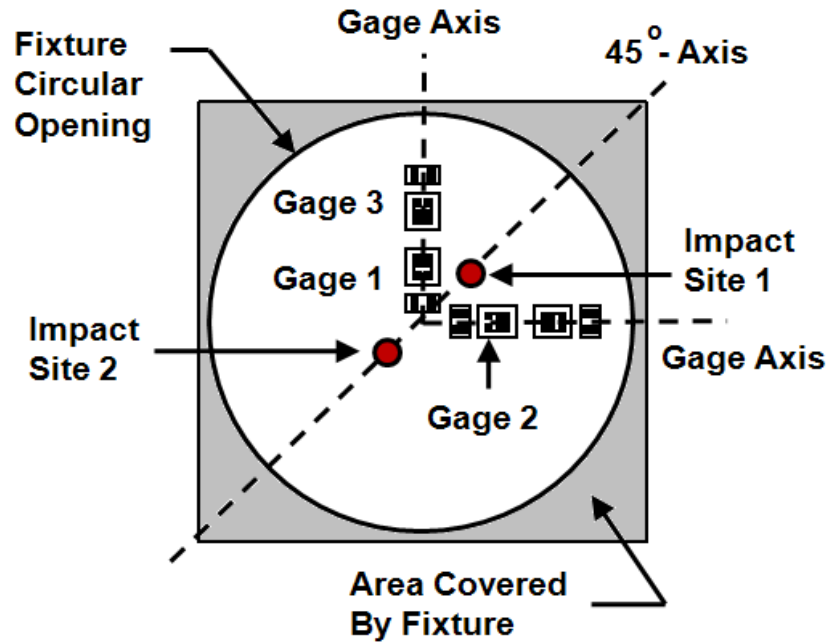


Figure 9.17: Specimen plate with gages and reference positions annotated. Impact sites 1 & 2 are 0.898 cm from center.

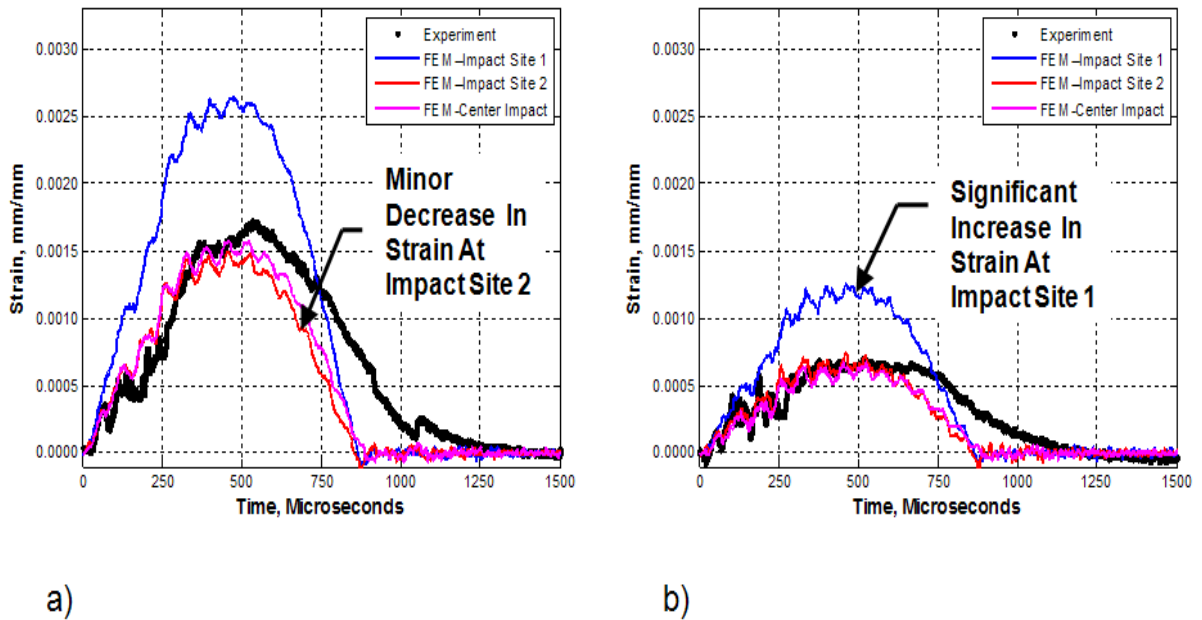


Figure 9.18: Test 9 strain histories & FEM comparisons with off-centered tup impact sites per Figure 9.17 using the Mori-Tanaka Needles model: a) strain gage 2, b) strain gage 3.

same nodes were used in the FEM for all three FEM strain histories). One might have the initial reaction that the strain histories at the two locations should change by roughly the same magnitude, meaning the strains measured from an impact at site 2 would be less than the nominal strains from a central impact while the strains measured from an impact at site 1 would be greater by a roughly equal magnitude. This could perhaps be the case if the dynamic load was spread over a larger area, but in fact the tup acts almost as a concentrated load to the plate. It is well-known (and was discussed in Chapter VII), that a concentrated load introduces a stress state to the plate that is significantly higher near the point of application of the load than slightly away from it. In theory, it was shown that these stresses were unbounded, but in physical reality these stresses are not unbounded (otherwise a plate would always fail under a concentrated load regardless of the magnitude). While the stresses are not unbounded, they are significantly higher near the point of application and this was evident in the contour stress plots of the previous section. This sharp increase in stress state is undoubtedly causing the sharp increase in associated strain measurement when measured from the impact at site 1. At impact site 2, the point of impact is sufficiently far away from the strain gage locations that the localized increase in stress/strain does not influence the measurements to the same degree.

9.5 Closing Remarks

In this chapter, four specific areas of the impact response of the plates were studied. The first was the plate and tup interaction. It was found that the tup remained in contact with the plate specimens throughout the entire impact event. The next area was the strain rate effects of the plate during the loading and unloading of the plate. During the loading of the plate, the FEM and experiment correlated fairly well; in the unloading of the plate, the FEM and experiment exhibit different behaviors that can be accounted for due to some modeling assumptions in the FEM that do not reflect some of the actual plate/fixture interactions. The stress distributions in the FGM plates were studied and compared to those from a homogeneous

plate. Finally, the effects of non-central impact loads on the plates were demonstrated through simulation. It was found that if the impact site is off-center such that the impact load is applied closer to the gages, the magnitude of the measured strains can increase significantly whereas an off-center impact a small distance farther away from the gages has a lesser effect.

These four areas are merely a sample of the physics that could be studied using the concepts discussed throughout this dissertation. *The key point in using the method discussed in this dissertation is that virtually any FGM system can be studied provided an accurate FEM can be developed.* Only limited experimental data can be collected over any impact event. If the computer simulations match the experimental data reasonably well, the simulations can be used to extrapolate other physics within the model. This is very important because the physics behind FGM impacts are not easily modeled with analytical theory, especially as the velocity and energy behind the impacts increases. While only four characteristics were studied here, volumes of work could be extrapolated from the finite element models to study the effects of FGM impacts at the global and local levels in the FGM plates. Further, given strong confidence in the modeling of the particular FGM system here, it is possible to study the same FGM system under a wide variety of geometries and configurations under similar impact loading conditions (i.e., impact velocities and energies). *This method for characterizing the impact response of FGM plates subject to impact loading is thus an invaluable contribution to the study of these materials and is one that has excellent potential for use in a large number of FGM applications.*

X. Conclusions

This research work represents a first attempt at characterizing the impact response of FGM plates; an area relatively unexplored by research engineers and scientists to date. The response of FGM plates subject to impact is of interest should FGMs be used as a thermal protection system on an aerospace platform. FGM plates used in such an application must be able to withstand a high-energy impact from a foreign object to avoid deterioration of strength of any substructure the FGM is intended to protect.

This dissertation provides a strong foundation from which research in the impact response of FGM structures can build. Since almost no treatment of this subject has been available before this work, it was necessary to simplify the FGM impact problem to studying the impact response of FGM plates in low-velocity regimes without a thermal environment other than that of room-temperature. *The **overall goal** of this study was to provide a unique method by which the impact response of functionally graded plates could be characterized for low-velocity, low- to medium-energy impact loads. Additionally, adequate material models for the anisotropic, non-homogeneous FGM had to be determined to properly study the physics of the local and global response of the structure subject to an impulsive load of large magnitude. The **objectives** of this research to meet these overall goals were to:*

- 1. Design and conduct impact experiments on metal-ceramic FGM plates to collect strain histories at various locations on the plate over the duration of the impact event.*
- 2. Construct a finite element simulation of the impact experiment that is sufficiently sophisticated to capture the dynamic effects of an impact load while at the same time is easily replicated by scientists and engineers in practice.*
- 3. Correlate the results from the experiments and finite element models to available analytical theory while drawing conclusions regarding the validity of analytical techniques available in the literature for future research.*

4. *Refine the FGM material models to more effectively simulate the experiment and enhance the accuracy of the results from which more detailed studies of the behavior of FGMs under dynamic loading can be made.*
5. *Provide analysis of the impact response of the FGM plates and make recommendations for engineers and scientists to improve performance and suitability for applications where resistance of impact loads are required.*

Each of these objectives was met in this research work and each represents a *major contribution* to the emerging field of functionally graded composites.

In this final chapter, the research performed in this dissertation is summarized with key conclusions and recommendations presented. The details of the work performed and the key conclusion from each chapter are listed to give a final overview of the entire study performed. Next, the most important contributions of this work are documented to demonstrate the relevance of the research to future investigators. The discussion continues with some concluding remarks provided assessing the strengths and shortfalls of the results, some comments with respect to some efforts that were not fruitful in this research, and also recommendations for future studies.

10.1 Summary of Research Conducted

The following is a recap of the research presented in this dissertation. *Key conclusions from each chapter are highlighted in italics, as appropriate.*

- Definition of the problem of interest, namely, determining a reliable method to characterize the impact response of an FGM plate under low-velocity, low- to medium-energy impact loading as a precursor to evaluating the response of such a plate under high-energy impact loads such as one might experience as thermal protection on a space-access vehicle (Chapter I).
- Demonstration, through a comprehensive literature review with respect to the current state of the art in FGM research, that a study of the impact response

of FGMs has been given little treatment to date (Chapter II). *Almost no experimental data of any kind has been collected with FGM specimens; thus a need exists to demonstrate static and dynamic concepts in FGM behavior beyond simulation only.*

- A review of relevant homogeneous and composite plate theory applicable to this research was presented (Chapter III).
- Selection of a model metal-ceramic FGM system, Ti-TiB, to study in a series of plate impact experiments (Chapter IV). A literature review of the FGM system was conducted to understand characteristics of the material prior to conducting impact tests in order to aid in interpretation of the results throughout the research. *The metal-ceramic Ti-TiB FGM system chosen was convenient for study here due to its availability, however, it is not likely that such an FGM system would actually be used in a thermal protection system on a space-access vehicle.*
- An experiment was designed to collect strain histories in monolithic and functionally graded plates over the duration of a low-velocity, low- to medium-energy impact event (Chapter V). Ten impact tests were conducted total, eight of which were successful tests with strain histories in the plate collected. *The key finding was that strain histories could be collected with a high degree of reliability, and the primary limitation in conducting a successful test rested solely on plate survivability over the test. The collection of the strain histories for the FGM plates provide invaluable data from which the impact response of FGMs demonstrated in simulation can be verified. This phase of the research met Objective 1.*
- Finite element models of the impact experiments were constructed to study the behavior of the monolithic and FGM plates under impact loading. Two separate material models were used to study the response, namely the two-phase material model and the homogenized-layers material model (Chapter VI). *Both the two-phase and homogenized-layers FEMs were shown to capture the response*

of the plates under impact loading relatively well using only published material properties. This phase of the research met Objective 2.

- Analytical plate theory presented in Chapter III was extended to study the plate experiments specifically. *It was shown that the load applied from the impact tests occurred over a sufficiently long period of time that quasi-static loading assumptions could be applied to estimate the maximum deflection of the plate during the impact event. Further, results from the FEM and experiments showed a strong correlation with analytical predictions of the maximum deformation of the plate for a simply-supported circular plate under the assumption of axisymmetric loading (Chapter VII).* This analytical model of the plate impact tests was a necessary component of the parameter estimation sequence used to refine the local material models for the FGMs so the physics of the impact events could be effectively captured.
- A parameter estimation sequence to effectively estimate the material properties of the FGM plates was formulated and demonstrated (Chapter VIII). The sequence was designed to enhance the accuracy of the finite element models. *The resulting estimates for material properties in the FGM from implementation of the parameter estimation sequence were shown to match well with published material properties for the Ti-TiB system. The material properties in the homogenized-layers FEM were modified accordingly and the strain histories from the resulting optimized model showed very good correlation with those from the experiments. This phase of the research met Objectives 3 and 4.*
- Characterization of the behavior of the impact experiments using the optimized FEM to study the physics of the plate impacts and behaviors during impact not obvious from the experimental data (Chapter IX). *The optimized FEMs showed the impact response of the FGM plates in the experiments could be correctly characterized and that the modeling of FGM plates could be extended to other static and dynamic FGM plate applications subject to small strains and deformations. This phase of the research met Objective 5.*

10.2 *Key Contributions*

This work has provided five invaluable contributions to the study of functionally graded composites:

- Fundamental understanding of the physics associated with FGM Response based on combination of experimental, computational, and analytical work that can be used as foundation for others studying these advanced composites for various applications.
- Developed and demonstrated a novel framework for studying the impact response of FGMs, valid and extendable in a wide variety of impact applications.
- Design of an experiment where strain histories in functionally graded plates over the duration of a low-velocity, low- to medium-energy impact could be obtained with a high degree of reliability.
- A significant amount of experimental data from the low-velocity, low- to medium-energy impact tests conducted with monolithic and FGM plate specimens. The cost and availability of functionally graded materials are such that experimental data of any kind is not readily available in the literature. In this sense, any credible experimental data is extremely useful to research scientists and engineers.
- Demonstration of two distinct modeling techniques that can be applied in commercial FEM software to model the global impact response of functionally graded composites. One modeling technique assumes graded layers are individually isotropic with material properties that are a function of the volume fractions of the constituents. The other model assumes a two-phase random distribution of the base constituents constrained by the local volume fraction ratios.
- Development of a novel parameter estimation sequence that effectively estimates the material properties of the FGM plates formulated to tie together the results

from experimental data, finite element simulations, and analytical theory of plate behavior. The results of the sequence were shown to match well with material data from other sources (for Ti-TiB FGMs) and the strain histories from the FEM matched very well with the analogous experimental strain histories from the impact tests.

- Demonstration of the FEM capabilities in characterizing the impact response of FGM plates under low-velocity, low- to medium-energy impact events.

Each of these contributions represents a significant addition to the current state-of-the-art in functionally graded material analysis. The work also creates a solid foundation from which higher energy impact studies can be performed using the chosen material system or other available FGM systems.

10.3 General Discussion

This chapter concludes with discussion on some points of interest with respect to the work performed that were not included in the earlier documentation.

First, this work represents a major contribution to the knowledge and understanding of FGM systems used in structural members. Almost no experimental data has been available until this time with respect to FGMs. The FGM plate strain histories were collected using a very harsh impact event. Analytical comparisons to the experimental data were shown to be valid under assumptions of elastic quasi-static theory, and computer simulations that incorporate dynamic effects matched the data fairly well. Such comparisons give engineers and scientists baseline results that can be used in their FGM studies. Before this work, nearly all FGM studies were based solely on simulation and analytical theory with no real-world data to substantiate claims. Further, the confidence gained in the modeling and understanding of FGM systems provide a solid foundation from which other applications of FGM systems can be reasonably and confidently studied.

It was known prior to testing that the Ti-TiB material system was a brittle system at high volume fractions of TiB based on the literature review presented in Chapter IV. However, it was not expected that the material would be highly brittle at even low volume fractions of TiB (for instance, 85% Ti - 15% TiB monolithic). A dynamic flexure test was designed as part of this research to capture plastic rate-dependent features for the system at different mixtures of Ti-TiB. This test was found to capture very well the strain-rate plasticity effects present in some ductile metals, but the Ti-TiB monolithic specimens exhibited virtually no plasticity before failing in the flexure tests. This elastic-to-failure brittle behavior was exhibited in the 15% Ti - 85% TiB monolithic plate tests 5 and 6 in this work and was found to occur during one of the FGM plate tests (test 10). This brittle behavior is almost certainly associated with the powder-metallurgy sintering process used to construct the FGMs and monolithic specimens. The powders of Ti are combined with TiB_2 powders at the outset and are fused by bringing the powders in the plate die to *near* the melting point of Ti. The ability of the bond between powders to withstand dynamic loads is highly suspect and would account for the brittle behavior in even high volume fractions of Ti. The goal of this work was not to conduct a material study on the Ti-TiB FGMs, but rather to use the FGMs as a metal-ceramic FGM system from which some experimental data could be collected for verification purposes. In this respect, the FGM and monolithic plate specimens performed their function adequately.

One proposed application for FGMs is fusion of thermal protection into load-bearing structure on a space-access vehicle. The Ti-TiB system would definitely not be a good candidate for this application given its brittle tendencies. Again, the Ti-TiB FGM system was merely a metal-ceramic system that was convenient to study due to its availability. Another FGM system is currently being studied at the University of Illinois Urbana-Champaign under a joint effort with the Structural Sciences Center of the Air Force Research Laboratory. Here, a titanium-zirconia (ZrO_2) system is being studied as a model FGM system. Zirconia is a ceramic material that has some favorable properties at high temperatures, namely low thermal conductivity,

plastic material response, and high toughness that can be very favorable to a thermal protection system undergoing impact loads (see [110], [66], [67], [68]). It was originally intended to conduct impact experiments with this FGM system but specimens could not be made available when this research work began. There are most certainly other FGM systems that could be constructed that would perform better than the Ti-TiB system, but as pointed out earlier, availability and cost are serious limitations when studying metal-ceramic FGMs. As the technology to manufacture them improves and the availability and cost decrease, it is likely that more suitable FGMs will be developed for a wide range of applications.

It is believed, but has not been verified, that failure of the cohesive bond between sintered powders in the FGM system is the critical failure mode. Had more material data been available for the system, a failure criteria could have been included in the ABAQUS FEMs that would account for cohesive bonds between elements. This would be a very nice feature to demonstrate in future finite element analyses (especially in brittle material systems), but this was not studied here.

The impact experiments designed and conducted were a great success overall. Data from the impact tests could be reliably collected, and failure of the specimens was generally the only limitation in data collection. The 15% Ti-85% TiB monolithic specimens failed immediately in their individual impact tests, but the FGMs did not fail (except midway through test 10) despite the higher velocities and energy levels and the fact that the top layer of the FGMs was in fact this TiB-rich composition. Clearly more needs to be understood about the Ti-TiB mixtures before more conclusions can be drawn.

Had more specimens been available, it is likely that a failure model for the Ti-TiB composites could have been generated. This would have been a major contribution that would have enhanced the effectiveness of the finite element model. The FGM plate test 10 was the only test that provided any insight into the failure of the plates. The strains measured in plate test 10 were only slightly higher than that mea-

sured in test 9. Whether or not the strain in plate 10 at failure is a good measure of the maximum deformation the FGM system can undergo is difficult to say. However, very few conclusions of any kind with respect to the tests where plates failed were made throughout this work.

The FEMs of the FGMs and plate impact experiments matched data very well and were constructed to use features of ABAQUS that were not necessarily unique to ABAQUS. That is, conceivably the plate impact problem could be studied using any number of commercial codes. The most complicated aspect of the FEMs was the nonlinear contact formulation. The contact interactions in the model seemed to work well overall, but as it was noted there were instances where improvements could have been made specifically to the experiments. There are obvious advantages and disadvantages to adding to the complexity of the specific model of the experiments. In this case, the goal was to keep the models as simple as possible in order to draw more broad conclusions and make the study of FGMs readily available to a wide variety of engineers and designers. In that respect, the objective was met very well. On the other hand, keeping the model simpler may have sacrificed understanding some of behaviors specific to the experiments. Unfortunately, the lack of material data for the Ti-TiB system made such a task unreasonable over the course of this work.

Lastly, one of the original intentions for conducting an impact study was to look closely at the wave propagation in the FGM plates. Limitations in the Dynatup prevented higher velocity impacts that might have been more oriented to the study of wave motion in the plates. The problem is interesting for an isotropic, homogeneous material, but is even more interesting for a multi-layered material where reflection, refraction, and transmission of waves locally becomes very important and more difficult to track apart from sophisticated numerical simulations. In these tests, the global deformations so dominated the response that the wave motion became almost insignificant in comparison to the global structural dynamic. This work has nonetheless provided a solid foundation in low-velocity impact studies from which higher velocity, higher energy impact studies can be conducted in future work.

Appendix A. Strain Gage Instrumentation

This appendix discusses some broad details associated with the instrumentation used to collect strain histories from the FGM plate specimens over the course of the impact experiments (Chapter V). The key components of the instrumentation system were the strain gages, the signal conditioner, and the data acquisition unit. The body of literature available concerning instrumentation is large; the majority of discussion in this section is summarized from Beckwith et al. [13]. The concepts used in this appendix can be referenced when studying the raw voltage histories from each experiment contained in Appendix B

A.1 Strain Gages

Strain gages rely on the phenomenon that the electrical resistance of some materials will change due to an applied mechanical stress and subsequent strain. For instance, a wire of finite length and diameter will exhibit a reduction in electrical resistance when the length is increased and the diameter is decreased (due to stretching). Foil strain gages (very thin flat wire with thin polymer backing) with linear pattern for strain measurements were used in the experiments performed in this work. An example strain gage is shown in Figure A.1. For strain gages placed on the surface of a specimen, the matrix backing material serves as an interface with the specimen transferring the deformation of the specimen to the grid material. The backing material provides a mechanical couple between the strain in the specimen and the strain in the gage material and ensures an accurate transfer of the strain in the test specimen to the applied strain of the gage material [135]. Furthermore, an appropriate backing material ensures a bond which electrically isolates the gage material from the test specimen. This allows the complete electrical signal generated during the straining of the gage material to be transmitted to the data collector.

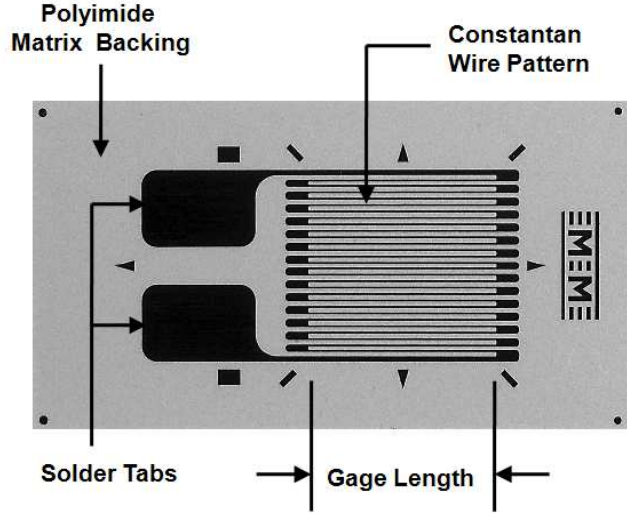


Figure A.1: Vishay 125AC series strain gage used in impact tests for collecting strain histories [127].

The gage strain sensitivity, which is also referred to as the gage factor (GF), is a dimensionless relationship expressed as

$$GF = \frac{\Delta R}{R} \frac{L}{\Delta L} \quad (\text{A.1})$$

R is the resistance in the gage, ΔR is the change in resistance, L is the initial length of the foil wire gage section, and ΔL is the change in length of the foil wire gage section. The gage factor is usually pre-determined by the manufacturer and is reported with other gage specifications. These gage specifications are important when calculating the measured strain on each specimen. The procedure for doing so is presented in a later section.

A.2 Signal Conditioner

The strain gages, once installed on the plate specimens, were wired into a signal conditioning unit. The purpose of the signal conditioning unit is to convert the resistance change (due to plate straining) in the strain gages into a meaningful quantity that can easily be measured. The signal conditioner used to perform this function in the impact experiments essentially consists of two main parts: (a) the Wheatstone

bridge circuit, and (b) a direct current (DC) differential amplifier. Each component will be discussed briefly here.

The first component, the Wheatstone bridge circuit, is a common resistive bridge circuit which provides a means for accurately detecting and measuring small changes in resistance. Figure A.2 shows a basic strain gage Wheatstone bridge circuit. R_1 , R_2 , R_3 , and R_4 are individual resistors arranged in a parallel circuit between nodes A and C. e_i , a DC input voltage, is input between these nodes and a voltage output, e_o , is then measured across nodes B and D. The individual values of i represent the current flowing through each resistor in the Wheatstone Bridge. The Wheatstone bridge circuit is used to measure changes in resistance by either (1) balancing the bridge by making known adjustments in one or more of the bridge arms until the voltage across the meter is equal to zero or (2) measuring the magnitude of unbalance from the meter connected to nodes B and D. In the example of the strain gages used in these experiments, each gage is connected to a separate Wheatstone bridge by wiring the strain gage to serve as R_1 in the circuit. Note that when negligible current flows through the meter attached to B and D, the bridge is simply a pair of voltage-dividing circuits (ABC and ADC) with output taken at the midpoints of the two voltage dividers. Further, the offset voltages of the two dividers cancel such that any small change in resistance between the two arms is detected by the attached meter. A balanced bridge circuit (voltage reading across the meter is zero) occurs when the following holds true (as shown in Figure A.2):

$$\frac{R_1}{R_2} = \frac{R_3}{R_4} \quad (\text{A.2})$$

The particular bridge arrangement for the impact test strain gages is termed a quarter bridge arrangement, where the designation indicates the number of active arms in the bridge circuit (each of the four segments with attached resistance is termed an arm of the bridge). Specifically, a strain gage serves as resistance R_1 , which is variable during the test, while the other three arms have resistances that do not change. Thus, the

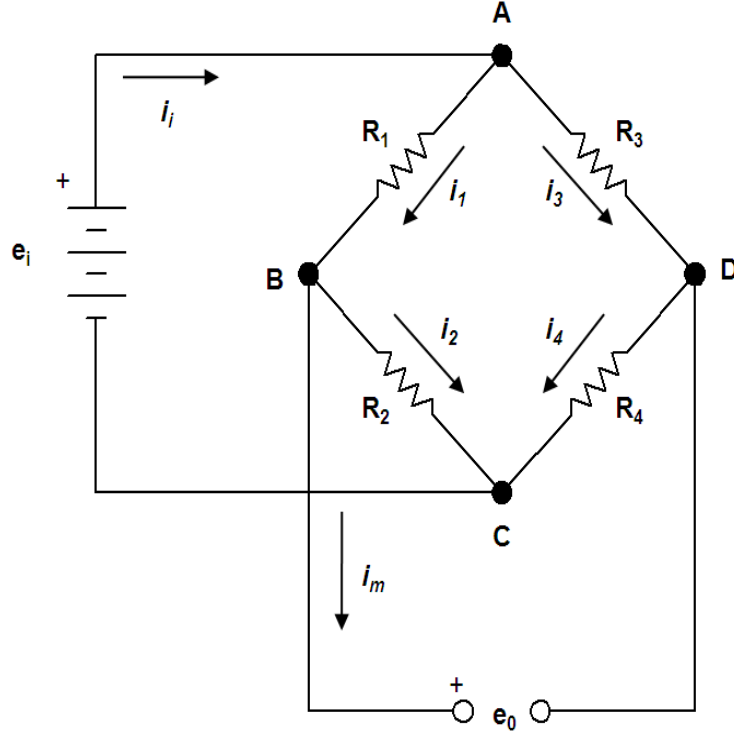


Figure A.2: Typical Wheatstone bridge circuit [13].

strain gage arm is the only active arm. Half and full bridge circuits are also possible for various applications but were not used here. The relationship between the input voltage and the output voltage is given by the following relation, without derivation:

$$e_o = e_i \left(\frac{R_2 R_3 - R_4 R_1}{(R_1 + R_2)(R_3 + R_4)} \right) \quad (\text{A.3})$$

When the bridge is balanced, the numerator in (A.3) is zero and thus e_o is zero. A change in voltage in the bridge for a change in resistance can be calculated from (A.3) by substituting one of the R_j ($j = 1, 2, 3, 4$) resistance values in the equation with some arbitrary $(R_j + \Delta R_j)$. In the strain gage bridge circuit, essentially the bridge is initially balanced; R_2 , R_3 , and R_4 remain constant; and R_1 changes through straining of the specimen. Thus, the changes in resistance R_1 are detected through e_o by applying the relation (A.3) and assuming the initial value of e_o is zero.

The second component of the signal conditioning system is the amplifier. The resistance changes detected as output voltage from the Wheatstone bridge may be very small, on the order of background noise, in which case an amplifier boosts the signal to a degree that can be more meaningful. Figure A.3 shows a typical DC operational amplifier used for such a purpose. The amplifier essentially accepts two inputs: an inverting input with (-) symbol and a noninverting input with (+) symbol. A difference voltage amplifier thus satisfies

$$e_o = G(e_+ - e_-) \quad (\text{A.4})$$

where G is the gain of the amplifier. The basic idea is the amplifier subtracts the inverting input voltage from the noninverting input voltage and multiplies the difference by a constant (gain). The amplification is powered by supply DC voltages (shown in Figure A.3). Generally these voltages are equal in magnitude and opposite in polarity, but not necessarily so. If a residual voltage is found to exist in the amplifier's output, an offset null adjust may be incorporated in the amplifier's circuitry to adjust the unwanted residual voltage toward zero.

The amplifier used in the signal conditioning units for this work was a DC differential operational amplifier, as shown in Figure A.4. The inputs e_{i1} and e_{i2} are the offset voltages from the Wheatstone bridge measured at nodes B and D in Figure A.2. If $R_1 = R_2$ and $R_3 = R_4$ (in Figure A.4) then the output voltage from the amplifier is related to the input voltages by

$$e_o = \frac{R_3}{R_1}(e_{i1} - e_{i2}) \quad (\text{A.5})$$

and the need for an offset null adjust is minimized if the input resistances at (-) and (+) are equal.

Before proceeding, a summary of the strain measurement process is in order. First, strain gages are bonded to a specimen and wired to a Wheatstone bridge cir-

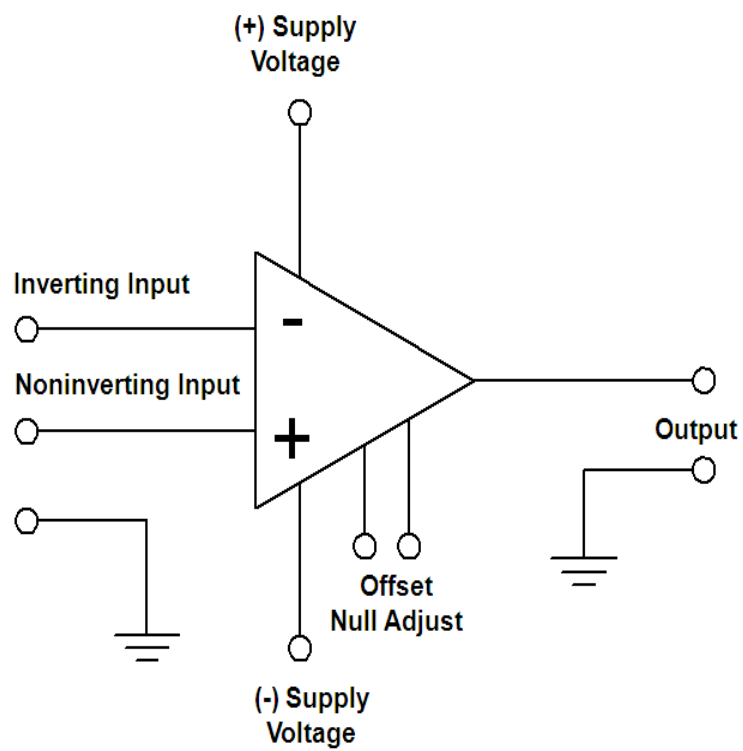


Figure A.3: Typical operational amplifier [13].

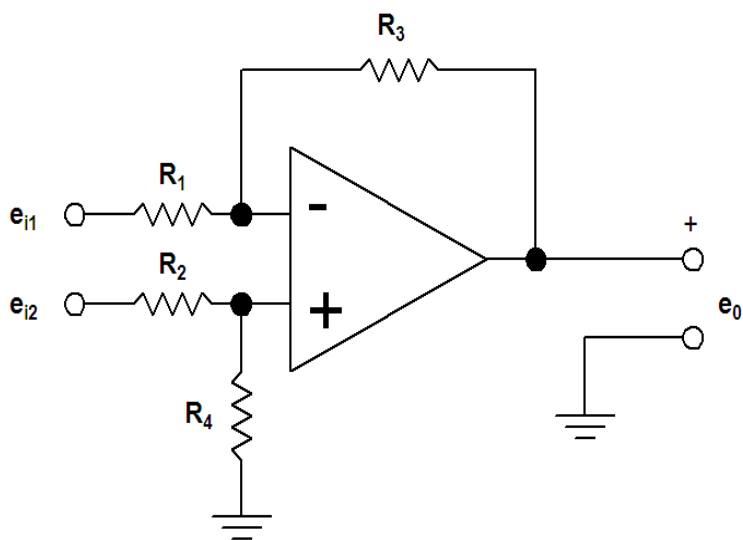


Figure A.4: Typical DC differential amplifier [13].

cuit (a gage is represented by R_1 in Figure A.2). The Wheatstone bridge circuit is powered by an input DC voltage source. The bridge is balanced such that the initial voltage reading output by the bridge arrangement is zero. The output voltages of the bridge circuit, measured at nodes B and D, are input to a DC differential operational amplifier. The specimen is strained, the resistance R_1 changes, the output from the Wheatstone bridge is input into an amplifier which amplifies the voltage difference and outputs the amplified voltage reading to a data acquisition unit, such as an oscilloscope (discussed later). To this point, the strain measurement is merely an amplified voltage signal. The next step is to then correlate the voltage signal to an analagous measure of strain (the procedure for this will be presented in the next section). Note that a separate signal conditioner unit was used for each strain gage.

The signal conditioners used in the tests additionally had a shunt calibration feature that was used to correlate the output voltage from the signal conditioning unit to the strain in the plate specimens. The shunt calibration feature is used in conjunction with the Wheatstone bridge circuit and is illustrated in Figure A.5. The shunt calibration feature introduces a “shunt” resistance R_s that can be switched on or off from the Wheatstone bridge circuit. When the switch is off, R_1 is the effective resistance across that arm of the bridge. When the switch is on, R_1 and R_s are two resistances in parallel, and the effective resistance R_e across that arm of the bridge is now

$$R_e = \frac{R_1 R_s}{R_1 + R_s} \quad (\text{A.6})$$

Note that the effective resistance of two parallel resistances is always less than the minimum of the two parallel resistances. Assuming initially the bridge circuit is balanced ($e_0 = 0$) and R_1 and R_s are known quantities, then substituting R_e in equation (A.6) into equation (A.3) for R_1 the resulting e_0 will be some value greater than zero. Thus, the shunt resistance at that location has excited the Wheatstone bridge away from its balance point and an output voltage can be read from the

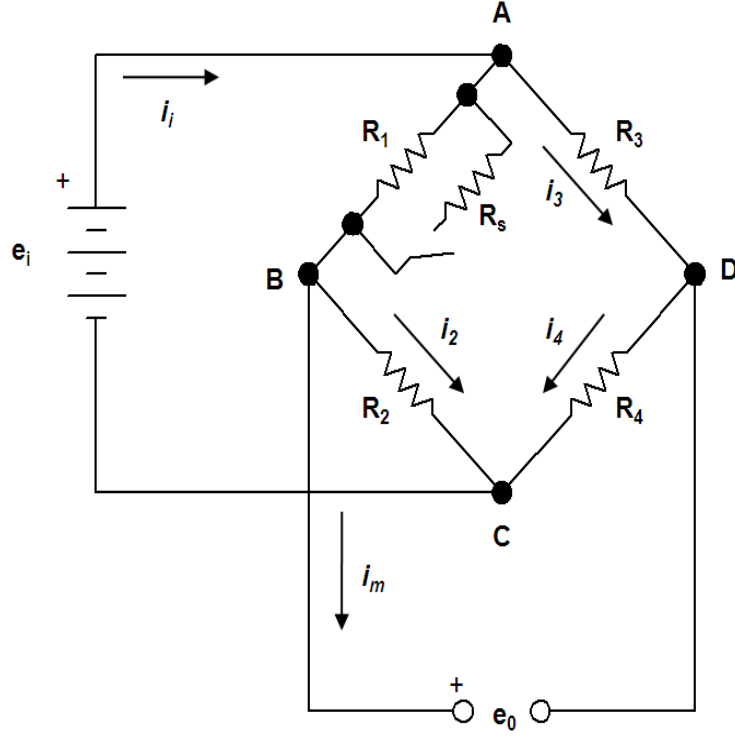


Figure A.5: Typical Wheatstone bridge circuit with a shunt resistance for calibration purposes [13].

output of the signal conditioner. This shunt resistance is a *known* quantity for a given unit, and thus the system can be calibrated to correlate the output voltage to a known change in resistance. This is how the mechanical strain from the strain gage is related to output voltage. Some signal conditioners have a (+) and (-) shunt calibration feature for calibration in tensile or compression gage loading. The (+) shunt calibration was shown in Figure A.5, that is, the bridge was excited to output a positive change in voltage according to equation (A.3). The (-) shunt calibration is accomplished by employing a similar shunt to the second arm in the circuit (the R_2) arm. Turning the shunt on arm 1 off and the shunt on arm 2 on (with same shunt resistance R_2), and applying equations (A.3) and (A.6), it can be shown that this results in a (-) voltage reading across the bridge output. Thus, the conditioner with the shunt calibration features can correlate tensile (+) voltage changes as well as (-) compressive voltage changes in linear strain gages.

A.3 Data Acquisition Unit

The last component of the instrumentation is the data acquisition unit. The voltage signals output from the signal conditioner are useless if they cannot be deciphered. Thus, an instrument capable of detecting, deciphering, and conveying the signals to the test engineer becomes necessary to the overall experimental process. In theory, any device capable of measuring a voltage could be used including a voltmeter. In this case, the goal is to record strain histories over a finite length of time while the plate specimens respond to impact loading. It is important to capture the voltage changes over the entire length of the impact event in order to capture the material response adequately. A voltmeter generally measures instantaneous voltages and cannot store a history of voltages over time. This makes such a device impractical for use in these tests. Further, the entire impact event can occur over a length of time on the order of a millisecond (1.0×10^{-3} sec). An oscilloscope, on the other hand, is capable of measuring voltages over time. Oscilloscopes vary widely in their capabilities, and therefore an oscilloscope with the capability to store a voltage-strain history over a brief period of time with sufficient resolution to capture strain effects on the order of microseconds (1.0×10^{-6} sec) is necessary.

The oscilloscope used to record strain histories from plate impacts stores the histories as voltage readings at discrete time intervals. The last step in acquiring the strain histories is to correlate the voltage readings to the actual physical strain in the specimen. Each bridge circuit was balanced before testing such that the voltage output from the strain gages was initially zero. A voltmeter was used to measure the voltage output from the signal conditioner for each gage with a (+) and (-) shunt calibration. It was not possible to obtain a perfect zero voltage from the initial balance, but in each case the value at balance was very close to zero. The shunt calibration values were each recorded and were essentially the same in magnitude but opposite in sign. Returning to equation (A.1) and noting that $\Delta L/L$ is essentially

linear strain, equation (A.1) can be rewritten as

$$\epsilon = \frac{1}{GF} \frac{\Delta R}{R} \quad (\text{A.7})$$

The change in resistance across arm 1 (the strain gage arm with gage resistance R_1) of the Wheatstone bridge due to a (+) shunt calibration is given by

$$\Delta R = R_1 - \frac{R_1 R_s}{R_1 + R_s} = \frac{R_1^2}{R_1 + R_s} \quad (\text{A.8})$$

and applied to equation (A.7):

$$\epsilon_e = \frac{1}{GF} \left(\frac{R_1}{R_1 + R_s} \right) \quad (\text{A.9})$$

ϵ_e is the equivalent strain from the calibration. To correct for any offset error in the balance and (+), (-) shunt calibration values, knowing that they should be the same in magnitude, the corrected calibration magnitude e_{cal} is determined by

$$e_{cal} = \frac{e_{cal}^+ - e_{cal}^-}{2} \quad (\text{A.10})$$

where the (+) and (-) superscripts on e_{cal} are voltmeter readings for the (+) and (-) calibrations, respectively. These (+) and (-) calibrations are effectively known resistance changes related to voltage outputs. These are essentially *simulated* strains, noting that a change in resistance of the Wheatstone bridge arm is induced much the same as a change in resistance across the Wheatstone bridge arm occurs as a strain gage follows a specimen's deformation. Thus, the voltages recorded over strain histories are related to strain by

$$\epsilon_g = \left(\frac{\epsilon_e}{e_{cal}} \right) e_g \quad (\text{A.11})$$

where ϵ_g is the measured strain in the gage and e_g is the voltage reading from the strain gage registered by the oscilloscope. The quantity (ϵ_e / e_{cal}) is an *individual constant*

(with units strain/Volt) *for each individual strain gage over the length of a single test if the test is assumed linear.* Thus, a separate value of (ϵ_e / e_{cal}) is calculated for each gage before the beginning of a test. The constant value of this quantity is multiplied by each of the voltage readings from the oscilloscope to calculate individual strain readings from each gage over the length of the impact test. In these tests, all strains were in fact linear-elastic so it is valid to treat this quantity as a constant. The shunt calibration readings for each gage and each test necessary to calculate the strains over the strain histories of each individual test were recorded and are found in Appendix B, along with an example of how to relate voltage data to physical strains.

Appendix B. Plate Experiments Raw Data

This appendix is a compilation of the data collected from all the plate impact experiments using the Dynatup. Each individual test includes two tables with the details and settings applied to each test for reference purposes. The histories plotted are the voltage readings from each strain gage over the entire window of data collection. The histories are not smoothed and all 10,000 data points are plotted in each figure without any smoothing or other processing of the data. *The complete test data record is given in this appendix and only selected results are presented in the main body of this document.* Refer to Chapter V for explanation of how the tests were conducted and explanation of terms.

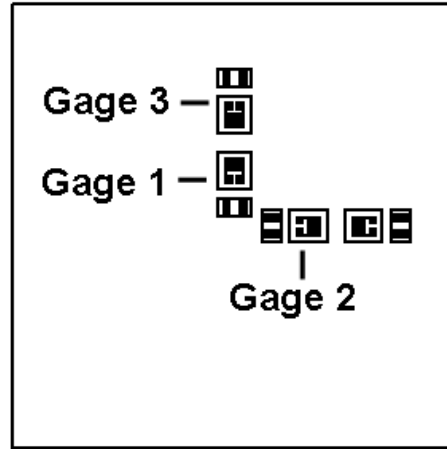


Figure B.1: Specimen plate with locations of strain gages for reference; see Figure 5.10 and 5.11. The fourth gage shown was not used.

Common Test Parameters for All Tests:

Parameter	Value	Units
Gage Factor, GF , Strain Gage 1	2.135	
Gage Factor, GF , Strain Gages 2, 3	2.100	
Strain Gage Resistances, R_1	350	Ohms
Shunt Resistance, R_s	49,000	Ohms

Example

Here an example calculation is provided for converting the voltage readings to strain [13]. See Chapter V for explanation of the terms and details on how the relations are developed. The example used will be from test 1, gage 1, in section B.1 of this appendix, but the same process can be used for all the strain gage voltage measurements.

1. Key numbers and parameters:

Gage Factor, GF , Strain Gage 1:	2.135	
Strain Gage Resistances, R_1 :	350	Ohms (Ω)
Shunt Resistance, R_s :	49,000	Ohms (Ω)
(+) Shunt Calibration, e_{cal}^+ :	+0.1776	Volts (V)
Zero Calibration, e_{cal}^0 :	-0.0008	Volts (V)
(-) Shunt Calibration, e_{cal}^- :	-0.1793	Volts (V)

2. Calculate equivalent strain ϵ_e from change in resistance due to shunt:

$$\epsilon_e = \frac{1}{GF} \left(\frac{R_1}{R_1 + R_s} \right) = \frac{1}{2.135} \left(\frac{350 \Omega}{350 \Omega + 49,000 \Omega} \right) = 0.003322$$

3. Calculate calibration voltage measured from (+) and (-) change in resistance due to shunt:

$$e_{cal} = \frac{e_{cal}^+ - e_{cal}^-}{2} = \frac{0.1776 \text{ V} - (-0.1793 \text{ V})}{2} = 0.1785 \text{ V}$$

4. Strain measured in gage (ϵ_g) is related to the voltage measurement e_g by:

$$\epsilon_g = \left(\frac{\epsilon_e}{e_{cal}} \right) e_g = \left(\frac{0.003322}{0.1785 \text{ V}} \right) e_g = \left(0.01861 \frac{\text{Strain}}{\text{Volt}} \right) e_g$$

5. Multiply each of the 10,000 voltage readings e_g in strain gage 1 by 0.01861 strain per Volt to obtain the strain value for that instant in the strain history.

B.1 Plate #1: Monolithic 100% Ti-0% TiB Specimen

Summary of Test Parameters and Settings:

Test Parameter	Value	Units
Crosshead Mass	13.06	kg
Crosshead Initial Height	0.508	m
Fixture Screw Torques	20.0	N-m
Dynatup Attachment Screw Torques	35.0	N-m
Actual Impact Velocity	3.040	m/s
Time Window for History	2000	μ -sec

Strain Gage Calibration (Cal), in Volts:

Location	Zero Cal	(+) Shunt Cal	(-) Shunt Cal
Gage 1	-0.0008	+0.1776	-0.1793
Gage 2	-0.0006	+0.1779	-0.1793
Gage 3	+0.0006	+0.1788	-0.1781

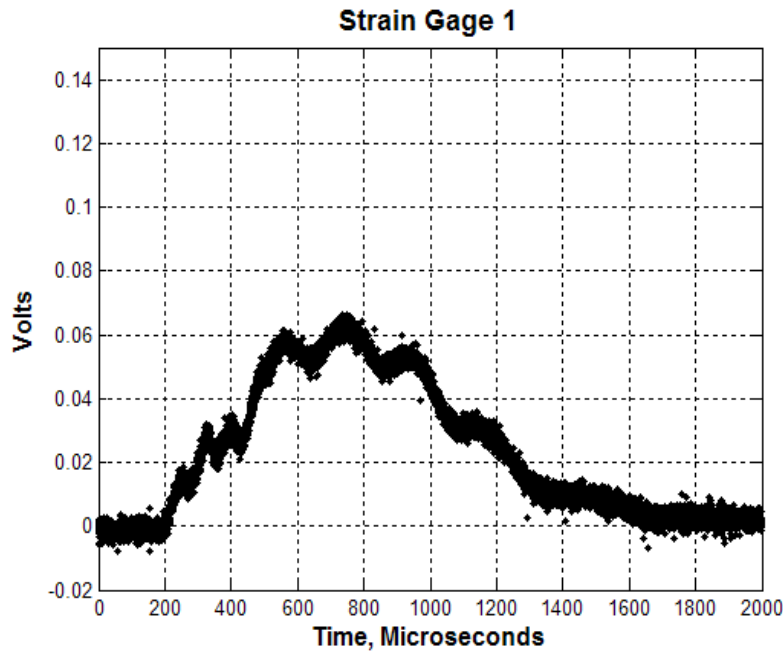


Figure B.2: Raw data strain history for specimen plate #1, 100% Ti - 0% TiB monolithic, strain gage 1.

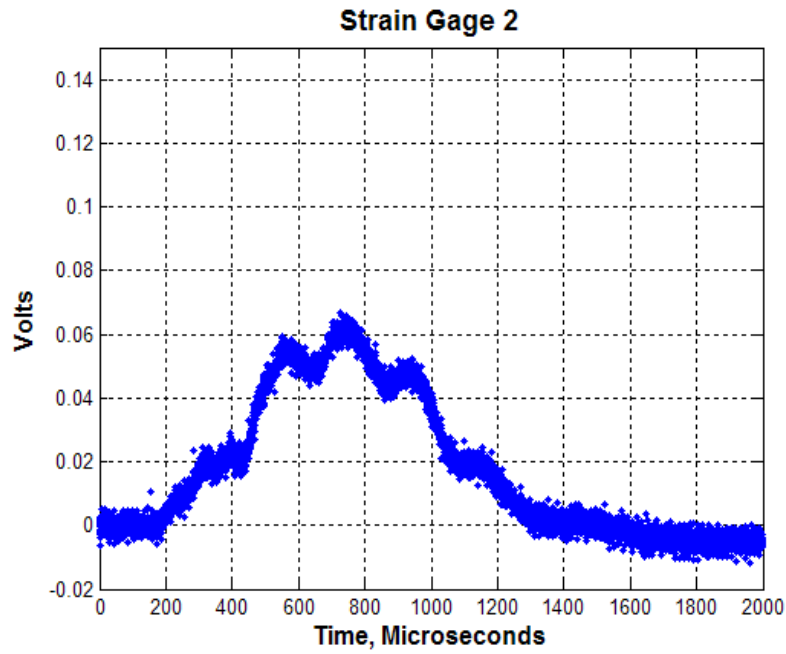


Figure B.3: Raw data strain history for specimen plate #1, 100% Ti - 0% TiB monolithic, strain gage 2.

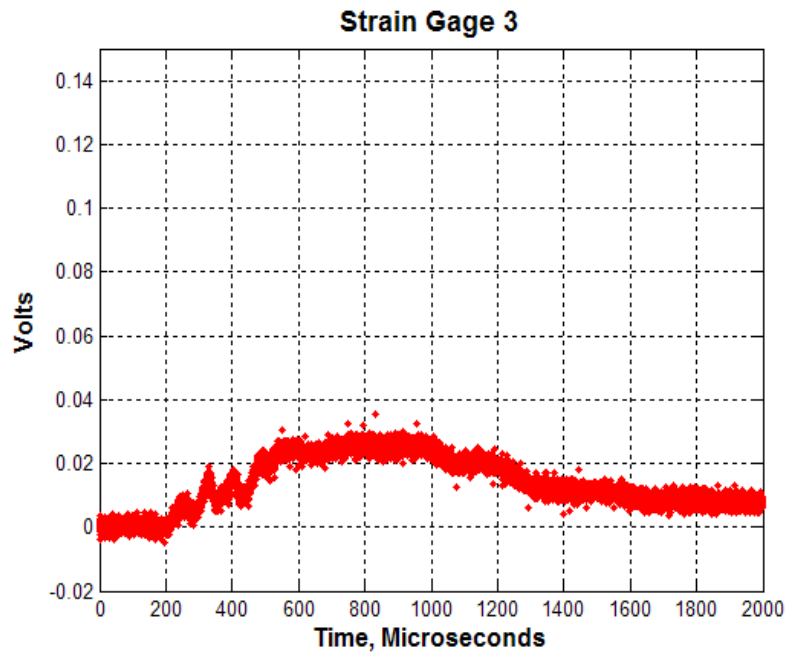


Figure B.4: Raw data strain history for specimen plate #1, 100% Ti - 0% TiB monolithic, strain gage 3.

B.2 Plate #2: Monolithic 100% Ti-0% TiB Specimen

Summary of Test Parameters and Settings:

Test Parameter	Value	Units
Crosshead Mass	13.06	kg
Crosshead Initial Height	0.635	m
Fixture Screw Torques	20.0	N-m
Dynatup Attachment Screw Torques	35.0	N-m
Actual Impact Velocity	3.476	m/s
Time Window for History	2000	μ -sec

Strain Gage Calibration (Cal), in Volts:

Location	Zero Cal	(+) Shunt Cal	(-) Shunt Cal
Gage 1	-0.0017	+0.1771	-0.1803
Gage 2	+0.0007	+0.1793	-0.1778
Gage 3	+0.0014	+0.1792	-0.1784

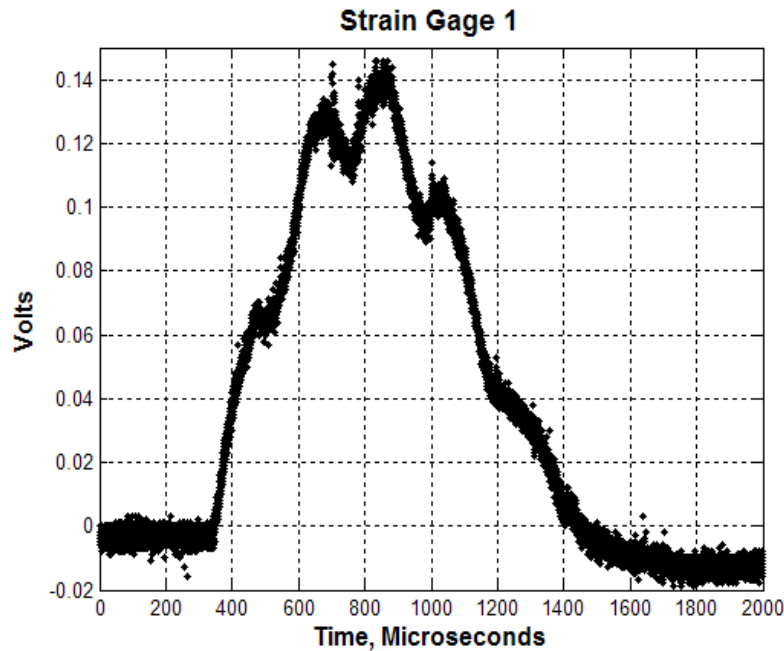


Figure B.5: Raw data strain history for specimen plate #2, 100% Ti - 0% TiB monolithic, strain gage 1.

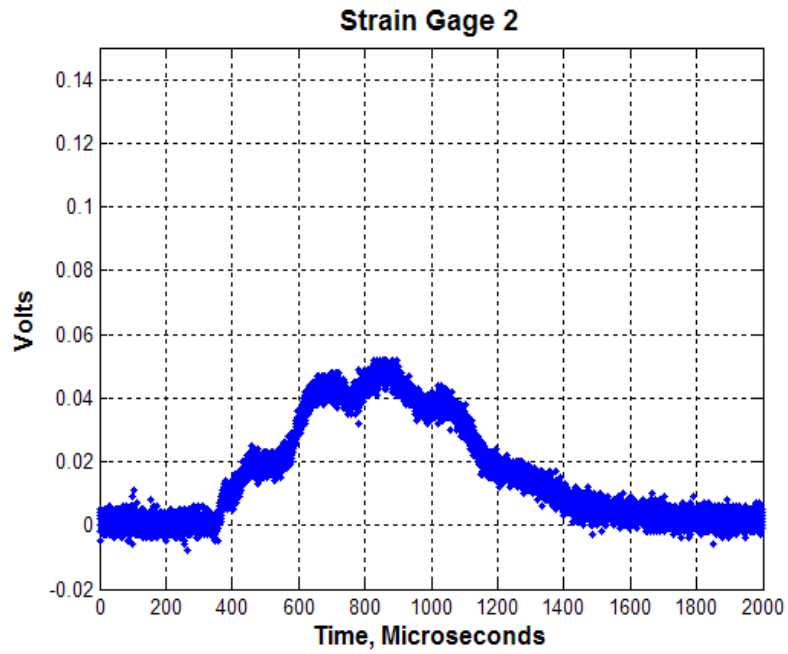


Figure B.6: Raw data strain history for specimen plate #2, 100% Ti - 0% TiB monolithic, strain gage 2.

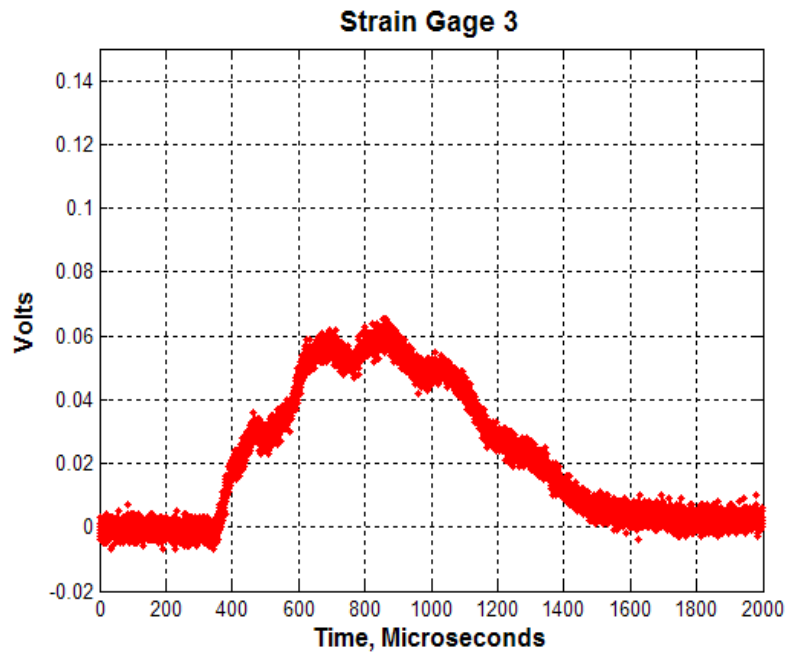


Figure B.7: Raw data strain history for specimen plate #2, 100% Ti - 0% TiB monolithic, strain gage 3.

B.3 Plate #3: Monolithic 85% Ti-15% TiB Specimen

Summary of Test Parameters and Settings:

Test Parameter	Value	Units
Crosshead Mass	13.06	kg
Crosshead Initial Height	0.508	m
Fixture Screw Torques	20.0	N-m
Dynatup Attachment Screw Torques	35.0	N-m
Actual Impact Velocity	3.050	m/s
Time Window for History	2000	μ -sec

Strain Gage Calibration (Cal), in Volts:

Location	Zero Cal	(+) Shunt Cal	(-) Shunt Cal
Gage 1	+0.0005	+0.1786	-0.1779
Gage 2	+0.0011	+0.1798	-0.1773
Gage 3	+0.0017	+0.1803	-0.1770

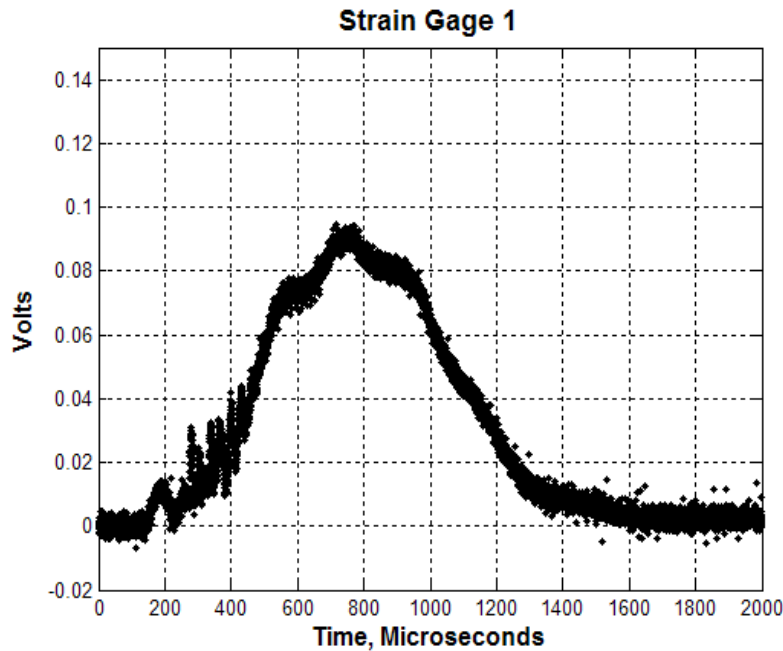


Figure B.8: Raw data strain history for specimen plate #3, 85% Ti - 15% TiB monolithic, strain gage 1.

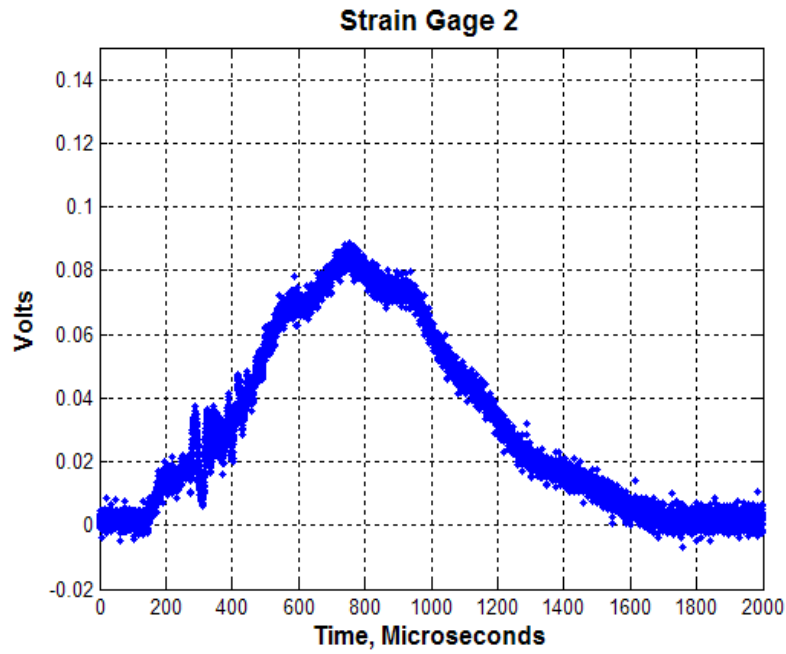


Figure B.9: Raw data strain history for specimen plate #3, 85% Ti - 15% TiB monolithic, strain gage 2.

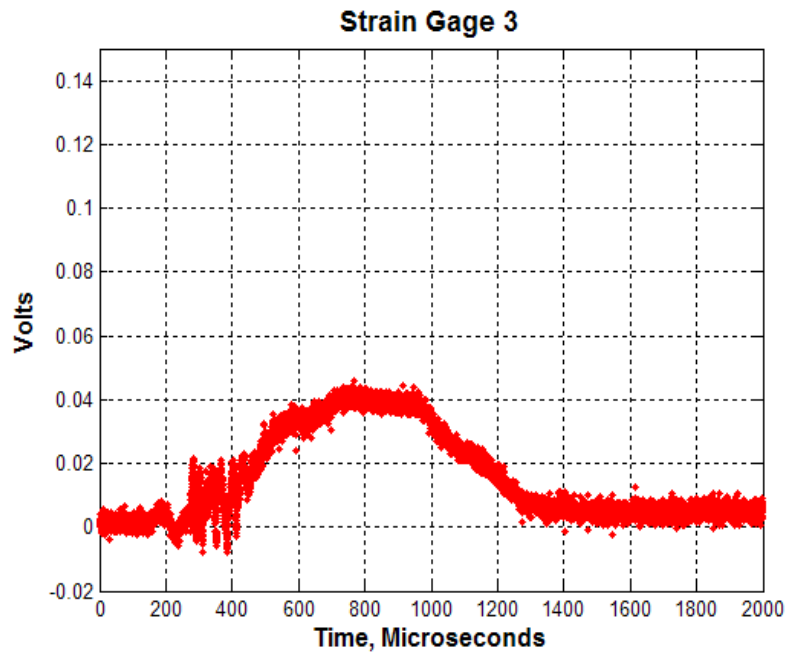


Figure B.10: Raw data strain history for specimen plate #3, 85% Ti - 15% TiB monolithic, strain gage 3.

B.4 Plate #4: Monolithic 85% Ti-15% TiB Specimen

Summary of Test Parameters and Settings:

Test Parameter	Value	Units
Crosshead Mass	13.06	kg
Crosshead Initial Height	0.635	m
Fixture Screw Torques	20.0	N-m
Dynatup Attachment Screw Torques	35.0	N-m
Actual Impact Velocity	3.479	m/s
Time Window for History	2000	μ -sec

Strain Gage Calibration (Cal), in Volts:

Location	Zero Cal	(+) Shunt Cal	(-) Shunt Cal
Gage 1	+0.0003	+0.1792	-0.1783
Gage 2	+0.0004	+0.1789	-0.1780
Gage 3	-0.0008	+0.1783	-0.1791

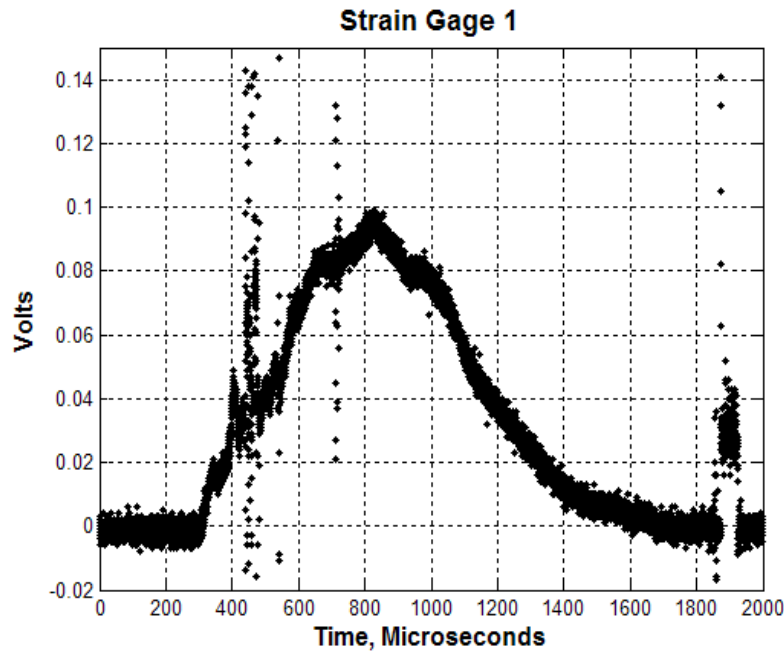


Figure B.11: Raw data strain history for specimen plate #4, 85% Ti - 15% TiB monolithic, strain gage 1.

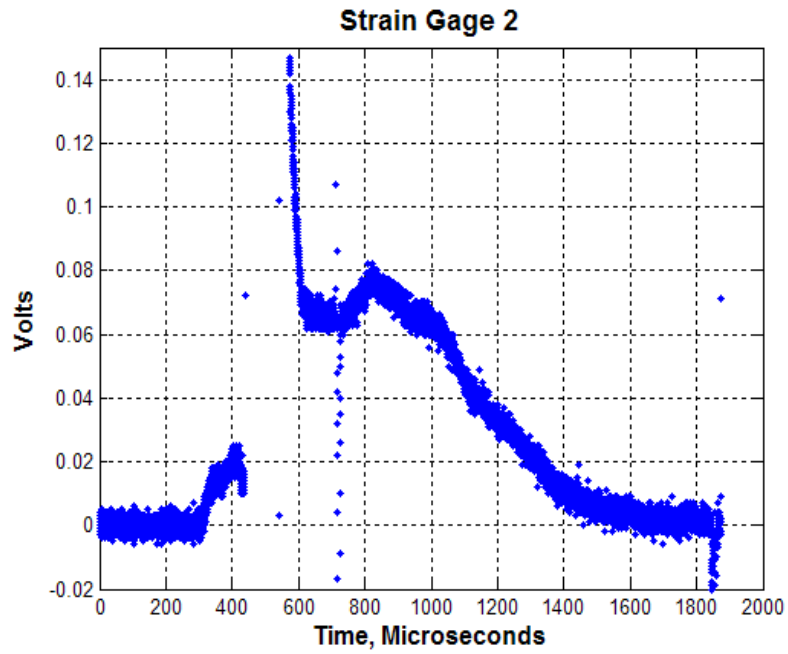


Figure B.12: Raw data strain history for specimen plate #4, 85% Ti - 15% TiB monolithic, strain gage 2.

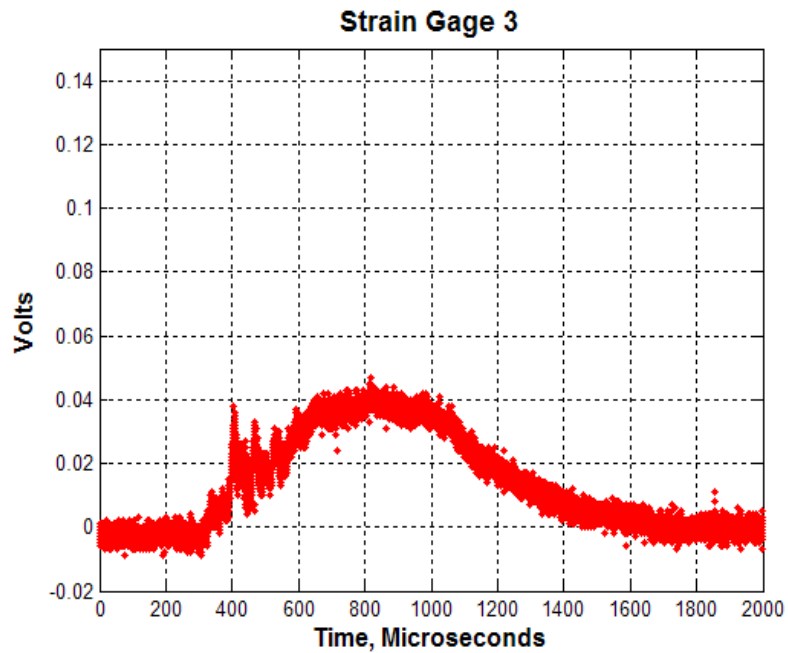


Figure B.13: Raw data strain history for specimen plate #4, 85% Ti - 15% TiB monolithic, strain gage 3.

B.5 Plate #5: Monolithic 15% Ti-85% TiB Specimen

Summary of Test Parameters and Settings:

Test Parameter	Value	Units
Crosshead Mass	13.06	kg
Crosshead Initial Height	0.381	m
Fixture Screw Torques	20.0	N-m
Dynatup Attachment Screw Torques	35.0	N-m
Actual Impact Velocity	2.585	m/s
Time Window for History	2000	μ -sec

Strain Gage Calibration (Cal), in Volts:

Location	Zero Cal	(+) Shunt Cal	(-) Shunt Cal
Gage 1	-0.0003	+0.1784	-0.1786
Gage 2	-0.0005	+0.1780	-0.1790
Gage 3	+0.0004	+0.1790	-0.1782

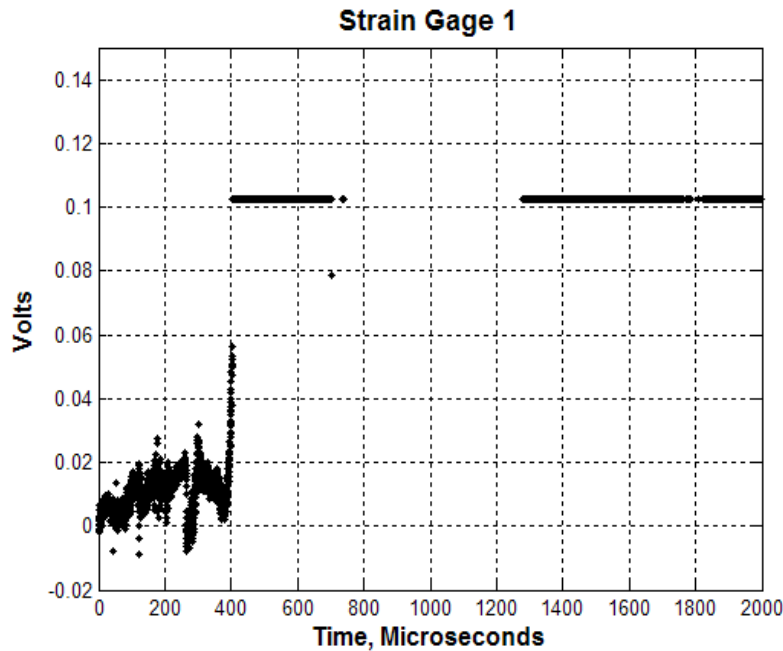


Figure B.14: Raw data strain history for specimen plate #5, 15% Ti - 85% TiB monolithic, strain gage 1.

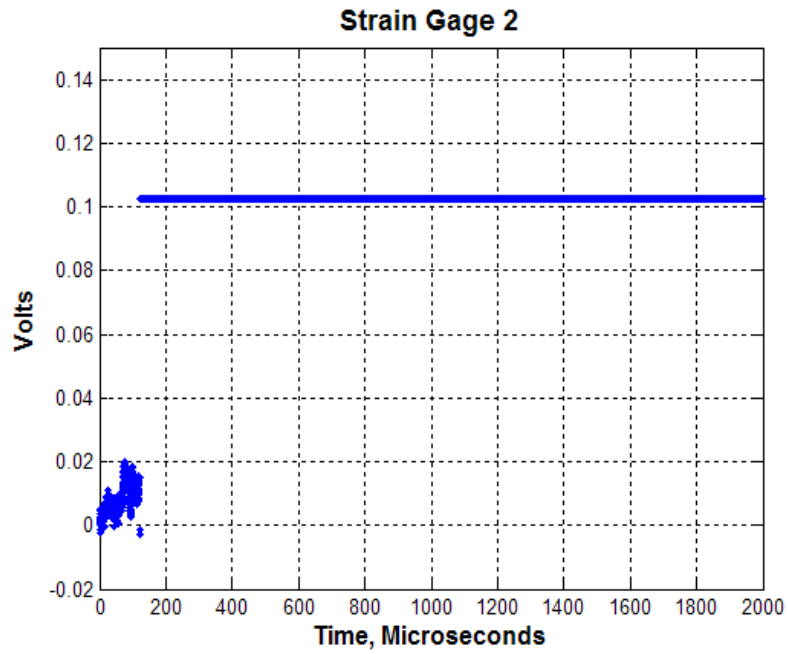


Figure B.15: Raw data strain history for specimen plate #5, 15% Ti - 85% TiB monolithic, strain gage 2.

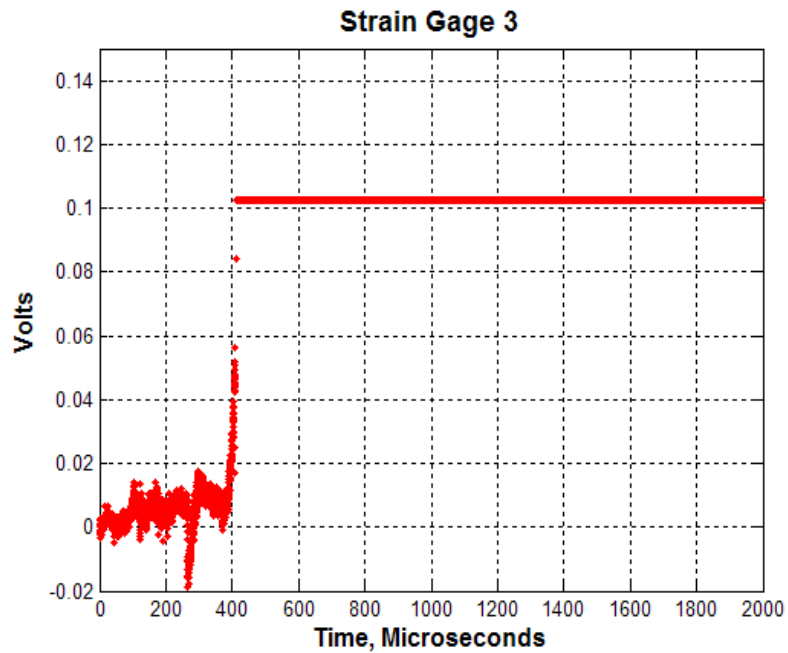


Figure B.16: Raw data strain history for specimen plate #5, 15% Ti - 85% TiB monolithic, strain gage 3.

B.6 Plate #6: Monolithic 15% Ti-85% TiB Specimen

Summary of Test Parameters and Settings:

Test Parameter	Value	Units
Crosshead Mass	13.06	kg
Crosshead Initial Height	0.508	m
Fixture Screw Torques	20.0	N-m
Dynatup Attachment Screw Torques	35.0	N-m
Actual Impact Velocity	3.050	m/s
Time Window for History	2000	μ -sec

Strain Gage Calibration (Cal), in Volts:

Location	Zero Cal	(+) Shunt Cal	(-) Shunt Cal
Gage 1	-0.0004	+0.1774	-0.1790
Gage 2	-0.0007	+0.1777	-0.1793
Gage 3	+0.0006	+0.1791	-0.1782

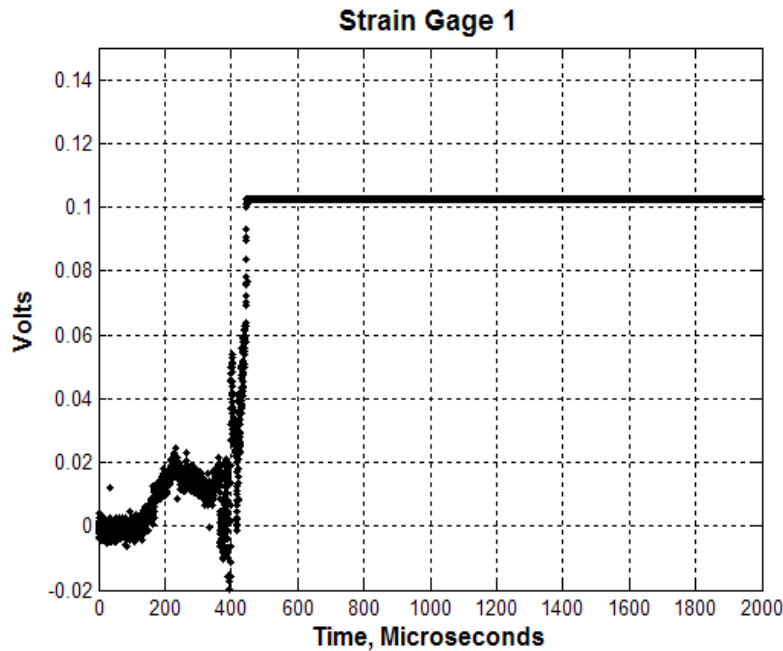


Figure B.17: Raw data strain history for specimen plate #6, 15% Ti - 85% TiB monolithic, strain gage 1.

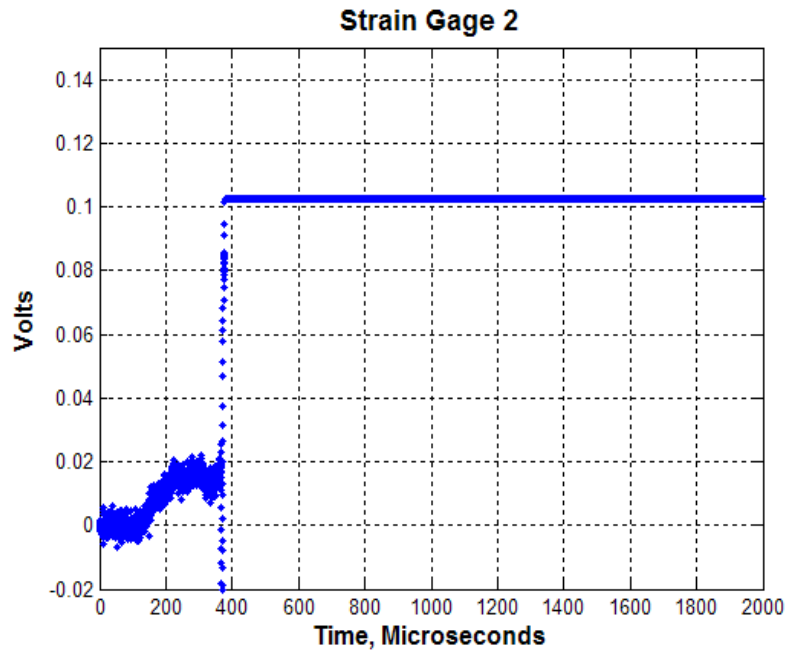


Figure B.18: Raw data strain history for specimen plate #6, 15% Ti - 85% TiB monolithic, strain gage 2.

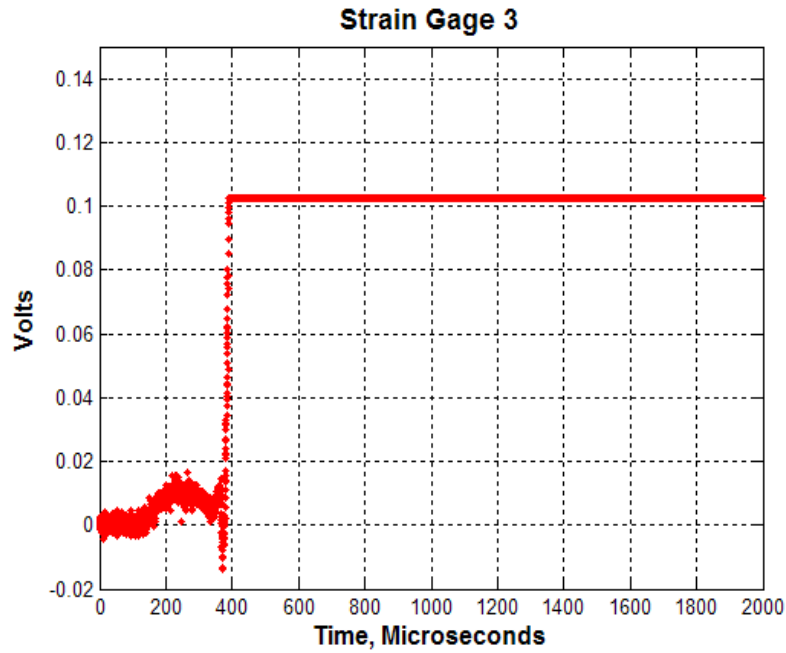


Figure B.19: Raw data strain history for specimen plate #6, 15% Ti - 85% TiB monolithic, strain gage 3.

B.7 Plate #7: Seven Layer Ti-TiB FGM Specimen

Summary of Test Parameters and Settings:

Test Parameter	Value	Units
Crosshead Mass	13.06	kg
Crosshead Initial Height	0.508	m
Fixture Screw Torques	20.0	N-m
Dynatup Attachment Screw Torques	35.0	N-m
Actual Impact Velocity	3.040	m/s
Time Window for History	2000	μ -sec

Strain Gage Calibration (Cal), in Volts:

Location	Zero Cal	(+) Shunt Cal	(-) Shunt Cal
Gage 1	+0.0008	+0.1792	-0.1777
Gage 2	-0.0011	+0.1773	-0.1797
Gage 3	+0.0002	+0.1789	-0.1784

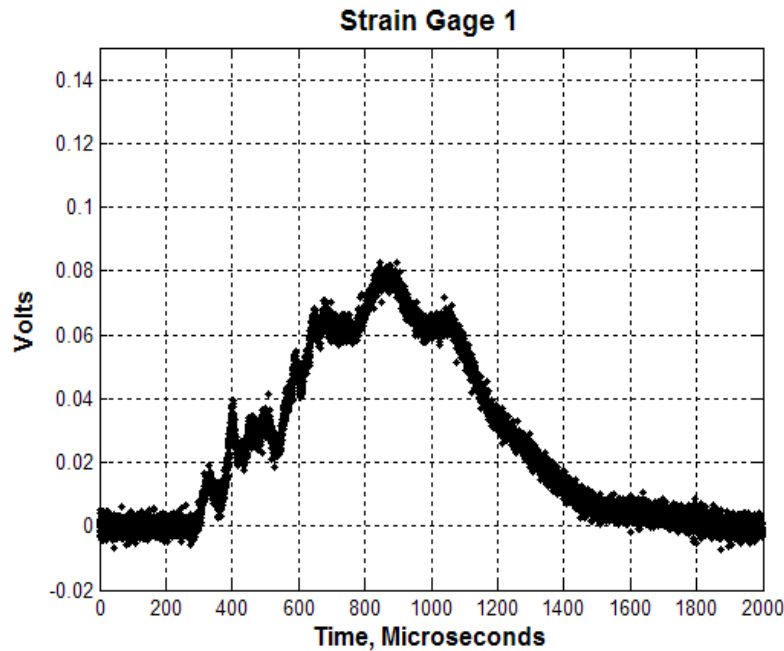


Figure B.20: Raw data strain history for specimen plate #7, seven-layer Ti-TiB FGM, strain gage 1.

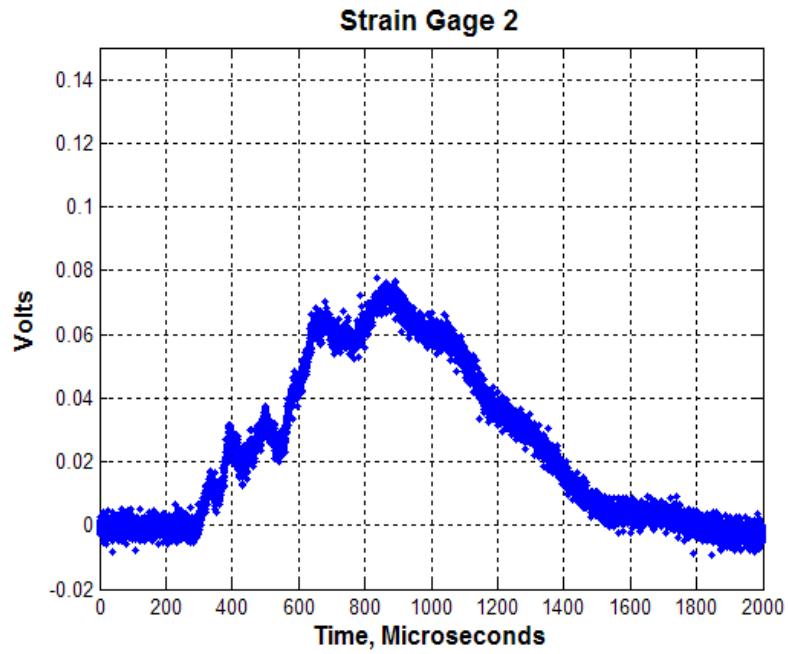


Figure B.21: Raw data strain history for specimen plate #7, seven-layer Ti-TiB FGM, strain gage 2.

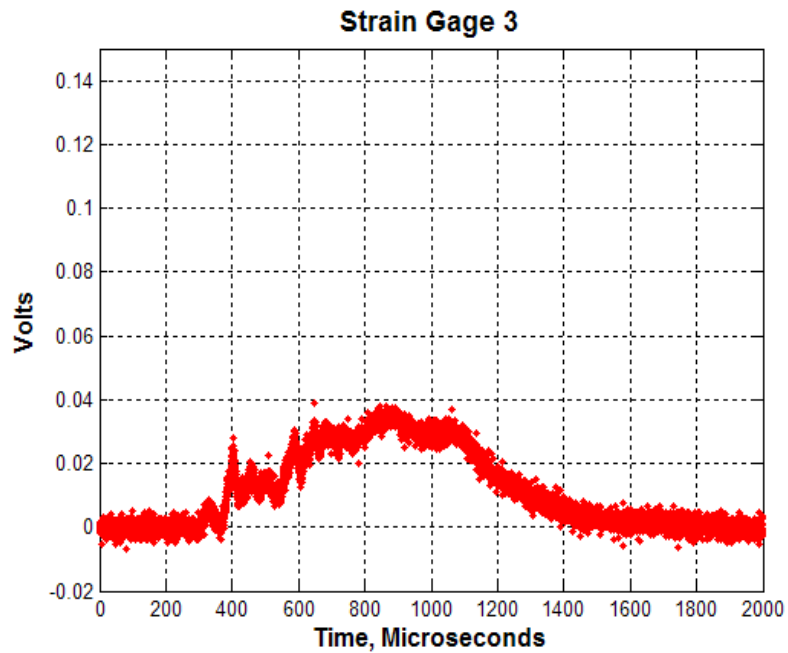


Figure B.22: Raw data strain history for specimen plate #7, seven-layer Ti-TiB FGM, strain gage 3.

B.8 Plate #8: Seven Layer Ti-TiB FGM Specimen

Summary of Test Parameters and Settings:

Test Parameter	Value	Units
Crosshead Mass	13.06	kg
Crosshead Initial Height	0.635	m
Fixture Screw Torques	20.0	N-m
Dynatup Attachment Screw Torques	35.0	N-m
Actual Impact Velocity	3.412	m/s
Time Window for History	2000	μ -sec

Strain Gage Calibration (Cal), in Volts:

Location	Zero Cal	(+) Shunt Cal	(-) Shunt Cal
Gage 1	+0.0002	+0.1788	-0.1784
Gage 2	+0.0012	+0.1796	-0.1773
Gage 3	-0.0007	+0.1779	-0.1794

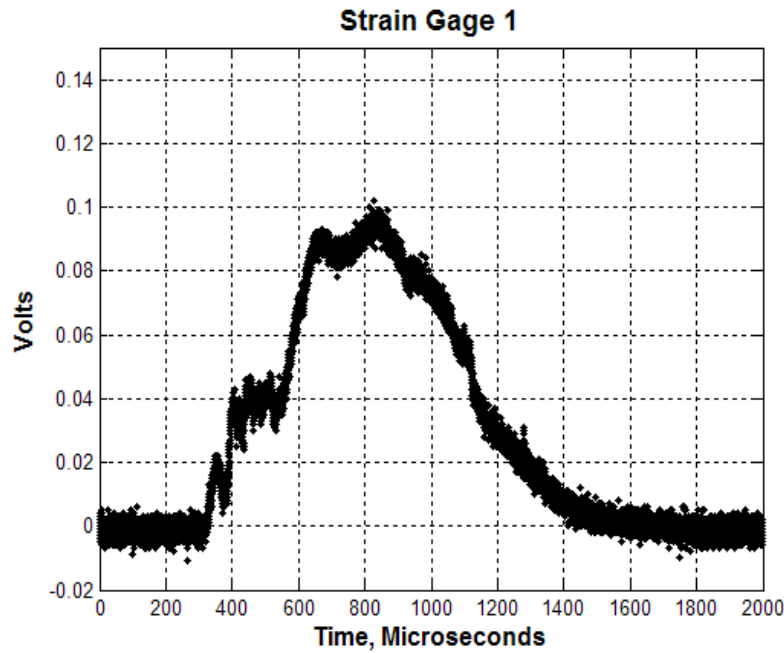


Figure B.23: Raw data strain history for specimen plate #8, seven-layer Ti-TiB FGM, strain gage 1.

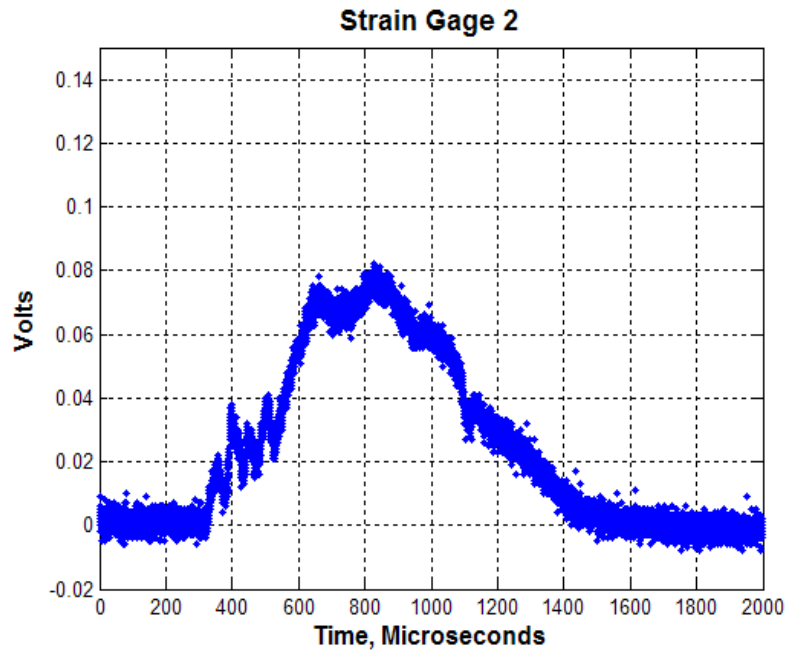


Figure B.24: Raw data strain history for specimen plate #8, seven-layer Ti-TiB FGM, strain gage 2.

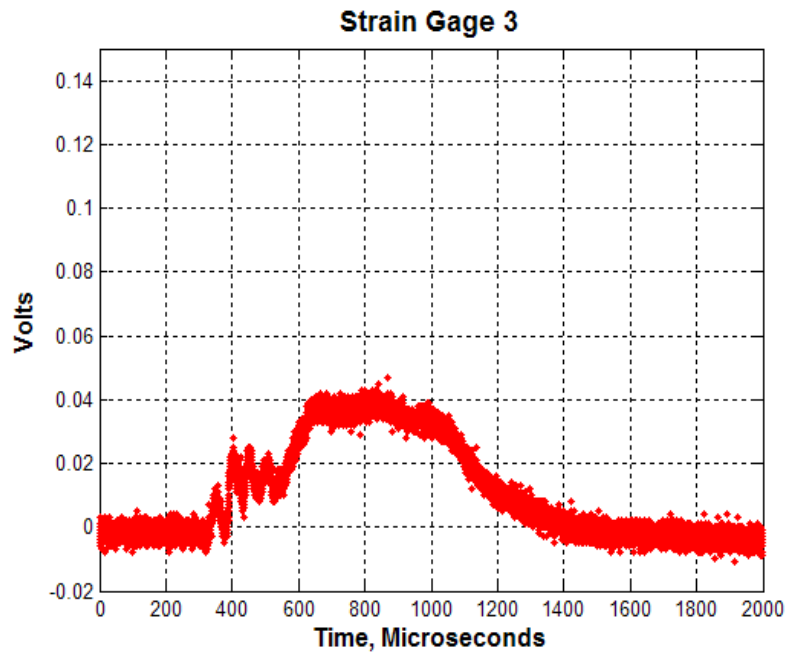


Figure B.25: Raw data strain history for specimen plate #8, seven-layer Ti-TiB FGM, strain gage 3.

B.9 Plate #9: Seven Layer Ti-TiB FGM Specimen

Summary of Test Parameters and Settings:

Test Parameter	Value	Units
Crosshead Mass	13.06	kg
Crosshead Initial Height	0.762	m
Fixture Screw Torques	20.0	N-m
Dynatup Attachment Screw Torques	35.0	N-m
Actual Impact Velocity	3.765	m/s
Time Window for History	2000	μ -sec

Strain Gage Calibration (Cal), in Volts:

Location	Zero Cal	(+) Shunt Cal	(-) Shunt Cal
Gage 1	+0.0004	+0.1786	-0.1781
Gage 2	+0.0007	+0.1791	-0.1779
Gage 3	+0.0004	+0.1790	-0.1783

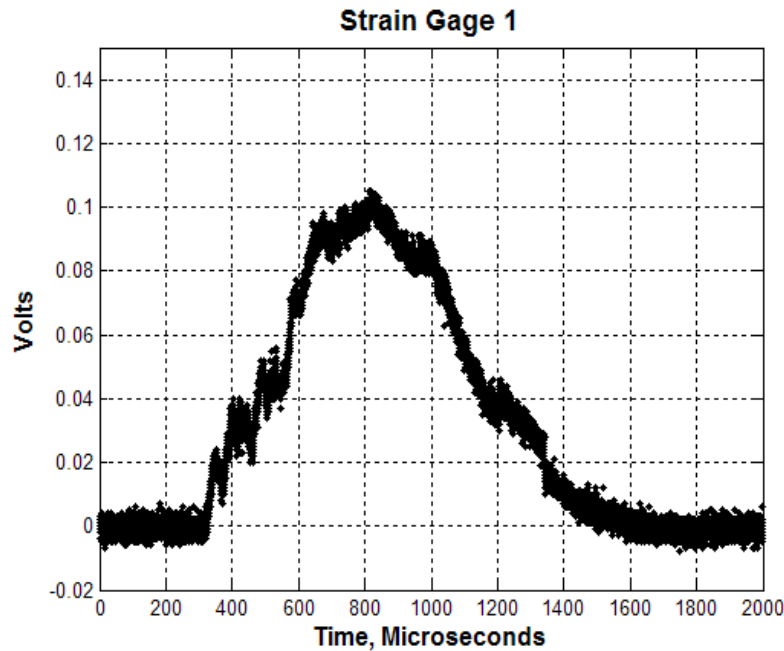


Figure B.26: Raw data strain history for specimen plate #9, seven-layer Ti-TiB FGM, strain gage 1.

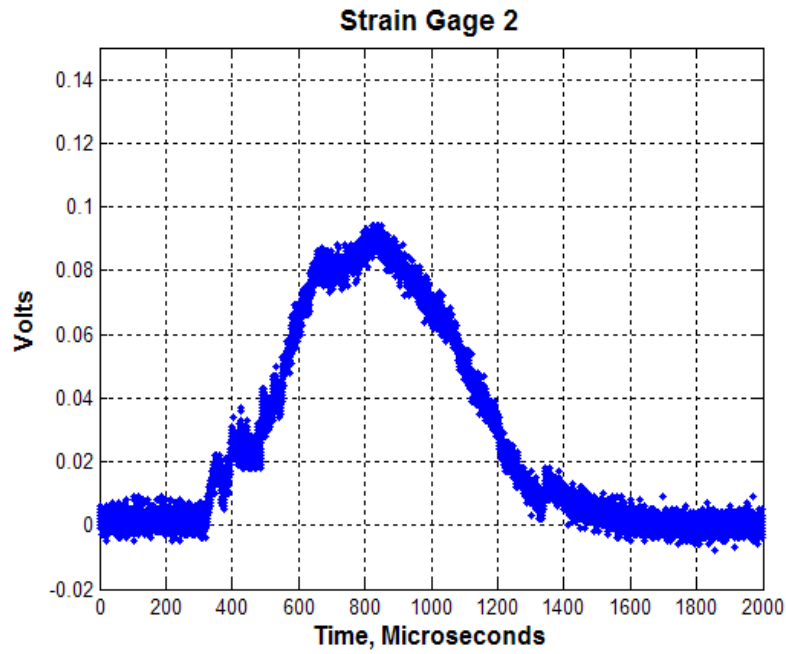


Figure B.27: Raw data strain history for specimen plate #9, seven-layer Ti-TiB FGM, strain gage 2.

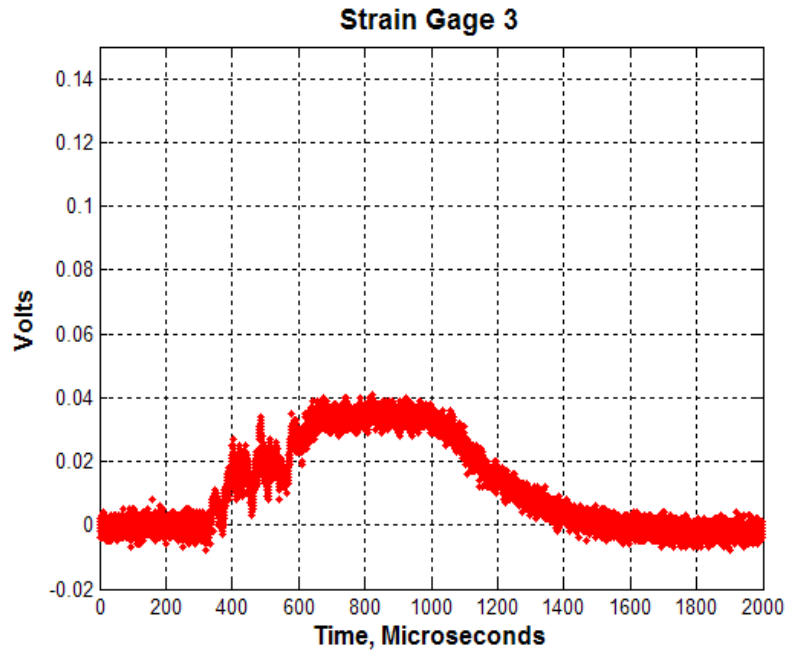


Figure B.28: Raw data strain history for specimen plate #9, seven-layer Ti-TiB FGM, strain gage 3.

B.10 Plate #10: Seven Layer Ti-TiB FGM Specimen

Summary of Test Parameters and Settings:

Test Parameter	Value	Units
Crosshead Mass	13.06	kg
Crosshead Initial Height	0.889	m
Fixture Screw Torques	20.0	N-m
Dynatup Attachment Screw Torques	35.0	N-m
Actual Impact Velocity	4.078	m/s
Time Window for History	2000	μ -sec

Strain Gage Calibration (Cal), in Volts:

Location	Zero Cal	(+) Shunt Cal	(-) Shunt Cal
Gage 1	-0.0016	+0.1769	-0.1801
Gage 2	-0.0004	+0.1783	-0.1788
Gage 3	+0.0013	+0.1800	-0.1773

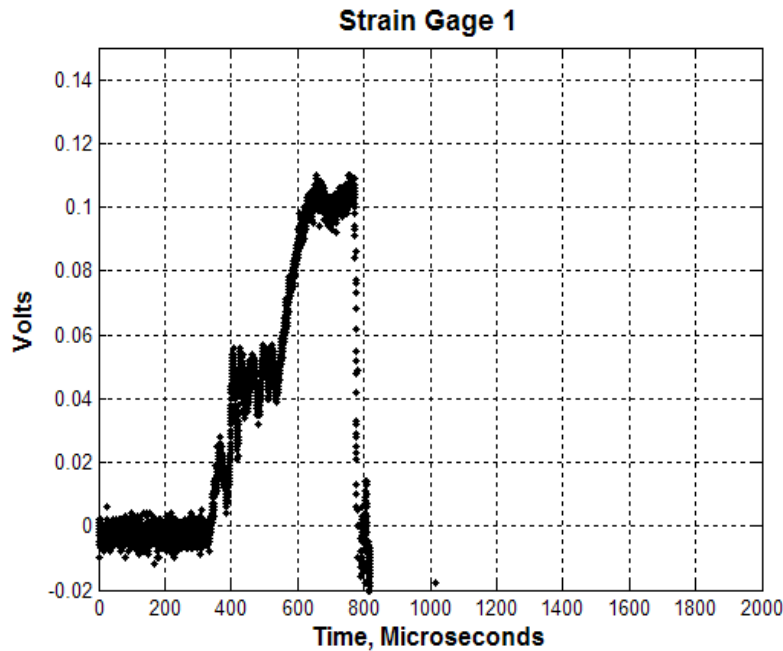


Figure B.29: Raw data strain history for specimen plate #10, seven-layer Ti-TiB FGM, strain gage 1.

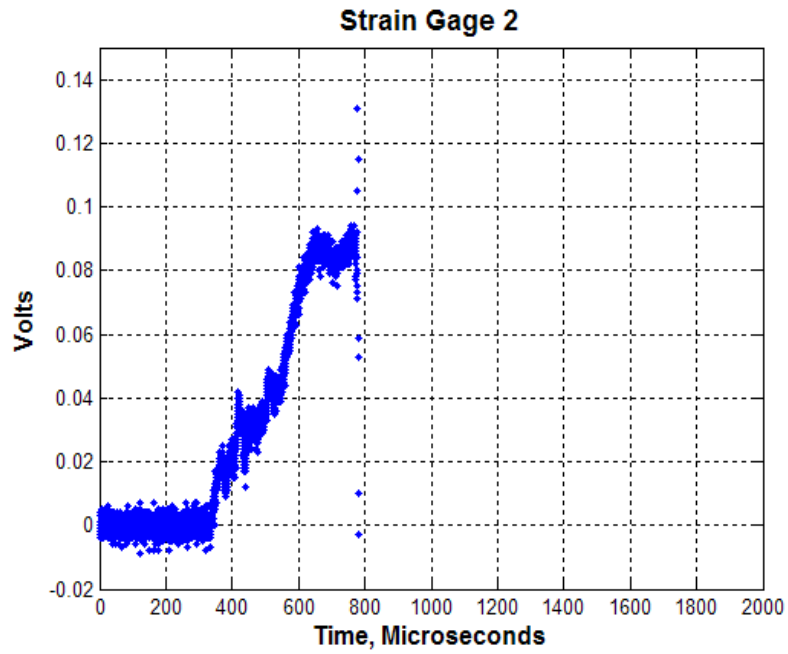


Figure B.30: Raw data strain history for specimen plate #10, seven-layer Ti-TiB FGM, strain gage 2.

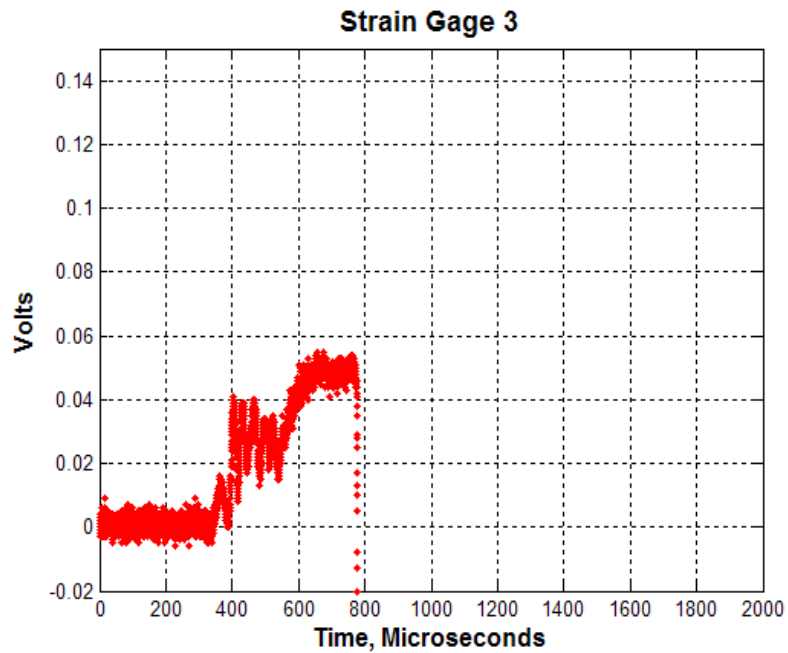


Figure B.31: Raw data strain history for specimen plate #10, seven-layer Ti-TiB FGM, strain gage 3.

Appendix C. Overview of Relevant Finite Element Theory

This appendix discusses selected portions of relevant finite theory associated with the studying the FGM plate impact problem, and more specifically topics associated with the commercial FEM code ABAQUS. The ABAQUS FEM code was used exclusively to study the plate impact problem. Therefore the majority of this appendix will revolve around concepts associated specifically with that program. This appendix is summarized directly from the ABAQUS v6.6 Theory Manual [3], with many concepts explained from other sources as noted. It is far beyond the scope of this document to present a comprehensive overview of general finite element theory; rather, brief synopses of key concepts required to model the FGM impacts are given for reference purposes, most of which are provided without derivation.

The topics in this appendix are organized as follows. First, the explicit integration numerical technique used by ABAQUS to study dynamic problems is explained. Next, the measures of deformation, strain, and stress applicable to the impact problem studied in this work are presented as used by ABAQUS. Once the measures of deformation, strain, and stress are explained, the governing equations solved by the explicit numerical technique are briefly discussed. The particular details associated with the elements used in the finite element models are explained in the context of the finite element discretization process. Finally, the basic theory behind the contact model used in the FEMs is presented to gain a more thorough understanding of the highly nonlinear contact interaction.

C.1 Explicit Integration Solution Scheme

This first section will be dedicated to the manner in which ABAQUS solves the governing equations of motion for the FEM. ABAQUS has the ability to solve a wide variety of solid mechanics problems in the context of finite element theory. This research used a specific solution module in ABAQUS known as “ABAQUS/Explicit.” The ABAQUS/Explicit module uses an explicit integration numerical technique to solve the governing equations associated with the system being studied. The solu-

tion method is specifically formulated to study *dynamic, time-dependent problems* with a high degree of material and geometric nonlinearity and is well-suited to wave propagation problems.

The details of the ABAQUS/Explicit solution scheme are briefly summarized below from [3]. The dynamics analysis procedure in ABAQUS/Explicit is based upon implementing an explicit integration rule while using diagonal element mass matrices. The equations of motion are integrated using the explicit central difference integration rule

$$\dot{\mathbf{u}}^{(i+1/2)} = \dot{\mathbf{u}}^{(i-1/2)} + \frac{\Delta t^{(i+1)} + \Delta t^{(i)}}{2} \ddot{\mathbf{u}}^{(i)} \quad (\text{C.1})$$

$$\mathbf{u}^{(i+1)} = \mathbf{u}^{(i)} + \Delta t^{(i+1)} \dot{\mathbf{u}}^{(i+1/2)} \quad (\text{C.2})$$

\mathbf{u} , $\dot{\mathbf{u}}$, and $\ddot{\mathbf{u}}$ refer to the displacement, velocity, and acceleration vectors. Superscript (i) is the increment number and $\pm 1/2$ are mid-increment values. The central difference integration operator is categorized as explicit because the kinematic state can be advanced knowing $\dot{\mathbf{u}}^{(i-1/2)}$ and $\ddot{\mathbf{u}}^{(i)}$ from the previous time step. The computational efficiency of the solution technique lies in the use of the diagonal element mass matrices, which are easily inverted to compute the accelerations at the beginning of time increment using

$$\mathbf{M} \ddot{\mathbf{u}}^{(i)} = F_{\text{EXT}}^{(i)} - F_{\text{INT}}^{(i)} \quad (\text{C.3})$$

$$\ddot{\mathbf{u}}^{(i)} = \mathbf{M}^{-1} \cdot (F_{\text{EXT}}^{(i)} - F_{\text{INT}}^{(i)}) \quad (\text{C.4})$$

\mathbf{M} is the diagonal mass matrix, F_{EXT} is the vector of applied external loads, and F_{INT} is the applied internal force vector determined by the choice of element, associated stress and strain measures, and material properties. More will be said on how the internal and external forces are resolved with respect to the finite element discretization later in this appendix. Equation (C.4) is essentially the classic mass multiplied by acceleration equals the sum of the external forces minus the sum of the

internal forces. The governing equations in ABAQUS/Explicit are simplified to fit into this framework for numerical evaluation. The midincrement velocities $\dot{\mathbf{u}}^{(i+1/2)}$, $\dot{\mathbf{u}}^{(i-1/2)}$, etc. require special treatment for initial conditions and certain constraints. Concerning presentation of results, state velocities are stored in ABAQUS as linear interpolation of the midincrement velocities

$$\dot{\mathbf{u}}^{(i+1)} = \dot{\mathbf{u}}^{(i+1/2)} + \frac{1}{2}\Delta t^{(i+1)}\ddot{\mathbf{u}}^{(i+1)} \quad (\text{C.5})$$

The central difference operator is not self starting because the midincrement velocity $\dot{\mathbf{u}}^{(-1/2)}$ needs to be defined at time $t = 0$ (increment $i = 0$). ABAQUS imposes the condition

$$\dot{\mathbf{u}}^{(+1/2)} = \dot{\mathbf{u}}^{(0)} + \frac{1}{2}\Delta t^{(1)}\ddot{\mathbf{u}}^{(0)} \quad (\text{C.6})$$

when substituted into the update expression (C.1) yields

$$\dot{\mathbf{u}}^{(-1/2)} = \dot{\mathbf{u}}^{(0)} - \frac{1}{2}\Delta t^{(0)}\ddot{\mathbf{u}}^{(0)} \quad (\text{C.7})$$

The explicit integration technique is conditionally stable, implying that the choice of time increment is bounded by a critical value beyond which the numerical solution is unstable. ABAQUS will automatically calculate stable time increments to solve dynamics problems, but the user can also specify a time increment of their own choosing. The internal ABAQUS algorithm that calculates the maximum stable time increment finds the minimum value over all the elements of the ratio of the characteristic element length to the dilatational wave speed of the element material.

The general flow of the explicit time integration process is as follows [14]:

1. Set time increment $i = 0$, define the initial conditions of the system: time $t^{(0)}$, $\mathbf{u}^{(0)} = \mathbf{0}$, $\dot{\mathbf{u}}^{(0)}$, $\sigma^{(0)}$.

2. Define the time incrementation $t^{(i)}$, $\Delta t^{(i)}$ over the analysis period and the externally applied load history $F_{\mathbf{INT}}$.
3. Compute the lumped mass matrix \mathbf{M} for the system.
4. Evaluate $\ddot{\mathbf{u}}^{(0)}$ from equation (C.4).
 - (a) The initial condition for the stresses in the system, $\sigma^{(0)}$, is used to evaluate the internal forces $F_{\mathbf{INT}}$. (σ here is simply an arbitrary stress measure associated with the appropriate strain measure in the constitutive model).
 - (b) The external forces $F_{\mathbf{EXT}}$ are evaluated based on the initially applied loads from the known load history.
5. Compute $\dot{\mathbf{u}}^{(-1/2)}$ according to (C.7).
6. Compute $\dot{\mathbf{u}}^{(i+\frac{1}{2})}$ according to (C.1).
7. Compute $\mathbf{u}^{(i+1)}$ according to (C.2).
8. Continue to next time increment: $i \leftarrow i + 1$.
9. If simulation is complete, output results; else continue.
10. Evaluate measures of deformation as required (presented in the next section): $\mathbf{D}^{i-1/2}$, \mathbf{F}^i , \mathbf{E}^i (\mathbf{E} is any appropriate strain measure associated with the stress measure σ in the constitutive model).
11. Calculate the stress σ^i by the chosen constitutive relation.
12. Evaluate $\ddot{\mathbf{u}}^{(i)}$ from equation (C.4).
 - (a) The stress in the system, $\sigma^{(i)}$, is used to evaluate the internal forces $F_{\mathbf{INT}}$.
 - (b) The external forces $F_{\mathbf{EXT}}$ are evaluated based on the applied loads from the known load history.
13. Set $i \leftarrow i - 1$. Compute $\dot{\mathbf{u}}^{(i+1)}$ according to (C.5). Reset $i \leftarrow i + 1$. This must be performed because $\ddot{\mathbf{u}}^{(i+1)}$ is not available until Step 12 is performed in the subsequent time step.
14. Go to Step 6.

C.2 Deformation, Strain, and Stress Definitions

It was pointed out in previous chapters that small displacement theory was very appropriate to studying the response of the functionally graded plates used in this research. In general, however, a strong understanding of how a system will likely behave under the loading conditions of interest is a key first step in attempting to construct an accurate finite element simulation of the response. This knowledge allows the engineer to select appropriate elements and constitutive models that will incorporate material characteristics effectively into the simulation. Various constitutive models may require different definitions of stress and strain conjugates for use within their respective framework. ABAQUS uses a continuum mechanics-based approach to relate the deformation, strain, and stress measures in its finite element formulations. This section outlines a few of the important details associated with this approach, summarized from ABAQUS v6.6 Theory Manual [3], Malvern [76], Belytschko et al. [14], and Khan & Huang [62] (refer to these works for more extensive derivations and discussions of the concepts presented). While not all the discussion presented in here is directly applicable to the work documented in this dissertation, it is included here to provide a broad understanding of how ABAQUS develops finite element solutions to a wide variety of engineering problems.

C.2.1 Deformation. Material deformation and movement can be described as follows. A particle is initially located within a body at a point \mathbf{X} in three-dimensional space and moves to a new position \mathbf{x} . (The notation here should not be confused with the notation used in Chapter VIII for the parameter estimation technique; the variables are wholly unrelated.) This is illustrated graphically in Figure C.1. The displacement of point \mathbf{X} to new position \mathbf{x} is given by

$$\mathbf{x} = \mathbf{X} + \mathbf{u} \quad (\text{C.8})$$

The coordinate system associated with the initial reference configuration of the material (\mathbf{X}) is called the *material* or *Lagrangian* coordinate system while the coordinate

system associated with the current material configuration (\mathbf{x}) is called the *spatial* or *Eulerian* coordinate system. The history of the location of the particle can be written as $\mathbf{x} = \mathbf{x}(\mathbf{X}, t)$. The inverse is true, that is, $\mathbf{X} = \mathbf{X}(\mathbf{x}, t)$. Given two neighboring particles at \mathbf{X} and $\mathbf{X} + d\mathbf{X}$, we know that

$$d\mathbf{x} = \frac{\partial \mathbf{x}}{\partial \mathbf{X}} \cdot d\mathbf{X} \quad (\text{C.9})$$

must hold in the current configuration. The deformation gradient \mathbf{F} is given by

$$\mathbf{F} = \frac{\partial \mathbf{x}}{\partial \mathbf{X}} \quad (\text{C.10})$$

and we note that equation (C.9) is written $d\mathbf{x} = \mathbf{F} \cdot d\mathbf{X}$. The initial infinitesimal gauge length between the two neighboring particles at their initial positions of \mathbf{X} and $\mathbf{X} + d\mathbf{X}$ is given by

$$dL^2 = d\mathbf{X}^T \cdot d\mathbf{X} \quad (\text{C.11})$$

and the infinitesimal length between the two particles at their final positions is similarly given by

$$dl^2 = d\mathbf{x}^T \cdot d\mathbf{x} \quad (\text{C.12})$$

The stretch ratio of the gauge length after deformation, λ , is given by $\lambda = dl/dL$. If the stretch ratio is equal to one, no strain of the gauge length has occurred.

It can be shown that the deformation gradient \mathbf{F} can be decomposed into the product of a rigid-body rotation tensor \mathbf{R} and a pure stretching tensor of three orthogonal directions (either \mathbf{V} or \mathbf{U}) as follows:

$$\mathbf{F} = \mathbf{V} \cdot \mathbf{R} = \mathbf{R} \cdot \mathbf{U} \quad (\text{C.13})$$

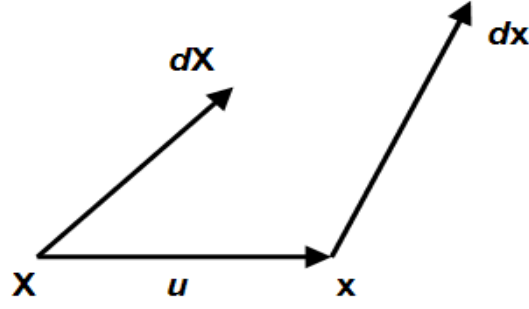


Figure C.1: Displacement, stretch, and rotation of material vector $d\mathbf{X}$ to new position $d\mathbf{x}$ [76].

Therefore, the motion and deformation of an infinitesimal volume element at \mathbf{X} consists of successive application of either (a) translation to \mathbf{x} , then rigid-body rotation by \mathbf{R} , and finally a stretch by \mathbf{V} or (b) a stretch by \mathbf{U} , then rigid-body rotation by \mathbf{R} , and finally translation to \mathbf{x} . Defining deformation of material particles in this fashion is well-suited to problems involving both large and small deformations.

Many materials behave with path and rate-dependency, and therefore constitutive relations must be defined in rate form. Refer to Figure C.2. The velocity of a material particle is $\mathbf{v} = \partial\mathbf{x}/\partial t$, where the Lagrangian reference frame is employed for following the material point through its motion. The velocity gradient between two neighboring particles is

$$d\mathbf{v} = \frac{\partial\mathbf{v}}{\partial\mathbf{x}} \cdot d\mathbf{x} = \mathbf{L} \cdot d\mathbf{x} \quad (\text{C.14})$$

$\mathbf{L} = \partial\mathbf{v}/\partial\mathbf{x}$ is the velocity gradient. Note that the following relations are also of interest:

$$d\mathbf{v} = \mathbf{L} \cdot d\mathbf{x} = \mathbf{L} \cdot \mathbf{F} \cdot d\mathbf{X} \quad (\text{C.15})$$

$$d\mathbf{v} = \frac{\partial}{\partial t} (\mathbf{F} \cdot d\mathbf{X}) = \dot{\mathbf{F}} \cdot d\mathbf{X} \quad (\text{C.16})$$

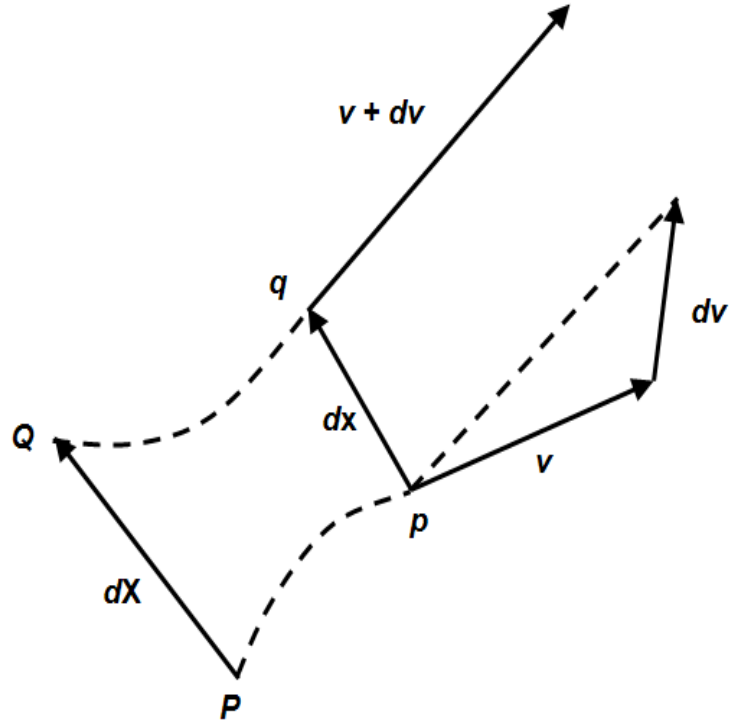


Figure C.2: Relative velocity dv of particle Q at point q relative to the particle P at point p [76].

Comparing equations (C.15) and (C.16), we see that $\dot{\mathbf{F}} = \mathbf{L} \cdot \mathbf{F}$. The velocity gradient \mathbf{L} is composed of the symmetric rate of deformation tensor \mathbf{D} and the anti-symmetric rotation rate (or “spin”) tensor \mathbf{W} such that

$$\mathbf{L} = \mathbf{D} + \mathbf{W} \quad (\text{C.17})$$

$$\mathbf{D} = \frac{1}{2} (\mathbf{L} + \mathbf{L}^T) \quad (\text{C.18})$$

$$\mathbf{W} = \frac{1}{2} (\mathbf{L} - \mathbf{L}^T) \quad (\text{C.19})$$

C.2.2 Strain and Strain Rate. Two strain measures that are directly tied to the deformation gradient are worth mentioning: the Green strain (Lagrangian coordinate system) and the Eulerian strain (Eulerian coordinate system). First, the Green strain is used occasionally for two reasons: (1) it is computationally convenient because it is directly related to the deformation gradient and (2) it is well suited to

structural problems where large deformations typically involve large rotations accompanied with small strains (recall that the deformation gradient can be decomposed into stretch and rotation contributions). The Green strain tensor \mathbf{E}^G is given by

$$\mathbf{E}^G = \frac{1}{2} (\mathbf{F}^T \cdot \mathbf{F} - \mathbf{I}) \quad (\text{C.20})$$

and can also be written in the form

$$E_{IJ}^G = \frac{1}{2} \left[\frac{\partial x_k}{\partial X_I} \frac{\partial x_k}{\partial X_J} - \delta_{IJ} \right] \quad (\text{C.21})$$

All subscripts have values 1–3. δ_{IJ} is the Kronecker Delta array where the elements of the array equal one when $I = J$ and zero everywhere else. The Green strain rate $\dot{\mathbf{E}}^G$ is

$$\dot{\mathbf{E}}^G = \frac{1}{2} (\dot{\mathbf{F}}^T \cdot \mathbf{F} + \mathbf{F}^T \cdot \dot{\mathbf{F}}) = \frac{1}{2} \mathbf{F}^T \cdot (\mathbf{L} + \mathbf{L}^T) \cdot \mathbf{F} = \mathbf{F}^T \cdot \mathbf{D} \cdot \mathbf{F} \quad (\text{C.22})$$

The Green strain and strain rate are associated with the Lagrangian material description. The corresponding Eulerian strain \mathbf{E} , associated with the Eulerian material description, is given by

$$\mathbf{E} = \frac{1}{2} (\mathbf{I} - (\mathbf{F}^{-1})^T \cdot \mathbf{F}^{-1}) \quad (\text{C.23})$$

and can also be written in the form

$$E_{km} = \frac{1}{2} \left[\delta_{ij} - \frac{\partial X_J}{\partial x_k} \frac{\partial X_J}{\partial x_m} \right] \quad (\text{C.24})$$

All subscripts have values 1–3. The Eulerian strain rate $\dot{\mathbf{E}}$ is

$$\dot{\mathbf{E}} = \mathbf{D} - (\mathbf{E} \cdot \mathbf{L} + \mathbf{L}^T \cdot \mathbf{E}) \quad (\text{C.25})$$

The Eulerian strain and strain rate tensors are equally valid for use but can be computationally expensive due to the need to calculate the inverse of the deformation gradient.

Before proceeding to stress measures associated with these strains, it is worthwhile to look at these strain measures in terms of displacement \mathbf{u} . The Green strain, in terms of displacement, can be found by evaluating equation (C.8) with the displacement gradient and applying equation (C.20):

$$E_{ij}^G = \frac{1}{2} \left[\frac{\partial u_i}{\partial X_j} + \frac{\partial u_j}{\partial X_i} + \frac{\partial u_k}{\partial X_i} \frac{\partial u_k}{\partial X_j} \right] \quad (\text{C.26})$$

and the Eulerian strain, in terms of displacement, can be found by evaluating equation (C.8) with the displacement gradient and applying equation (C.23):

$$E_{ij} = \frac{1}{2} \left[\frac{\partial u_i}{\partial x_j} + \frac{\partial u_j}{\partial x_i} - \frac{\partial u_k}{\partial x_i} \frac{\partial u_k}{\partial x_j} \right] \quad (\text{C.27})$$

If the displacements u_i with respect to the Lagrangian coordinates X_i or the Eulerian coordinates x_i are small compared to unity, the squares and products of the derivatives can be ignored in comparison to the linear terms. The remaining terms are called the small-strain components. *When the displacements and displacement gradients are sufficiently small, as in the case of linear theory of elasticity, the distinction between the two small-strain definitions is usually ignored [76].* This is an important conclusion with regard to the impact problem studied in this work since the maximum strains in the experimental strain histories rarely exceeded 0.2% (see Chapter V) and almost no global plasticity was observed in the plate specimens.

C.2.3 Stress. Once the deformation history in a body is defined, the analyst generally has all the necessary information to describe the response. The deformation history can then be related to either the Lagrangian or Eulerian coordinate systems, depending on which coordinate system is most convenient to describe the system response. The strain definitions are related to a stress definition appropriate to the

coordinate system chosen, or stress conjugate, through a constitutive model. Before any choice of constitutive model relating the stress-strain conjugates directly can be made, it is first necessary to define stress measures in the coordinate systems.

It was stated earlier that ABAQUS uses the Green strain tensor extensively in its formulations for computational convenience. The Green strain tensor is a Lagrangian strain description and therefore requires a Lagrangian associated stress measure; specifically the Second-Piola Kirchhoff stress tensor Σ^{II} . Σ^{II} is termed a *pseudo-stress* tensor because of the fact that it is measured with respect to the initial material configuration. Refer to Figure C.3. A force $\mathbf{d}\tilde{\mathbf{P}}$ acting on the infinitesimal undeformed area $\mathbf{d}\mathbf{S}_0$ with unit normal $\hat{\mathbf{N}}$ is related to the force vector $\mathbf{d}\mathbf{P}$ on the deformed area $\mathbf{d}\mathbf{S}$ by

$$\mathbf{d}\tilde{\mathbf{P}} = \mathbf{F}^{-1} \cdot \mathbf{d}\mathbf{P} \quad (\text{C.28})$$

If the traction vectors \mathbf{t}^0 and $\tilde{\mathbf{t}}$ are defined by

$$\mathbf{t}^0 dS_0 = \mathbf{d}\mathbf{P} = \mathbf{t} dS \quad (\text{C.29})$$

$$\tilde{\mathbf{t}} dS_0 = \mathbf{d}\tilde{\mathbf{P}} = \mathbf{F}^{-1} \cdot \mathbf{t} dS \quad (\text{C.30})$$

then the Second Piola-Kirchhoff stress tensor Σ^{II} is related to the traction vectors \mathbf{t}^0 and $\tilde{\mathbf{t}}$ by

$$\tilde{\mathbf{t}} = \hat{\mathbf{N}} \cdot \Sigma^{\text{II}} = \mathbf{F}^{-1} \cdot \mathbf{t}^0 \quad (\text{C.31})$$

More simply put, the Second Piola-Kirchhoff stress tensor relates the stress state due to a load to its undeformed configuration. The Cauchy stress tensor σ , on the other hand, relates the stress state to a load to its deformed or current configuration. For this reason, the Cauchy stress tensor is termed a *true* stress tensor. The Cauchy stress is always reported in ABAQUS because it is generally of more interest to engineers as the direct measure of the traction being carried per unit area by any internal surface in a body under consideration. The Cauchy stress is associated with the Eulerian reference frame and defines the stress state at the current material configuration.

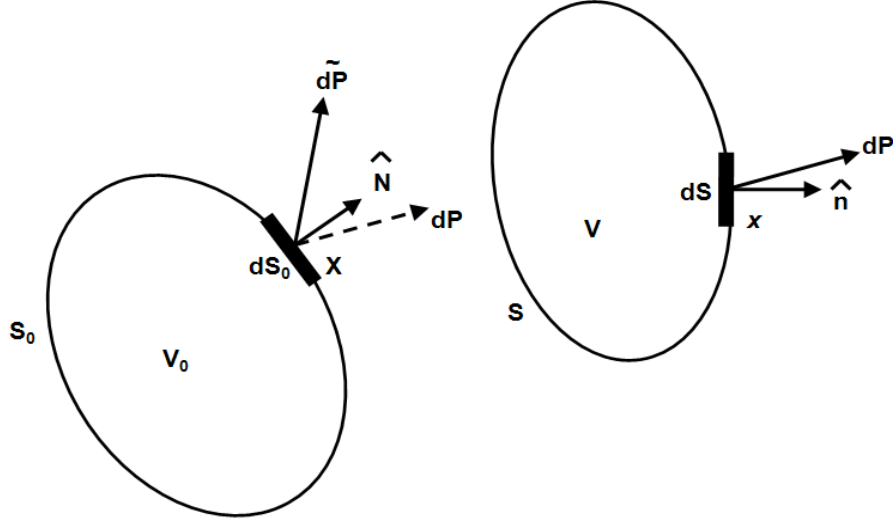


Figure C.3: Force vectors for stress definitions in the undeformed state (subscript 0) and the deformed state [76].

The 2nd Piola-Kirchhoff stress tensor is related to the Cauchy stress tensor by

$$\sigma = \frac{dV_0}{dV} \mathbf{F} \cdot \boldsymbol{\Sigma}^{\text{II}} \cdot \mathbf{F}^T \quad (\text{C.32})$$

where dV is the current (infinitesimal) volume and dV_0 is the reference (infinitesimal) volume.

The stress and strain conjugates presented in this section will be referred to periodically through the remainder of this appendix.

C.3 Governing Equations

This section will present the governing equations of interest in this work within the framework of ABAQUS/Explicit. These equations will be discussed very briefly without derivation based on the ABAQUS v.6.6 Theory Manual [3] and the text by Belytschko et al. [14]. The equations apply to Lagrangian finite element meshes, meaning the mesh and nodes follow the material through deformation (as opposed to Eulerian meshes where material flows through the fixed nodes and mesh). The two

sets of governing equations are more or less equivalent but are associated with one coordinate system versus the other coordinate system. The equations are based on the concept of virtual power, which in words, states that the virtual inertial (kinetic, subscript *kin*) power is equal to the difference between rate of virtual work (\dot{W}) performed by external loads (subscript *ext*) and the virtual rate of internal work (subscript *int*). In equation form, without derivation, the virtual power is given by

$$\begin{aligned}\delta\dot{W}_{kin} &= \delta\dot{W}_{ext} - \delta\dot{W}_{int} \\ \int_V \delta\mathbf{v} \cdot \rho\dot{\mathbf{v}}dV &= \left(\int_S \delta\mathbf{v} \cdot \mathbf{\Phi} dS + \int_V \delta\mathbf{v} \cdot \mathcal{F}dV \right) - \int_V \frac{\partial(\delta\mathbf{v})}{\partial\mathbf{x}} \sigma dV \quad (\text{C.33})\end{aligned}$$

where \mathcal{F} are body forces and $\mathbf{\Phi}$ are surface tractions. The symbol δ in front of the velocities signifies that these are “virtual” velocities that must be admissible functions according to the calculus of variations (a thorough treatment of this is beyond the scope of this appendix). This governing equation is used if the constitutive equation for the material is based on the spatial (Eulerian) reference frame. A constitutive model such as this would relate, for instance, Eulerian strain to Cauchy stress. This formulation is associated with what is called an *updated Lagrangian mesh*, that is, the governing equations are based on the current, or “updated,” configuration of the body. In the usual finite element discretization,

$$\begin{aligned}\mathbf{u} &= \mathbf{u} = [\mathbf{N}] \mathbf{u}_I \\ \mathbf{v} &= \dot{\mathbf{u}} = [\mathbf{N}] \dot{\mathbf{v}}_I \\ \mathbf{a} &= \ddot{\mathbf{u}} = [\mathbf{N}] \mathbf{a}_I\end{aligned} \quad (\text{C.34})$$

Here, \mathbf{u} , \mathbf{v} , \mathbf{a} are general displacements, velocities, and accelerations and a subscript *I* refers to nodal displacements, velocities, and accelerations of the element. $[\mathbf{N}]$ are the element’s interpolating shape functions. The virtual velocities $\delta\mathbf{v}$ are related to virtual velocities at element nodes by

$$\delta\mathbf{v} = \delta\mathbf{v}_I [\mathbf{N}] \quad (\text{C.35})$$

Substituting this relation into the virtual power equation and bringing all integrals to the left side of the equation yields

$$\delta \mathbf{v} \left\{ \int_V [\mathbf{N}] \cdot \rho \dot{\mathbf{v}} dV - \left(\int_S [\mathbf{N}] \cdot \boldsymbol{\Phi} dS + \int_V [\mathbf{N}] \cdot \mathcal{F} dV \right) + \int_V \frac{\partial [\mathbf{N}]}{\partial \mathbf{x}} \sigma dV \right\} = 0 \quad (\text{C.36})$$

For a non-trivial solution to the equation, the terms in brackets must equal zero:

$$\left\{ \int_V [\mathbf{N}] \cdot \rho \dot{\mathbf{v}} dV - \left(\int_S [\mathbf{N}] \cdot \boldsymbol{\Phi} dS + \int_V [\mathbf{N}] \cdot \mathcal{F} dV \right) + \int_V \frac{\partial [\mathbf{N}]}{\partial \mathbf{x}} \sigma dV \right\} = 0 \quad (\text{C.37})$$

Equation (C.37) is nothing more than stating the sum of the forces is equal to mass multiplied by acceleration. That is,

$$\begin{aligned} \mathbf{M} \ddot{\mathbf{u}} &= \int_V [\mathbf{N}] \cdot \rho \dot{\mathbf{v}} dV = \left(\int_V \rho [\mathbf{N}] [\mathbf{N}] dV \right) \dot{\mathbf{v}}_{\mathbf{I}} \\ F_{\text{EXT}} &= \left(\int_S [\mathbf{N}] \cdot \boldsymbol{\Phi} dS + \int_V [\mathbf{N}] \cdot \mathcal{F} dV \right) \\ F_{\text{INT}} &= \int_V \frac{\partial [\mathbf{N}]}{\partial \mathbf{x}} \sigma dV \end{aligned} \quad (\text{C.38})$$

which is merely in the form of equation (C.4)

$$\mathbf{M} \ddot{\mathbf{u}} = F_{\text{EXT}} - F_{\text{INT}}$$

The second set of governing equations are exactly the same except instead of the spatial-Eulerian reference frame, the material-Lagrangian reference frame is used. Using the relations of the previous section, the deformation-strains-stresses in the Eulerian frame must be transformed to the Lagrangian frame (subscript 0). Rather

than rewriting the entire formulation, only the final equations will be shown:

$$\begin{aligned}
\mathbf{M}\ddot{\mathbf{u}} &= \int_{V_0} [\mathbf{N}] \cdot \rho_0 \dot{\mathbf{v}} dV_0 = \left(\int_{V_0} \rho_0 [\mathbf{N}] [\mathbf{N}] dV_0 \right) \dot{\mathbf{v}}_{\mathbf{I}} \\
F_{\text{EXT}} &= \left(\int_{S_0} [\mathbf{N}] \cdot \boldsymbol{\Phi} dS_0 + \int_{V_0} [\mathbf{N}] \cdot \mathcal{F} dV_0 \right) \\
F_{\text{INT}} &= \int_{V_0} \frac{\partial [\mathbf{N}]}{\partial \mathbf{X}} (\boldsymbol{\Sigma}^{\mathbf{I}} \cdot \mathbf{F}^T) dV_0
\end{aligned} \tag{C.39}$$

and fits into the framework of equation (C.4). This set of governing equations is called the *total Lagrangian formulation* since the “total” deformation is always related back to the initial reference configuration.

C.4 Solid Continuum Finite Elements

Eight-noded linear isoparametric hexahedral bricks were used to construct all the three-dimensional finite element models in this study. The precise element used in ABAQUS was the “C3D8R” element. The element’s name is actually code-letters for a continuum (C) element in three dimensions (3D) with eight nodes (8) and stiffness determined by reduced integration (R). These elements were chosen for their computational efficiency and their versatility in a wide range of nonlinear applications, including contact analyses and re-meshing with large deformations (the small-strain/linear-elastic nature of the FGM plates during the impact experiments did not require these features during modeling, but this was not known at the outset). Here, the details associated with these elements *in the context of this research work* are presented. *Note that from this point forward, the spatial coordinate system (including the Cauchy stress–Eulerian strain conjugates) will be used in all equations and discussion as ABAQUS used this coordinate system for the constitutive relations and reported results.* However, also note that since the strains were relatively small in this work, the differences that would have occurred if a Lagrangian-based constitutive model and reference frame had been used instead would be negligible [76]. This section is summarized from the ABAQUS v6.6 Theory Manual [3], with supporting discussions

drawn heavily from the popular finite element texts by Cook et al. [31] and Belytschko et al. [14].

C.4.1 Isoparametric Element Formulation. The elements are isoparametric, implying that the same shape functions are used to interpolate (or “map”) displacement and geometry information for the element based on a reference configuration. Refer to Figure C.4. The coordinates \mathbf{x} and displacement \mathbf{u} at a point within the element are given by

$$\begin{aligned}\mathbf{x} &= [\mathbf{N}]\mathbf{x}_i \\ \mathbf{u} &= [\mathbf{N}]\mathbf{u}_i\end{aligned}\tag{C.40}$$

where $\mathbf{x}_i = (x_i, y_i, z_i)$ are the actual (Cartesian) coordinates of node $i = 1, \dots, 8$ and $\mathbf{u}_i = (u_i, v_i, w_i)$ are the displacements of i -th node in the actual coordinate system (in our case rectangular Cartesian coordinates). The eight shape functions in $[\mathbf{N}]$ used in these hexahedrons are

$$\begin{aligned}N_1 &= \frac{1}{8} (1 - g) (1 - h) (1 - r) \\ N_2 &= \frac{1}{8} (1 + g) (1 - h) (1 - r) \\ N_3 &= \frac{1}{8} (1 + g) (1 + h) (1 - r) \\ N_4 &= \frac{1}{8} (1 - g) (1 + h) (1 - r) \\ N_5 &= \frac{1}{8} (1 - g) (1 - h) (1 + r) \\ N_6 &= \frac{1}{8} (1 + g) (1 - h) (1 + r) \\ N_7 &= \frac{1}{8} (1 + g) (1 + h) (1 + r) \\ N_8 &= \frac{1}{8} (1 - g) (1 + h) (1 + r)\end{aligned}\tag{C.41}$$

g , h , and r are the *reference* coordinates shown in Figure C.4. One chooses a point in the reference coordinates within the element domain, then substitutes the (g, h, r) co-

ordinates into (C.41) and applies the equations (C.40) to obtain the actual coordinate location and displacements at that reference point. The use of the isoparametric formulation of elements between actual and reference coordinate systems has numerical advantages that simplify the analyses of complex geometries. The Jacobian matrix is defined by:

$$[\mathbf{J}] = \begin{bmatrix} N_{i,g}x_i & N_{i,g}y_i & N_{i,g}z_i \\ N_{i,h}x_i & N_{i,h}y_i & N_{i,h}z_i \\ N_{i,r}x_i & N_{i,r}y_i & N_{i,r}z_i \end{bmatrix} \quad (\text{C.42})$$

The comma in the usual subscript notation represents the partial derivative is taken with respect to the variable after the comma and the repeated subscript implies summation. The determinant of the Jacobian matrix, $J = \det[\mathbf{J}]$, is essentially a scale factor between the reference and physical size of the elements.

C.4.2 Constitutive Relation. The FGM plates were observed to be elastic to failure during the impact tests. The eight-noded linear brick elements were used with an isotropic, linear-elastic constitutive relation. In *rectangular Cartesian coordinates*, the linear-elastic stress-strain relations for an isotropic material are

$$\begin{Bmatrix} \sigma_{xx} \\ \sigma_{yy} \\ \sigma_{zz} \\ \sigma_{xy} \\ \sigma_{xz} \\ \sigma_{yz} \end{Bmatrix} = \begin{bmatrix} \lambda + 2\mu & \lambda & \lambda & 0 & 0 & 0 \\ \lambda & \lambda + 2\mu & \lambda & 0 & 0 & 0 \\ \lambda & \lambda & \lambda + 2\mu & 0 & 0 & 0 \\ 0 & 0 & 0 & \mu & 0 & 0 \\ 0 & 0 & 0 & 0 & \mu & 0 \\ 0 & 0 & 0 & 0 & 0 & \mu \end{bmatrix} \begin{Bmatrix} \epsilon_{xx} \\ \epsilon_{yy} \\ \epsilon_{zz} \\ 2\epsilon_{xy} \\ 2\epsilon_{xz} \\ 2\epsilon_{yz} \end{Bmatrix} \quad (\text{C.43})$$

which is more conveniently written as

$$\sigma = [\mathbf{C}_{el}] \epsilon \quad (\text{C.44})$$

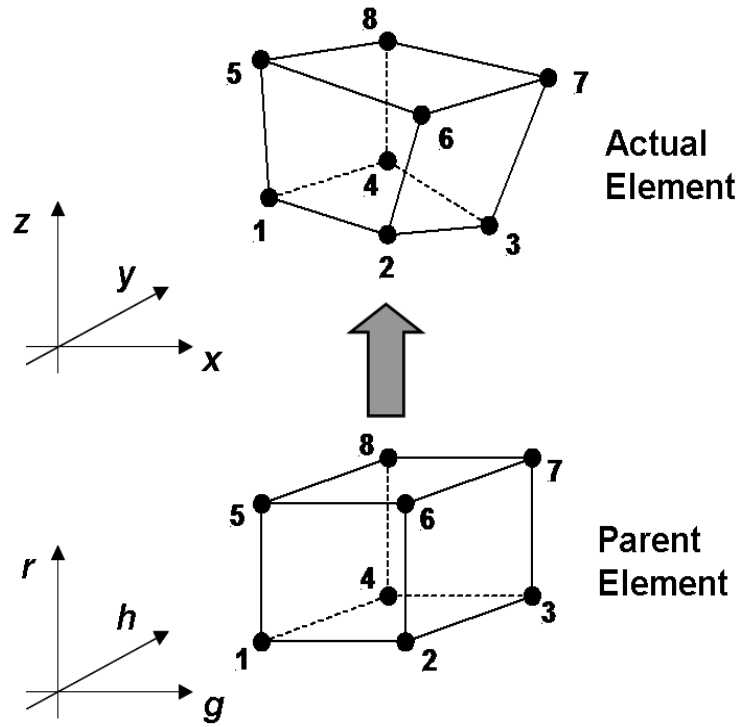


Figure C.4: Isoparametric hexahedral element geometry. The (g, h, r) coordinates of nodes 1-8 in the parent domain are $(-1, -1, -1)$, $(+1, -1, -1)$, $(+1, +1, -1)$, $(-1, +1, -1)$, $(-1, -1, +1)$, $(+1, -1, +1)$, $(+1, +1, +1)$, $(-1, +1, +1)$, respectively.

where $[\mathbf{C}_{el}]$ is the elastic stiffness matrix, σ is the Cauchy stress tensor and ϵ is the (Eulerian) elastic strain tensor. (Earlier the Eulerian strain tensor was denoted \mathbf{E} ; here the notation is changed to avoid confusion between strain components and the elastic modulus while also maintaining consistency with the strain notation used in the chapters contained in the main body of this work.) The parameters λ and μ are the Lamé constants (*not to be confused with Lagrange multipliers, used in Chapter VIII*), which are related to the elastic modulus and Poisson's ratio by

$$\lambda = \frac{\nu E}{(1 + \nu)(1 - 2\nu)} \quad (\text{C.45})$$

$$\mu = \frac{E}{2(1 + \nu)} \quad (\text{C.46})$$

The strains were small throughout the impact tests (on the order of 0.2% strain or less). When small strains and rotations are involved, the distinction between the Eulerian and Lagrangian reference frames in constitutive models is generally ignored [76].

C.4.3 Quadrature. ABAQUS uses numerical techniques to solve the governing equations for a finite element model. As shown in the previous section, integration of functions over a domain is an operation that features prominently in the governing equations. A common numerical technique for approximating the integral of a function is called quadrature. There are many versions of quadrature, but essentially all evaluate a function at specific points, multiply the evaluated function by a weighting factor, then add the results. Gaussian quadrature is used by ABAQUS, and this form of quadrature is designed to choose evaluation points and weights to minimize error in the integration especially for polynomial functions (which is precisely what we have based on the choice of shape functions). The goal of this section is to briefly point out the role of Gaussian quadrature and comment how its implementation affects the solution of the finite element model. Applied to the isoparametric three-dimensional

Table C.1: Sampling point locations and weight factors for Gauss quadrature over the interval $g = -1$ to $g = +1$ [31], [143].

Order n	Degree of Precision	Sampling Pt. Locations g_i	Weight Factor W_i
1	1	0	2
2	3	$\pm 1/\sqrt{3}$	1
3	5	$\pm\sqrt{0.6}$	5/9
		0	8/9

element, the Gauss quadrature takes the following mathematical form:

$$I = \int_{-1}^1 \int_{-1}^1 \int_{-1}^1 f(g, h, r) dg dh dr \approx \sum_i \sum_j \sum_k W_i W_j W_k f(g_i, h_j, r_k) \quad (\text{C.47})$$

where the W variables are weight factors. The Gaussian points and weights are shown in Table C.1. To explain the table, a function f can be approximated by sampling the function at 1, 2, or 3 points and applying the associated weights to those points (actually there is no limit to the number of points and associated weights that can be used; many numerical analysis texts have tables constructed to assist for this purpose). The more Gaussian points that are used to evaluate f , the more accurate the results will be. For a polynomial of degree $2n - 1$, it turns out that Gaussian quadrature exactly integrates the function f if n or more points are used. This is what is meant by the “degree of precision.” For instance, a polynomial of degree five requires a minimum of three Gaussian points with associated weights to integrate the function exactly. In multiple dimensions, as in the case of our elements, quadrature is performed by evaluating f at the points listed in Table C.1 with associated weights in three dimensions as suggested in equation (C.47).

Recall that the three-dimensional element is a linear element because the shape functions used to interpolate the displacements are linear functions in three-dimensions. $\partial[\mathbf{N}]/\partial\mathbf{x}$ and $\partial[\mathbf{N}]/\partial\mathbf{X}$ in (C.38) and (C.39) are functions of g , h , and r . If the constitutive relation $[\mathbf{C}_{el}]$ is a constant (as in our case), then the integrand will contain

polynomial squares of g , h , and r . To integrate this *exactly* requires a minimum of two Gauss points in each coordinate direction, or eight integration points total. Unfortunately for the linear three-dimensional brick element, exactly integrating the relation to determine the internal forces can cause an element defect called “locking,” meaning that the response of the element for certain deformation modes when under load can be magnitudes of order larger than it is in reality. This is a by-product of the assumed displacement fields and the imposed conditions on the elements in the model, not on the integration procedure itself. The full integration (meaning the exact integration) of the internal forces merely includes this element defect if it exists given the conditions of the model. One remedy to this problem is approximating the internal forces by one order less than is required to exactly integrate the expression. In the case of the linear brick, one order of quadrature less would reduce the integration points from a $2 \times 2 \times 2$ arrangement to a single quadrature point at the center of the brick. This has the effect of softening the element since some of the internal force contributions are now approximated instead of exact. Underintegrating the internal forces can additionally increase computational efficiency without necessarily decreasing the accuracy of the element. However, underintegrating all modes throughout the entire element can actually *introduce* element defects such as spurious deformation modes under certain modeling conditions that can produce results just as infeasible as an element experiencing locking. In ABAQUS, a compromise is met by selectively underintegrating certain deformation modes (associated with deviatoric stresses) and fully integrating other modes (associated with hydrostatic stresses). This allows for computational efficiency, reduces locking, and can reduce potentially spurious modes. The “reduced integration” feature associated with the C3D8R element refers to this process.

C.5 Contact Algorithm

The impact problem requires that contact be established between the specimen plate and the tup in the finite element models. Contact is additionally specified

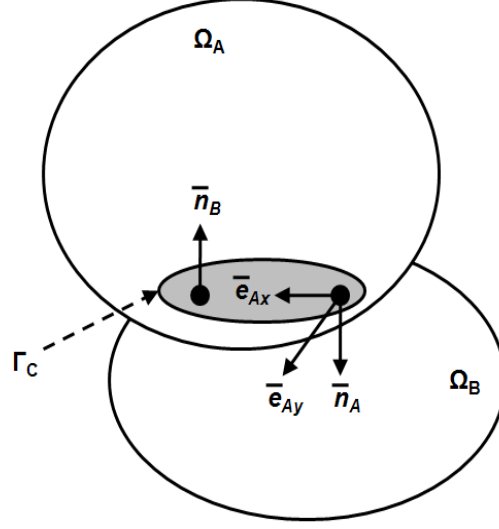


Figure C.5: Two bodies, Ω_A & Ω_B , in contact over surface Γ_C [14].

between fastener screws and various components of the specimen plate fixture as well as between the plate specimen and the fixture itself. Modeling contact in a finite element model is a highly-nonlinear process in the governing equations and the mathematics behind contact analysis are far beyond the scope of this appendix. Since contact between components constitutes a large part of the load transfer and boundary conditions in the finite element model, it is worth presenting a few key concepts concerning the implementation in ABAQUS. The focus here will be definition of contact between two surfaces, traction conditions due to contact, and high-level implementation of contact in the global FEM. No derivations are presented for brevity purposes and the goal is to provide a rudimentary understanding of how contact is analyzed in the FEMs. The theory presented in this discussion is summarized from Belytschko et al. [14]; references to the ABAQUS implementation are taken from the ABAQUS v6.6 Theory Manual [3].

Assume two bodies, Ω_A and Ω_B shown in Figure C.5, bounded by (surfaces) Γ_A and Γ_B . The bodies come together and are in contact together. The interface

between the two bodies is defined by Γ_C :

$$\Gamma_C = \Gamma_A \cap \Gamma_B \quad (\text{C.48})$$

At the contact interface (or contact surface), a local coordinate system is established at each point of contact on each surface, and unit vectors tangent to the surface can be defined (For Γ_A , $\bar{\mathbf{e}}_{Ax}$ and $\bar{\mathbf{e}}_{Ay}$ are the tangent unit vectors; for Γ_B , $\bar{\mathbf{e}}_{Bx}$ and $\bar{\mathbf{e}}_{By}$ are the unit vectors). The cross product of the unit vectors at a point on one of the surfaces is a vector normal to the surface ($\bar{\mathbf{n}}_A$ and $\bar{\mathbf{n}}_B$, respectively). On the contact surface, the following is assumed to hold:

$$\bar{\mathbf{n}}_A = -\bar{\mathbf{n}}_B \quad (\text{C.49})$$

This is merely the mathematical equivalent of stating the normal vectors of the surface at a contact point are opposite in direction. The velocity fields of bodies Ω_A and Ω_B are \mathbf{v}_A and \mathbf{v}_B and can be expressed in terms of their normal and tangential (superscripts N and T) components:

$$\mathbf{v}_A = v_A^N \bar{\mathbf{n}}_A + \mathbf{v}_A^T, \quad v_A^N = \mathbf{v}_A \cdot \bar{\mathbf{n}}_A \quad (\text{C.50})$$

$$\mathbf{v}_B = v_B^N \bar{\mathbf{n}}_B + \mathbf{v}_B^T, \quad v_B^N = \mathbf{v}_B \cdot \bar{\mathbf{n}}_B \quad (\text{C.51})$$

The bodies Ω_A and Ω_B are governed by the conservation of mass, momentum, and energy. The conservation of momentum must be satisfied at the contact interface and the traction across the interface cannot be tensile. These conditions will now be addressed specifically in order to define kinematic conditions for contact. First, the bodies are not allowed to interpenetrate each other, that is

$$\Omega_A \cap \Omega_B = 0 \quad (\text{C.52})$$

Interpenetrability is often viewed from a rate form at each point on the contact surface through the following relation:

$$\gamma^N = \mathbf{v}_A \cdot \bar{\mathbf{n}}_A + \mathbf{v}_B \cdot \bar{\mathbf{n}}_B = (\mathbf{v}_A - \mathbf{v}_B) \cdot \bar{\mathbf{n}}_A \equiv v_A^N - v_B^N \leq 0 \text{ on } \Gamma_C \quad (\text{C.53})$$

γ^N is called the rate of interpenetrability. When the two bodies are in contact, γ^N is zero. When they separate, the constant is less than zero.

Next, the tractions across the interface must observe the conservation of momentum. The sum of the tractions (\mathbf{t}) across the interface must be zero:

$$\mathbf{t}_A + \mathbf{t}_B = \mathbf{0} \quad (\text{C.54})$$

The normal tractions are given by

$$t_A^N = \mathbf{t}_A \cdot \bar{\mathbf{n}}_A \quad (\text{C.55})$$

$$t_B^N = \mathbf{t}_B \cdot \bar{\mathbf{n}}_B \quad (\text{C.56})$$

$$(\text{C.57})$$

and the normal tractions observe

$$t_A^N + t_B^N = 0 \quad (\text{C.58})$$

The normal tractions on the surfaces of the bodies can only be compressive. When the bodies are separated, the tractions are zero. When the bodies are in contact, they satisfy the subsequent relations. The tangential tractions across the contact surface are given by

$$\mathbf{t}_A^T = \mathbf{t}_A - t_A^N \bar{\mathbf{n}}_A \quad (\text{C.59})$$

$$\mathbf{t}_B^T = \mathbf{t}_B - t_B^N \bar{\mathbf{n}}_B \quad (\text{C.60})$$

and must also satisfy

$$\mathbf{t}_A^T + \mathbf{t}_B^T = \mathbf{0} \quad (\text{C.61})$$

In the case of frictionless models, the tangential tractions are zero. The interpenetrability rate γ^N and the normal traction components t^N can be combined into a single contact condition which can be useful:

$$t^N \gamma^N = 0 \quad (\text{C.62})$$

When two bodies are in contact, γ^N is zero; when the two bodies are separated, the traction t^N is zero. Thus, (C.62) is satisfied regardless of the contact state between the two bodies.

The previous paragraphs looked at the kinematic conditions for contact from a velocity standpoint. Similar conditions can be determined based on a displacement formulation. The equations and formulation for displacement conditions are complicated and not presented, but it is simple to visualize conceptually what occurs under the formulation. The displacement formulation assesses the position of the bodies over time and determines when and to what degree the bodies have interpenetrated each other. If the bodies have interpenetrated, the displacements are corrected to enforce the necessary contact conditions. The velocity and displacement conditions for contact can more or less be used independent of each other to assess contact, but in ABAQUS and other finite element codes they are often used together to efficiently model the contact interaction.

In ABAQUS, the user specifies two or more surfaces that are expected to come into contact during a simulation. The surfaces contain nodes which may or may not be coincident with each other once contact occurs; therefore the contact solution is based on the surface locations and the load is distributed along element edges. Contact in ABAQUS during a dynamic analysis is assessed at each time step. If the surfaces of the bodies are geometrically positioned relative to each other such that contact must be enforced, the required tractions are applied to each surface. If the surfaces

are geometrically positioned such that contact will not occur, the tractions are not applied. It should also be noted that only surfaces defined on bodies expected to come into contact are included in the contact formulation. Contact enforcement will not be applied to surfaces and bodies where contact enforcements have not been defined that actually do come into contact in the FEM. The result of this will be highly erroneous solutions. Contact in finite element models is a highly nonlinear process due to its “on-off” nature that can introduce sharp discontinuities to displacement and velocity fields during the course of solving the governing equations.

ABAQUS allows definition of two types of pressure-displacement relations in association with contact enforcement. The first is “hard” contact where the pressure is zero if no contact; interpenetration is zero if contact occurs and applied pressure is nonzero. This type of contact enforcement was used in the FEMs in this research. The second type of relation that can be applied is a pressure-displacement curve from known behavior of two bodies and materials relative to each other. The curves may take on linear, exponential, piece-wise continuous, or tabulated form in ABAQUS, and the curves are usually produced from experimental data. In this case, when contact has not been established, no load is applied to the element. When contact between surfaces does occur, a stiffness contribution from the pressure-displacement relationship must be included and enforced. The traction applied is related to the provided pressure-displacement relation.

The technique used to strictly enforce contact in ABAQUS for this work was a kinematic predictor/corrector contact algorithm. In hard contact, no penetrations are allowed using this algorithm. A brief summary of how this algorithm works is as follows (taken from [2]). First, contact surfaces in the model are chosen; two surfaces at a time. One surface is designated as a “master” surface, and the other surface is designated as a “slave” surface (doing so is for solution purposes but also has some physical application). When choosing such surfaces as master or slave, the slave surface is generally assumed to conform to the shape of the master surface and thus the master surface is usually chosen to be a less deformable surface than that

of the slave (but not necessarily so). ABAQUS solves for the state of the model in a given time increment assuming that no contact occurs. ABAQUS will then determine which nodes associated with the slave surface in the “predicted” state penetrate the master surface. The depth of each slave node’s penetration, the mass associated with it, and the time increment are used to calculate a resisting force required to oppose penetration. In other words, the resisting force is the force which would have caused the slave node to exactly contact the master surface had it been applied immediately during the current time increment. The resisting forces of all slave nodes are then distributed to the nodes on the master surface. The mass of each contacting slave node is also distributed to the master surface nodes and added to their mass to determine the total inertial mass of the contacting interfaces. ABAQUS will then use these distributed forces and masses to calculate an acceleration “correction” for the master surface nodes. Acceleration corrections for the slave nodes are then determined using the predicted penetration for each node, the time increment, and the acceleration corrections for the master surface nodes. ABAQUS uses these acceleration corrections to obtain a corrected configuration in which the contact constraints are enforced. When using this contact enforcement algorithm, it is still possible for the master surface to penetrate the slave surface in the corrected configuration, but the effect can be minimized by refining the mesh associated with the master-slave contact surfaces.

Bibliography

1. “Columbia Accident Investigation Board”, August 2003. Final Report.
2. “ABAQUS v6.6 Analysis User’s Manual”, 2006.
3. “ABAQUS v6.6 Theory Manual”, 2006.
4. April 2007. Correspondence with BAE Systems Sales Engineer Greg Nelson.
5. Abrate, S. “Functionally Graded Plates Behave Like Homogeneous Plates”. *Composites: Part B*, 39:151–158, 2008.
6. Amundsen, R. M., C. P. Leonard, and W. E. Bruce III. “Hyper-X Hot Structures Comparison of Thermal Analysis and Flight Data”. *15th Annual Thermal and Fluids Analysis Workshop*. NASA, Pasadena, California, September 2004.
7. Apostol, T. M. *Mathematical Analysis*. Addison-Wesley-Longman, Menlo Park, CA, 1974.
8. Arora, J. S. *Introduction to Optimum Design*. McGraw-Hill, Inc., New York, NY, 1989.
9. Atri, R. R., K. S. Ravichandran, and S. K. Jha. “Elastic Properties of In-Situ Processed Ti-TiB Composites Measured By Impulse Excitation of Vibration”. *Materials Science and Engineering A*, 271:150–159, 1999.
10. Avallone, E. A. and T. Baumeister III. *Marks’ Standard Handbook for Mechanical Engineers*. McGraw-Hill Companies, Inc., New York, NY, tenth edition, 1996.
11. Bahtui, A. and M. R. Eslami. “Coupled Thermoelasticity of Functionally Graded cylindrical Shells”. *Mechanics Research Communications*, 34:1–18, 2007.
12. Banks-Sills, L., R. Eliasi, and Y. Berlin. “Modeling of Functionally Graded Materials in Dynamic Analyses”. *Composites, Part B*, 33:7–15, 2002.
13. Beckwith, T. G., R. D. Marangoni, and J. H. Lienhard. *Mechanical Measurements*. Addison-Wesley Publishing Co., Reading, MA, fifth edition, 1993.
14. Belytschko, T., W.K. Liu, and B. Moran. *Nonlinear Finite Elements for Continua and Structures*. John Wiley & Sons, Inc., New York, NY, 2000.
15. Benveniste, Y. “A New Approach to the Application of Mori-Tanaka’s Theory in Composite Materials”. *Mechanics of Materials*, 6:147–157, 1987.
16. Berryman, J. G. “Long-Wavelength Propagation in Composite Elastic Media I: Spherical Inclusions”. *Journal of the Acoustical Society of America*, 68(6):1809–1819, 1980.

17. Berryman, J. G. “Long-Wavelength Propagation in Composite Elastic Media II: Ellipsoidal Inclusions”. *Journal of the Acoustical Society of America*, 68(6):1820–1831, 1980.
18. Birman, V. and L. W. Byrd. “Modeling and Analysis of Functionally Graded Materials and Structures”. *Applied Mechanics Reviews*, 60:195–216, 2007.
19. Blitz, J. and G. Simpson. *Ultrasonic Methods of Non-Destructive Testing*. Chapman & Hall, London, UK, 1996.
20. Blosser, M. L. *Development of Metallic Thermal Protection Systems for the Reusable Launch Vehicle*. Technical Memorandum 110296, NASA, October 1996.
21. Boresi, A. P., R. J. Schmidt, and O. M. Sidebottom. *Advanced Mechanics of Materials*. John Wiley & Sons, Inc., New York, NY, fifth edition, 1993.
22. Box, G. E. P. and D. W. Behnken. “Some New Three Level Designs for the Study of Quantitative Variables”. *Technometrics*, 2:455–475, 1960.
23. Bruck, H. A. “A One-Dimensional Model for Designing Functionally Graded Materials to Manage Stress Waves”. *International Journal of Solids and Structures*, 37:6383–6395, 2000.
24. Byrd, L., T. Beberniss, B. Chapman, G. Cooley, and J. Feie. “Dynamic Response of Layered TiB/Ti Functionally Graded Material Specimens”. *Proceedings of FGM2006 Multiscale and Functionally Graded Materials Conference*. American Institute of Physics, Honolulu, Hawaii, October 2006.
25. Carpenter, R. D., W. W. Liang, G. H. Paulino, J. C. Gibeling, and Z. A. Munir. “Fracture Testing and Analysis of a Layered Functionally Graded Ti/TiB Beam in 3-Point Bending”. *Materials Science Forum*, 308-311:837–842, 1999.
26. Chapman, B. D. *Characterization of Functionally Graded Materials*. Master’s thesis, Graduate School of Engineering, Air Force Institute of Technology (AFIT), Wright-Patterson AFB, OH, March 2006. AFIT/GAE/ENY/06-M05.
27. Chichili, D. R., K. T. Ramesh, and K. J. Hemker. “The High-Strain-Rate Response of Alpha-Titanium: Experiments, Deformation Mechanisms and Modeling”. *Acta Materialia*, 46(3):1025–1043, 1998.
28. Cho, J. R. and J. H. Choi. “A Yield-Criteria Tailoring of the Volume Fraction in Metal-Ceramic Functionally Graded Material”. *European Journal of Mechanics A/Solids*, 23:271–281, 2004.
29. Cleveland, W. S. “Robust Locally Weighted Regression and Smoothing Scatterplots”. *Journal of American Statistical Association*, 74(368):829–836, 1979.
30. Cleveland, W. S. and S. J. Devlin. “Locally Weighted Regression: An Approach to Regression Analysis by Local Fitting”. *Journal of American Statistical Association*, 83(403):596–610, 1988.

31. Cook, R. D., D. S. Malkus, M. E. Plesha, and R. J. Witt. *Concepts and Applications of Finite Element Analysis*. John Wiley & Sons, Inc., New York, NY, fourth edition, 2002.
32. Cooley, W. G. *Application of Functionally Graded Materials in Aircraft Structures*. Master's thesis, Graduate School of Engineering, Air Force Institute of Technology (AETC), Wright-Patterson AFB, OH, March 2005. AFIT/GAE/ENY/05-M04.
33. Curry, D. M. *Space Shuttle Orbiter Thermal Protection System Design and Flight Experience*. Technical Memorandum 104773, NASA, July 1993.
34. Daniel, I. M. and O. Ishai. *Engineering Mechanics of Composite Materials*. Oxford University Press, New York, NY, second edition, 2006.
35. Daryabeigi, K., M. L. Blosser, and K. E. Wurster. "Displacements of Metallic Thermal Protection System Panels During Reentry". *Ninth AIAA/ASME Joint Thermophysics & Heat Transfer Conference, San Francisco, CA*. NASA Langley Research Center, Hampton, VA, June 2006.
36. Decker, B. F. and J. S. Kasper. "The Crystal Structure of TiB". *Acta Crystallographica*, 7:77–80, 1954.
37. Dennis, J. E. and R. B. Schnabel. *Numerical Methods for Unconstrained Optimization and Nonlinear Equations*. Society for Industrial and Applied Mathematics, Philadelphia, PA, 1983.
38. Drake, J. T., R. L. Williamson, and B. H. Rabin. "Finite Element Analysis of Thermal Residual Stresses at Graded Ceramic-Metal Interfaces, Part II: Interface Optimization for Residual Stress Reduction". *Journal of Applied Physics*, 74(2):1321–1326, 1993.
39. Drumheller, D. S. *Introduction to Wave Propagation in Nonlinear Fluids and Solids*. Cambridge University Press, Cambridge, UK, 1998.
40. Felbeck, D. K. *Strength and Fracture of Engineering Solids*. Prentice-Hall, Englewood Cliffs, NJ, 1984.
41. Finot, M., S. Suresh, C. Bull, and S. Sampath. "Curvature Changes During Thermal Cycling of a Compositionally Graded Ni-Al₂O₃ Multi-Layered Material". *Materials Science and Engineering*, A-205:59–71, 1996.
42. Fischmeister, H. and B. Karlsson. "Plasticity of Two-Phase Materials with a Coarse Microstructure". *Zeitschrift fur Metallkunde*, 68:311–327, 1977.
43. Follansbee, P. S. and G. T. Gray. "An Analysis of the Low Temperature, Low and High Strain-Rate Deformation of Ti-6Al-4V". *Metallurgical Transactions A*, 20A:863–874, 1989.
44. Follansbee, P. S. and U. F. Kocks. "A Constitutive Description of the Deformation of Copper Based on the Use of the Mechanical Threshold Stress as an Internal State Variable". *Acta Metallurgica*, 36(1):81–93, 1988.

45. General Research Corp., Dynatup Products, Santa Barbara, CA. *Model 8250 Impact Test Machine*.
46. Giannakopoulos, A. E., S. Suresh, M. Finot, and M. Olsson. "Elastoplastic Analysis of Thermal Cycling: Layered Materials with Compositional Gradients". *Acta Metallurgica et Materialia*, 43(4):1335–1354, 1995.
47. Gill, P. E., W. Murray, and M. H. Wright. *Practical Optimization*. Academic Press, London, UK, 1981.
48. Goldsmith, W. *Impact: The Theory and Physical Behaviour of Colliding Solids*. Edward Arnold, Ltd., London, UK, 1960.
49. Gong, S. W., K. Y. Lam, and J. N. Reddy. "The Elastic Response of Functionally Graded Cylindrical Shells to Low-Velocity Impact". *International Journal of Impact Engineering*, 22(4):397–417, 1999.
50. Graff, K. *Wave Motion in Elastic Solids*. Ohio State University Press, Columbus, OH, 1975.
51. Greszczuk, L. B. and H. Chao. *Investigation of Brittle Fractures in Graphite-Epoxy Composites Subjected to Impact*. Technical Memorandum USAAMRDL-TR-75-15, Army Air Mobility Research and Development Laboratory, May 1975.
52. Haftka, R. T., Z. Gurdal, and M. P. Kamat. *Elements of Structural Optimization*. Kluwer Academic Publishers, Boston, MA, second edition, 1990.
53. Hashin, Z. and S. Shtrikman. "A Variational Approach to the Theory of the Elastic Behaviour of Multiphase Materials". *Journal of the Mechanics and Physics of Solids*, 11:127–140, 1963.
54. Hellier, C. (editor). *Handbook of Nondestructive Evaluation*. McGraw-Hill, Inc., New York, NY, 2001.
55. Hill, M. R. and W. Lin. "Residual Stress Measurement in a Ceramic-Metallic Graded Material". *Journal of Engineering Materials and Technology*, 124:185–191, 2002.
56. Hill, R. "A Self-Consistent Mechanics of Composite Materials". *Journal of the Mechanics and Physics of Solids*, 13:213–222, 1965.
57. Hsieh, J. J. and L. T. Lee. "An Inverse Problem for a Functionally Graded Elliptical Plate with Large Deflection and Slightly Disturbed Boundary". *International Journal of Solids and Structures*, 43:5981–5993, 2006.
58. Javaheri, R. and M. R. Eslami. "Buckling of Functionally Graded Plates Under In-Plane Compressive Loading". *ZAMM*, 82(4):277–283, 2002.
59. Javaheri, R. and M. R. Eslami. "Thermal Buckling of Functionally Graded Plates". *AIAA Journal*, 40(1):162–169, 2002.

60. Javaheri, R. and M. R. Eslami. "Thermal Buckling of Functionally Graded Plates Based on Higher Order Theory". *Journal of Thermal Stresses*, 25:603–625, 2002.
61. Jr., T. L. Becker, R. M. Cannon, and R. O. Ritchie. "An Approximate Method for Residual Stress Calculation in Functionally Graded Materials". *Mechanics of Materials*, 32:85–97, 2000.
62. Khan, A. S. and S. Huang. *Continuum Theory of Plasticity*. John Wiley & Sons, Inc., New York, NY, 1995.
63. Kieback, B., A. Neubrand, and H. Riedel. "Processing Techniques for Functionally Graded Materials". *Materials Science and Engineering A*, 362:81–105, 2003.
64. Lambros, J., A. Narayanaswamy, M. H. Santare, and G. Anlas. "Manufacture and Testing of a Functionally Graded Material". *Journal of Engineering Materials and Technology*, 121:488–493, 1999.
65. Lambros, J., M. H. Santare, H. Li, and G. H. Sapna III. "A Novel Technique for the Fabrication of Laboratory Scale Functionally Graded Materials". *Experimental Mechanics*, 39(3):184–190, 1999.
66. Lankford, J. "Plastic Deformation of Partially Stabilized Zirconia". *Communications of the American Ceramic Society*, C212–C213, November 1983.
67. Lankford, J. "The Influence of Temperature and Loading Rate on Flow and Fracture of Partially Stabilized Zirconia". *Journal of Materials Science*, 20:53–59, 1985.
68. Lankford, J. "Inverse Strain Rate Effects and Microplasticity in Zirconia Crystals". *Journal of Material Science Letters*, 8(8):947–949, 1989.
69. Lawson, J. and J. Erjavec. *Modern Statistics for Engineering and Quality Improvement*. Duxbury/Thomas Learning, Inc., Pacific Grove, CA, 2001.
70. Lee, W. S. and C. F. Lin. "Plastic Deformation and Fracture Behaviour of Ti-6Al-4V Alloy Loaded with High Strain Rate Under Various Temperatures". *Materials Science and Engineering*, A241:48–59, 1998.
71. Li, Y. and K. T. Ramesh. "Influence of Particle Volume Fraction, Shape, and Aspect Ratio on the Behavior of Particle-Reinforced Metal-Matrix Composites at High Rates of Strain". *Acta Materialia*, 46(16):5633–5646, 1998.
72. Li, Y., K. T. Ramesh, and E. S. C. Chin. "Viscoplastic Deformations and Compressive Damage in an A359/SiC_p Metal-Matrix Composite". *Acta Materialia*, 48:1563–1573, 2000.
73. Li, Y., K. T. Ramesh, and E. S. C. Chin. "Dynamic Characterization of Layered and Graded Structures Under Impulsive Loading". *International Journal of Solids and Structures*, 38:6045–6061, 2001.

74. Loy, C. T., K. Y. Lam, and J. N. Reddy. "Vibration of Functionally Graded Cylindrical Shells". *International Journal of Mechanical Sciences*, 41(3):309–324, 1999.
75. Luciano, R. and J. R. Willis. "Non-Local Constitutive Equations for Functionally Graded Materials". *Mechanics of Materials*, 36:1195–1206, 2004.
76. Malvern, L. *Introduction to the Mechanics of a Continuous Medium*. Prentice-Hall, Inc., Upper Saddle River, NJ, 1969.
77. McIntire, P., A. S. Birks, and R. E. Green Jr. (editors). *Nondestructive Testing Handbook: Volume Seven, Ultrasonic Testing*. American Society for Nondestructive Testing, Inc., second edition, 1991.
78. Mecking, H. and U. F. Kocks. "Kinetics of Flow and Strain-Hardening". *Acta Metallurgica*, 29:1865–1875, 1981.
79. Meyers, M. A., G. Subhash, B. K. Kad, and L. Prasad. "Evolution of Microstructure and Shear-Band Formation in α -HCP Titanium". *Mechanics of Materials*, 17:175–193, 1994.
80. Mindlin, R. D. "Influence of Rotary Inertia and Shear on Flexural Motions of Isotropic Elastic Plates". *ASME Journal of Applied Mechanics*, 18(1):31–38, 1951.
81. Mori, T. and K. Tanaka. "Average Stress in Matrix and Average Elastic Energy of Materials with Misfitting Inclusions". *Acta Metallurgica*, 21:571–574, 1973.
82. Myers, R. H. and D. C. Montgomery. *Response Surface Methodology: Process and Product Optimization Using Designed Variables*. John Wiley & Sons, Inc., New York, NY, 1995.
83. Na, K. S. and J. H. Kim. "Three-Dimensional Thermomechanical Buckling of Functionally Graded Materials". *AIAA Journal*, 43(7):1605–1612, 2005.
84. Nemat-Nasser, S., W. G. Guo, and J. Y. Cheng. "Mechanical Properties and Deformation Mechanisms of a Commercially Pure Titanium". *Acta Materialia*, 47(13):3705–3720, 1999.
85. Ng, T. Y., K. Y. Lam, K. M. Liew, and J. N. Reddy. "Dynamic Stability Analysis of Functionally Graded Cylindrical Shells Under Periodic Axial Loading". *International Journal of Solids and Structures*, 38:1295–1309, 2001.
86. Oberg, E., F. D. Jones, H. L. Horton, and H. H. Ryffell. *Machinery's Handbook*. Industrial Press, Inc., New York, NY, 26th edition, 2000.
87. Pai, P. F. and A. N. Palazotto. "Two-Dimensional Sublamination Theory for Analysis of Functionally Graded Plates". *Journal of Sound and Vibration*, 308:164–189, 2007.
88. Palazotto, A. N. and S. T. Dennis. *Nonlinear Analysis of Shell Structures*. American Institute of Aeronautics and Astronautics, Washington, D. C., 1992.

89. Panda, K. B. and K. S. Ravichandran. "Synthesis of Ductile Titanium-Titanium Boride (Ti-TiB) Composites with a Beta-Titanium Matrix: The Nature of TiB Formation and Composite Properties". *Metallurgical and Materials Transactions A*, 34:1371–1385, 2003.
90. Panda, K. B. and K. S. Ravichandran. "First Principles Determination of Elastic Constants and Chemical Bonding of Titanium Boride (TiB) On the Basis of Density Functional Theory". *Acta Materialia*, 54:1641–1657, 2006.
91. Parameswaran, V. and A. Shukla. "Processing and Characterization of a Model Functionally Gradient Material". *Journal of Materials Science*, 35:21–29, 2000.
92. Pradhan, S. C., C. T. Loy, K. Y. Lam, and J. N. Reddy. "Vibration Characteristics of Functionally Graded Cylindrical Shells Under Various Boundary Conditions". *Applied Acoustics*, 61:111–129, 2000.
93. Prakesh, T. and M. Ganapathi. "Asymmetric Flexural Vibration and Thermoelastic Stability of FGM Circular Plates Using Finite Element Method". *Composites, Part B*, 37:642–649, 2006.
94. Praveen, G. N. and J. N. Reddy. "Nonlinear Transient Thermoelastic Analysis of Functionally Graded Ceramic-Metal Plates". *International Journal of Solids and Structures*, 35(33):4457–4476, 1998.
95. Prime, M. B. "Residual Stress Measurement by Successive Extension of a Slot: The Crack Compliance Method". *Applied Mechanics Review*, 52(2):75–96, 1999.
96. Ravichandran, K. S. "Thermal Residual Stresses in a Functionally Graded Material System". *Materials Science and Engineering*, A-201:269–276, 1995.
97. Ravichandran, K. S., K. B. Panda, and S. S. Sahay. "TiBw-Reinforced Ti Composites: Processing, Properties, Application Prospects, and Research Needs". *JOM : The Journal of the Minerals, Metals & Materials Society*, 56(5):42–48, 2004.
98. Reddy, J. N. "Analysis of Functionally Graded Plates". *International Journal for Numerical Methods in Engineering*, 47:663–684, 2000.
99. Reddy, J. N. *Mechanics of Laminated Composite Plates and Shells: Theory and Analysis*. CRC Press, Boca Raton, FL, second edition, 2004.
100. Reddy, J. N. *Theory and Analysis of Elastic Plates and Shells*. CRC Press, Boca Raton, FL, second edition, 2006.
101. Reddy, J. N. and Z.-Q. Cheng. "Three-Dimensional Thermomechanical Deformations of Functionally Graded Rectangular Plates". *European Journal of Mechanics-A/Solids*, 20(5):841–860, 2001.
102. Reddy, J. N. and Z.-Q. Cheng. "Frequency Correspondence Between Membranes and Functionally Graded Spherical Shallow Shells of Polygonal Planform". *International Journal of Mechanical Sciences*, 44(5):967–985, 2002.

103. Reddy, J. N., C. M. Wang, and S. Kitipornchai. "Axisymmetric Bending of Functionally Graded Circular and Annular Plates". *European Journal of Mechanics and Solids*, 18:185–199, 1999.
104. Reissner, E. "On Bending of Elastic Plates". *Quarterly of Applied Mathematics*, 5(1):55–68, 1947.
105. Reiter, T. and G. J. Dvorak. "Micromechanical Models for Graded Composite Materials". *Journal of the Mechanics and Physics of Solids*, 45(8):1281–1302, 1997.
106. Reiter, T. and G. J. Dvorak. "Micromechanical Models for Graded Composite Materials II: Thermomechanical Loading". *Journal of the Mechanics and Physics of Solids*, 46(9):1655–1673, 1998.
107. Rosen, R. S., S. P. Paddon, and M. E. Kassner. "The Variation of the Yield Stress of Ti Alloys with Strain Rate at High Temperatures". *Journal of Materials Engineering and Performance*, 8(3):361–367, 1999.
108. Saada, A. S. *Elasticity: Theory and Applications*. Krieger Publishing Co., Malabar, FL, second edition, 1993.
109. Sahay, S. S., K. S. Ravichandran, R. Atri, B. Chen, and J. Rubin. "Evolution of Microstructure and Phases In Situ Processed Ti-TiB Composites Containing High Volume Fractions of TiB Whiskers". *Journal of Materials Research*, 14(11):4214–4223, 1999.
110. Schwartz, M. (editor). *Handbook of Structural Ceramics*. McGraw-Hill, Inc., New York, NY, 1992.
111. Shao, Z. S. "Mechanical and Thermal Stresses of a Functionally Graded Circular Hollow Cylinder with Finite Length". *International Journal of Pressure Vessels and Piping*, 82:155–163, 2005.
112. Shao, Z. S. and T. J. Wang. "Three-Dimensional Solutions for the Stress Fields in Functionally Graded Cylindrical Panel with Finite Length Subjected to Thermal/Mechanical Loads". *International Journal of Solids and Structures*, 43:3856–3874, 2006.
113. Shariat, B. A. Samsam and M. R. Eslami. "Thermal Buckling of Imperfect Functionally Graded Plates". *International Journal of Solids and Structures*, 43:4082–4096, 2006.
114. Shariat, B. A. Samsam and M. R. Eslami. "Buckling of Thick Functionally Graded Plates Under Mechanical and Thermal Loads". *Composite Structures*, 78:433–439, 2007.
115. Shariat, B. A. Samsam, R. Javaheri, and M. R. Eslami. "Buckling of Imperfect Functionally Graded Plates Under In-Plane Compressive Loading". *Thin-Walled Structures*, 43:1020–1036, 2005.

116. Shen, H.-S. "Nonlinear Bending Response of Functionally Graded Plates Subjected to Transverse Loads and in Thermal Environments". *International Journal of Mechanical Sciences*, 44:561–584, 2002.
117. Shen, H.-S. "Postbuckling Analysis of Axially-Loaded Functionally Graded Cylindrical Shells in Thermal Environments". *Composite Science and Technology*, 62:977–987, 2002.
118. Smith, W. *Principles of Materials Science and Engineering*. McGraw-Hill Companies, Inc., New York, NY, third edition, 1999.
119. Soedel, W. *Vibrations of Shells and Plates*. Marcel Dekker, Inc., New York, NY, third edition, 2004.
120. Sofiyev, A. H. "The Stability of Functionally Graded Truncated Conical Shells Subjected to Aperiodic Impulsive Loading". *International Journal of Solids and Structures*, 41:3411–3424, 2004.
121. Sundararajan, N., T. Prakesh, and M. Ganapathi. "Dynamic Buckling of Functionally Graded Spherical Caps". *AIAA Journal*, 44(5):1097–1102, 2006.
122. Suresh, S. and A. Mortensen. *Fundamentals of Functionally Graded Materials: Processing and Thermomechanical Behaviour of Graded Metals and Metal-Ceramic Composites*. IOM Communications, Ltd., Cambridge, UK, 1998.
123. Tamura, I., Y. Tomota, and H. Ozawa. "Strength and Ductility of FeNiC Alloys Composed of Austenite and Martensite with Various Strength". *Proceedings of the Third International Conference on Strength of Metals and Alloys*, volume 1, 611–615. 1973.
124. Timoshenko, S. and S. Woinowsky-Krieger. *Theory of Plates and Shells*. McGraw-Hill Book Co., New York, NY, second edition, 1959.
125. Ugural, A. C. *Stresses in Plates and Shells*. McGraw-Hill Co., New York, NY, second edition, 1999.
126. Vel, S. S. and R. C. Batra. "Exact Solution for Thermoelastic Deformations of Functionally Graded Thick Rectangular Plates". *AIAA Journal*, 40(7):1421–1433, 2002.
127. Vishay Micro-Measurements. *125AC Series Strain Gages*, April 2006. Document 11193.
128. Vishay Micro-Measurements. *M-Bond AE-15*, December 2006. Document 11012.
129. Vishay Micro-Measurements. *Bondable Terminals*, March 2007. Document 11022.
130. Vishay Micro-Measurements. *High Elongation Strain Measurements*, April 2007. Application Note TT-605, Document No. 11085.

131. Vishay Micro-Measurements. *Wire, Cable, and Accessories*, November 2007. Document 11024.
132. Wang, C. M., J. N. Reddy, and K. H. Lee. *Shear Deformable Beams and Plates: Relationships with Classical Solutions*. Elsevier, New York, NY, 2000.
133. Westergaard, H. M. "Stresses in Concrete Pavements Computed By Theoretical Analysis". *Public Roads—U.S. Dept. of Agriculture*, 7(2):25–35, 1926.
134. Williamson, R. L., B. H. Rabin, and J. T. Drake. "Finite Element Analysis of Thermal Residual Stresses at Graded Ceramic-Metal Interfaces, Part I: Model Description and Geometrical Effects". *Journal of Applied Physics*, 74(2):1310–1320, 1993.
135. Window, A. L. and G. S. Holister (editors). *Strain Gauge Technology*. Applied Science Publishers, London, UK, 1982.
136. Woo, J. and S. A. Meguid. "Nonlinear Analysis of Functionally Graded Plates and Shallow Shells". *International Journal of Solids and Structures*, 38:7409–7421, 2001.
137. Yang, J., K. M. Liew, and S. Kitipornchai. "Imperfection Sensitivity of the Post-Buckling Behavior of Higher-Order Shear Deformable Functionally Graded Plates". *International Journal of Solids and Structures*, 43:5247–5266, 2006.
138. Yang, J. and H.-S. Shen. "Dynamic Response of Initially Stressed Functionally Graded Rectangular Thin Plates". *Composite Structures*, 54:497–508, 2001.
139. Yang, J. and H.-S. Shen. "Vibration Characteristics and Transient Response of Shear Deformable Functionally Graded Plates in Thermal Environments". *Journal of Sound and Vibration*, 255(3):579–602, 2002.
140. Yin, H. M., G. H. Paulino, W. G. Buttlar, and L. Z. Sun. "Micromechanics-Based Thermoelastic Model for Functionally Graded Particulate Materials with Particle Interactions". *Journal of the Mechanics and Physics of Solids*, 55:132–160, 2007.
141. Young, W. C. and R. G. Budynas (editors). *Roark's Formulas for Stress and Strain*. McGraw-Hill Companies, New York, NY, seventh edition, 2002.
142. Zukas, J. A., T. Nicholas, H. F. Swift, L. B. Greszczuk, and D. R. Curran. *Impact Dynamics*. John Wiley & Sons, Inc., New York, NY, 1982.
143. Zwillinger, D. (editor). *CRC Standard Mathematical Tables and Formulae*. Chapman & Hall, CRC Press, Boca Raton, FL, thirty-first edition, 2003.

Vita

Captain Reid A. Larson graduated Summa Cum Laude with a Bachelor of Science degree in Mechanical Engineering from the University of North Dakota in May 2000. Immediately after graduation he continued his studies at the University of North Dakota and graduated with a Master of Science degree in Mechanical Engineering in May 2003.

While studying for his Master's degree, Reid was hired by Cirrus Design Corporation, a manufacturer of general aviation aircraft, and served as a Liaison Engineer at the Grand Forks, North Dakota facility. In this capacity, he was responsible for designing structural repairs to the all-composite airframes of the SR-20 and SR-22 aircraft. In addition, Reid was responsible for production improvements to streamline manufacturing processes.

Reid attended the Officer Training School (OTS) and was commissioned in the United States Air Force in June 2003. Immediately after completing OTS, his first assignment was in the Air Force Research Laboratory, Control Sciences Division, at Wright-Patterson AFB, OH. In this position, he served as a Developmental Flight Controls Engineer and conducted research associated with autonomous cooperative control of unmanned vehicles. In August 2005, he was next assigned to the Air Force Institute of Technology, Wright-Patterson AFB, OH, to complete Ph.D. studies in Aerospace Engineering which he began in January 2004 as a part-time student.

Captain Larson's research interests include the areas of solid mechanics, structural integrity, composite materials, optimization & optimal control, and manufacturing techniques.

Permanent address: 2950 Hobson Way
Air Force Institute of Technology
Wright-Patterson AFB, OH 45433

REPORT DOCUMENTATION PAGE					<i>Form Approved</i> <i>OMB No. 0704-0188</i>	
The public reporting burden for this collection of information is estimated to average 1 hour per response, including the time for reviewing instructions, searching existing data sources, gathering and maintaining the data needed, and completing and reviewing the collection of information. Send comments regarding this burden estimate or any other aspect of this collection of information, including suggestions for reducing this burden to Department of Defense, Washington Headquarters Services, Directorate for Information Operations and Reports (0704-0188), 1215 Jefferson Davis Highway, Suite 1204, Arlington, VA 22202-4302. Respondents should be aware that notwithstanding any other provision of law, no person shall be subject to any penalty for failing to comply with a collection of information if it does not display a currently valid OMB control number. PLEASE DO NOT RETURN YOUR FORM TO THE ABOVE ADDRESS.						
1. REPORT DATE (DD-MM-YYYY) 11-09-2008		2. REPORT TYPE Doctoral Dissertation			3. DATES COVERED (From — To) Aug 2005 — Sep 2008	
4. TITLE AND SUBTITLE A Novel Method For Characterizing the Impact Response of Functionally Graded Plates				5a. CONTRACT NUMBER		
				5b. GRANT NUMBER		
				5c. PROGRAM ELEMENT NUMBER		
6. AUTHOR(S) Reid A. Larson, Captain, USAF				5d. PROJECT NUMBER ENY 07-402		
				5e. TASK NUMBER		
				5f. WORK UNIT NUMBER		
7. PERFORMING ORGANIZATION NAME(S) AND ADDRESS(ES) Air Force Institute of Technology Graduate School of Engineering and Management (AFIT/EN) 2950 Hobson Way WPAFB OH 45433-7765					8. PERFORMING ORGANIZATION REPORT NUMBER AFIT/DS/ENY/08-06	
9. SPONSORING / MONITORING AGENCY NAME(S) AND ADDRESS(ES) AFRL/RBSM Attn: Dr. Ravinder Chona 2790 D Street, Bldg 65 WPAFB OH 45433					10. SPONSOR/MONITOR'S ACRONYM(S)	
					11. SPONSOR/MONITOR'S REPORT NUMBER(S)	
12. DISTRIBUTION / AVAILABILITY STATEMENT Approved for Public Release; Distribution Unlimited						
13. SUPPLEMENTARY NOTES						
14. ABSTRACT Functionally graded material (FGM) plates are advanced composites with properties that vary continuously through the thickness of the plate. Metal-ceramic FGM plates have been proposed for use in thermal protection systems where a metal-rich interior surface of the plate gradually transitions to a ceramic-rich exterior surface of the plate. The ability of FGMs to resist impact loads must be demonstrated before using them in high-temperature environments in service. This dissertation presents a novel technique by which the impact response of FGM plates is characterized for low-velocity, low-to medium-energy impact loads. An experiment was designed where strain histories in FGM plates were collected during impact events. These strain histories were used to validate a finite element simulation of the test. An optimization technique was applied to estimate local material properties in the FGM plate to enhance the finite element simulation. The optimized simulation captured the physics of the impact events. The method allows research & design engineers to make informed decisions necessary to implement FGM plates in aerospace platforms.						
15. SUBJECT TERMS functionally graded materials, impact dynamics, parameter estimation, finite elements, thermal protection systems						
16. SECURITY CLASSIFICATION OF:			17. LIMITATION OF ABSTRACT UU	18. NUMBER OF PAGES 368	19a. NAME OF RESPONSIBLE PERSON Dr. Anthony N. Palazotto, AFIT/ENY	
a. REPORT U	b. ABSTRACT U	c. THIS PAGE U			19b. TELEPHONE NUMBER (include area code) (937) 255-3636, ext 4599	